STUDIES ON NANOSTRUCTURED METAL OXIDES AS PROSPECTIVE ANODES FOR LITHIUM ION BATTERIES

BY

CHRISTIE THOMAS CHERIAN

(M.Sc., COCHIN UNIVERSITY OF SCIENCE AND TECHNOLOGY)

A THESIS SUBMITTED

FOR THE DEGREE OF DOCTOR OF PHILOSOPHY

DEPARTMENT OF PHYSICS

NATIONAL UNIVERSITY OF SINGAPORE

2013

Declaration

I hereby declare that this thesis is my original work and it has been written by me in its entirety. I have duly acknowledged all the sources of information which have been used in the thesis.

This thesis has also not been submitted for any degree in any university previously.

Christie Thomas Cherian

22-01-2013

Acknowledgements

First and foremostly, I would like to express my sincere gratitude and heartfelt thanks to my supervisors; Prof. B.V.R. Chowdari and Assoc. Prof Sow Chorng Haur of the Physics Department for the great contribution and their wide knowledge, incessant encouragement and guidance which was a great help to build up a good basis for the thesis.

I owe my sincere thanks to Prof G. V. Subba Rao for his advice during my entire research endeavor. His observations and comments helped me to establish the overall direction of the research and to move ahead.

I am thankful to Dr M.V. Reddy for helping me with the experimental techniques involved in the synthesis and characterization of anode materials.

The financial support by way of research scholarship and facilities from National University of Singapore is gratefully acknowledged.

My sincere thanks to my lab mates Mr.Shahul, Mr.Wu, Dr. Yogesh, Dr.Das, Dr.Aravindan and Dr. Prabhu for all the help and memorable moment shared and special thanks to Dr. Sundaramurthy and Mr. Minrui for the fruitful collaborative projects. It is my humble duty to express my gratitude to the entire academic and administrative staff of the Department of Physics. I thank Mr. Suradi and other staff from Physics workshop for their support. The help rendered by our lab officer Mr. Karim and Ms Foo is worth acknowledging.

I am grateful to the staff of the Chemical, Molecular and Materials Analysis Centre of the Department of Chemistry for helping me with the thermal and elemental

analysis on powder samples. For support with microscopy, I would like to thank Ms. Zhang Jixuan from Materials Science and Engineering, NUS.

My biggest personal thanks go to my friend Aparna and her husband, Bibin for their unconditional love, support and the homemade delicious food. My heartfelt thanks to my roomies Anand, Rikas, Risal and Robin who gifted me a lot of loving and unforgettable moments. My countless thanks to my dearest friends Bivin, Bivitha and Minu for their spirited support throughout my research studies. More than my friends, we are a single family.

I would like to thank my relatives and friends for their kindness, confidence and spirited support outside of academia. I am indebted to my parents, Prof. Cherian Thomas and Prof. Susan Cherian, for their prayers, consistent encouragement and motivation. Very special thanks to my very special brother, Benmon, for his love and affection. I also gratefully acknowledge the influence of my sister, Angel and my brother-in law, Jino and little Jeremy. I owe my loving thanks to my better half, Merry who came to my life during the last semester of my PhD studies. Without her encouragement and understanding, it would have been impossible for me to finish the thesis writing so soon.

Finally, my utmost gratitude is to God who directed me to take up this assignment.

Contents

Summary

The higher volumetric (Wh l^{-1}) and gravimetric energy (Wh kg^{-1}) storage capabilities are the key characteristics of the lithium ion batteries (LIBs), leading to smaller and lighter cells compared to other conventional battery systems. Thus LIBs paved the way for the proliferation of portable battery-powered electronic devices. Utilizing novel materials as well as engineering novel and even conventional materials in a nano-scale level have been the second-phase driver leading the direction of research and development of LIBs for clean energy transportation. The goal of the present work is to establish the synthetic methods and measurement procedures necessary to investigate various oxide nanostructures for use in Li-ion batteries. Anode materials for lithium ion batteries can be classified into three different categories based on their energy storage mechanisms: intercalation- based materials, conversion-reaction-based materials and alloying-reaction based materials. Representative materials from each category are prepared in nano-scale and the effects of cycling voltage range, particle size and morphology on the anodic performance of these materials are illustrated in the thesis.

Ti-based oxides have been considered as potential 'intercalation' anode materials since they exhibit excellent Li-ion insertion/extraction reversibility with small structural change. It is of significant interest to examine the Li-cycling of doped TiO_2 as doping can modify the charge transfer and the unit cell dimensions of TiO_2. Nitrogen and fluorine co-doped-TiO_2 of composition, $TiO_{1.9}(N_{0.05}F_{0.15})$ (hereafter TiO_2(N, F)) is synthesised by simple solid state method. Its conversion to nano-phase rutile after high energy ball-milling, and their Li-storage and cycling properties in the

voltage range, 1-2.8 V vs. Li are investigated. But the maximum attainable capacity of intercalation based anodes is much lower than that of conversion' reaction based materials. Iron based binary and ternary oxides as prospective anode materials due to their high capacity from conversion reaction, environment friendliness, abundance and low cost. In this project, iron oxides such as Fe_2O_3 and $NiFe_2O_4$ are fabricated in nano-scale by electrospinning and its electrochemical performance is evaluated in the voltage range 0.005- 3.0 V. The morphological changes of the $NiFe_2O_4$ nanofibers and nanoparticles during the Li-cycling are investigated in detail. Molybdates can also be considered as 'conversion' reaction based oxides due to the ability of the metal ions to exist in several oxidation states in these oxides, ranging from 3^+ to 6^+ for Mo, reversibly reacting with Li delivering high capacity, at potentials lower than 2 V. Molybdates of general formula, $AMoO_4$ (A= Co, Zn, Ni) are synthesized by polymer precursor method and citric acid assisted microwave assisted method to tune the particle size and morphology. The role of counter cations and effect of morphology on the Li-cycling behaviour of molybdates have been investigated. The reaction potentials of these 'conversion' reaction based oxides are relatively higher than that of commercial graphite which leads to lower cell potential then finally to lower energy density than that expected from high capacities.

On the other hand Li-alloying elements can reversibly react with large amount of Li at relatively low voltage vs. Li. Among the Li-alloying materials, Sn and Si have been considered as the most attractive anode materials for Li-ion batteries because it has the highest gravimetric and volumetric capacity and is also abundant, cheap, and environmentally benign. Sn based binary and ternary oxides have been studied as

anode materials since they can be reduced to Sn by Li and hence could be used as precursors for $Li_{4.4}Sn$ alloys. Here, nanostructures of a simple tin oxide, SnO and a ternary oxide, Zn_2SnO_4 are synthesized and the effects of proper voltage range and morphology on its Li-cycling performance are investigated. The structural and morphological evolutions of the Zn_2SnO_4 nanowires upon lithium insertion/de-insertion are also studied.

List of Figures

List of Tables

List of Publications

1. (N, F)-co-doped TiO_2: Synthesis, anatase-rutile conversion and Li-cycling properties.
   Christie T. Cherian, M. V. Reddy, Travis Magdaleno, Chorng Haur Sow, K. V. Ramanujachary, G. V. Subba Rao and B. V. R. Chowdari.
   CrystEngComm, 2012, 14, 978-986, DOI: 10.1039/C1CE05685A

2. Electro-spun Fe_2O_3 nanorods as stable high capacity anode material for Li-ion battery.
   Christie T. Cherian, J. Sundaramurthy, M. Kalaivani , P. Ragupathy , P. Suresh Kumar , V. Thavasi, M. V. Reddy , Chorng Haur Sow , S. G. Mhaisalkar , S. Ramakrishna and B. V. R. Chowdari.
   Journal of Materials Chemistry, 2012, 22, 12198-12204, DOI: 10.1039/C2JM31053H.

3. Li-cycling properties of nano-crystalline $(Ni_{1-x}Zn_x)Fe_2O_4$.
   Christie T. Cherian, M. V. Reddy, G. V. Subba Rao, Chorng Haur Sow, B. V. R. Chowdari.
   Journal of Solid State Electrochemistry, 2012, 16, 5, 1823-1832, DOI: 10.1007/s10008-012-1662-2.

4. Facile synthesis and Li-storage performance of SnO nanoparticles and microcrystals.
   Christie T. Cherian, M. V. Reddy, Chorng Haur Sow, B. V. R. Chowdari.
   RSC advances, 2012; DOI: 10.1039/c2ra22867j.

5. Interconnected network of $CoMoO_4$ sub-micron particles as high capacity anode material for Lithium ion batteries.
   Christie T. Cherian, M. V. Reddy, Chorng Haur Sow, B. V. R. Chowdari.
   ACS Applied Materials and Interfaces, 2012; DOI: 10.1021/am302583c.

6. Morphologically robust $NiFe_2O_4$ nanofibers as high capacity Li-ion battery anode material.
   Christie T. Cherian *et al*. (Submitted to Energy & Environmental Science)

7. Zn_2SnO_4 nanowire network vs. nanoparticles: Electrochemical performance as anode material in Lithium ion battery and morphological studies using ex-situ TEM.
   Christie T. Cherian *et al*. (Submitted to IOP Nanotechnology)

Chapter 1 Introduction to Lithium Ion Batteries

1.1 Motivation

Batteries provide a means for storing energy and as such they have become an indispensable entity in modern-day life. The higher volumetric (Wh l^{-1}) and gravimetric energy (Wh kg^{-1}) storage capabilities are the key characteristics of the lithium ion batteries (LIBs), leading to smaller and lighter cells compared to the conventional sealed nickel– cadmium (Ni–Cd), nickel-metal hydride (Ni-MH), and valve-regulated lead acid (VRLA) battery systems (Figure 1.1).[1] A typical LIB demonstrates a capacity and power about 150 Ah kg^{-1} and over 200 Wh kg^{-1}, respectively. The favorable electrochemical performance in terms of energy densities and advancements in system design and manufacturing have made LIBs, the enabling technology for the proliferation of portable battery-powered electronic devices, especially notebook computers and mobile phone applications. As the global economy begins to strain under the pressure of rising petroleum prices and environmental concerns, research have spurred into the development of various types of clean energy transportation systems such as Hybrid Electric Vehicles (HEVs), Battery Electric Vehicles (BEVs) and Plug-In Hybrid Electric Vehicles (PHEVs).[2] For BEVs, batteries with stored energies of 5–30 kWh for electric cars and up to 100 kWh for electric buses are required; whereas HEVs hold 1–5 kWh of stored energy, and focus more exclusively on high power discharge.[2] Thus the recent market demands for advanced lithium-ion batteries emphasize not only high-energy density but also very high-power density. The power parameters are largely defined by the kinetics of the electrochemical reaction, the surface area and thickness of the electrodes, the internal resistance of the individual cells, and the size and design of the cells.[3] Extensive studies on these aspects are needed in

order to fasten the current move to the next phase. Utilizing novel materials as well as engineering novel and even conventional materials in a nano-scale level have been the second-phase driver leading the direction of research and development of LIBs.

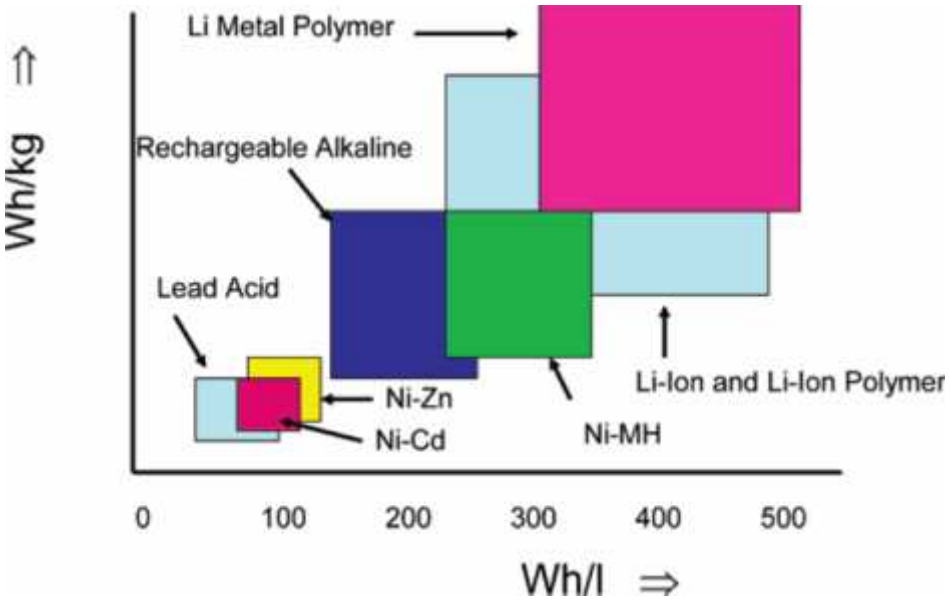

Figure 1.1 Comparison of the different battery technologies in terms of volumetric (Wh l^{-1}) and gravimetric (Wh kg^{-1}) energy density. Reprinted with permission from Winter, M., Brodd, R. (2004). "What Are Batteries, Fuel Cells, and Supercapacitors?" Chem. Rev., 2004, 104:4245-4269.

1.2 Electrochemical energy storage and conversion

A battery is a device that converts the chemical energy contained in its active materials directly into electric energy by means of an electrochemical oxidation-reduction (redox) reaction. In the case of a rechargeable system, the battery is recharged by a reversal of the process. This type of reaction involves the transfer of electrons from one material to another through an external electric circuit. In a non-electrochemical redox reaction, such as rusting or burning, the transfer of electrons occurs directly and only heat is involved. A battery consists of an array of cells, connected in series or parallel, or both, depending on the desired output

voltage and capacity. A cell is the basic electrochemical unit which consists of an assembly of electrodes, separators, electrolyte, container and terminals. The cell consists of three major components [4]:

i. The anode or negative electrode- the reducing or fuel electrode, which gives up electrons to the external circuit and is oxidized during the electrochemical reaction.

ii. The cathode or positive electrode- the oxidizing electrode, which accepts electrons from the external circuit and is reduced during the electrochemical reaction.

iii. The electrolyte- the ionic conductor, which provides the medium for transfer of charge, as ions, inside the cell between the anode and cathode. The electrolyte is typically a liquid, such as water or other solvents, with dissolved salts, acids, or alkalis to impart ionic conductivity. The electrolyte must have good ionic conductivity but not be electronically conductive, as this would cause internal short-circuiting. Other important characteristics are non-reactivity with the electrode materials, little change in properties with change in temperature, safety in handling, and low cost.

iv. Separator- physically the anode and cathode electrodes are electronically isolated in the cell to prevent internal short-circuiting, but are surrounded by the electrolyte. In practical cell designs, a separator material is used to separate the anode and cathode electrodes. The separator, however, is permeable to the electrolyte in order to maintain the desired ionic conductivity.

1.2.1 Primary and secondary batteries

Electrochemical cells and batteries are identified as primary (non-rechargeable) or secondary (rechargeable), depending on their capability of being electrically recharged. Primary batteries are not capable of being recharged electrically and hence are discharged once and discarded. Carbon-zinc, also known as the Leclanché battery, is the least expensive primary battery and comes with consumer devices when batteries are included. These general purpose batteries are used for applications with low power drain, such as remote controls, flashlights, children's toys and wall clocks. Another most common primary batteries for consumers is the alkaline-manganese, or alkaline for short. Secondary batteries can be recharged electrically, after discharge, to their original condition by passing current through them in the opposite direction to that of the discharge current. They are storage devices for electric energy and are known also as storage batteries or accumulators. Main secondary batteries include[3-5]:

- Lead Acid - One of the oldest rechargeable battery systems; is rugged, forgiving if abused and economical in price; has a low specific energy and limited cycle life. Lead acid is used for wheelchairs, golf cars, personnel carriers, emergency lighting and uninterruptible power supply (UPS).
- Nickel-cadmium (NiCd) - Mature and well understood; is used where long service life, high discharge current, extreme temperatures and economical price are of importance. Due to environmental concerns, NiCd is being replaced with other chemistries. Main applications are power tools, two-way radios, aircraft and UPS. 'Memory effect' is the major disadvantage.
- Nickel-metal-hydride (NiMH) - NiMH batteries are very similar to NiCd batteries: they use the same material for the cathode (NiOOH). The

difference is that instead of using cadmium for the anode, NiMH uses a hydrogen-absorbing alloy. NiMH is used for medical instruments, hybrid cars and industrial applications. NiMH is available in AA and AAA cells for consumer use. The main issues with NiMH are high self-discharge rate and limitations on design i.e. other than optimal cylindrical shapes reduce energy density and cycle life.

- Lithium-ion (Li-ion) - Lithium-ion batteries are very common in consumer electronics. Most phones are powered with this technology, because of their high energy density, low self-discharge and wide variety of shapes in which the cells are available. Besides that, Li-ion batteries have no 'memory-effect'. It is more expensive than nickel- and lead acid systems and needs protection circuit for safety.

1.2.2 Thermodynamics

The voltage of an electrochemical cell (E^0_{cell}) is determined by the difference in electrochemical potential of the positive (E^0_{pos}) and negative electrodes (E^0_{neg}) i.e.

$$E^0_{cell} = E^0_{pos} - E^0_{neg} \quad \text{eqn. 1.1}$$

From a thermodynamic standpoint, the cell voltage can also be calculated from the free energy of the electrochemical reaction (ΔG): The basic thermodynamics for a reversible electrochemical reaction is given by eqn. 1.2.

$$\Delta G = \Delta H - T\Delta S \quad \text{eqn. 1.2}$$

where ΔG is the Gibbs free energy, or the available energy in a reaction for the useful work, ΔH is the enthalpy, or the energy released by the reaction, ΔS is the entropy, and T is the absolute temperature, with TΔS being the heat associated with the reaction. The terms ΔG, ΔH and ΔS are state functions and depend only

on the identity of the electrode materials and the initial and final states of the reactions. [6]

The change in the free energy of a cell reaction is the driving force which enables a battery to deliver electrical energy to an external circuit. Thus the maximum electric energy that can be delivered by the chemicals depends on the change in free energy G of the electrochemical couple as per eqn. 1.3.

$$\Delta G = -nFE \qquad \text{eqn. 1.3}$$

where F = Faradays constant (96485 sec A per mol), n is number of electrons involved in stoichiometric reaction, E is the voltage of the cell with the specific chemical reaction. Eqn. 1.3 represents a balance between the chemical and electric driving forces upon the ions under open circuit conditions; hence E refers to the open circuit potential of a cell where there is no current flowing. The voltage of the cell is unique for each reaction couple. The amount of electricity produced, nF, is determined by the total amount of materials available for reactions and can be thought of as a capacity factor; the voltage can be considered to be an intensity factor.

The change of free energy for a given species *i* defines the chemical potential. The chemical potential, μ_i, for species *i* is related to another thermodynamic quantity, the activity a_i, by defining the relation given in eqn. 1.4.

$$\mu_i = \mu_i^0 + RT \ln a_i \qquad \text{eqn. 1.4}$$

where μ_i^0 is a constant, the value of the chemical potential of species *i* in its standard state. R is the gas constant, and T the absolute temperature. Consider an electrochemical cell in which the activity of species *i* is different in the two

electrodes, a_i (A) in the negative electrode and a_i (C) in the positive electrode. [7] The difference between the chemical potential on the positive side and that on the negative side is

$$\mu_i(A) - \mu_i(C) = RT\, ln \frac{a_i(A)}{a_i(C)} \qquad \text{eqn. 1.5}$$

If this chemical potential difference is balanced by the electrostatic energy from eqn. 1.3, we have

$$\Delta E = \Delta E^{\circ} - \frac{RT}{nF} \ln \frac{a_i(A)}{a_i(C)} \qquad \text{eqn. 1.6}$$

The equation 1.6 is known as Nernst equation, which relates the measurable cell voltage to the chemical difference across an electrochemical cell. If the activity of species *i* in one of the electrodes is a standard reference value, the Nernst equation provides the relative electrical potential of the other electrode. [7]

1.2.3 Design

During the discharge of electrochemical cells, it is a general requirement that if maximum energy and power are to be derived from the cell, particularly for heavy-duty applications such as electric vehicles, then the voltage of the cell should remain as high and as constant as possible. This requirement is never fully realized in practice because the internal resistance (impedance) of cells and polarization effects at the electrodes lower the practical voltage and the rate at which the electrochemical reactions can take place. These limitations are controlled to a large extent not only by the cell design but also by the type of electrochemical reaction that occurs at the individual electrodes and by the ionic conductivity of the electrolyte.

Figure 1.2 shows a schematic of the relative electron energies in the electrodes and the aqueous electrolyte of a battery cell at thermodynamic equilibrium. The energy gap, E_g, is the electrolyte potential window between the lowest unoccupied molecular orbital (LUMO) and the highest occupied molecular orbital (HOMO) of the electrolyte. [8] The two electrodes are usually the electronic conductive anode (reductant) and the cathode (oxidant) materials with electrochemical potentials of μ_A and μ_C (Fermi energies ε_F), respectively. Unless a passivating solid electrolyte interface (SEI) layer creates a barrier for electron transfer across the electrode/electrolyte interface, an anode with a μ_A above the LUMO will reduce the electrolyte, whereas a cathode with a μ_C below the HOMO will oxidize the electrolyte. Therefore, it is important to locate the electrochemical electrode potentials μ_A and μ_C within the thermodynamically stable potential window of the electrolyte, which constrains the open circuit voltage, V_{oc}, of a full cell battery to $eV_{oc} = \mu_A - \mu_C \leq E_g$ (e: magnitude of the electron charge). However, the formation of SEI layer at the electrode/electrolyte boundary helps to maintain kinetic stability to a larger V_{oc}, if $eV_{oc} - E_g$ is not too large. [8, 9]

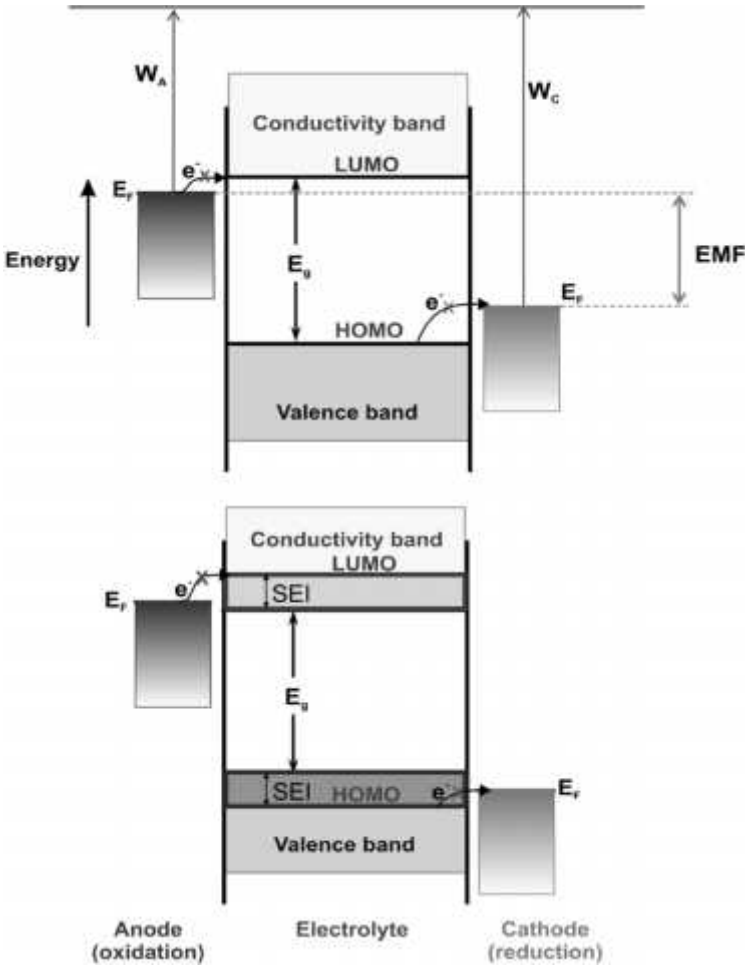

Figure 1.2 Electrolyte/electrode interface energy diagram in a Li-ion cell at open circuit. Reprinted with permission from '*Material problems and prospects of li-ion batteries for vehicles applications*' by J. Molenda in Functional Materials Letters Vol. 4, No. 2 (2011) 107–112.

1.2.4 Terminology

To compare the energy content of cells, the terms 'specific energy' (expressed in Wh/kg) and 'energy density' (in Wh/L) are used. The specific energy of the battery in watt-hours per kilogram (Wh/kg) is defined by the product of the battery voltage, V, and the electrochemical capacity of the electrodes, the unit of which is ampere-hour per kilogram (Ah/kg). The capacity of the electrode is the current output capability of an electrode, cell, or battery over a period of time, usually expressed in ampere-hours. The theoretical specific capacity of an electrode material can be calculated in mAh g^{-1} based on eqn. 1.7.

$$C = \frac{n \times F}{M_w \times 3600} \times 1000 \qquad \text{eqn. 1.7}$$

where n is number of lithium used in moles; F is Faraday constant, 96,485 sec A per mol and M_w is molecular weight in grams. The volumetric energy density is given in terms of watt-hours per liter (Wh/liter), which is an important parameter when the available space for the battery is a prime consideration. The specific power, which defines the rate at which the battery can be discharged, is given as watts per kilogram (W/kg) and the power density is expressed in watts per liter (W/liter).

1.3 Lithium ion battery technology

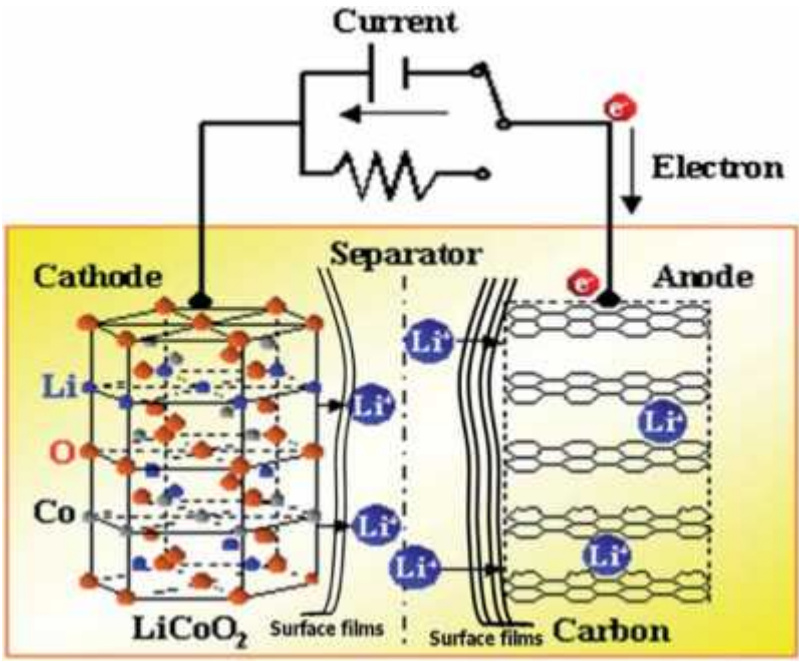

Figure 1.3 Illustration of the charge–discharge process involved in a lithium-ion cell consisting of graphite as the anode and layered $LiCoO_2$ as the cathode. *Reprinted from [13] with permission of Royal Society of Chemistry.*

The concept of rechargeable lithium-ion battery started with the discovery of intercalation compounds, such as Li_xMO_2 (M = Co, Ni) which were initially proposed by Goodenough and are still widely used today.[10] The discovery of low-voltage, lithium-intercalation, carbonaceous materials that are highly

reversible led to the commercialization of $Li_xC_6/Li_{1-x}CoO_2$ cells by Sony in 1991.[11] Lithium-ion (Li-ion) batteries are comprised of cells that employ lithium intercalation compounds as the positive and negative materials. As a battery is charged / discharged, lithium ions (Li) exchange between the positive and negative electrodes. The positive electrode material is typically a metal oxide with a layered structure, such as lithium cobalt oxide ($LiCoO_2$), or a material with a tunneled structure, such as lithium manganese oxide ($LiMn_2O_4$), on a current collector of aluminum foil.[10, 12] The negative electrode material is typically a graphitic carbon, also a layered material, on a copper current collector. They are also referred to as rocking chair batteries as the lithium ions ‘‘rock’’ back and forth between the positive and negative electrodes as the cell is charged and discharged as shown in Figure 1.3. In the charge/ discharge process, lithium ions are inserted or extracted from interstitial space between atomic layers within the active materials.

On charging, Li^+ ions are de-intercalated from the layered $LiCoO_2$ cathode host, transferred across the electrolyte, and intercalated between the graphite layers in the anode. During discharge, this process is reversed where the electrons pass around the external circuit to power various systems. [14] On discharge, to retain the charge neutrality in the electrodes, Li^+ cations are released from the anode to the electrolyte, and they enter the cathode, whereas electrons leave the anode via an external circuit to do useful work before entering the cathode. The energy conversion in the so-called rocking-chair cells is completed via the following reactions. [14, 15]

Cathode half cell reaction: $LiCoO_2 \longrightarrow Li_{1-x}CoO_2 + xLi^+ + xe^-$

eqn. 1.8

Anode half cell reaction: $Li_xC_6 \longrightarrow xLi^+ + xe^- + C_6$

eqn. 1.9

Full Cell Reaction: $Li_xC_6 + Li_{1-x}CoO_2 \longrightarrow C_6 + LiCoO_2$, E= 3.7 V at 25°C

eqn. 1.10

The process is reversed on charge in a rechargeable Li-ion battery. Consequently, the magnitude of the electric current in the external circuit must match the internal ionic current within the battery for charge neutrality. The ionic current density depends on the rate of ion transfer in the electrolyte, the electrode, and across the electrode/electrolyte interface. Therefore, at high current densities, the reversible capacity decreases because the ionic motion within an electrode and/or across an electrode/electrolyte interface is too slow to reach the equilibrium charge distribution.

1.3.1 Anode materials

Lithium metal is very attractive anode material, since it can be more easily handled (though with care) than other alkali metals and more significantly, the lightest and the most electropositive among the alkali metal family. The low density of lithium metal (0.534g/cc) leads to the highest specific capacity value of 3860 mAh g^{-1}, which stands exceptional. [16] Such advantages in using lithium metal for batteries were first demonstrated in the 1970s with primary lithium cells. But the highly reactive lithium metal reacts with organic electrolyte solvent results in the formation of a non-uniform, lithium alkyl carbonate passivation film on the anode surface, which is a lithium-ion conductor but an electronic insulator. Although Li-ions can pass through this film, an althernative which is the plating of a fresh surface of lithium upon charge is favoured. The lithium deposition accumulates after repeated cycles, leading to the growth of lithium dendrites. Eventually battery

is short circuited, resulting in failure of the cell. The growth of the passivation film will also trigger cell failure because of a rapid increase in cell impedance and a decrease in efficiency. Safety issues along with the high cost associated with the lithium-metal process have thus stimulated research for developing alternative anode materials. This dendrite problem was circumvented by substituting lithium metal for an alloy with aluminum in the first commercialized lithium-ion battery by Exxon, but extreme volume changes of the alloy electrodes during the recharging process have limited the reversibility of the cell to only a small number of cycles. Such volume changes still impose limitations on tin and silicon alloy-type anodes, which are currently being extensively studied. Anode materials for LIBs can be classified into three different categories based on their energy storage mechanisms:

i. Intercalation- based materials.
ii. Conversion-reaction-based materials.
iii. Alloying-reaction based materials.

1.3.1.1 Intercalation based anode materials

Insertion electrode materials are included in the majority of ambient-temperature rechargeable batteries. The reason for their widespread application is the fact that electrochemical insertion (electroinsertion) reactions are intrinsically simple and reversible. The term electroinsertion refers to a host/guest solid-state redox reaction involving electrochemical charge transfer coupled with insertion of mobile guest ions from an electrolyte into the structure of a solid host, which is a mixed electronic and ionic conductor. The major structural features of the host are kept after the insertion of the guests. Various insertion materials have been proposed for negative electrodes of rechargeable lithium batteries, for example, transition-metal

oxides ($LiMoO_2$, $LiWO_2$) and chalcogenides ($LiTiS_2$), carbons etc. At present mostly carbons are used as the negative electrode of commercial rechargeable lithium batteries: i) because they exhibit both higher specific charges and more negative redox potentials than most metal oxides, chalcogenides, and polymers; and ii) due to their dimensional stability, they show better cycling performance.

Carbon materials can be classified into three categories: graphites, soft carbons and hard carbons. The criterion to distinguish between them is the degree of graphitization of materials or the graphitization temperature. In graphites, graphitic phases are well developed in a macroscopic dimension, which is practically

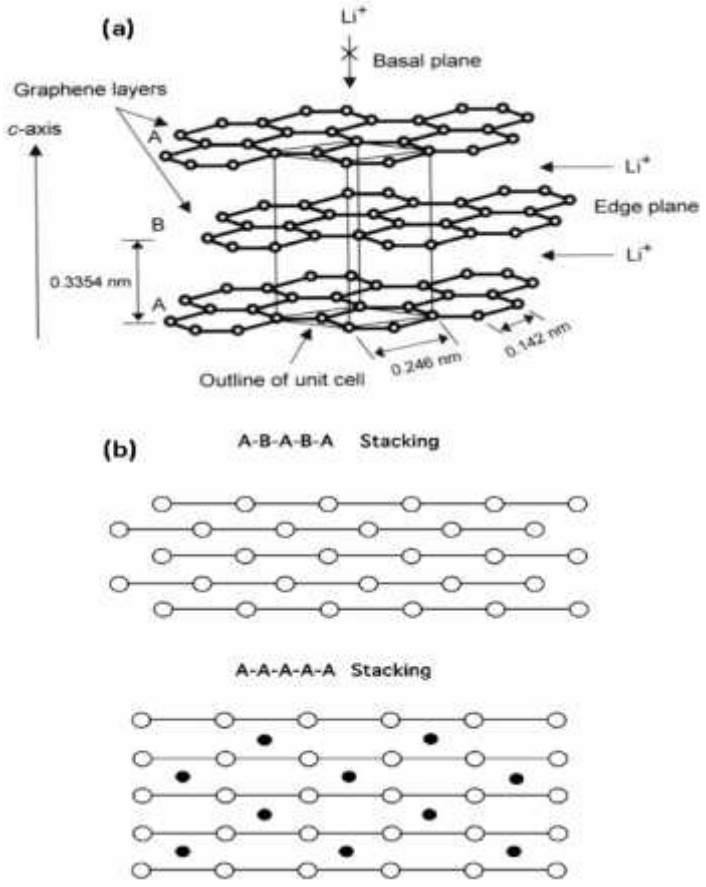

Figure 1.4 (a) Crystal structure of hexagonal graphite showing the ABAB.. stacking of graphene sheets and the unit cell. *Reprinted from [17] with permission.* (b) Difference between A-B-A-B-A stacking and A-A-A-A stacking when Li-ion is inserted. The black circles are Li-ions. *Reprinted from [18] with permission.*

obtained from nature (natural graphites) or by heating graphitizable precursors at temperature higher than 2800 °C. Lithium can be inserted in to graphitic structure up to a maximum concentration of one Li per six carbons, LiC_6. One of the major influences of lithium in the graphite crystal structure is that the stacking of graphene layers is changed by the insertion of Li, as shown in Figure 1.4. It changes from A-B-A-B-A stacking to A-A-A-A-A stacking. High crystallinity of stacked graphene layers with 0.335 nm spacing between planes shows 10 % volume expansion upon lithiation. The carbons that are used in commercial batteries have been heated to temperatures over about 2,400 °C**.** The rate of graphitization increases upon a rise in temperature. Capacities typically range from 300 to 350 mAh g^{-1} whereas the maximum theoretical value (for LiC_6) is 372 mAh g^{-1}.

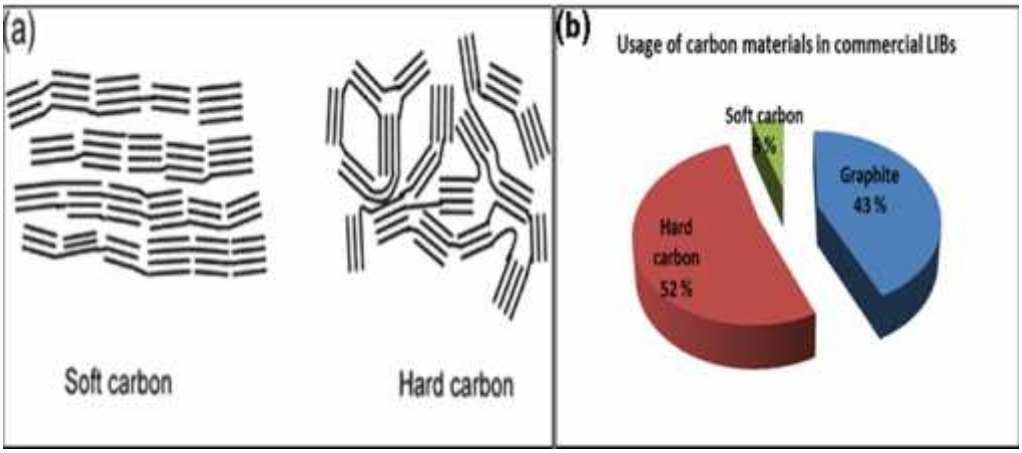

Figure 1.5 (a) Conventional structure model for soft and hard carbon. *Reprinted from [19] with permission from Elsevier*. (b) Usage of carbon materials in commercial LIBs.

Soft carbons are generally produced by the pyrolysis of liquid materials such as petroleum pitch, at relatively low temperatures from 1000 to 2400 ° C. The graphene layers are neatly stacked as shown in Figure 1.5(a) but there is less long range order with around 0.375 nm (but variable) spacing between planes. The

smaller crystallite size enables SCs (as well as HCs) potentially to accommodate high rate charge/discharge. HCs come from non-graphitizable precursors that cannot be graphitized even beyond 2500 ° C. They can have a substantial amount of nanoporosity. It is clear from Figure 1.5(a) that the layers of carbon atoms in HCs are not neatly stacked with a serious non-crystallinity in terms of long range order. They show macroscopically isotropic properties with more than 0.38 nm spacing between planes. HCs have an intercalation capacity higher than that of graphitic carbon with x=1.2- 5 corresponding to a capacity of 400 mAh g^{-1} to 2000 mAh g^{-1}. The spacing, fairly larger than that of other carbons enables hard carbons to accommodate volume change during lithiation/delithiation, potentially leading to better cycleability. [14] The high capacity and poor efficiency of HCs can be understood by their abundant Li + intercalation sites. The insertion sites of Li^+ in HCs include (1) partially charge transferring sites for Li^+ adsorption, (2) intercalation sites like graphite, (3) cluster gaps between edges of carbon hexagon clusters, (4) microvoids surrounded by hexagonal planes and (5) heteroatomic sites created as atomic defects. The first three types of insertion sites are present also in soft carbon. [17] The various (or broadly defined) energetics of HCs related to lithiation before reaching 0 V are responsible for a capacitive behavior of potential profiles at a constant current charging. Even after reaching 0 V, there is an additional capacity attributed to the lithiation into microvoids. To fully utilize the extra capacity to obtain high energy density, potentiostatic charging at 0 V is needed. In the commercial LIBS, well-ordered graphites such as mesocarbon microbeads (MCMB) heat treated at 3000°C and natural graphite, and non-graphitizing carbons (hard carbon) heat-treated presumably at around 1100°C,

have been mainly used as indicated in Figure 1.5(b). Typical capacity values of different carbon based anode materials are detailed in Table 1-1.

Material	Initial Capacity mAh g^{-1}	Reversible Capacity mAh g^{-1}	Irreversible Capacity mAh g^{-1}	First cycle efficiency, %
Graphite	390	360	30	92
Hard carbon	480	370	90	77
Soft Carbon	275	235	40	85

Table 1-1 Comparison of typical capacities of various carbonaceous anode materials.

Due to electrochemical reduction (charge) of the carbon host, lithium ions from the electrolyte penetrate into the carbon and form a lithium/carbon intercalation compound, Li_xC_n. This reversible faradaic reaction of lithiation/delithiation proceeds at less than 0.25 V versus Li/Li^+ , delivering reversible capacity practically at more than 360 mAh g^{-1} (theoretically at 372 mAh g^{-1} or 975 mAh cm^{-3}) with high discharge/charge efficiency approaching 100 % ($\eta \sim 100\%$). However, there are irreversible reactions during the first charge (lithiation) process in which constituents of electrolyte are cathodically decomposed. For example, ethylene carbonate, the most common conventional solvent of electrolytes for LIBs, is decomposed between 0.5 V and 0.7 V to form a passive layer on the surface of graphite. Practically, more than 90% efficiency of discharge to charge is observed at the first cycle with the initial capacity of 390 mAh g^{-1}.

Once a stable passive layer called the solid-electrolyte interface (SEI) layer is formed, charge/discharge reversibility leading to long-term cycleability is obtained. Therefore, the properties of the SEI layer should be emphasized as they

decide the performances and stability of battery cells. The SEI layer should be electronically insulating to block electron pathway from electrode to molecules in electrolyte so that electrolyte decomposition does not proceeds any more after the formation of SEI layers. Simultaneously, the SEI layer should be ionically, especially Li^+ - ionically, conductive, enabling the mass transfer of Li^+ from electrolyte to the interlayer spaces of graphite. The different scenarios relevant to surface film development on graphite electrodes and their aging is depicted in Figure 1.6.

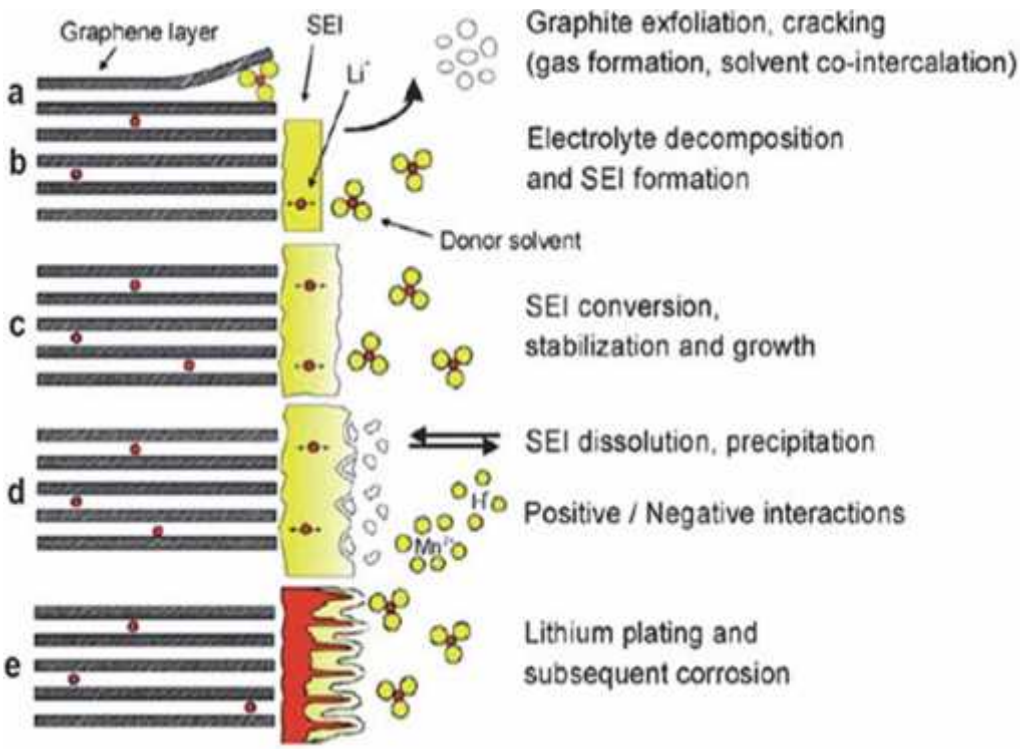

Figure 1.6 The different scenarios relevant to surface film development on graphite electrodes and their aging. (a) At high potentials (<1 V) before passivating surface films are formed. (b) At low enough potentials and in the right solution composition. (c) The surface films reach a steady state when they are thick enough to fully block electron transfer from Li–C to the solution. (d) Upon aging. (e) In an uncontrolled situation, a dangerous deposition of Li metal can occur during cathodic polarization. *Reprinted from [13] with permission from Royal society of Chemistry.*

The spinel $Li_4Ti_5O_{12}$ material, as an alternative anode to carbon, has been extensively studied as one of the most promising anode candidates for rechargeable Li-ion batteries.[20] $Li_4Ti_5O_{12}$ can accommodate three Li ions with a theoretical specific capacity of 175 mAh g^{-1} at a flat potential of 1.55 V, corresponding to a chemical formula of $Li_7Ti_5O_{12}$. A negligible volume change of only 0.2% is caused between both end members of $Li_4Ti_5O_{12}$ and $Li_7Ti_5O_{12}$ accompanied by a change of the lattice axis from 8.3595 Å to 8.3538 Å, and as a result it is a ‘‘zero strain’’ material with excellent cycling stability. It has a high potential around 1.5 V (vs. Li/Li+), which avoids the battery short circuit caused by the formation of lithium dendrites to achieve safe operation. $Li_4Ti_5O_{12}$ has intrinsic disadvantages of low electronic conductivity ($<10^{-13}$ S cm^{-1}), and slow lithium-ion diffusion (10^{-9}–10^{-13} cm^2s^{-1}), which restrict its wide practical application in lithium ion batteries.

1.3.1.2 Conversion-reaction-based materials

The electrochemical reaction of graphite with lithium goes through an insertion process limited by the number of vacant sites available in the crystalline structure and the maximum affordable capacity of this anode is limited to values close to the theoretical one (372 mAh g^{-1}) corresponding to a LiC_6 stoichiometry. Graphite electrode works at a potential that is only several tens of millivolts above the potential of the Li/Li^+ redox couple. The electrolyte solutions based on lithium salts dissolved in organic solvent are not stable in this voltage range, and leads to side reactions. Fortunately, the side products are deposited on the electrode surface forming SEI, whose irreversible character is only observed during the first cell charge. Although stable at room temperature, the SEI passivating abilities degrade rather fast when the temperature increases, hence making the Li-ion batteries quite sensitive to temperatures as low as 50°C. Considering these facts, the study of

alternative anode materials remains opened, and of transition metal oxides with higher working voltages can be regarded as potential anode materials for LIBS.

In 2000, Poizot *et al*. reported the reversible electrochemical activity of nano-sized transition metal oxides with lithium via heterogeneous conversion reaction mechanism. [21] The mechanism of Li reactivity differs from the classical processes and based on the electrochemically driven in situ formation of metal nanoparticles during the first discharge, which enables the formation and decomposition of Li_2O upon subsequent cycling. Conversion reactions are those in which an active electrode material, M_aX_b, is consumed by Li and reduced to the metal M and a corresponding lithium compound, according to the general reaction given in eqn. 1.11.

$$M_aX_b + nb\ Li \leftrightarrows a\ M + b\ Li_nX \qquad \text{eqn. 1.11}$$

where M = transition metal (Ti, V, Cr, Mn, Fe, Co, Ni, Cu, Mo, W, Ru), X = anion (O, N, F, S and P) and n = number of negative charge of X.

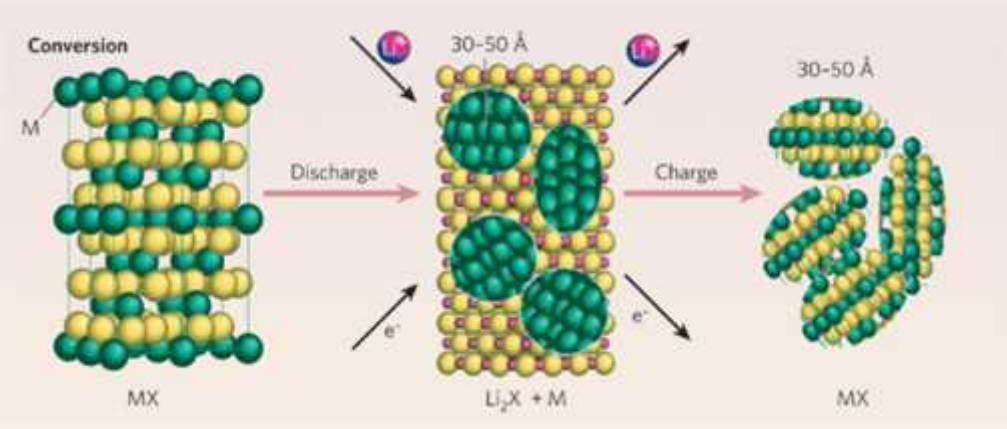

Figure 1.7 Schematic representation showing the reaction mechanism occurring during discharge for conversion reaction. *Reprinted from [22] with permission of Nature publishing group.*

In general, an increase in the M–X bond ionicity results in an increase in the output voltage associated with the reaction (eqn. 1.11). [23] Therefore, the output voltage of the reaction can be expected to increase from the highly covalent metal nitrides and sulfides, to the metal oxides, through the inductive effect polyanions (metal phosphates, metal borates), and finally to the highly ionic metal fluoride. The availability of this reaction can be accessed from the thermodynamical data. The Gibbs free energy of the overall reaction (eqn. 1.11) can be calculated from the free energy values of the oxides. [24]

$\Delta G^{o}r = b\,\Delta G^{o}_{f}(Li_nX) - \Delta G^{o}_{f}(M_aX_b) < 0$ eqn. 1.12

Hence, those metal oxides/nitrides/flourides/sulphides/phosphides with less negative values of ΔG^{o}_{f} will lead to feasible conversion reactions.

The key to the reversibility of the conversion reaction seems to lie in the formation of metal nanoparticles upon complete reduction. Owing to the large amount of interfacial surface, these metal nanoparticles are very active toward the decomposition of the matrix of the lithium binary compound (L_nX) in which they are embedded, when a reverse polarization is applied. The nanoscopic character of the metal particles has shown to be maintained even after several reduction-oxidation cycles. [25]

The structural degradation on the first discharge is complete, unlike the topotatic reaction occurring in insertion reactions. Oxide anions migrate from the transition to the alkaline metal, yielding a biphasic state constituted by nanodomains of M and Li_2O as shown in Figure 1.7. Although different techniques have evidenced the metal oxidation upon charging, the recovery of the initial framework has not been ever reported. The diffusion of the oxide anions is favored by the large interfacial

region existing among the nanometric domains, although it is quite lower than the lithium diffusion in the insertion compounds. [24]

When considering theoretical capacity of graphite (372 mAh g^{-1}), the use of conversion-reaction-based compounds looks feasible but they have some shortcomings. [6, 24] First, their efficiencies of discharge to charge are not as good as that of graphite so that cycleability is seriously poor. The conversion reactions have intrinsically limited reversibilities and large volume changes of the conversion-reaction-based anode materials during lithiation/delithiation could lead to pulverization or electric isolation. Second, their reaction potentials (E_{conv}) at which the potential profiles become plateau are relatively higher than that of graphite. The higher E_{conv} leads to lower cell potential then finally to lower energy density than that expected from capacities. Also, these transition metal oxides are characterized by a low electronic conductivity. Consequently, the electrochemical reaction is kinetically poor, and discharge and charge curves polarize approximately 1 V from the emf value.

1.3.1.3 Alloying/de-alloying reaction-based anode materials

Since Dey demonstrated that Li metal can electrochemically alloy with other metals at room temperature in an organic electrolyte electrochemical cell, Li-alloying reactions with metallic or semi-metallic elements and various compounds have been widely investigated.[26] Li alloy forming elements such as Sn, Si, Sb, Ge, Zn, Al, In, Bi, Cd etc. are considered as prospective anode materials due to their ability to reversibly react with large amount of Li thereby delivering high capacity at relatively low voltage vs. Li as in eqn. 1.13.[27]

$$XM + YLi^{+} + Ye^{-} \leftrightarrow M_xLi_y \qquad \text{eqn. 1.13}$$

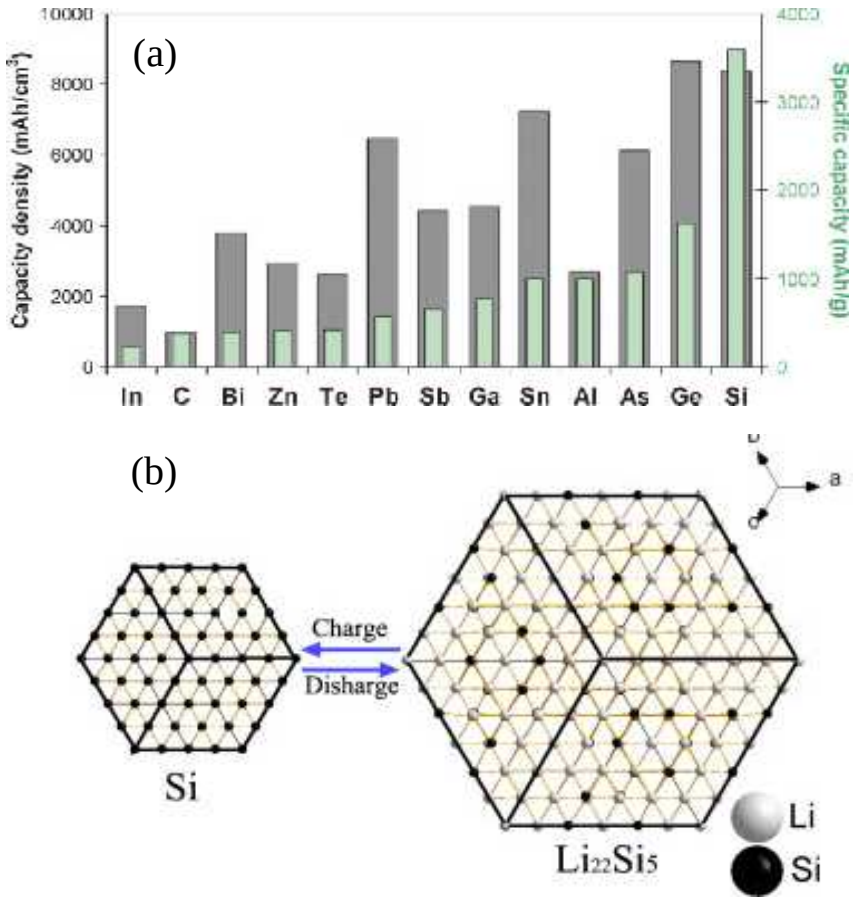

Figure 1.8(a) Specific capacities and capacity densities for selected alloying reactions. Values for graphite are given as a reference. *Reprinted from [28] with permission of Royal Socity of Chemistry*. (b) Schematic representation of unit cell volume variation of Si during charge-discharge process. *Reprinted from* [29] *with permission of Elsevier.*

The most distinguished characteristic of the alloying reaction- based materials is the high theoretical capacities: 4,200 mAh g^{-1} for Si to $Li_{4.4}Si$, 1600 mAh g^{-1} for Ge to $Li_{4.4}Ge$, 993 mAh g^{-1} for Al to LiAl, 960 mAh g^{-1} for Sn to $Li_{4.4}Sn$ and 660 mAh g^{-1} for Sb to Li_3Sb.[30] Figure 1.8(a) shows the comparison of these anode materials in mass capacity and energy density. Among the Li-alloying materials, Sn and Si have been considered as the most attractive anode materials for Li-ion batteries because it has the highest gravimetric and volumetric capacity and is also abundant, cheap, and environmentally benign. Si is discharged at a fairly well defined plateau potential of 0.4 V while it is charged or lithiated broadly from 0.4

V to 0 V versus Li/Li^+. Fig. 1.7(b) displays the illustration of volume change from Si to the full-discharge state of $Li_{22}Si_5$. In the whole charge and discharge process, Si undergoes a volume change of about 300% (expansion in discharge and contraction in charge).[29] It results in pulverization of electrode material and loss of electric contact between materials grains and eventual capacity fading upon prolonged cycling. It is also difficult to fabricate alloys/intermettallics in nanoform with different morphologies where as oxides can be easily synthesized in several morphologies.

Many tin-based intermetallics and their composites have already been examined as lithium storage materials.[31] The most lithium rich Li–Sn alloy phase is $Li_{17}Sn_4$ so that 4.25 atoms of lithium can be accommodated into each Sn atom and its maximum gravimetric capacity is 960 mAh g^{-1} with a working potential of about 0.5 V (vs. Li/Li^+).[32] In 1997, Fuji announced its Stalion battery, which employed an amorphous tin composite oxide (TCO) anode based on alloying/de-alloying reaction, but it was not commercialized because of its large irreversible capacity during the first cycle.[24] Since then, Sony developed its Nexelion battery in 2005 using an anode material mainly composed of a Sn/Co/C composite with Ti metal, synthesized by a high energy mechanical milling process.[33] Not only composite materials, but also nanosized particles and nanostructured materials have also been suggested in order to alleviate the mechanical strain generated due to the volume change as the Li ions are inserted to and extracted from the host electrode materials. Table 1-2 provides a comparison of various electrochemical aspects of Sn and Si with carbon and lithium titanate.

Materials	Li	C	$Li_4Ti_5O_{12}$	Si	Sn
Density (g cm^{-3})	0.53	2.25	3.5	2.33	7.29
Lithiated phase	Li	LiC_6	$Li_7Ti_5O_{12}$	$Li_{4.4}Si$	$Li_{4.4}Sn$
Theoretical specific capacity (mAh g^{-1})	3862	372	175	4200	994
Theoretical charge density (mAh cm^{-3})	2047	837	613	9786	7246
Volume change (%)	100	12	1	320	260
Potential vs. Li (V)	0	0.05	1.6	0.4	0.6

Table 1-2 Comparison of the theoretical specific capacity, charge density, volume change and onset potential of various anode materials.

The basic strategies to overcome the volume-expansion induced problems consist of (i) using some counter (matrix) elements in conjunction with the alloy–forming anode, but at the cost of achievable reversible capacity. The active alloying-reaction-based materials are mixed with buffer phases which can be an empty space or nonreactive (inert) materials. More improvement has been achieved by using a second phase in order to accommodate the excessive volume changes occurring during the cycling. It must also assure electronic and ionic conductivity throughout the electrode, (ii) choice of proper voltage range keeping a tradeoff between capacity value and capacity stability, (iii) decreasing the size to nanometer range so that relatively low number of atoms per grain leads to less volume change upon cycling and thus the mechanical strain generated within the particles is effectively reduced in comparison to micron-size particles, (iv) fabricating 1D nanostructures such as nanowires as electrode materials provides better

accommodation of strain and efficient electron transport through an anisotropic 1D pathway, in addition to benefits of the nano-scale dimensions.[24]

1.3.1.4 Potential candidates for anode materials in LIBs

Various metals, such as Al, Si, Sn, and Sb, and intermetallic compounds, such as SnSb, Cu_6Sn_5, and Cu_2Sb, have received considerable attention because they react with lithium, either by lithium insertion or by a combination of lithium insertion into and metal displacement from a host structure at a potential above that of a Li_xC_6 electrode. These metal/intermetallic electrodes should therefore be potentially safer than Li_xC_6 electrodes. The electrochemical performance of these metal and intermetallic electrodes is limited by huge unit cell volume variation during the uptake of lithium and by a large irreversible capacity loss that commonly occurs during the initial cycle of the lithium cells.

Even if anode materials are being evolved in terms of energy density from graphite to non-graphite materials, the new materials including the conversion-reaction-based compounds and the alloying-reaction-based metals are not predicted to be adopted as a main active material for the time being. The early commercialized products with the conversion-reaction- based compounds or the alloying-reaction-based metals is not for upgrading their energy density seriously but for demonstrating the feasibility of the brand-new materials in real cells. The IT industries manufacturing cell phones and laptops have a tendency ready to accept new technologies. Therefore, application of the novel materials would begin on LIBs for an IT mobile market (not yet for emerging markets such as xEVs and ESSs). As of now, the favorite anode compositions of automotive LIB manufactures are: graphites, soft carbons (SCs) or hard carbons (HCs) as a single composition, a mixture of them (typically two of them) and $Li_4Ti_5O_{12}$ (LTO).

1.3.2 Cathode materials

Graphite–$LiCoO_2$ became the leading Li-ion battery system that at present powers most of the portable electronic devices: cellular phone, laptops, digital cameras, etc. It has three times higher potential (>3.6 V) and two to three times higher gravimetric energy density (120–150 Wh/kg) than the usual Ni-Cd batteries.[3] Hence, finding of positive-electrode materials with superior energy density to $LiCoO_2$ for lithium-ion batteries may be difficult. Intensive studies have been directed at finding materials with higher voltage and/or larger rechargeable capacity than $LiCoO_2$.[16] The main requirements for cathode materials for LIBs are[8]: (i) A transition metal ion in the insertion compound cathode with large work function to maximize the cell voltage, (ii) large amount of lithium insertion/extraction to maximize the cell capacity, (iii) reversible lithium insertion/extraction process with no or minimal changes in the host structure over the entire range of lithium insertion/ extraction, (iv) chemical stability for both redox forms of cathode couple, (v) good electronic and Li+ conductivities of the material to minimize cell polarizations and, (vi) the voltage profile should be relatively continuous, without large voltage steps that can complicate power managements in devices. Finally, the insertion compound should be inexpensive, environmentally friendly and lightweight to minimize the battery weight. Up to now, three types of cathode materials have been investigated intensively. [8, 16]

i. Layered transition metal oxides.
ii. Mn-based spinels.
iii. Polyanion-type cathode materials.

1.3.2.1 Layered transition metal oxides

Layered transition metal oxides cathode materials have several advantages: fully developed synthetic routes, high capacity and ability for facile processing. However, they all have an unavoidable shortcoming, i.e. oxygen evolution at high charging potential.[13] It could cause serious safety issues for practical application. Thus layered lithiated transition metal oxides such as $LiCoO_2$ or $LiNi_{1-x-y}Co_xMn_yO_2$ ($0<x, y<1$) are widely used as cathode materials only in small-scale batteries for portable electronic equipments.

The ordered rock salt type α-$NaFeO_2$ of a general formulae $LiMO_2$ (M=V, Cr, Co, Ni, Mn) play especially important role among layered or 2D Li-intercalation compounds.[34] These families of compounds proposed by Goodenough are still used exclusively in today's lithium-ion batteries. Oxides with the general formula $LiMO_2$ (M = V, Cr, Co, and Ni) crystallize in a layered structure in which the Li^+ and M^{3+} ions occupy the alternate (111) planes of the rock salt structure to give a layered sequence of –O–Li–O–M–O– along the c axis. The Li^+ and M^{3+} ions occupy the octahedral interstitial sites of the cubic close-packed oxygen array. This structure is also called the O3 layered structure, since the Li^+ ions occupy the octahedral sites (O referring to octahedral) and there are three MO_2 sheets per unit cell. This structure with covalently bonded MO_2 layers allows a reversible extraction/insertion of lithium ions from/into the lithium planes. The lithium-ion movement between the MO_2 layers provides fast two-dimensional lithium-ion diffusion, and the edge-shared MO_6 octahedral arrangement with a direct M-M interaction provides good electronic conductivity. As a result, the $LiMO_2$ oxides have become attractive cathode candidates for lithium-ion batteries. [8]

During charging process, Li^+ is reversibly removed from the interlayer structure and Co^{3+} is oxidized to Co^{4+}. On the complete removal of the lithium, the oxygen layers rearrange themselves to give hexagonal close packing of the oxygen in CoO_2. Between these composition limits, several phases are formed with varying degrees of distortion of the ccp oxygen lattice. The reversible amount of lithium extraction x in $Li_{1-x}CoO_2$ is usually below 0.5. Further de-lithiation results in a transition from a monoclinic phase to a hexagonal one at about 4.2 V. [35] This transformation leads to the drastic shrinkage and cation disorder with Li entering into the 3b sites of Co. The higher concentration of the oxidized form of cobalt (IV) at $x > 0.5$ leads to its dissolution. All these factors result in the deterioration of electrochemical performance.[35] Thus even if the theoretical capacity is estimated at 274 mAh g^{-1} under the assumption that $LiCoO_2$ is completely delithiated to CoO_2 , the capacity is practically obtained only at 130–150 mAh g^{-1} with around half delithiation to $Li_{1-x}CoO_2$ where x is up to 0.5. [8]

$LiNiO_2$ is iso-structural with $LiCoO_2$ and shows larger rechargeable capacity than that of $LiCoO_2$, but lower operating voltage with sloping charge and discharge curves. [36] Due to the very close lattice constants of layered $LiNiO_2$ (*Rm3* space group) to that of cubic structured $LiNiO_2$ (*Fm3m*), which is inactive in non-aqueous lithium cells, the cation mixing of Li^+ and Ni^{3+} occurs very easily without any dimensional mismatch compared with that of $LiCoO_2$. Thus $LiNiO_2$ layered oxide is more difficult to prepare compared with $LiCoO_2$, and even a small mixing of cations in $LiNiO_2$ strongly influences its stability in electrochemical intercalation processes and electrochemical properties such as reversible capacity and working voltage.[35] Because $LiNiO_2$ and $LiCoO_2$ (or $LiAlO_2$) form a solid solution, $LiCo_xNi_{1-x}O_2$ and $LiAl_xNi_{1-x}O_2$ including $LiAl_xCo_yNi_{1-x-y}O_2$ ($x+y<0.25$),

were extensively examined. These positive-electrode materials usually show larger rechargeable capacities than that of $LiCoO_2$. However, their lower operating voltage than that of $LiCoO_2$ effectively cancels out their larger capacity when the energy density is calculated. [35, 36]

$LiMnO_2$ could be considered as the most interesting member of the $LiMO_2$ layered cathodes due to its high theoretical capacity of 285 mAh g^{-1}, low price, and environmentally friendly character. However, in contrast with the previously discussed $LiCoO_2$ and $LiNiO_2$, $LiMnO_2$ cannot be prepared by solid-state reaction method due to the similarity of Li^+ and Mn^{3+} ionic radii, which does not favor the formation of a true layered structure. The X-ray diffraction (XRD) studies revealed that for $LiMnO_2$ there is the distortion from the ideal rhombohedral symmetry due to the presence of the Jahn–Teller active Mn^{3+} ion (high spin d4). Therefore, there was coexistence of both monoclinic and rhombohedral structures for $LiMnO_2$. However, removal of half of the lithium resulted in the oxidation of manganese to Mn^{4+} and reduction of the Jahn–Teller effect, which resulted in the rhombohedral indexing for $Li_{0.5}MnO_2$. The electrochemical performance of this material was poor and discharge capacity dropped from 220 mAh g^{-1} at the initial cycle to only 130 mAh g^{-1} in the subsequent cycle.

The consideration of advantages and disadvantages of $LiCoO_2$, $LiMnO_2$, and $LiNiO_2$ cathode materials has led to the proposition of the mixed transition metal oxides as the alternative of $LiCoO_2$. Ternary transient metal component systems of Li-Ni-Mn-Co-O ($LiNi_xMn_yCo_zO_2$ with $x + y + z = 1$ or NMC) has been developed as a cathode active material. The most representative composition is $LiCo_{1/3}Ni_{1/3}Mn_{1/3}O_2$. The representative NMC shows about 170 mAh g^{-1} discharge capacity at 4.4 V cut-off with excellent cycle retention. As the amount of nickel

ions which are placed in lithium ion layers is reduced due to the addition of cobalt, its rate capability is also improved. $LiCo_{1/3}Ni_{1/3}Mn_{1/3}O_2$ consists of Co^{3+}, Ni^{2+}, and Mn^{4+} while $LiNi_{1/2}Mn_{1/2}O_2$ consists of Ni^{2+} and Mn^{4+}. Although operating voltage of $LiCo_{1/3}Ni_{1/3}Mn_{1/3}O_2$ is slightly lower than that of $LiCoO_2$, rechargeable capacity is larger, so that lithium-ion battery consisting of $LiCo_{1/3}Ni_{1/3}Mn_{1/3}O_2$ and graphite is equivalent or superior to current lithium-ion batteries of $LiCoO_2$ and graphite with respect to energy density. $LiNi_{1/2}Mn_{1/2}O_2$ shows almost the same operating voltage and rechargeable capacity as those of $LiCo_{1/3}Ni_{1/3}Mn_{1/3}O_2$. However, electrochemically-active $LiNi_{1/2}Mn_{1/2}O_2$ is difficult to prepare and the exact crystal structure is still unknown. Although $LiNi_{1/2}Mn_{1/2}O_2$ is not fully understood, it has superior properties to $LiCoO_2$ and has similar characteristic to $LiCo_{1/3}Ni_{1/3}Mn_{1/3}O_2$. $LiNi_{1/2}Mn_{1/2}O_2$ and $LiCo_{1/3}Ni_{1/3}Mn_{1/3}O_2$ may replace $LiCoO_2$ as the positive electrode of choice, in future.[15]

1.3.2.2 Spinel Cathode Materials

Mn-based spinels such as $LiMn_2O_4$ have also several advantages such as low cost, environmental benignness and good thermal stability, thus it is a good candidate for cathode materials for power tools applications.[37] $LiMn_2O_4$ having a spinel-framework structure has been extensively examined because it shows a flat operating voltage of 3.95–4.1V with theoretical capacity of 148 mAh g^{-1}. It has been developed as a possible alternative to $LiCoO_2$. Lithium is reversibly extracted/inserted into spinel structure and this process is accompanied by a reversible Mn^{3+}/Mn^{4+} redox reaction. However, the electrochemical performance of this cathode material is strongly affected by its quality, that is, stoichiometry and oxygen deficiency, grain size, and morphology. [35] $LiMn_2O_4$ has problems related to drastic capacity fading due to the dispropotionation of Mn^{3+} at the electrode

surface, Jahn–Teller distortion and decomposition of the electrolyte at high-voltage regions. Therefore, much research efforts have been devoted to improve the electrochemical performance of the $LiMn_2O_4$ spinel. To stabilize the structure of $LiMn_2O_4$ and to improve its capacity retention, the Mn was substituted for other cations. Thus other possible 5V materials include $Li[Ni^{2+}_{1/2}Mn^{4+}_{3/2}]O_4$ with a superstructure and an extremely flat operating voltage of 4.75 V against lithium. This is ca. 0.8 V higher than that of $LiCoO_2$, with rechargeable capacity of 135 mAh g^{-1}.

1.3.2.3 Polyanionic Cathode Materials

The peculiar structure of 2D oxide cathode materials with general formulae $Li_{1-x}MO_2$ (M= Co, Ni, Cr, Mn) leads to structural instabilities when number 'x' of extracted lithium is high. Goodenough [38] and Thackerey [12] had envisioned the concept of 3D insertion/extraction positive electrodes. This led to the discovery of new cathode family with 3D framework structures. These framework structures are not built from the close packing of oxygen atoms but built on the polyanions such as tetrahedral $(XO_4)^{n-}$ (X= P, S, Mo, V) group. These materials include compounds with a NASICON-type crystal lattice $Li_yM_2(XO_4)_3$ (here M is Ni,Co, Mn, Fe, Ti or V and X is S, P, As, Mo or W), an olivine-type crystal lattice Li_yMXO_4 (here M is Fe, Co, Mn or Ni and X is P, Mo, W or S), and polyanion materials with tavorite related structures. All these are materials with open 3D frameworks, which are available for Li migration.[16] Polyanion cathode materials possess higher thermal stability than conventional used layered transition-metal oxides due to the strong covalently bonded oxygen atoms, which make them more suitable for large-scale Li-ion battery applications, by virtue of their better safety properties.[39]

The polyanion cathode materials most intensively investigated are phosphates ($LiMPO_4$, with M= Fe, Mn, Co or Ni) with ordered olivine structure. As a new class of cathode materials for lithium ion batteries, polyanion compounds have attracted great interest since the first report on the electrochemical performance of $LiFePO_4$ by Padhi *et al*. [38] The application of iron-based compounds as a cathode for lithium batteries shows several advantages, including abundant cheap raw materials, high thermal stability and relatively low toxicity. However, the iron-based oxides containing O_2 as the anion suffer problems for the cathode designer, as in these oxides the Fe^{4+}/Fe^{3+} redox energy tends to lie too far below the Fermi energy of a lithium anode while the Fe^{3+}/Fe^{2+} couple is too close to it. The strong covalent bonding within the $(PO4)_3$ polyanion reduces the covalent bonding to the iron ion, which lowers the Fe^{3+}/Fe^{2+} couple redox energy to a suitable level of a flat voltage of 3.4 V versus Li/Li+. Besides its suitable high operating voltage, $LiFePO_4$ possesses appreciable theoretical capacity (ca. 160 mAh g^{-1}), corresponding to the theoretical energy density 580 Wh kg^{-1} versus Li electrode, which is above the practical value of $LiCoO_2$ (supposing that only 0.5 Li+ can be cycled). However, achievable energy density of a lithium-ion battery consisting of $LiFePO_4$ and graphite is less than that of current lithium-ion batteries mainly due to its lower operating voltage and smaller density than $LiCoO_2$. Replacing the transition-metal ion Fe^{2+} by Mn^{2+}, Co^{2+}, and Ni^{2+} increases the redox potential significantly from 3.45 V in $LiFePO_4$ to 4.1, 4.8, and 5.1 V, respectively, in $LiMnPO_4$, $LiCoPO_4$, and $LiNiPO_4$ because of the changes in the positions of the various redox couples. It is well known that the redox energies of transition metal $M^{2+/3+}$ couples decrease as we go from left to right on the periodic table because of

the increase in the nuclear charge, the extra electrons being added to the same principal quantum number.

Despite the many advantages associated with $LiFePO_4$, there are some drawbacks with $LiFePO_4$. The key drawbacks for the commercial application are its low intrinsic electric conductivity (10^{-9} S cm^{-1}), low packing density and poor one dimension lithium ion diffusion. Many studies have mainly been concentrated on optimizing the synthetic strategy, surface conducting modification, particle size reducing, cation doping on lithium and/or iron sites and so forth. The application of carbon coating and particle downsizing did the trick to circumvent the conductivity issue, thus making $LiFePO_4$ a front runner for large-scale battery production in less than a decade.

The success story of $LiFePO_4$ had great effect in the battery community. It opened up a gamut of polyanionic compounds to explore and apply as possible cathode systems. Even though $LiFePO_4$ has become successful because of its low cost and good safety characteristics, its energy density is limited because of the lower operating voltage (3.4 V), lower theoretical capacity (~170 mAh g^{-1}), and lower crystallographic density. In this regard, polyanion-containing frameworks that can accept two lithium ions per transition metal atom would help to realize high capacities and energy densities. Consequently, many polyanionic compounds have been introduced in the last decade, such as $Li_3M_2(PO_4)_3$ (M= V, Ti, Fe), Li_2MSiO_4 (M=Fe, Mn, Co)[40], $LiMBO_3$ (M= Fe, V)[41], $LiMPO_4F$ [42, 43]and $LiMSO_4F$ (M= Fe, V)[44]. Many of these materials are based on well-known minerals (e.g., $LiMSO_4F$ belongs to the tavorite class of minerals) with complete understanding of their crystal structure and basic physical-chemical properties. The new class of silicates, Li_2MSiO_4 (M = Fe, Mn, and Co) [40] offers the possibility of reversibly

extracting/inserting two lithium ions per formula unit with a theoretical capacity around ~333 $mAhg^{-1}$. Orthosilicate materials reveal very low electrical conductivity (10^{-12} - 10^{-15} S cm^{-1} at room temperature) and carbon coating of the materials is required.

A new family of polyanionic cathode systems is alkali metal pyrophosphate with general formula $AM^{III}P_2O7$ or $A_2M^{II}P_2O_7$ (A= Li, Na; M= Fe, Co, Mn, V, Ti etc.).[45, 46] Nishimura *et al*.[47] reported a novel pyrophosphate system with a disordered structure, namely $Li_2FeP_2O_7$, delivering a reversible capacity of ~ 110 $mAhg^{-1}$ with an $Fe^{2+/3+}$ redox activity located at 3.5 V, being the highest potential among all $(PO_4)_n$ - based cathodes. Contrary to $LiFePO_4$, this pyrophosphate could realize one-electron theoretical capacity without the need of carbon coating or particle downsizing. $Li_2FeP_2O_7$ offers excellent thermal/chemical stability, easy synthesis, a two-dimensional channel enabling efficient Li-diffusion and possibility of two-electron redox reaction. Pyrophosphates can easily be prepared by conventional one-step solid-state synthesis in the temperature range of 500–600 ° C.[47]

1.3.3 Electrolytes

The energy density of the lithium-ion battery can be improved through appropriate use of existing or new electrode materials. The choice of electrolyte is crucial in designing the actual lithium-ion battery. The criteria differ, depending on different types of electrolytes, which may be an organic liquid, a polymer, or an inorganic solid electrolyte. Other than a large electrochemical window E_g, there are several additional requirements that need to be satisfied including the following: (1) Li-ion conductivity $\sigma_{Li} > 10^{-4}$ S cm^{-1} over the temperature range of the battery operation, an electronic conductivity $\sigma_e < 10^{-10}$ S cm^{-1}, (2) a transference number $\sigma_{Li} / \sigma_{total} \approx$

1, where σ_{total} includes conductivities by other ions in the electrolyte as well as σ_{Li} + σ_{e}., (3) low toxicity, (4) low cost, (5) a passivating SEI layer being formed and retained during cycling, and (6) nonflammable and non-explosive if short-circuited. [22]

While the capacity of a cell relies on the electrodes, the cell lifetimes are mainly governed by the electrode–electrolyte interface side reactions. Breaking the SEI layer can result in lithium dendrite growth and can short-circuit a cell with dangerous consequences. Furthermore, the cathode-electrolyte interface has received little attention, despite its equally crucial role. Its importance is augmented with the need for higher voltage cathode materials that exceed the electrochemical resistance of the electrolyte oxidation and even favor catalytic decomposition. The limited mobility (ionic conductivity) of the Li^+ cations through the SEI and bulk electrolyte is the biggest contributor to limited battery power.[13, 48] It is believed that improved SEI formation, perhaps through the use of additives, may be essential for not only permitting higher potential cell cycling, but also for long cycle/calendar life and improved safety. The strategy developed to address such critical issues is to modify the electrode surface by coating or encapsulating the electrode grains with either an inorganic or an organic phase through chemical or physical means. This concept was successfully applied to the layered $LiCoO_2$ and spinel $LiMn_2O_4$ cathode by minimizing the direct electrode–electrolyte contact area. However, the main difficulty in understanding the electrode–electrolyte interface stems from a lack of available techniques to probe at a local level. Thus, efforts aimed at developing new characterization techniques must be strongly pursue.

Commercial Li-ion batteries are based on nonaqueous electrolytes.[22, 49] Typically, an electrolyte consists of three main components: the lithium salt (LiX), the solvent, and the additives. In state-of-the-art Li-ion batteries, $LiPF_6$ is predominantly used as the electrolyte salt due to its high conductivity in carbonate solvent mixtures and the ability to form a passivating layer at the cathode aluminum current collector, which prevents aluminum corrosion. But $LiPF_6$ also has several drawbacks including thermal instability with lithiated graphite anodes and delithiated transition metal oxide cathodes, as well as the generation of hydrofluoric acid (HF) with water which is always present in trace amounts in Li-ion batteries. HF dissolves transition metal ions from the cathode, which leads to capacity fading, especially at elevated temperature. [13, 48] Thus, the use of $LiPF_6$ is a compromise as currently there is no other lithium salt available which performs better than $LiPF_6$. Currently, in most commercially available Li-ion batteries electrolytes, mixtures based on cyclic and acyclic carbonate solvents are used. The cyclic carbonates have a high dielectric constant, which is an important feature for enabling the dissolution of a sufficient amount of lithium salt. However, the viscosity of cyclic carbonates is rather high, and acyclic carbonates with low viscosity must therefore be added to decrease the viscosity of the resulting electrolyte. One approach to increase the safety of Li-ion batteries is to reduce the flammability of the electrolyte systems by adding flame retardants or solvents with high flash points. These compounds are mostly incorporated as additives or co-solvents to the currently used electrolyte system.

For an aqueous electrolyte, $E_g \approx 1.3$ eV limits the V_{oc}. Therefore, to obtain higher V_{oc} and energy density CV_{oc} for a battery cell, an electrolyte with a larger E_g is required. This in turn led to the use of a non-aqueous liquid or polymer electrolyte

containing soluble lithium salts in which the limiting μ_C of the cathode is determined by both the HOMO of the salt and that of the solvent. Lithium metal would be the ideal anode, but the $\varepsilon_F = \mu_A$ of lithium lies above the LUMO of practical known non-aqueous electrolytes.

Innovative efforts to develop new electrolyte solutions are underway. An important class of new solvents that is being examined in connection with Li ion batteries is ionic liquids that offer wide electrochemical windows and good safety features. Ionic liquids (ILs) have excellent qualities that could render them very relevant for use in advanced Li-ion batteries, including high anodic stability, low volatility and low flammability. Their main drawbacks are their high viscosities, problems in wetting particle pores in composite structures, and low ionic conductivity at low temperatures. Recent years have seen increasing efforts to test ILs as solvents or additives in Li-ion battery systems.[13] Considerable progress has also been made in developing ‘‘polymer-gel’’ systems in which a liquid electrolyte component is immobilized in a polymer matrix. Although the Li-ion conductivity of these gel electrolytes is slightly inferior to that of pure liquid electrolyte systems, the ability to manufacture cells with laminated electrodes and electrolytes has provided much flexibility in the design of lithium ion cells. Moreover, cells with polymer-gel electrolytes are construed to be safer than those containing liquid electrolytes; they can also be easily constructed with lightweight packaging materials such as aluminum foil, thereby significantly improving the energy density of the cells.[29]

1.4 Nanomaterials for LIBs

Applications such as EV/HEVs require both high energy and high power densities which can be supplied by nanostructured materials as electrodes and

electrolytes. The progress of the Li-ion battery will depend heavily on understanding of the synthesis, electrode engineering, and electrochemistry of nanostructures, and this will be an important aspect of future research. There are many promises and challenges of using nanoparticles as active material in Li-ion batteries.[50] The advantages are often linked to the disadvantages, as in the case of increased specific surface area, which allows for a higher flux of Li-ions across the charge transfer interface while increasing side reaction between the electrode and the electrolyte.

Advantages

i. They enable electrode reactions to occur that cannot take place for materials composed of micrometer-sized particles.[50] For example, upon intercalation of ca. 0.03 Li per Fe_2O_3, hexagonal structure of micrometric α-Fe_2O_3 transforms to a cubic structure which is irreversible. In contrast, nanometric α-Fe_2O_3 sample, composed of well-crystallized 20 nm particles, reportedly allows monophasic, reversible Li intercalation into the hexagonal structure up to 0.6 Li per Fe_2O_3. [45]

ii. The reduced dimension increases significantly the rate of lithium insertion/removal, because of the short distances for lithium-ion transport within the particles. The characteristic time constant for diffusion is given by $t=L^2/D$, where L is the diffusion length and D the diffusion constant. The time t for intercalation decreases with the square of the particle size on replacing micrometer with nanometer particles.[50]

iii. Electron transport within the particles is also enhanced by nanometer-sized particles, as described for lithium ions.[50]

iv. A high surface area permits a high contact area with the electrolyte. This results in a higher flux of Li-ion transport across the electrode /electrolyte interface and as a result, less impedance in the charge transfer reaction.[50]

v. For very small particles, the chemical potentials for lithium ions and electrons may be modified, resulting in a change of electrode potential (thermodynamics of the reaction).[50]

vi. The range of composition over which solid solutions exist is often more extensive for nanoparticles and the strain associated with intercalation is often better accommodated.[50]

Disadvantages

i. Nanoparticles may be more difficult to synthesize and it is difficult to control their dimensions.

ii. High electrolyte/electrode surface area may lead to more significant side reactions with the electrolyte, and more difficulty maintaining interparticle contact.[50]

iii. The density of a nanopowder is generally less than the same material formed from micrometer-sized particles. The volume of the electrode increases for the same mass of material thus reducing the volumetric energy density.

1.5 Goal of this work and thesis layout

The goal of this work is to establish the synthetic methods and measurement procedures necessary to investigate various nanostructures for use in Li-ion batteries. As described in section 1.3.1, anode materials for lithium ion batteries can be classified into three different categories based on their energy storage

mechanisms: intercalation- based materials, conversion-reaction-based materials and alloying-reaction based materials. Representative materials from each category are prepared in nano-scale and the effects of cycling voltage range, particle size and morphology on the anodic performance of these materials are illustrated in the thesis.

Chapter 1 describes various types of batteries, the underlying thermodynamics and general design of a battery. Then the principle of operation and development of LIBs are described followed by brief overview on the anodes, cathodes and electrolytes for LIBs. The experimental techniques employed in the synthesis, physical and electrochemical characterization of the materials have been described in chapter 2. The project began with investigations into the preparation of electrodes with simple oxide nano-materials as active material and its Li-storage properties, as done with doped TiO_2 nanoparticles and Fe_2O_3 nanofibers in Chapter 3 and Chapter 4, respectively. TiO_2 is a simple oxide based on Li-intercalation storage mechanism whereas Fe_2O_3 is a 'conversion' reaction based oxide material. The maximum attainable capacity of intercalation based anodes is much lower than that of 'conversion' reaction based materials. $NiFe_2O_4$ is a prospective anode material due to their high theoretical capacity from conversion reaction, environment friendliness and abundance of Ni and Fe. The synthesis and Li-cycling studies of $NiFe_2O_4$ nanoparticles and nanofibres, described in Chapter 5, provides valuable insights into the link between morphological robustness and electrochemical performance. Furthermore, an in-depth analysis of charge storage and transfer is provided for $NiFe_2O_4$ nanofibres are discoursed through electrochemical impedance spectroscopy. Molybdates can also be considered as 'conversion' reaction based anode materials due to the ability of the metal ions to

exist in several oxidation states in these oxides, ranging from 3^+ to 6^+ for Mo, reversibly reacting with Li delivering high capacity, at potentials lower than 2 V. In chapter 6, molybdates of general formula, $AMoO_4$ (A= Co, Zn, Ni) are synthesized by polymer precursor method and citric acid assisted microwave method. The role of counter cations and effect of morphology on the Li-cycling behaviour of molybdates have been investigated. A novel polymer precursor method for the synthesis of macroporous molybdates ($AMoO_4$, A= Co, Zn, Ni) is established and the powders are tested as anode material for Li-ion batteries.

The reaction potentials of all these 'conversion' reaction based oxides are relatively higher than that of commercial graphite which leads to lower cell potential then finally to lower energy density than that expected from high capacities. On the other hand Li-alloying elements can reversibly react with large amount of Li at relatively low voltage vs. Li. Among the Li-alloying materials, Sn and Si have been considered as the most attractive anode materials for Li-ion batteries because it has the highest gravimetric and volumetric capacity and is also abundant, cheap, and environmentally benign. Sn based binary and ternary oxides have been studied as anode materials since they can be reduced to Sn by Li and hence could be used as precursors for $Li_{4.4}Sn$ alloys. The effects of voltage range and morphology on the electrochemical performances are evaluated for Sn based oxides such as SnO and Zn_2SnO_4 nanostructures and are presented in chapter 7. The morphological evolution of Zn_2SnO_4 nanowires during cycling is also investigated in the chapter. These research tasks represent some of the critical issues such as voltage range of cycling, size and morphology, involved in the electrochemical performance of various nano-scale active materials in Li-ion

batteries. Summary of significant findings and possible future works are provided in chapter 8.

1.6 References

1. Zhang, L., *Batteries, Rechargeable,* in *Encyclopedia of Materials: Science and Technology (Second Edition)*, K.H.J.B. Editors-in-Chief: , et al., Editors. 2001, Elsevier: Oxford. p. 463-483.
2. Pollet, B.G., I. Staffell, and J.L. Shang, *Current status of hybrid, battery and fuel cell electric vehicles: From electrochemistry to market prospects.* Electrochimica Acta, (0).
3. Cleveland, C.J., ed. *Encyclopedia of Energy, Volumes 1 - 6*. Elsevier. 127-139.
4. Linden, D. and T.B. Reddy, *Handbook of Batteries (3rd Edition)*, 2002, McGraw-Hill.
5. Nishio, K. and N. Furukawa, *Practical Batteries*, in *Handbook of Battery Materials*2011, Wiley-VCH Verlag GmbH & Co. KGaA. p. 27-85.
6. Winter, M. and R.J. Brodd, *What Are Batteries, Fuel Cells, and Supercapacitors?* Chemical Reviews, 2004. **104**(10): p. 4245-4270.
7. Huggins, R.A., *Advanced Batteries*, 2009, Springer US. p. 1-23.
8. Manthiram, A. and T. Muraliganth, *Lithium Intercalation Cathode Materials for Lithium-Ion Batteries*, in *Handbook of Battery Materials*2011, Wiley-VCH Verlag GmbH & Co. KGaA. p. 341-375.
9. Goodenough, J.B., *General Concepts*, in *Lithium Ion Batteries* 2007, Wiley-VCH Verlag GmbH. p. 1-25.
10. Mizushima, K., et al., *Li_xCoO_2 (0<x<-1): A new cathode material for batteries of high energy density.* Materials Research Bulletin, 1980. **15**(6): p. 783-789.

11. Condon, J.B., *Chapter 1 - An Overview of Physisorption*, in *Surface Area and Porosity Determinations by Physisorption* 2006, Elsevier Science: Amsterdam. p. 1-27.

12. Thackeray, M.M., et al., *Lithium insertion into manganese spinels.* Materials Research Bulletin, 1983. **18**(4): p. 461-472.

13. Etacheri, V., et al., *Challenges in the development of advanced Li-ion batteries: a review.* Energy & Environmental Science, 2011. **4**(9): p. 3243-3262.

14. Daiwon, C., W. Wei, and Y. Zhenguo, *Material Challenges and Perspectives*, in *Lithium-Ion Batteries* 2011, CRC Press. p. 1-50.

15. Whittingham, M.S., *Lithium Batteries and Cathode Materials.* Chemical Reviews, 2004. **104**(10): p. 4271-4302.

16. Kraytsberg, A. and Y. Ein-Eli, *Higher, Stronger, Better...A Review of 5 Volt Cathode Materials for Advanced Lithium-Ion Batteries.* Advanced Energy Materials, 2012. **2**(8): p. 922-939.

17. Ogumi, Z. and M. Inaba, *Carbon Anodes*, in *Advances in Lithium-Ion Batteries*, W. Schalkwijk and B. Scrosati, Editors. 2002, Springer US. p. 79-101.

18. *Negative Electrodes in Lithium Cells*, in *Advanced Batteries* 2009, Springer US. p. 123-149.

19. Franklin, R.E., *Crystallite Growth in Graphitizing and Non-Graphitizing Carbons.* Proceedings of the Royal Society of London. Series A. Mathematical and Physical Sciences, 1951. **209**(1097): p. 196-218.

20. Zhu, G.-N., Y.-G. Wang, and Y.-Y. Xia, *Ti-based compounds as anode materials for Li-ion batteries.* Energy & Environmental Science, 2012. **5**(5): p. 6652-6667.

21. Poizot, P., et al., *Nano-sized transition-metal oxides as negative-electrode materials for lithium-ion batteries.* Nature, 2000. **407**(6803): p. 496-499.

22. Armand, M. and J.M. Tarascon, *Building better batteries.* Nature, 2008. **451**(7179): p. 652-657.

23. Tarascon, J.M. and M. Armand, *Issues and challenges facing rechargeable lithium batteries.* Nature, 2001. **414**(6861): p. 359-367.

24. Ricardo, A., et al., *Anode Materials for Lithium-Ion Batteries*, in *Lithium-Ion Batteries*2011, CRC Press. p. 97-146.

25. Cabana, J., et al., *Beyond Intercalation-Based Li-Ion Batteries: The State of the Art and Challenges of Electrode Materials Reacting Through Conversion Reactions.* Advanced Materials, 2010. **22**(35): p. E170-E192.

26. Dey, A.N., *Electrochemical Studies on the Effect of Water in Nonaqueous Electrolytes.* Journal of The Electrochemical Society, 1967. **114**(8): p. 823-824.

27. Huggins, R.A., *Lithium alloy negative electrodes formed from convertible oxides.* Solid State Ionics, 1998. **113–115**(0): p. 57-67.

28. Palacin, M.R., *Recent advances in rechargeable battery materials: a chemist's perspective.* Chemical Society Reviews, 2009. **38**(9): p. 2565-2575.

29. Ding, N., et al., *Improvement of cyclability of Si as anode for Li-ion batteries.* Journal of Power Sources, 2009. **192**(2): p. 644-651.

30. Park, C.-M., et al., *Li-alloy based anode materials for Li secondary batteries.* Chemical Society Reviews, 2010. **39**(8).

31. Winter, M. and J.O. Besenhard, *Electrochemical lithiation of tin and tin-based intermetallics and composites.* Electrochimica Acta, 1999. **45**(1–2): p. 31-50.

32. Zhang, W.-J., *A review of the electrochemical performance of alloy anodes for lithium-ion batteries.* Journal of Power Sources, 2011. **196**(1): p. 13-24.

33. Info., S. *sony's new nexelion hybrid lithium ion batteries to have thirty-percent more capacity than conventional offering* 2005 [cited 2012 November 7]; Available from: http://www.sony.net/SonyInfo/News/Press/200502/05-006E/.

34. Goodenough, J., *Oxide Cathodes*, in *Advances in Lithium-Ion Batteries*, W. Schalkwijk and B. Scrosati, Editors. 2002, Springer US. p. 135-154.

35. Zhumabay, B. and T. Izumi, *Cathode Materials for Lithium-Ion Batteries*, in *Lithium-Ion Batteries* 2011, CRC Press. p. 51-96.

36. Park, B., Y. Kim, and J. Cho, *Cathodes Based on $LiCoO_2$ and $LiNiO_2$*, in *Lithium Batteries*, G.-A. Nazri and G. Pistoia, Editors. 2003, Springer US. p. 410-444.

37. Xia, Y. and M. Yoshio, *Spinel Cathode Materials for Lithium-Ion Batteries*, in *Lithium Batteries*, G.-A. Nazri and G. Pistoia, Editors. 2003, Springer US. p. 361-380.

38. Padhi, A.K., K.S. Nanjundaswamy, and J.B. Goodenough, *Phospho-olivines as Positive-Electrode Materials for Rechargeable Lithium Batteries.* Journal of The Electrochemical Society, 1997. **144**(4): p. 1188-1194.

39. Gong, Z. and Y. Yang, *Recent advances in the research of polyanion-type cathode materials for Li-ion batteries.* Energy & Environmental Science, 2011. **4**(9): p. 3223-3242.

40. Dominko, R., et al., *Structure and electrochemical performance of Li_2MnSiO_4 and Li_2FeSiO_4 as potential Li-battery cathode materials.* Electrochemistry Communications, 2006. **8**(2): p. 217-222.

41. Yamada, A., et al., *Lithium Iron Borates as High-Capacity Battery Electrodes.* Advanced Materials, 2010. **22**(32): p. 3583-3587.

42. Barker, J., M.Y. Saidi, and J.L. Swoyer, *A Comparative Investigation of the Li Insertion Properties of the Novel Fluorophosphate Phases, $NaVPO_4F$ and $LiVPO_4F$* Journal of The Electrochemical Society, 2004. **151**(10): p. A1670-A1677.

43. Ellis, B.L., et al., *A multifunctional 3.5 V iron-based phosphate cathode for rechargeable batteries.* Nat Mater, 2007. **6**(10): p. 749-753.

44. Tripathi, R., et al., *Scalable Synthesis of Tavorite $LiFeSO_4F$ and $NaFeSO_4F$ Cathode Materials.* Angewandte Chemie International Edition, 2010. **49**(46): p. 8738-8742.

45. Jain, G., M. Balasubramanian, and J.J. Xu, *Structural Studies of Lithium Intercalation in a Nanocrystalline α-Fe_2O_3 Compound.* Chemistry of Materials, 2005. **18**(2): p. 423-434.

46. Zhou, H., et al., *Iron and Manganese Pyrophosphates as Cathodes for Lithium-Ion Batteries.* Chemistry of Materials, 2010. **23**(2): p. 293-300.

47. Nishimura, S.-i., et al., *New Lithium Iron Pyrophosphate as 3.5 V Class Cathode Material for Lithium Ion Battery.* Journal of the American Chemical Society, 2010. **132**(39): p. 13596-13597.

48. Alexandra, L.-B., H. Wesley, and P. Stefano, *Electrolytes for Lithium-Ion Batteries*, in *Lithium-Ion Batteries* 2011, CRC Press. p. 147-196.

49. Xu, K., *Nonaqueous Liquid Electrolytes for Lithium-Based Rechargeable Batteries.* Chemical reviews, 2004. **104**: p. 15.

50. Bruce, P.G., B. Scrosati, and J.-M. Tarascon, *Nanomaterials for Rechargeable Lithium Batteries.* Angewandte Chemie International Edition, 2008. **47**(16): p. 2930-2946.

Chapter 2 Experimental Techniques

2.1 Abstract

The experimental techniques involved in the synthesis and characterization of anode materials and the principles thereof, have been described in this chapter.

2.2 Introduction

This Chapter is a brief overview of the methods and principle involved in synthesis, physical and electrochemical characterization of various mixed metal/metal-oxide powders investigated as lithium ion battery (LIB) anode. Electrospinning, vapour transport method, polymer precursor method, solution precipitation, high energy ballmilling and urea assisted microwave method have been adopted as the synthetic procedures. Physical characterization techniques include X-ray diffraction (XRD), Rietveld refinement of XRD data, Raman spectroscopy, scanning electron microscopy and transmission electron microscopy. Electrochemical studies are carried out by galvanostatic cycling, cyclic voltammetry, and electrochemical impedance spectroscopy. The details of electrode fabrication, coin cell assembly and the electrochemical characterization have also been discussed.

2.3 Material synthesis

Apart from conventional solid state method, the materials have been prepared by polymer precursor method, electro-spinning technique, Vapor-Transport Nanowire Growth, urea assisted microwave synthesis, high energy ballmilling and solution method (co-precipitation, hydrothermal etc.).

2.3.1 Polymer precursor method

Nanocrystalline metal molybdates such as $AMoO_4$ (where A=Co, Zn, Ni) with porous structure have been prepared from the complete evaporation of a polymer-based metal complex precursor solution. [1] The precursor solution was constituted of the metal ions that were in aqueous solution through complexation with ethylene diamine tetraacetic acid in the presence of diethanolamine, and a polymeric reagent, which was an aqueous solution mixture of sucrose and polyvinyl alcohol. Complete dehydration of the precursor solution generated a mesoporous carbon-rich precursor mass, heat treatment at temperatures 500°C, of which resulted in the respective metal molybdate phase. [2]

2.3.2 Electrospinning technique

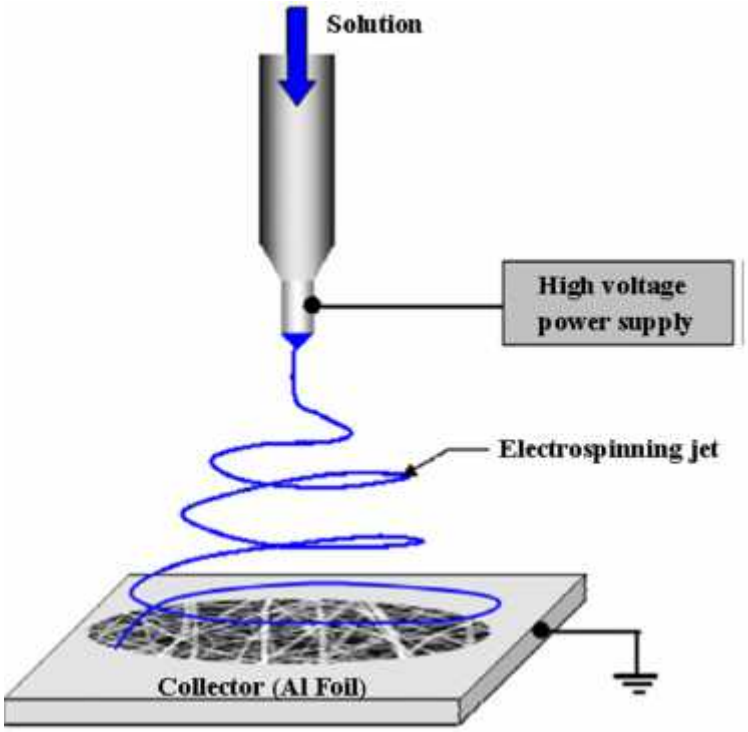

Figure 2.1 Electrospinning setup for nanofiber fabrication.

Electro-spinning is a straightforward, cheap and unique method to produce novel fibers with diameter in the range of 100 nm and even less. [3] A schematic

representation of electrospinning set uo is shown in Figure 2.1. Polymer solutions/liquid crystals/suspensions of solid particles or emulsions can be electrospun by a field of about 1 kV/cm. The electric force results in an electrically charged jet of polymer solution outflowing from a droplet tip. After the jet flows away from the droplet in a nearly straight line, it bends into a complex path and other changes in shape occur, during which electrical forces stretch and thin it by very large ratios. After the solvent evaporates, solidified nanofibers are left. The electrospun nanofibres are heat treated to obtain the crystalline phase of desired material[4, 5]. In the present study, electrospinning and subsequent heat treatment is adopted to fabricate Fe_2O_3, $NiFe_2O_4$ and molybdate nanofibres.

2.3.3 Vapour transport method

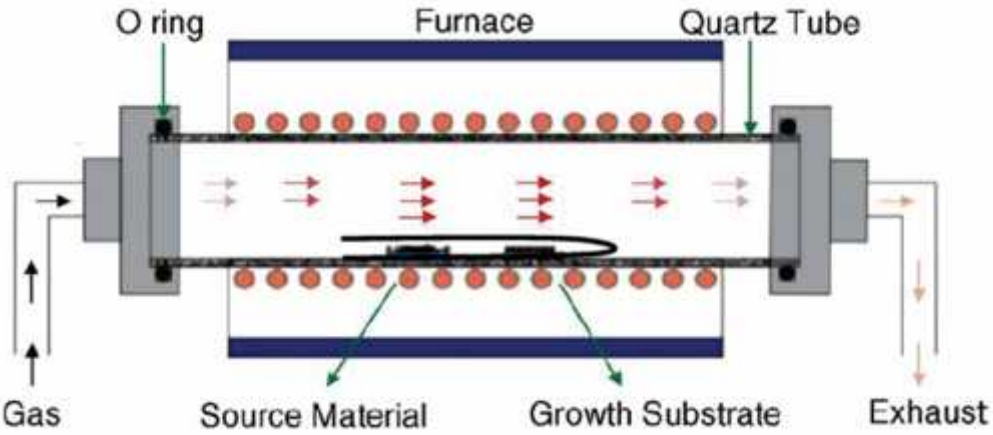

Figure 2.2 Vapour transport setup for nanowire growth.

Vapor-transport metal oxide nanowire growth is a type of chemical vapour deposition method in which the source materials are supplied via thermal evaporation rather than compressed gas sources. [6] One end of the tube (the inlet side) is hooked up to mass flow controllers (MFCs) which regulate the input flow the compressed carrier/process gases. The other end of the tube (outlet/exhaust side) is hooked up either to an exhaust or a vacuum pump depending on whether

atmospheric pressure or vacuum is desired. As shown in the Figure 2.2, at the middle of the quartz tube, one end closed small quartz tube is placed. The source material is positioned at the open end and then downstream is placed the growth substrate. Regardless of the process pressure of the tube (either atmospheric or vacuum), a carrier gas is supplied at the inlet end of the tube via a MFC in order to direct the transport of the evaporated source species to the downstream growth substrate. This carrier gas is typically either Ar or N_2. The carrier gas species and flow rate are important parameters for nanowire growth. Here, Zn_2SnO_4 nanowires are grown on stainless steel substrates by vapour transport deposition method.

2.3.4 Solution combustion method

The solution combustion method is economical and simple, to synthesize simple and mixed metal oxides.[7-9] The solution combustion method utilizes the exothermic reaction between metal nitrates (oxidizer) and fuel. The heating of desired metal salts with some organic compounds such as glycine, urea, or citric acid, etc. results in self combustion that generates intense heat by exothermic reaction. The use of microwaves in combustion synthesis has several advantages for the synthesis of many organic and inorganic materials compared to conventional methods. The foremost of these advantages are the short time periods for the synthesis, enhanced reaction kinetics, and the reactant selectivity during energy transfer from the microwave field that assists the stabilization of the meta-stable phase of the material. Therefore, it is possible to control both the kinetic and thermodynamic factors of the chemical reactions using microwaves in the combustion process.[10] Here, the solid solutions, $(Ni_{1-x}Zn_x)\ Fe_2O_4$ (x= 0, 0.2, 0.4, 0.6, 0.8, 1) were prepared by citrate gel auto combustion method reported by

Hankare *et al*.[11] $CoMoO_4$, $ZnMoO_4$ and $NiMoO_4$ nanoparticles are synthesized by citric acid assisted microwave method.

2.3.5 High energy ballmilling

Ballmilling is a mechanochemical processing techinique that can be defined as a powder processing technique involving deformation, fracturing and cold welding of the particles during repeated collisions with a ball. [12] During ballmilling, the mechanical energy is transferred to the particles of the reactants, causing many changes to the particles such as deformation, friction, fracture, amorphisation, quenching and so on. After milling, a product phase is formed at the interfaces of the reactant particles. The main advantage of this method is its simplicity in the synthesis process, effective mixing accompanying a breaking of chemical bonds and their recombination and a decrease in energy expenses as well as the cost of the materials. In our lab, we use SPEX 8000D Dual Mixer which is shown in Figure 2.3. It is an efficient two-clamp laboratory mill, also called shaker mill or high-energy ball mill. Features include a variable-range electronic timer, dual clamps for multiple sample capacity, safety interlock system, and forced-air cooling. For efficiency, clamps are run in balance with the same vial and load in each clamp. It reduces samples to analytical fineness and can be utilized for mechanical alloying and nanomilling. In the present study, rutile-TiO_2 and SnO nanoparticles are prepared by ballmilling. [13]

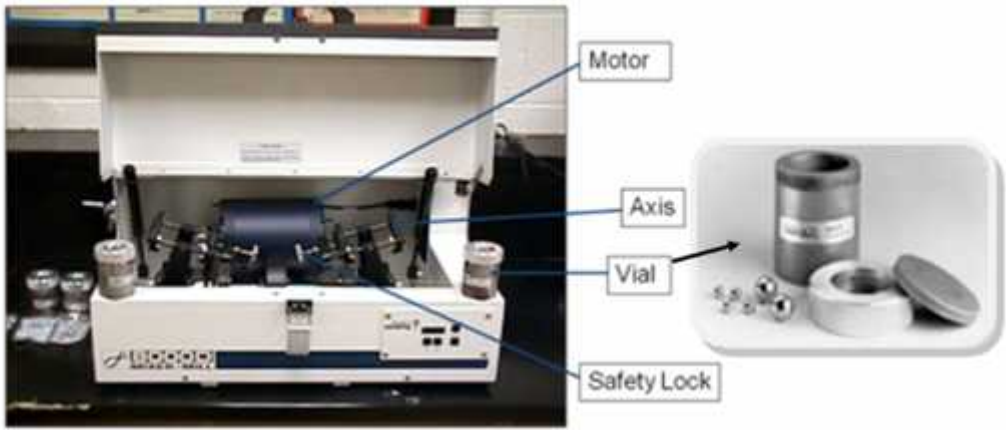

Figure 2.3 High energy ball mill, SPEX-8000D

2.3.6 Solvothermal synthesis

Solvothermal synthesis is a method for preparing a variety of materials such as metals, semiconductors, ceramics, and polymers. The process involves the use of a solvent under moderate to high pressure (typically between 1 atm and 10,000 atm) and temperature (typically between 100°C and 500°C) that facilitates the interaction of precursors during synthesis. If water is used as the solvent, the method is called “hydrothermal synthesis.” The synthesis under hydrothermal conditions is usually performed below the supercritical temperature of water (374 °C). The process can be used to prepare different geometries including thin films, bulk powders, single crystals, and nanocrystals. In addition, the morphology (sphere (3D), rod (2D), or wire (1D)) of the crystals formed is controlled by manipulating the solvent supersaturation, chemical of interest concentration, and kinetic control. The method can be used to prepare thermodynamically stable and metastable states including novel materials that cannot be easily formed from other synthetic routes. Here Fe_3O_4 nanospheres, nanorods and nanorings are prepared by hydrothermal method.

2.4 Characterization techniques

2.4.1 X-ray diffraction

X-ray diffraction (XRD) is widely used for the identification of bulk, crystalline structures[14]. The generated electromagnetic waves of the X-rays are several thousand electron volts, usually originating from the interaction of high energy electrons with a copper target (8.05 keV, 0.154 nm). This radiation penetrates surfaces and interacts with the solid's internal structure.

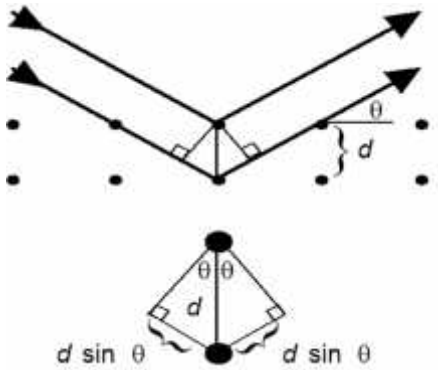

Figure 2.4 Bragg diffraction: Two beams with identical wavelength and phase approach a crystalline solid and are scattered off different atoms within it.

Constructive interference occurs when the scattered waves remain in phase after interference i.e. the path difference is equal to an integer multiple of the wavelength (Figure 2.4). The path difference between two waves undergoing constructive interference is given by $2d\sin\theta$, where θ is the scattering angle. The detector receives a set of interference signals at different angles, θ, which correspond to the lattice spacing based on Bragg's law [15, 16]:

$$n\lambda = 2d \sin\theta; \; n = 1, 2 \qquad \text{eqn. 2.1}$$

where d is the distance between two atomic planes (lattice spacing), n is an integer called the order of reflectance, λ is the wavelength of the electromagnetic radiation, and θ is the angle between the incident beam and normal to the reflecting

crystalline plane. The lattice spacing, d, is characteristic and therefore can be used to identify crystal structure and atomic composition. With the help of eqn. 2.1, the interplanar spacing, d can be readily calculated.

Indexing is the first step adopted in X-ray analysis. It is the process of determining the unit cell parameters from the peak positions. To index a powder diffraction pattern, it is necessary to assign Miller indices, hkl, to each peak. The International Centre for Diffraction Data (ICDD) provides the standard powder diffraction patterns of a large number of compounds in the form of JCPDS cards. The structure of an unknown compound can be roughly identified by comparing with the data summarized in these cards. The exact crystal structure and unit cell parameters are evaluated from the XRD data with the help of TOPAS software using Rietveld refinement technique.

According to the theory of diffraction [14, 17], the pattern of polycrystalline samples consists of sharp lines (Full Width at Half Maximum (FWHM) in the order of seconds of an arc). In practice, the lines always present some degree of broadening which is determined by the crystallite size distribution, by the presence, nature and extension of lattice strains, and by the spectral distribution of energy. The peak profile can thus be regarded as an interaction of the spectral distribution of the X-ray radiation with the instrument (instrumental broadening) and the real structure of the sample (sample broadening). According to Scherrer [18], it is possible to determine the average coherence length, which can be roughly approximated to the average crystallite size, by measuring the FWHM of the diffraction peaks corrected for the contributions from the diffractometer as shown in eqn. 2.2.

$$B_{hkl} = \frac{0.89\lambda}{L\cos\theta} \qquad \text{eqn. 2.2}$$

where B_{hkl} is FWHM, λ the wavelength of incident beam, L the average size of crystallites, and θ the diffraction angle. The instrumental contribution (B_{inst}) can be subtracted from the experimental data by running a strain-free, flawless standard either mixed with the sample or in a separate experiment under the same conditions, or by annealing part of the sample and obtain its diffraction pattern. The annealed material supposedly consists of perfect crystals large enough so that any line broadening should be caused solely by instrumental effects. By subtracting these effects from the pattern of the non-annealed sample, the remaining broadening is due to the particle size distribution. If the peak shape is lorentzian, $B = B_{hkl} - B_{inst}$ whereas if the peak shape is guassian, $B = \sqrt{B_{hkl}^2 - B_{inst}^2}$.

2.4.2 Brunauer-Emmett-Teller specific surface area

Stephen Brunauer, Paul Hugh Emmett, and Edward Teller derived a relation from a statistical and gas-kinetic model on the principle that increasing adsorbate partial pressure over a dry powder corresponds to increasing mono and multi-layer adsorptive build up. [19] This measurement technique is based on the physical adsorption of nitrogen or helium at low, constant temperatures. This physical adsorption of a gas over the entire exposed surface of a material and the filling of pores is called physisorption. The main characteristics of Physical adsorption are low heats of adsorption, no violent or disruptive structural changes, involvement of multiple layers of adsorbate, thus allowing for pore measurements, inhibit of physical adsorption at high temperature. Adsorption equilibrium is achieved

quickly since no activation energy is generally required. It is fully reversible, allowing adsorbate to fully adsorb and desorb. When a gas or vapour phase is brought into contact with a solid, part of it is taken up and remains on the outside attached to the surface. In physisorption (physical adsorption), there is a weak Van der Waals attraction between the adsorbate and the solid surface. In our experiments, liquid nitrogen was used, having a boiling temperature of 77 K. This technique measures gas uptake (adsorption) for increasing partial pressure over a dry powder sample and the release of gas (desorption) at decreasing partial pressures. The resulting measurements produce adsorption isotherms which relate amount adsorbed to the relative pressure, from which the specific surface are (SSA) of the powder is obtained. It is also a useful tool to characterize porous materials allowing for the determination of pore size distribution and porosity.

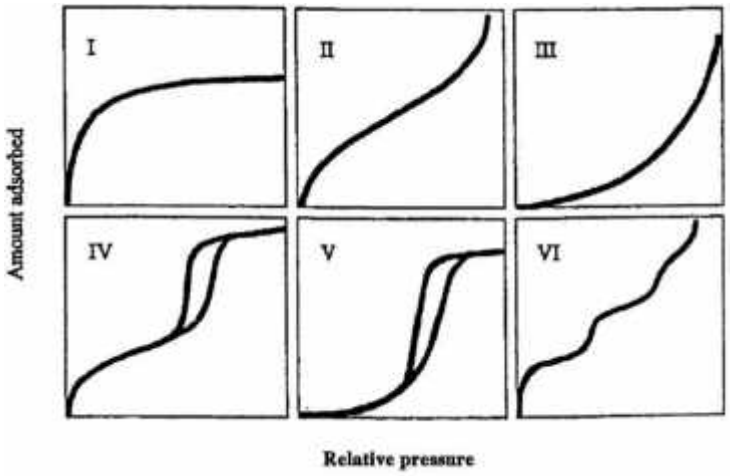

Figure 2.5 Different types of isotherm.

An Adsorption Isotherm is obtained by measuring the amount of gas adsorbed across a wide range of relative pressures at a constant temperature (typically liquid N_2, 77K). Conversely desorption isotherms are achieved by measuring gas removed as pressure is reduced. There are 6 types of isotherms as described by Brunauer, Deming and Teller and are shown in Figure 2.5. [20, 21]

Type I -This is characteristic of either a chemisorption isotherm (in which case the final upswing at high pressures may not be present) or physisorption on a material that has extremely fine pores (micropores).

Type II - This is characteristic of a material, which is not porous, or possibly macroporous, and has a high energy of adsorption.

Type III - This is characteristic of a material, which is not porous, or possibly macroporous, and has a low energy of adsorption.

Type IV -This is characteristic of a material, which contains mesoporosity and has a high energy of adsorption. These often contain hysteresis attributed to the mesoporosity.

Type V - This is characteristic of a material, which contains mesoporosity and has a low energy of adsorption. These often contain hysteresis attributed to the mesoporosity

Type VI- This type of isotherm is attributed to several possibilities the most likely being, if the temperature is below the adsorptive triple point, that the adsorbate is more like a solid forming a structured layer, i.e. epitaxial growth. Other possible explanations include specific pore size distribution. If the steps are at the low pressure portion of the isotherm, then the steps may be due to two or more distinct energies of adsorption. If the steps are at the high pressure part of the isotherm, then the steps might be due to sharp steps on the adsorbate surface. Hysteresis loop is due to the phenomenon of the desorption isotherm being different from the adsorption isotherm. The amount of adsorbate is greater for desorption. Hysteresis loops are classified into four types. These types were given the designation of H1–

H4 by an IUPAC committee. [21] The characteristics and conventional interpretation of these hysteresis loops are given in Table 2-1. [21]

Type	Characteristics	Usual interpretation
H1	Nearly vertical and parallel adsorption and desorption branches	Regular even pores without interconnecting channels.
H2	Sloping adsorption branch and nearly vertical desorption branch.	Pores with narrow and wide sections possible interconnecting channels.
H3	Sloping adsorption and desorption branches covering a large range of P/P_s with underlying type II isotherm.	Slit-like pores for which adsorbent–adsorbate pair which would yield a type II isotherm without pores.
H4	Underlying type I isotherm with large range for the hysteresis loop	Slit-like pore for the type I adsorbent–adsorbate pair.

Table 2-1 Characteristics and interpretation of Hysteresis loops.

The BET surface area measurement is crucial in understanding the behavior of a material, as material reacts with its surroundings via its surface, a higher surface area material is more likely to react faster, dissolve faster and adsorb more gas than a similar material with a lower surface area.

The BET equation is given by

$$\frac{1}{W\left(\left(\frac{P_O}{P}\right)-1\right)} = \frac{1}{W_m C} + \frac{C-1}{W_m C}\left(\frac{P}{P_O}\right) \qquad \text{eqn. 2.3}$$

W= weight of gas adsorbed, $\frac{P}{P_o}$ = relative pressure, W_m= weight of adsorbate as monolayer, C= BET constant. BET equation requires a linear plot of $\frac{1}{\left[W\left(\frac{P}{P_O}\right)-1\right]}$

against $\frac{P}{P_o}$. The slope of the plot will be, s= $\frac{C-1}{W_m C}$ and the intercept will be, i = $\frac{1}{W_m C}$. So weight of the monolayer is given by, $W_m = \frac{1}{s+i}$. The total surface area can then be

$$S_t = \frac{W_m N A_{cs}}{M} \qquad \text{eqn. 2.4}$$

where N= Avagadro number, M=molecular weight of adsorbate, A_{cs}= adsorbate cross sectional area (16.2 $Å^2$ for Nitrogen). Specific Surface Area (SSA) is then determined by total surface area divided by the sample weight. Assuming that the particles are spherical, non-porous, smooth, and mono-disperse, the mean primary particle size can be calculated

$$d_{BET} = 6\ (\rho \times SSA)\text{-}1 \qquad \text{eqn. 2.5}$$

where ρ is the powder's bulk density and SSA is the mass specific surface area. The d_{BET} describes the volume to surface diameter and can be described as the average primary particle diameter, but d_{BET} provides no information on the particle size distribution of the powder.

2.4.3 Scanning electron microscopy

The scanning electron microscope (SEM) uses a focused beam of high-energy electrons to generate a variety of signals at the surface of solid specimens. The signals that derive from electron-sample interactions reveal information about the sample including external morphology (texture), chemical composition, crystalline structure and orientation of materials making up the sample. In scanning electron microscopy, visual inspection of the surface of a material utilizes signals of two types, secondary and backscattered electrons. Secondary and backscattered

electrons are constantly being produced from the surface of the specimen while under the electron beam; however they are a result of two separate types of interaction. Secondary electrons are a result of the inelastic collision and scattering of incident electrons with specimen electrons. They are generally characterized by possessing energies of less than 50 eV. They are used to reveal the surface structure of a material with a resolution of ~10 nm or better. Backscattered electrons are a result of an elastic collision and scattering event between incident electrons and specimen nuclei or electrons. Backscattered electrons can be generated further from the surface of the material and help to resolve topographical contrast and atomic number contrast with a resolution of greater than 1 micron.

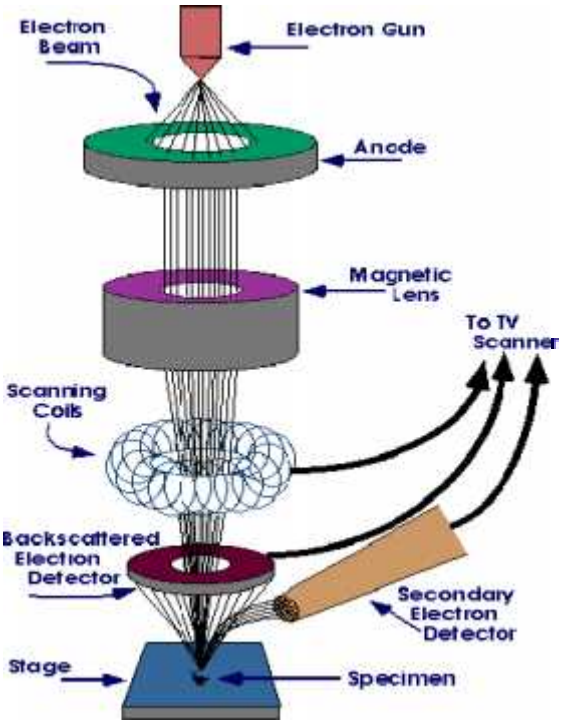

Figure 2.6 Schematic diagram of scanning electron microscope. Diagram courtesy: Iowa State University, http://www.mse.iastate.edu/microscopy/whatsem.html

While there are several types of signals that are generated from a specimen under an electron beam, the x-ray signal is typically the only other signal that is used for scanning electron microscopy. When the beam electrons scatter in-elastically,

tightly bound inner shell electrons may be ejected from the target atoms if the beam energy is higher than the critical excitation energy, E_c (also known as X-ray absorption edge energy), of the target atomic shell. The energy of the beam electron is diminished by an amount equal to E_c and subsequent relaxation of the target atom from its excited state involving the transfer of an outer shell electron to the ionized inner shell, results in the generation of a characteristic X-ray. The x-ray signal can originate from further down into the surface of the specimen and allows for determination of elemental composition through EDS (energy dispersive x-ray spectroscopy) analysis of characteristic x-ray signals.

Essential components of all SEMs include an electron source ("Gun"), electron lenses, sample stage, detectors for all signals of interest , display / data output devices and other infrastructure requirements such as power supply, vacuum system, cooling system, vibration-free floor, room free of ambient magnetic and electric fields. SEMs always have at least one detector (usually a secondary electron detector), and most have additional detectors. The specific capabilities of a particular instrument are critically dependent on which detectors it accommodates.

2.4.4 Transmission electron microscopy

A Transmission Electron Microscope (TEM) utilizes energetic electrons to provide morphologic, compositional and crystallographic information on samples. The high energy electrons, up to 300 kV accelerating voltage, are accelerated to nearly the speed of light. The electron beam behaves like a wavefront with wavelength about a million times shorter than light-waves. At a maximum potential magnification of 1 nanometer, TEMs are the most powerful microscopes.

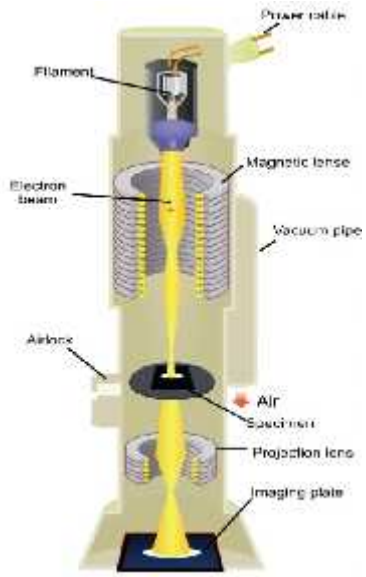

Figure 2.7 Schematic diagram of transmission electron microscope. Diagram Courtesy: The Chinese University of Hong Kong, http://www.hk-phy.org/atomic_world/tem/tem02_e.html

TEM consist of the various components such as an electron source, thermionic gun, electron beam, electromagnetic lenses, vacuum chamber, 2 Condensers, sample stage and phosphor or fluorescent screen and is shown in Figure 2.7. A TEM functions under the same basic principles as an optical microscope. In a TEM, electrons replace photons, electromagnetic lenses replace glass lenses and images are viewed on a screen rather than through an eyepiece. There are essentially three types of lenses used to form the final image in the TEM. These are the condenser, objective, and projector lenses. The main function of the condenser lens is to concentrate and focus the beam of electrons coming off of the filament onto the sample to give a uniformly illuminated sample. The objective lens and its associated pole pieces are the heart of the TEM and the most critical of all the lenses. It forms the initial enlarged image of the illuminated portion of the specimen in a plane that is suitable for further enlargement by the projector lens.

When an electron beam passes through a thin-section specimen of a material, electrons are scattered. The sophisticated system of electromagnetic

lenses focuses the scattered electrons into an image or a diffraction pattern, or a nano-analytical spectrum, depending on the mode of operation. Each of these modes offers a different insight about the specimen. The imaging mode provides a highly magnified view of the micro- and nanostructure while in the high resolution imaging mode a direct map of atomic arrangements can be obtained (high resolution TEM or HRTEM). The diffraction mode (selected area electron diffraction, SAED) displays accurate information about the local crystal structure. The nano-analytical modes (x-ray and electron spectrometry) give an idea about the elements that are present in the tiny volume of material.

TEM builds an image by way of differential contrast. Those electrons that pass through the sample go on to form the image while those that are stopped or deflected by dense atoms in the specimen are subtracted from the image. In this way a black and white image is formed. Some electrons pass close to heavy atom and are thus only slightly deflected. Thus many of these scattered electrons eventually make their way down the column and contribute to the image. In order to eliminate these scattered electrons from the image an aperture is placed in the objective lens that will stop all those electrons that have deviated from the optical path. The smaller the aperture used, the more of these scattered electrons will be stopped and the greater will be the image contrast. The projector lens is to project the final magnified image onto the phosphor screen or photographic emulsion. It is in the projector lens that the majority of the magnification occurs. Thus total magnification is a product of the objective and projector magnifications. For higher magnifications an intermediate lens is often added between the objective and projector lenses. This lens serves to further magnify the image.

The requirements of a good TEM sample include 1) electron beam transparency which limits maximum thickness to 5 μm and 2) clean surface (free from contaminants). TEM samples are prepared following this procedure (1) Grind the powder in agate mortar and pestle 2) suspend the powder in an organic solvents in an ultrasonic bath, 3) deposit suspended particles on to a TEM copper grid coated with carbon. If crystal sizes are significantly larger than 1 μm, mechanically thinning of these particles is needed.

2.5 Fabrication of coin cell

2.5.1 Electrode fabrication

The composite electrodes consisting of thick slurry of electrode material, conducting carbon (Super P, MMM Ensaco) and binder (Kynar 2801) in the weight ratio 70:15:15 were fabricated. The organic solvent, 1-methyl 2-pyrrolidone (NMP, Merck) was used as the mixing medium for slurry. The thick and uniform slurry was coated onto an etched copper foil by the doctor blade technique. Mixing the conducting carbon imparts good inter-particle electronic conductivity among the grains of active material. PVDF (Kynar) acts as a binder and helps the coating to adhere well to the metal foil. Copper, due to its excellent electronic conductivity and non-alloying nature with Li-metal, is chosen as the current collector for the electrode material. Drying at 80°C in an air oven for 24 h facilitates the evaporation of NMP. The dried thick film (20-30 μm) of composite electrodes were pressed between twin rollers (Soei Singapore Scientific Quartz Co.) at about 1500 kPa pressure prior to cutting in to circular discs of diameter 16 mm, to ensure good adherence of composite electrode material on to the Cu-foil. The composite

electrode pieces were then dried at 70˚C for 12 h in vacuum oven and transferred to the Glove box for cell fabrication.

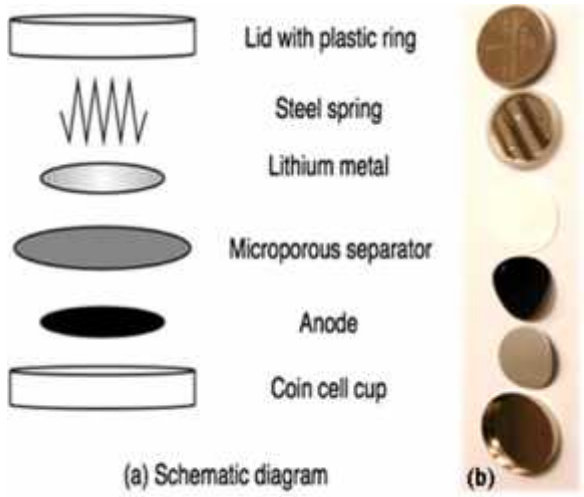

Figure 2.8 (a) Schematic of coin cell assembly. (b) Photograph of the parts and fabricated coin cell.

2.5.2 Coin cell assembly

The coin-cells were fabricated inside the Ar-filled glove-box using electrodes as cathodes and Li metal foil as anodes. The glove box (MBraun, Germany) maintains less than 1 ppm of H_2O and less than 5 ppm of O_2. For making a coin cell, standard stainless-steel cups and lids fitted with a plastic ring are used for the casing. Coin cells (size, 2016; 20 mm diameter and 1.6 mm thick) comprise composite electrode, 'Celgard 2502' polypropylene micro-porous membrane or glass micro-fiber filter (Whatman) as the separators and the 1M $LiPF_6$, dissolved in ethylene carbonate (EC) and diethyl carbonate (DEC) (1:1 by volume, Merck Selectipur LP40) as the electrolyte and Li metal (Kyokuto Metal Co., Japan) foil as counter electrode (Figure 2.8(a)). The electrode is placed in the centre of the cup which forms the positive terminal of the cell and is wetted with a few drops of the electrolyte. This is covered with the micro-porous separator that is permeable to

the Li-ions but prevents electronic movement between the two electrodes. It is further wetted with few drops of the electrolyte. Circular Li metal disc of the size 13 mm diameter and ~0.59 mm thick is placed centrally on the separator. To ensure good sealing of the battery, a steel spring is welded to the steel lid which then rests over Li-metal disc and forms the negative terminal of the cell. Finally, hermetic sealing is done with a mechanical press (Econo Engineering Pte. Ltd., Singapore and Housen Corporation, Japan).

The assembled cells (Figure 2.8(b)) are then transferred out of the glove box and are aged for 24 h at ambient temperature (to ensure the percolation of the electrolyte in to the electrode material) before performing any experiments. The Li-metal is used as the counter and reference electrode whose voltage is fixed arbitrarily as zero. In contact with electrolyte, it provides infinite Li-ions. Hence, the composite electrode in the cell reacts with maximum possible amount of Li during discharge. During charge-process, Li-ions will get reduced and deposited on to Li-metal. Such a cell configuration employing one working electrode and one counter (reference) electrode is called half-cell configuration. Thus, the capacity of cell with Li-counter electrode is in fact the practical capacity of the active material under investigation.

2.6 Electrochemical methods

2.6.1 Galavanostatic cycling

Galvanostatic cycling (or cyclic chronopotentiometry) is an important method for the electrochemical evaluation of battery materials. A constant current (I) is applied to the cell and the potential is monitored as a function of time (t). The total

amount of charge passed per unit mass (m) of electrode material, i.e. the specific capacity C, during complete discharge (or charge) is given by:

$$C = \frac{I*t}{m} \qquad \text{eqn. 2.6}$$

'I','t', 'm' are expressed in mill ampere, hour and gram respectively. So the unit of specific capacity will be mAh g^{-1}. Data from galvanostatic measurements are often displayed as cell voltage E as a function of C. The cyclability of the material is usually presented as the total charge or discharge capacity, C, as a function of cycle number.

We have done galvanostatic cycling studies on the cells consisting the synthesized electrode as cathodes with respect to Li-metal as counter electrode at ambient temperature (RT=27ºC) by computer controlled Bitrode multiple battery tester (model SCN, Bitrode, USA) for a fairly large number of charge-discharge cycles. The resultant output of the measurement is in the form of data comprising step discharge-charge time, variation of voltage and overall energy output (discharge/charge capacity) in terms of mA.h (coulombs). The specific discharge/charge capacity (mAh g^{-1}) and the number of moles of Li can then be deduced from the known weight of the active material (and its molecular weight). The theoretical specific capacity of a compound is calculated assuming that all the Li per formula unit of the compound participate in the electrochemical reaction and is given by:

$$\text{Sp. Theor. cap. (C, mAh/g)} = \frac{(F \times n_{Li})}{M \times 3600} \times 1000 \qquad \text{eqn. 2.7}$$

where F=Faraday's constant (96,500 coulombs per gm. equiv.), n_{Li}= number of Li participating per formula unit of the compound (e.g., n_{Li}= 2 for FeO), M= molecular weight.

For example, the theoretical reversible specific capacity of FeO is

$$\text{Sp. Theor. cap. (mAh/g)} = \frac{(96500 \times 2)}{72 \times 3600} \times 1000 = 745$$

Similarly, the actual amount of Li participating in charge-discharge process is calculated from the experimental values of specific capacities. A comparison of the galvanostatic cycling response in terms of the achievable capacities and cycleability with the theoretical results, help to decide the suitability of the compound for its application as anode for LIB.

2.6.2 Cyclic voltammetry

An experiment in which the potential applied to the working electrode is swept at a constant sweep rate and the resulting current measured as a function of potential is called a voltammetry experiment. Cyclic voltammetry is a very versatile electrochemical technique which allows probing the mechanics of redox and transport properties of a system in solution. In cyclic voltammetry, the potential of the working electrode is swept at a specific sweep rate (in microvolts / second), and measures the resulting current vs. time curve. Usually the sweep is reversed at a specific switching potential, hence the name cyclic voltammetry. Since the sweep rate is constant and the initial and final switching potentials are known, one can easily convert time to potential, and the usual protocol is to record current vs. applied potential. The potential is scanned back and forth linearly with time between two extreme values – the switching potentials using triangular potential waveform (see Figure 2.9(a)). When the potential of the working electrode is more positive than that of a redox couple present in the solution, the corresponding species may be oxidized (i.e. electrons going from the solution to the electrode) and produce an anodic current. Similarly, on the return scan, as the

working electrode potential becomes more negative than the reduction potential of a redox couple, reduction (i.e. electrons flowing away from the electrode) may occur to cause a cathodic current. By IUPAC convention, anodic currents are positive and cathodic currents are negative.A typical voltammogram i.e. the resulting current vs. applied potential curve (curve ABCDEFG) for an ideal, reversible system is shown in Figure 2.9(b).

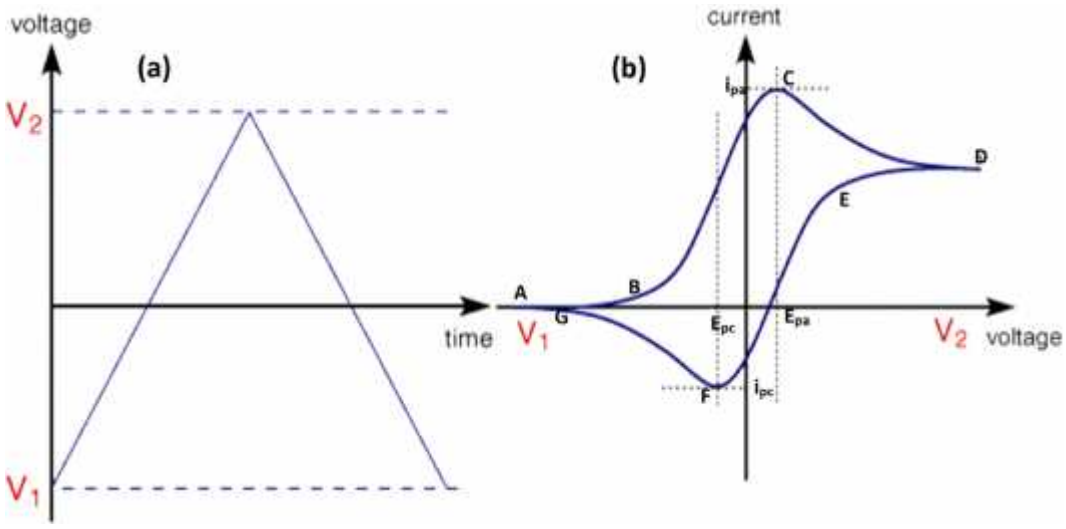

Figure 2.9 (a) A cyclic voltammetry potential waveform with switching potentials (b) The expected response of a reversible redox couple during a single potential cycle.

The scan shown starts at a slightly negative potential, *(A)* up to some positive switching value, *(D)* at which the scan is reversed back to the starting potential. The current is first observed to peak at E_{pa} (with value i_{pa}) indicating that an oxidation is taking place and then drops due to depletion of the reducing species from the diffusion layer. During the return scan the processes are reversed (reduction is now occurring) and a peak current is observed at E_{pc} (corresponding value, i_{pc}).

Providing that the charge–transfer reaction is reversible, that there is no surface interaction between the electrode and the reagents, and that the redox products are stable (at least in the time frame of the experiment), the ratio of the reverse and the forward current $i_{pc}/i_{pa} = 1.0$. In addition, for such a system it can be shown that:

- the corresponding peak potentials E_{pa} and E_{pc} are independent of scan rate and concentration.
- the formal potential for a reversible couple $E^{0'}$ is centered between E_{pa} and E_{pc}: $E^{0'} = (E_{pa} + E_{pc})/2$
- the separation between peaks is given by $\Delta E_p = E_{pa} - E_{pc} = 59/n$ mV (for a n electron transfer reaction) at all scan rates .

Larger values of ΔEp, which increase with increasing scan rate, are characteristic of slow electron transfer kinetics. Thus the potential scan-rate is used as diagnostic tool to distinguish between reversible (diffusion-controlled) and irreversible (charge-transfer controlled) kinetics of electrode process. The expression of the peak current (A) for the forward sweep in a reversible system at 298 K is given by the Randles–Sevcik equation:

$$i_{pf} = (2.69 \times 10^5)\, n^{\frac{3}{2}}\, A\, D^{\frac{1}{2}}\, \nu^{\frac{1}{2}}\, C^* \quad \text{eqn. 2.8}$$

where n is the number of electron equivalent exchanged during the redox process, A (cm^2) the active area of the working electrode, D ($cm^2\ s^{-1}$) and C^* (mol cm^{-3}) the diffusion coefficient and the bulk concentration of the electroactive species; v is the voltage scan rate ($V\ s^{-1}$).

2.6.3 Rate capability experiments

Rate capability experimentation is a useful technique to assess the electrochemical performance of an electrode and its active material. The most common term used

to express batteries ability to deliver current is its 'rated capacity'. Rated capacity is specified in Ampere hour at a specific discharge rate. For example, a battery rated 200 Ah (for a 10 h discharge rate) will deliver 20 A of current for 10 hours under standard temperature conditions. The discharge rate can also be specified in its charge rate or C rate, which is expressed as a multiple of the rated capacity of the cell. If a battery have a rating of 200 Ah at a C/10 discharge rate, then the current is given by C/10 = 200/10 =20 A. Battery capacity varies with discharge rate. The higher the C rate, the lower the cell capacity. The current rate 1C can be defined as the total deliverable reversible capacity of the electrode material in 1h. In our rate capability studies, following method is adopted to calculate C rate. Suppose x mAh g^{-1} is the theoretical capacity. If the applied current densities are 50 mA g^{-1}, 100 mA g^{-1}, 200 mA g^{-1} etc., then the corresponding C-rates are 50/x, 100/x, 200/x etc.

2.6.4 Electrochemical impedance spectroscopy

Electrochemical Impedance Spectroscopy (EIS) is a powerful technique for understanding electrochemical systems. Complex items, such as batteries, contain many areas of resistance and capacitance due to their physical structure and electrochemistry. Any electrochemical cell can be described in terms of an equivalent electric circuit, which is a combination of resistances, capacitances, and complex impedances (and inductances, in the case of very high frequencies).[22] Impedance spectroscopy (IS) is a tool used to characterize the equivalent circuit of the item by measuring its complex impedance across a spectrum of frequencies. This technique involves a determination of cell impedance, in response to a small (-5 mV amplitude) ac signal at any constant DC potential (preferably at the OCV to minimize the Dc currents), over a range of frequencies ranging typically from

10^6Hz to 10^{-3} Hz and hence the term impedance spectroscopy.[23] A circuit element's ability to resist the flow of an electrical current is defined in terms of the ratio between voltage, V, and current, I, as in Ohm's law:

$$R = \frac{V}{I} \qquad \text{eqn. 2.9}$$

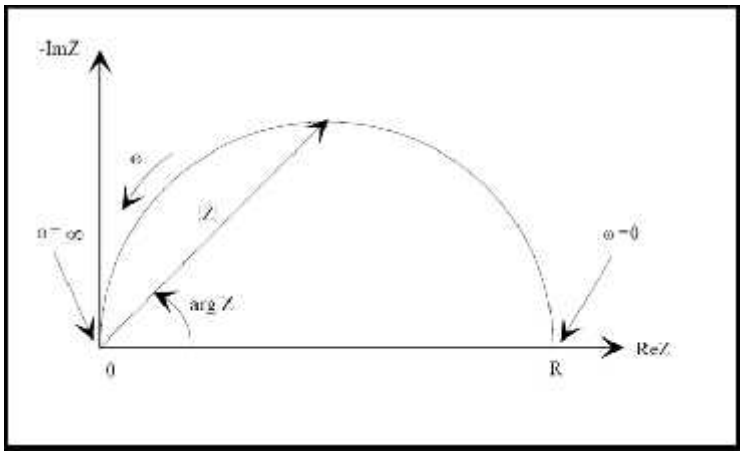

Figure 2.10 Nyquist plot with impedance vector.

This relationship only applies to ideal resistors. The resistance of an ideal circuit is not independent of frequency as ideal resistances are. So the term impedance is used in place of resistance for real circuits. An impedance, $Z(\omega) = Z' + jZ''$ is such a vector quantity and can be plotted in the plane with either rectangular or polar coordinates as displayed in Figure 2.10. Here, the impedance is represented as a vector diagram which displays the real (in-phase, Z′) and imaginary components (out of phase, Z") of a complex system. Such plots at each frequency are known as Nyquist plots. [22]

If a sinusoidal potential excitation is applied, the response to this potential will be an AC current signal. This current signal can be analyzed as a sum of sinusoidal functions (a Fourier series). [22] A multitude of fundamental microscopic processes take place throughout the cell when it is electrically stimulated which

will lead to the overall electrical response. In our electrochemical impedance spectroscopy (EIS) experiments, the cell is held in equilibrium at a fixed dc potential and a small amplitude ac signal (5-10 mV) is superimposed on it. The response of the system to this perturbation from equilibrium is measured in terms of amplitude and phase of resultant current which gives the overall impedance of the cell. The frequency of the ac signal is varied to study the impedance variation of the cell as a function of frequency. As shown in Fig. 2.11, the EIS spectra in the frequency range 10^{5}~10^{-2} Hz are interpreted in terms of the following physical phenomena in an order of decreasing frequency: (i) a high frequency semicircle because of the presence of a surface layer; (ii) a middle to high frequency semicircle related to the electronic properties of the material; (iii) a middle frequency semicircle associated with charge transfer, and finally, and (iv) the very low frequency incline line attributed to the solid state diffusion. [24]

If an electric circuit produces the same response as the electrochemical cell does when the same excitation signal is imposed, it is called the electrochemical equivalent circuit (EEC) of the cell. Quantitative data may be obtained from EIS by modeling the circuits and these models can be designed using the combination of resistors and capacitors in series or parallel fashion such that each equivalent circuit element corresponds to a component of the electrochemical cell and thus the model simulates the experimental impedance spectrum. A resistor may be used to indicate the ohmic resistance of the cell, which includes the resistances of the electrolyte, electrode base metal, electrode leads, terminals, etc. A semicircle on a complex-plane diagram (i.e. imaginary part, Z'' vs. real part Z') indicates the presence of a parallel combination of a resistor and a capacitor if Z'' is negative, or a parallel combination of a resistor and an inductor if Z'' is positive.

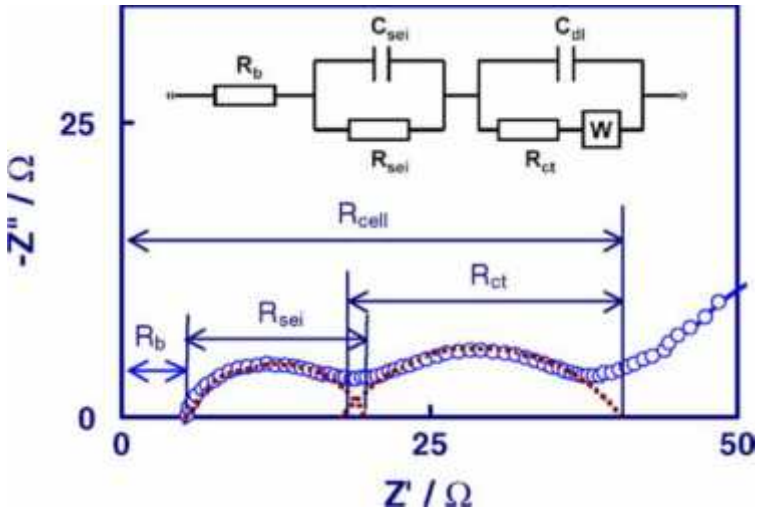

Figure 2.11 Typical EIS of the Li-ion cell and the equivalent circuit used to fit the EIS. *Reprinted from [25] with permission from Elsevier.*

An EEC model built for a typical EIS spectrum of a Li-ion cell is shown in A semicircle on a complex-plane diagram (i.e. imaginary part, Z″ vs. real part Z′) indicates the presence of a parallel combination of a resistor and a capacitor if Z″ is negative, or a parallel combination of a resistor and an inductor if Z″ is positive.

Figure 2.11.[25] The R_b is bulk resistance of the cell, which reflects electric conductivity of the electrolyte, separator, and electrodes; R_{sei} and C_{sei} are resistance and capacitance of the solid-state interface layer formed on the surface of the electrodes, which correspond to the semicircle at high frequencies; R_{ct} and C_{dl} are faradic charge-transfer resistance and its relative double-layer capacitance, which correspond to the semicircle at medium frequencies. An electrical double layer exists on the interface between an electrode and its surrounding electrolyte. This double layer is formed as ions from the solution "stick on" the electrode surface. The charged electrode is separated from the charged ions. The separation is very small, often on the order of angstroms. Charges separated by an insulator form a capacitor. On a bare metal immersed in an electrolyte, there will be 20 to 60 μF of capacitance for every 1 cm^2 of electrode area. The value of the double layer

capacitance depends on many variables such as electrode potential, temperature, ionic concentrations, types of ions, oxide layers, electrode roughness, impurity adsorption, etc.

W is the Warburg impedance related to a combination of the diffusion effects of lithium ion on the interface between the active material particles and electrolyte, which is generally indicated by a straight sloping line at low frequency end. At high frequencies the Warburg impedance is small since diffusing reactants do not have to move very far. At low frequencies the reactants have to diffuse farther, increasing the Warburg-impedance. On a Nyquist Plot, the Warburg impedance appears as a diagonal line with a slope of 45°. On a Bode Plot, the Warburg impedance exhibits a phase shift of 45°. The combination of R_{ct} and W is called faradic impedance, which reflects kinetics of the cell reactions. Low R_{ct} generally corresponds to a fast kinetics of the faradic reaction.

Since in practice, the Nyquist plots show depressed a semicircle (A semicircle on a complex-plane diagram (i.e. imaginary part, Z″ vs. real part Z′) indicates the presence of a parallel combination of a resistor and a capacitor if Z″ is negative, or a parallel combination of a resistor and an inductor if Z″ is positive.

Figure 2.11) which is an indication of deviation from the ideal behavior, therefore, constant phase elements (CPE) are used instead of the pure capacitors. The impedance of a CPE can be expressed as:

$$Z = (\frac{1}{Y_0})(j\omega)^{-\alpha} \qquad \text{eqn. 2.10}$$

α = an exponent that equals 1 for a capacitor. Y_0 = C = the capacitance when α =1. For a constant phase element, the exponent α is less than one. The "double layer capacitor" on real cells often behaves like a CPE, not a capacitor.

2.7 References

1. Pramanik, P., *A novel chemical route for the preparation of nanosized oxides, phosphates, vanadates, molybdates and tungstates using polymer precursors.* Bulletin of Materials Science, 1999. **22**(3): p. 335-339.
2. Sen, A. and P. Pramanik, *Low-temperature synthesis of nano-sized metal molybdate powders.* Materials Letters, 2001. **50**(5–6): p. 287-294.
3. Teo, W.E. and S. Ramakrishna, *A review on electrospinning design and nanofibre assemblies.* Nanotechnology, 2006. **17**(14): p. R89.
4. *Basics Relevant to Electrospinning*, in *An Introduction To Electrospinning And Nanofibers*. p. 22-89.
5. Goodenough, J.B., *General Concepts*, in *Lithium Ion Batteries*2007, Wiley-VCH Verlag GmbH. p. 1-25.
6. Wang, Z.L., *FUNCTIONAL OXIDE NANOBELTS: Materials, Properties and Potential Applications in Nanosystems and Biotechnology.* Annual Review of Physical Chemistry, 2004. **55**: p. 159–96.
7. Mimani, T. and K. Patil, *Solution combustion synthesis of nanoscale oxides and their composites.* Materials Physics and Mechanics(Russia), 2001. **4**(2): p. 134-137.
8. Mukasyan, A.S. and P. Dinka, *Novel approaches to solution-combustion synthesis of nanomaterials.* International Journal of Self-Propagating High-Temperature Synthesis, 2007. **16**(1): p. 23-35.
9. Patil, K.C., S.T. Aruna, and T. Mimani, *Combustion synthesis: an update.* Current Opinion in Solid State and Materials Science, 2002. **6**(6): p. 507-512.

10. Sahu, R.K., et al., *Microwave-assisted combustion synthesis of Ni powder using urea.* . Journal of Materials Research, 2006. **21**: p. 1664-1673.

11. Hankare, P., et al., *Synthesis and characterization of cobalt substituted zinc ferri-chromites prepared by sol–gel auto-combustion method.* Journal of Materials Science: Materials in Electronics, 2011. **22**(8): p. 1109-1115.

12. Yadav, T.P., R.M. Yadav, and D.P. Singh, *Mechanical Milling: a Top Down Approach for the Synthesis of Nanomaterials and Nanocomposites.* Nanoscience and Nanotechnology, 2012. **2**(3): p. 22-48.

13. Yang, L.C., et al., *High-energy ball milling:Materials for lithium-ion batteries by mechanochemical methods*, 2010. p. 361-408.

14. Birkholz, M., *Principles of X-ray Diffraction*, in *Thin Film Analysis by X-Ray Scattering*2006, Wiley-VCH Verlag GmbH & Co. KGaA. p. 1-40.

15. Copeland, L.E. and R.H. Bragg, *QUANTITATIVE X-RAY DIFFRACTION ANALYSIS.* Analytical Chemistry, 1958. **30**(2): p. 196-201.

16. Bragg, W.L., *The structure of some crystals as indicated by their diffraction of x-rays.* Proceedings of the Royal Society of London Series a-Containing Papers of a Mathematical and Physical Character, 1913. **89**(610): p. 248-277.

17. Sommerfeld, A., *The theory of the diffraction of x-rays.* Physikalische Zeitschrift, 1900. **2**: p. 55-60.

18. Scherrer, P., *Bestimmung der Grösse und der inneren Struktur von Kolloidteilchen mittels Röntgenstrahlen.* Nachr. Ges. Wiss. Göttingen 1918. **26**: p. 98-100.

19. Brunauer, S., P.H. Emmett, and E. Teller, *Adsorption of Gases in Multimolecular Layers.* Journal of the American Chemical Society, 1938. **60**(2): p. 309-319.

20. Brunauer, S., et al., *On a Theory of the van der Waals Adsorption of Gases.* Journal of the American Chemical Society, 1940. **62**(7): p. 1723-1732.

21. Condon, J.B., *Chapter 1 - An Overview of Physisorption*, in *Surface Area and Porosity Determinations by Physisorption*2006, Elsevier Science: Amsterdam. p. 1-27.

22. Macdonald, J.R. and W.B. Johnson, *Fundamentals of Impedance Spectroscopy*, in *Impedance Spectroscopy*2005, John Wiley & Sons, Inc. p. 1-26.

23. Ratnakumar, B.V., M.C. Smart, and S. Surampudi. *Electrochemical impedance spectroscopy and its applications to lithium ion cells*. in *Battery Conference on Applications and Advances, 2002. The Seventeenth Annual*. 2002.

24. Quan-Chao Zhuang, X.-Y.Q., Shou-Dong Xu, Ying-Huai Qiang and Shi-Gang Sun, *Lithium Ion Batteries - New Developments*, in *Diagnosis of Electrochemical Impedance Spectroscopy in Lithium-Ion Batteries*, I.B. (Ed.), Editor 2012, InTech.

25. Zhang, S.S., K. Xu, and T.R. Jow, *Electrochemical impedance study on the low temperature of Li-ion batteries.* Electrochimica Acta, 2004. **49**(7): p. 1057-1061.

Chapter 3 (N, F)-co-doped TiO_2 : Synthesis, anatase-rutile conversion and Li-cycling properties[G]

3.1 Introduction

Being abundant, low cost and environmentally benign along with some performance advantages, nanostructured titanium -based materials have been widely studied as anodes for LIBs. [1] Ti-based oxides such as $Li_4Ti_5O_{12}$, $Li_2Ti_3O_7$, $Li_2Ti_6O_{13}$, $H_2Ti_3O_7$ and TiO_2-B have been considered as potential alternative anode materials to traditional carbon-based anodes, since they exhibit excellent Li-ion insertion/extraction reversibility with small structural change and a much higher operating voltage ranging from 3 to 1 V (vs. Li/Li+) ensuring a better safety of the battery by avoiding the problem of lithium dendrites. [2] An excellent recent review summarises the results of various Ti-oxides and composites. [1]

$Li_4Ti_5O_{12}$ can accommodate 3 Li ions with a theoretical capacity of 175 mAh g^{-1}, at a high potential around 1.5 V (*vs.* Li/Li^+) which enhances battery safety by avoiding lithium dendrite formation. A negligible volume change of 0.2%, is caused between both end members, spinel-$Li_4Ti_5O_{12}$ and rock salt structured $Li_7Ti_5O_{12}$ accompanied by a change of the lattice axis from 8.3595 Å to 8.3538 Å. [2] While $Li_4Ti_5O_{12}$ is a low cost, non-toxic and 'zero strain' host for reversible Li-insertion/extraction, its low specific capacity (175 mAh g^{-1}) and poor rate capability are the main drawbacks. [1] It has an inherent insulating property due to the presence of empty Ti 3d state, which seriously hinders its high rate performance. Generally metal ion doping and surface coatings are employed to increase the ionic and electronic conductivity of bulk lithium titanate. Nanostructured $Li_4Ti_5O_{12}$ gained more attention as high rate anode materials for

[*] Christie T. Cherian, M. V. Reddy, Travis Magdaleno, Chorng-Haur Sow, K. V. Ramanujachary, G. V. Subba Rao and B. V. R. Chowdari , CrystEngComm, 2012,14, 978-986

LIBs due to the reduction in Li-diffusion pathway and better electrode-electrolyte contact. [2]

In comparison, TiO_2 offers a capacity up to its theoretical value at 335 mAh g^{-1} (one mole of Li per mole of TiO_2). Many polymorphs of TiO_2, namely TiO_2-B (bronze, *C*2/*m*), anatase TiO_2 (*I*4$_1$/*amd*), rutile TiO_2(*P*4$_2$/*mnm*), brookite (*Pbca*), , TiO_2-R (ramsdellite, *Pbnm*), TiO_2-H (hollandite, *I*4/*m*), TiO_2-II (columbite, *Pbcn*) and TiO_2-III (baddeleyite, *P*2$_1$/c) have been studied for their Li cycleability. [1, 3-9] Rutile TiO_2, anatase TiO_2 and brookite TiO_2 are three stable crystalline forms of TiO_2 whereas monoclinic TiO_2-B, tetragonal TiO_2-H and ramsdellite TiO_2-R are metastable. Both TiO_2-B and TiO_2-H first transform into the anatase polymorph when heated above 550 and 410 °C, respectively which finally converts to rutile at higher temperature. On the other hand, TiO_2-R undergoes conversion to brookite upon heating to 367 °C. Li-reaction with the TiO_2 polymorphs is expressed as;

$$TiO_2 + xLi^+ + xe^- \longleftrightarrow Li_xTiO_2 \qquad \text{eqn. 3.1}$$

where x is varied with different TiO_2 polymorphs, morphology and crystallographic orientation. [2]

TiO_2-B possesses a higher specific capacity than other compounds in the Li–Ti–O system or other polymorphs of titania like anatase or rutile. It has a monoclinic (space group C2/m) structure composed of edge and corner-sharing TiO_6 octahedra. [10] One of its most interesting structural features lies in the characteristic parallel channels running along the [010] orientation which favourable for the fast incorporation and diffusion of Li ions. It is also found out that the kinetics of lithium storage in TiO_2-B is found to be governed by the mixing effects of a pseudo-capacitive faradic process and diffusion limited solid-state reactions, which are further dependent on microstructures of different TiO_2-B

materials. Recently LIBs with TiO_2(B) as anode and $LiFePO_4$ or $Li[Ni_{0.5}Mn_{1.5}]O_4$ as cathode have been fabricated and tested for their performance. [4]

Anatase-TiO_2 is the most electrochemically active among the various polymorphs and its performance depends on the particle size and morphology. [1] When intercalated with Li, anatase-TiO_2 undergoes spontaneous phase separation into Li-poor ($Li_{0.01}TiO_2$) and Li-rich ($Li_{0.6}TiO_2$) domains on a scale of several tens of nanometres. [11] This two- phase equilibrium in the electrodes provides a plateau in potential, with some hysteresis as only the relative phase fractions vary upon continued Li-cycling. [1, 11] Rutile phase is the most thermodynamically stable polymorph of TiO_2. It is known that microcrystalline rutile polymorph of TiO_2 can intercalate only negligible amount of Li at room temperature. However, recent studies on nano-sized rutile-TiO_2 have shown that up to ~0.5 mole of Li per mole of TiO_2 can be reversibly intercalated and this value is comparable to that shown by anatase-TiO_2. [1, 6]

L.D. Noailles *et al.* [9] investigated hollandite-type TiO_2 structure as an insertion electrode material for lithium batteries. Unlike isostructural α-MnO_2 materials, this TiO_2 structure is anhydrous and does not contain water molecules within the 2×2 channels of the structure. The absence of oxygen within the central cavity limits the amount of lithium that can be accommodated within the structure. The inserted lithium ions are strongly bound, in distorted tetrahedral coordination, to the oxygen ions of the framework at the corners of the 2×2 channels, making it difficult to extract the lithium electrochemically from the electrode structure in lithium cells. Hollandite-TiO_2 materials, therefore, appear to have limited use as insertion electrodes for lithium batteries. [9] In the case of TiO_2 (R), a high capacity of 336 mAh g^{-1} can be obtained but its usefulness as an anode is more

limited since half of its capacity is developed at a higher average voltage. Lithium insertion in to TiO_2-R can be roughly divided into two regimes which are characterised by distinct voltage ranges. [12] Insertion of the first half of Li ions takes place over a wide voltage window, in an almost steadily declining manner, whereas insertion of the second half is achieved at a low constant voltage. Electrochemical studies show that first 0.5 Li/Ti is inserted over a wide potential range from 2.3 to 1.3 V, with an average value of 1.8 V, similar to that of TiO_2-H. The additional Li is inserted at a low, almost constant voltage of 1.3 V that resembles the Li insertion in anatase TiO_2. [12]

By doping TiO_2 with a few atomic % of nitrogen (N) at the O-site, the effective band-gap of 3.1 eV was found to be lowered, and thus, the N-doped TiO_2 was found to show much improved photcatalytic activity extending to the visible region. [13-15] Simillarly, fluorine (F) doped TiO_2 also shows improved photocatalytic property. [16] It is also possible to co-dope TiO_2 with N and F, and several researchers reported the synthesis, characterisation [17-22] and photocatalytic behaviour. [17-20, 22] In all cases, the anatase-polymorph of TiO_2 is stabilized and a vastly improved visible light response and excellent photocatalytic activity were observed with respect to degradation of dyes and organic pollutants. It was concluded that the synergistic effect of co-doping is able to improve the photocatalytic activity. [20, 22]

Surprisingly, there are no reports on the Li-storage and cycling of N-doped or (N, F)-co-doped TiO_2 in the literature. There is only one study by Jung *et al.* [23] on the nominally 10% and 21% F-doped mesoporous anatase-TiO_2, who found that both the doped compounds showed much improved Li-cycling properties, in comparison to the undoped-TiO_2. In addition, the 10% F-doped TiO_2

showed very good current (C)-rate capability, when tested up to 30 C. Hence, it is of significant interest to examine the Li-cycling of (N, F)-co-doped TiO_2. Here, we report the synthesis of (N,F)-co-doped-TiO_2 of composition, $TiO_{1.9}(N_{0.05}F_{0.15})$ (hereafter TiO_2(N, F)), its conversion to nano-phase rutile after high energy ball-milling, and the Li-storage and cycling properties in the voltage range, 1-2.8 V vs Li. It is found that nano-phase rutile TiO_2(N, F) can reversibly cycle Li up to 0.65 mole (210 mAh g^{-1}), with good capcity retention. For comparison, the undoped nano-phase rutile TiO_2 was also studied.

3.2 Experimental

Anatase-TiO_2(N,F) was prepared by pyro-ammonolysis of TiF_3. The starting chemical, TiF_3 (Alfa Aesar, 99% purity) is dried at 120°C and the lightly pressed pellets were heated at 360°C for 2 h in the flowing NH_3 gas in a tubular furnace (Carbolite, UK). After cooling, the powder was recovered, ground and reheated in NH_3 gas to ensure completion of the reaction. Part of the as-prepared TiO_2(N,F) was subjected to high energy ball-milling (HEB) (SPEX-8000D Mixer/Miller, USA), at 1400 rpm for 18 h, with 10 h of interval after each 6 h of milling. Stainless steel vial and balls (10 g) were used with a ball-to-powder weight ratio of 5:1. Anatase-TiO_2 (Aldrich, 99.9%) was also subjected to HEB under similar conditions.

The compounds were characterized by powder X-ray diffraction (XRD) (Philips X'PERT MPD, Cu Kα radn.) and the data were Rietveld refined using TOPAS software, R 2.1 version. For morphology studies, SEM (JEOL JSM–6700F, Field Emission Electron Microscope) and high resolution transmission electron microscope (HR-TEM) (JEOL JEM 2100 operating at 200 kV) were

employed. Raman spectra (Renishaw Raman system 2000) were recorded at room temperature. Elemental analysis was carried out on the as-prepared TiO_2(N,F) to ascertain the Ti, N, F contents. The oxygen content was not determined but estimated from the difference in the percentages of the other elements. The Ti-content is determined by the inductively coupled plasma optical emission spectrometer (ICP-OES; Perkin Elmer Dual-View Optima DV) system. Sample dissolution is carried out by Milestone microwave laboratory system, USA, using the acid mixture, $HF/HNO_3/HCl$. CHNS analyzer (Elementar vario MICRO cube, USA) was used to analyse the nitrogen content. Ion chromatography (IC) technique was used to analyse the flourine content (Metrohm AG - MIC-2 Advanced, Germany). The sensitivity of the system could be increased by using chemical suppression for anions. The MIC-2 system contains Metrohm Suppressor Module, which is incorporated in the 820 IC Separation center which is equipped with a column oven which lowers the detection limits even further, particularly when working with a high background conductivity. The instrumentation also includes 830 interface, 833 liquid handling unit for regeneration and rinsing, 732 detector and 813 compact autosampler. The compound is digested in aqua regia for nitrogen and fluorine analysis.

The electrodes for Li-cycling were prepared by the doctor-blade technique using a mixture of the active material (TiO_2(N,F) or TiO_2), Super P carbon (MMM Ensaco) and binder (Kynar 2801) in the mass ratio 70:15:15, using an etched Cu-foil (thickness 10 μm) as the current collector. The electrode area and mass of active material were 2 cm^2 and 3–4 mg, respectively. Coin-type test cells (size 2016) were assembled in an argon-filled glove box (MBraun, Germany) and the cell components were Li metal (Kyokuto Metal Co., Japan) foil as counter

electrode, glass micro-fiber filter (GF/F, Whatman Int.Ltd., Maidstone, England) as the separator and 1M $LiPF_6$ in ethylene carbonate (EC) and dimethyl carbonate (DMC) (1:1 by volume, Merck Selectipur LP40) as the electrolyte. The cyclic voltammetry and galvanostatic discharge-charge cycling of the cells were carried out at room temperature (25°C) by computer controlled MacPile II (Biologic, France) unit and Bitrode multiple battery tester (model SCN, Bitrode, USA), respectively. Ex situ XRD of the cycled electrodes was carried out as follows: Two cells were fabricated with TiO_2(N,F) electrodes and aged for 24 h. They were discharged to 1.0 V at a current rate of 30 mAg^{-1} and held for 3 h. One cell was subsequently charged to 2.8 V and held for 3 h. The cells were dismantled in the glove box, the electrodes were recovered along with the Cu-foil, washed with anhydrous DMC to remove the $LiPF_6$ salt from the electrode, dried and then mounted on the XRD holder (Al-metal) along with a protective adhesive tape. For ex-situ TEM, sample is scrapped off from the electrode after dismantling the cell inside the glove box. The recovered powder was dispersed in ethanol and part of it is pipetted out on to the copper grid (Aldrich) and dried.

3.3 Results and discussion

3.3.1 Crystal structure and morphology

3.3.1.1 Anatase-TiO_2(N,F)

The as prepared TiO_2(N,F) is pale-green in colour. Figure 3.1(a), (b) show the XRD patterns of the as-prepared TiO_2(N,F) and the commercial TiO_2. All the peaks of TiO_2(N,F) can be indexed as anatase phase with a trace of impurity peak due to TiF_3.

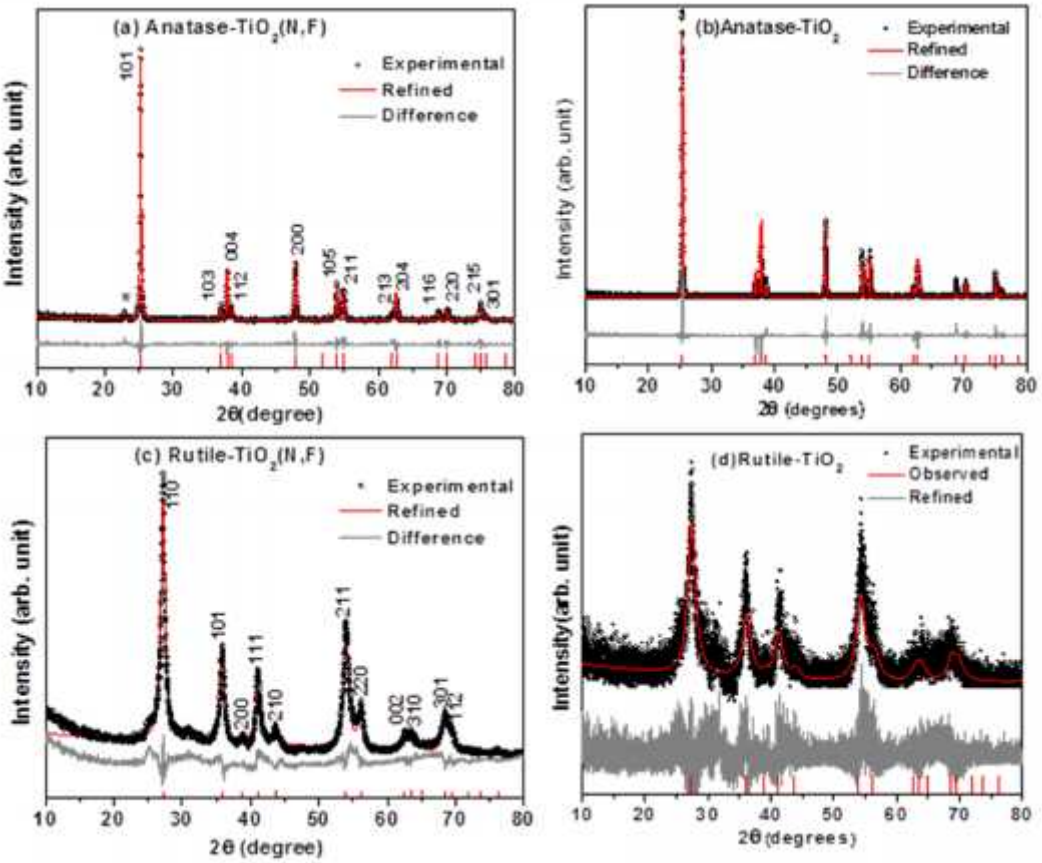

Figure 3.1 X-ray diffraction (XRD, Cu Kα radiation.) pattern (dotted lines) compared with Rietveld refined profile (full line). (a) Anatase- TiO_2(N,F). Asterisk is an impurity peak due to TiF_3. (b) Anatase- TiO_2 (commercial). (c) Nano-rutile-TiO_2(N,F). (d) Nano-rutile-TiO_2. (c) and (d) are obtained by high energy ball-milling of (a) and (b) respectively. The difference pattern and Miller indices are shown.

The lattice parameters, evaluated from the Rietveld refined XRD data (with space group I41/*amd*) are : a = 3.796(1) Å and c = 9.494(0) Å. These values agree well with those reported by Seibel *et al.* [21] namely, a = 3.7970(0) Å and c = 9.4994(1) Å for the composition $TiO_{1.89}N_{0.05}F_{0.06}$. It may be mentioned here that Seibel *et al.*[21] used $(NH_4)_2TiF_6$ as the starting material whereas presently, we used TiF_3. The Rietveld parameters are: R_{wp} = 25.3; R_p = 16.1; GOF=1.2 and R_{Bragg}=2.1. For comparison, the lattice parameters of commercial anatase-TiO_2 are evaluated to be, a = 3.780(4) Å and c = 9.511(4) Å. The Rietveld parameters are: R_{wp} = 17.8; R_p = 11.4; GOF=1.3 and R_{Bragg}=3.9. Thus, it is clear that TiO_2 (N,F) has a more open

structure than anatase-TiO_2 (larger *a* and smaller *c*). The unit cell volume of doped TiO2 system is 136.32 $Å^3$ whereas that of undoped anatase TiO_2 is 135.89 $Å^3$.

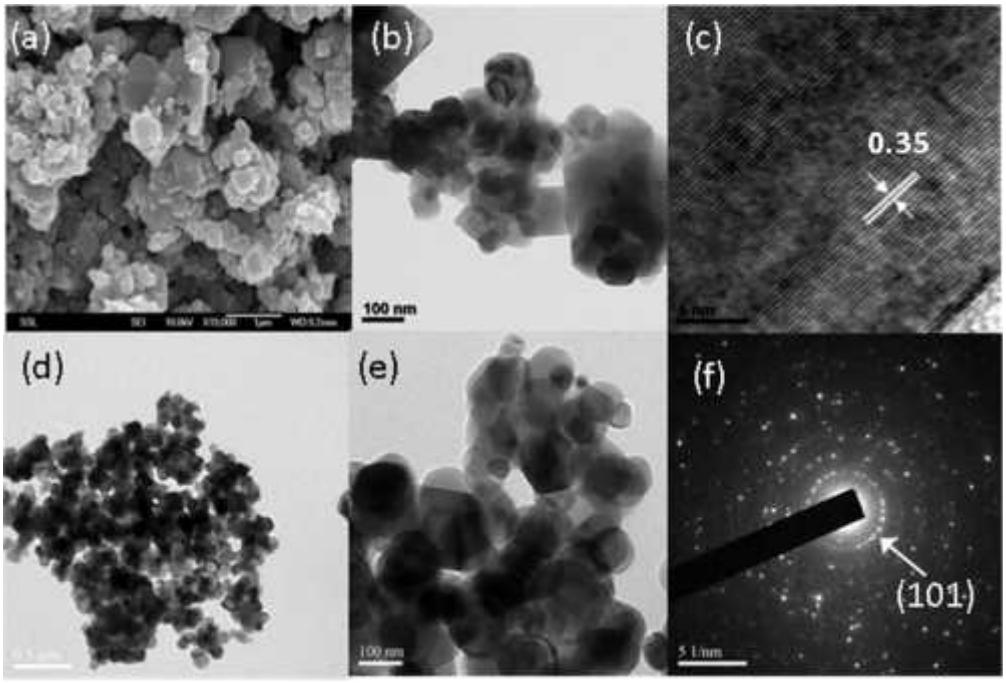

Figure 3.2 (a) SEM photograph of anatase-TiO_2(N,F). Scale bar is 1 μm. (b) TEM photograph of anatase-TiO_2(N,F) showing plate-like morphology. Scale bar is 100 nm. (c) HRTEM lattice image of anatase-TiO_2(N,F). Scale bar is 5 nm. (d) TEM photograph of commercial anatase-TiO_2. Scale bar is 0.5 μm. (e) TEM photograph of commercial anatase-TiO_2. Scale bar is 100 nm. (f) SAED pattern of commercial anatase-TiO_2.

The SEM and TEM images of the anatase TiO_2(N,F) are shown in Figure 3.2(a) and (b). As can be seen, sub-micron size, agglomerated plate like morphology is clearly evident. The HR-TEM lattice image is shown in Figure 3.2(c). The evaluated interplanar distance 0.35(±0.02) nm is in agreement with the d-value of (101) plane (0.348 nm).The TEM images of commercial anatase-TiO_2 are shown in Figure 3.2(d) and (e) which confirm micron sized particles (~150 nm) with slightly irregular morphology. The selected area electron diffraction (SAED) pattern is shown in Figure 3.2(f) and consists of well-defined bright spots. The pattern has been indexed and the inter-planar distance of (101) plane is found to be 0.34 (±0.02) nm which is in good agreement with XRD data.

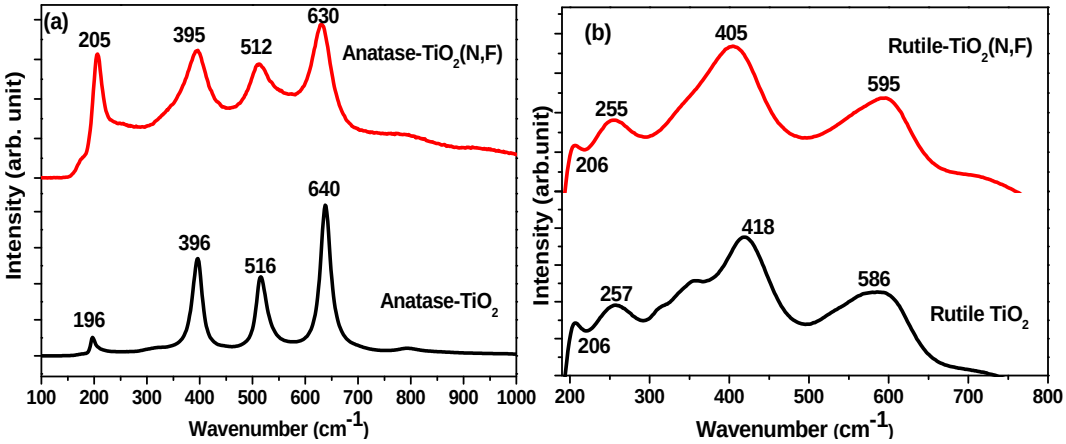

Figure 3.3 Raman spectra. (a) Anatase-TiO_2(N,F) and commercial anatase-TiO_2. (b) Nano rutile- TiO_2(N,F) and nano rutile-TiO_2 obtained by high energy ball-milling of the respective anatase polymorphs. Numbers refer to band positions in cm^{-1}.

The anatase structure of TiO_2(N,F) is further verified by the Raman spectroscopy studies. According to the factor group analysis based on the space group and crystal structure of anatase-TiO_2, the 15 optical modes have the irreducible representation, $1A_{1g} + 1A_{2u} + 2B_{1g} + 1B_{2u} + 3E_g + 2E_u$. The A_{1g}, B_{1g} and E_g modes are Raman active and the modes A_{2u} and E_u are infrared active. The B_{2u} mode is inactive in both Raman and IR spectra. [24] The Raman spectrum of anatase-TiO_2 (Aldrich, 99%) and -TiO_2(N,F) are shown in Figure 3.3(a). The spectrum of TiO_2 is comprised of four Raman modes with strong intensities at 196, 396, 516, and 640 (±3) cm^{-1}, which are in good agreement with the Raman bands of single crystal anatase-TiO_2 reported by Ohsaka *et al.*[24], namely 197 (E_g-mode), 399 (B_{1g}), 516 (A_{1g}) and 639 (E_g) cm^{-1}. As shown in Figure 3.3(a), the four Raman bands at 205, 395, 512 and 630 (±3) cm^{-1} are observed for the anatase TiO_2(N,F), clearly indicating the similarities between the two compounds except for a slight broadening and shift in the band positions.

The elemental analysis of the as prepared TiO_2(N,F) yielded weight percentages of Ti, N, F to be 58.19 %, 0.83 % and 3.47 % respectively. The oxygen content, not

estimated, is assumed to be the difference. The chemical formula that is derived from the analysis is $TiO_{1.9}N_{0.05}F_{0.15}$. While the nitrogen content is same as that reported by Seibel *et al*.[21], the fluorine content is overestimated in the present case, since the XRD pattern indicated a low intensity impurity peak, due to TiF_3 (Figure 3.1).Thus, the actual F-content in the compound is in the range, 6 to 8 atom % and closely resembles the value of Seibel *et al*. [21]

3.3.1.2 Anatase to rutile conversion by high energy ball-milling

The as prepared TiO_2(N,F) and commercial TiO_2 were subjected to HEB as described in the experimental section. The colour of the ball-milled TiO_2(N,F) is similar to that of the starting anatase-TiO_2(N,F). The powder XRD pattern of the ball-milled TiO_2(N,F) is shown in Figure 3.1(c). Surprisingly, it bears no resemblance to the anatase-TiO_2(N,F) structure, and instead corresponds to the rutile-type structure. The XRD peaks are broad, indicating the nano-phase rutile nature of the material. [25-27] Rutile is the most stable form of TiO_2 and anatase phase gets transformed to rutile phase upon HEB. The Rietveld refined XRD data with the space group, P42/*mnm*, gave the tetragonal lattice parameters, a =4.623(1) Å and c =2.964(3) Å. The Rietveld parameters are: R_{wp} = 6.0; R_p = 12.6; GOF=2.1 and R_{Bragg}=3.0. The crystallite size estimated from the Scherrer's equation using the TOPAS software is 13 (±3) nm. For comparison, the ball-milled commercial anatase-TiO_2 was also found to transform to the rutile-TiO_2 structure (Figure 3.1(d)). The XRD pattern shows broad peaks characteristic of nano-size and the fitted lattice parameters are: a = 4.613(2) Å and c = 2.953(6) Å, which are in good agreement with the literature data (JCPDS card 21-1276: a = 4.593 Å and c = 2.959 Å) and the crystallite size is found to be 10 (±3) nm. The slightly larger a and c values of nano-rutile TiO_2(N,F) in comparison to the nano-rutile TiO_2

indicate a more open structure in the former compound. It is well-known that anatase- TiO_2 transforms irreversibly to the rutile- TiO_2 up on heating in air to temperatures, 600-700°C. The transformation of both anatase-TiO_2 and anatase-TiO_2(N,F) to the respective rutile-types upon high energy ball-milling (HEB) can be understood as due to the local heating of the particles, to temperatures as high as 500-600 °C during HEB, which is caused by the collisions between the grinding medium and the vial and also amongst the grinding balls. [28] In order to avoid excessive heating of the particles, HEB was carried out in steps, after resting for a sufficient period of time.

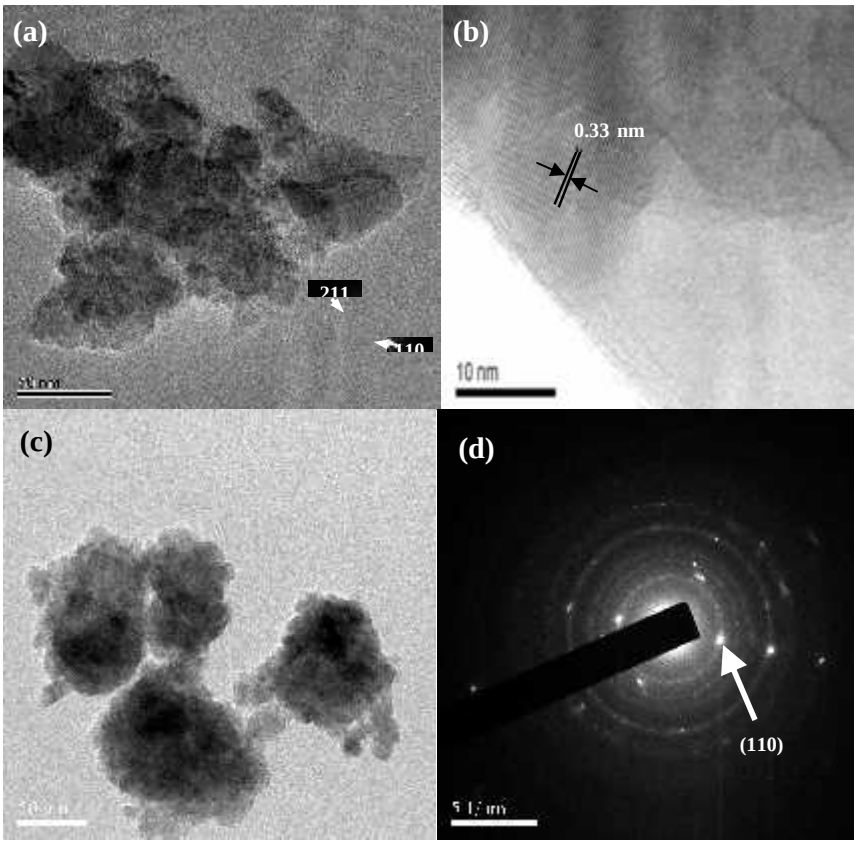

Figure 3.4 (a) TEM photograph of nanophase rutile-TiO_2(N,F) showing agglomerates of nano-size particles. Scale bar is 50 nm. Inset shows the SAED pattern and selected Miller indices. (b) HRTEM lattice image of nanophase rutile-TiO_2(N,F). Scale bar is 10 nm. (c) TEM photograph of nanophase rutile-TiO_2. Scale bar is 50 nm. (f) SAED pattern of nanophase rutile-TiO_2. Miller index (110) is shown.

Figure 3.4(a) and (b) show the TEM photograph and the HR-TEM lattice image, respectively, of the rutile-TiO_2(N,F). Aggregates of nano-size particles, 10-20 nm are clearly seen. The lattice image of rutile-TiO_2(N,F) shows randomly oriented nano-crystalline regions, and the measured interplanar spacing of 0.33(±0.02) nm matches well with the d-value (0.327 nm) of the Miller index, (110) of the rutile- TiO_2(N,F). Inset of Figure 3.4(a) shows the SAED pattern of rutile-TiO_2(N,F) which consists of diffuse rings and spots confirming the existence of nano-crystalline regions. Figure 3.4(c) shows the TEM photograph of ball-milled TiO_2 (commercial) indicating aggragates of nanopartcles. The SAED pattern of rutile-TiO_2 (Figure 3.4 (d)) also shows diffuse ring and spots and the calculated d-value is 0.32 (±0.02) nm which corresponds to (110) plane.

The nano-phase nature and the structure of rutile-TiO_2(N,F) are confirmed by the Raman spectrum shown in Figure 3.3(b). For comparison, the Raman spectrum of rutile-TiO_2, which is obtained by the HEB of the anatase- TiO_2 is also shown. As can be seen, the spectra of both the compounds look very similar and do not bear any resemblance to the respective anatase-type polymorphs. Further, the Raman bands are broad, indicating nano-phase nature of both the materials. [25] The bands of rutile-TiO_2(N,F) are: two low-intensity bands at 206 and 255 (±7) cm^{-1}, and two high- intensity bands at 405 and 595 (±7) cm^{-1}, whereas those of the rutile-TiO_2 are, two low-intensity bands at 206 and 257 (±7) cm^{-1}, and two high- intensity bands at 418 (E_g -mode) and 586 (±7) (A_{1g} -mode) cm^{-1}. As per the factor group analysis, the tetragonal rutile-TiO_2 has four Raman-active modes E_g, A_{1g}, B_{1g} and B_{2g} of which the E_g and A_{1g} modes possess high intensity. [24] Yang *et al*.[25] reported two strong Raman bands at 441 and 607 cm^{-1} and a low-intensity band at 241 cm^{-1} in the hydrothermally prepared nano-phase rutile-TiO_2. The latter band

and the low intensity bands presently observed at ~206 cm^{-1} and at ~250 cm^{-1} are due to two phonon scattering (combination bands) which indicates high degree of anharmonicity of the structure. [24-26] The Raman peak-broadening and small frequency shifting of the bands in nano rutile-TiO_2(N,F) and rutile- TiO_2 in comparison to the literature data on rutile-TiO_2 [24, 26] can be attributed to the differences in the particle size as well as slight non-stoichiometry.

3.3.2 Li-storage and cycling properties

3.3.2.1 Galvanostatic cycling

3.3.2.1.1 Anatase-TiO_2(N,F)

The galvanostatic cycling response in the form of voltage vs. capacity profiles of anatase-TiO_2(N,F) in the voltage range, 1-2.8 V vs. Li at the current, 30 mA g^{-1} are shown in Figure 3.5(a). The profiles of selected cycles only are shown for the sake of clarity. Firstly, the cell is discharged from the open circuit voltage (OCV= 2.6 V) to 1 V vs. Li. The voltage steeply drops to ~1.8 V followed by a plateau region up to a capacity of 60 mAh g^{-1} and afterwards, a sloping voltage profile is seen yielding a capacity of 130 mAh g^{-1}. This corresponds to an uptake of 0.4 mole of Li per mole of TiO_2(N,F). Accordingly, to maintain the charge balance, 0.4 mole of Ti^{4+} will be reduced to Ti^{3+} in the lattice. A negligible amount of Li (~0.03 mole) is inserted before the plateau regime starts at 1.73 V and the voltage plateau corresponds to a two-phase coexistence as discussed by Yang *et al*.[1] and Wagemaker *et al*. [11]

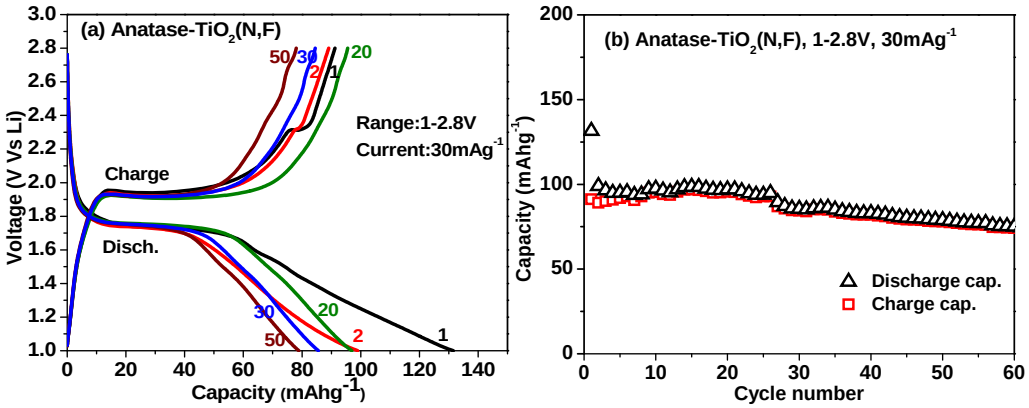

Figure 3.5 Anatase-TiO_2(N,F). (a) Voltage vs. capacity profiles. Numbers refer to cycle number. (b) Capacity vs. cycle number plot. Voltage range: 1-2.8 V vs Li; current: 30 mA g^{-1} (0.3C).

When the cell is charged to 2.8 V, the voltage profile shows a sharp increase and a clear plateau at ~1.95 V is seen up to 60 mAh g^{-1} followed by an upward sloping region. The latter is ascribed to electrode polarization. There is a small potential plateau at 2.3 V, possibly due to slight structural re-arrangement of the lattice, and as expected, this plateau disappears during the second and subsequent charge profiles (Figure 3.5 (a)).The first charge capacity is 90 mAh g^{-1} (0.27 mole of Li). The second discharge capacity is 100 mAh g^{-1} whereas the corresponding charge capacity is 88 mAh g^{-1}. With an increase in the cycle number, the charge capacity slowly increases and matches with that of the discharge capacity (Figure 3.5 (a)). The capacity vs. cycle number plot, shown in Figure 3.5(b), indicates that a reversible capacity of 95(±3) mAh g^{-1} is maintained after 5 cycles which is stable up to 25 cycles and the coulombic efficiency reaches ~98 %. Assuming 1 C = 95 mA g^{-1} (C-rates are the rate of discharge (or charge) as compared to the capacity of the battery. If the capacity is stable, the stable capacity, x mAh g^{-1} can be taken as reference ie. 1 C = x mA g^{-1}), the applied current rate corresponds to 0.3 C. In the range, 25-60 cycles, the reversible capacity fades slowly, at a rate of ~ 0.6 mAh g^{-1} per cycle.

It is pertinent to compare the performance of anatase TiO_2(N,F) with that of micron-size commercial anatase TiO_2 (Aldrich) reported by Subramanian *et al*.[29]. When cycled between 1.0 V to 2.5 V at a current of 0.31 mA cm^{-2}, they observed a first-discharge capacity (Li-insertion) of 75 mAh g^{-1} (0.22 mole of Li per mole) and the corresponding reversible (charge) capacity was 37 mAh g^{-1} (~0.11 mole of Li). The capacity degraded continuously and after 5 cycles, the capacity dropped to 16 mAh g^{-1} (~0.05 mole of Li). Thus, it can be concluded that co-doping of N and F in to TiO_2 to yield TiO_2(N,F) has a large beneficial effect on the Li-cycling due to a more open structure, reduction in the band gap and the fact that N^{3-} and F^- are more electronegative than the O^{2-} ion. It may be possible to improve the performance if anatase-TiO_2(N,F) can be realised in the nano-form.

To investigate the nature of the phases formed after insertion and extraction of Li, ex-situ-XRD and -TEM studies were carried out on the electrode material.

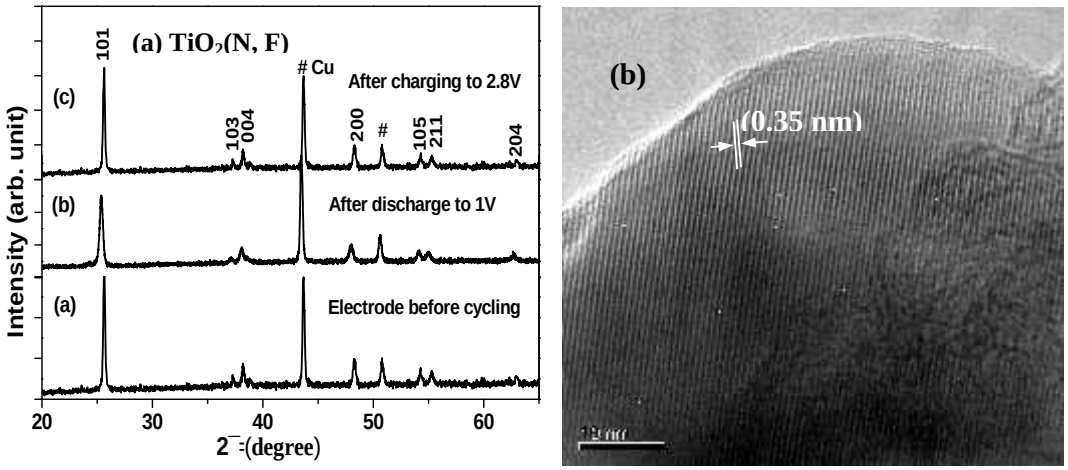

Figure 3.6 (a) The XRD patterns. (i) Anatase-TiO_2(N,F) composite electrode. (ii) Electrode after discharge to 1 V. (iii) Electrode charged to 2.8 V after 2 cycles. Miller indices are shown. Lines due to Cu substrate are indicated. Cu Kα radiation. (b) HRTEM lattice image of the electrode after charging to 2.8 V after 2 cycles. Scale bar is 10 nm.

The XRD patterns of the bare, discharged and charged electrodes are shown in Figure 3.6(a). The pattern after discharge to 1 V indicates that the crystal structure

remains intact but there is a slight shift of selected peaks to a lower 2θ, showing slight expansion of the anatase structure after the insertion of 0.4 mole of Li. A similar expansion of the unit cell and a change in the crystal symmetry to orthorhombic structure upon Li intercalation of anatase-TiO_2 and a net increase of unit cell volume by ~4 %, have also been reported in the literature [1, 30]. The XRD pattern of the charged electrode (at 2.8V after 2 cycles) compares well with that of the bare electrode which indicates that anatase-TiO_2(N,F) structure is completely recovered. The HR-TEM lattice image of the charged electrode shows crystalline and amorphous regions and the interplanar spacing of 0.35(±0.02) nm corresponds to Miller index (101) of anatase-TiO_2(N,F) (Figure 3.6(b)).

3.3.2.1.2 Nano-rutile TiO_2(N,F) and nano-rutile-TiO_2

The voltage-capacity profiles of the nano-phase rutile TiO_2(N,F) show continuous sloping curves during both discharge and charge process which indicates that Li insertion/extraction reaction may be occurring through single-phase solid solution domain (Figure 3.7(a)). This result is in agreement with the various literature reports on the Li-cycling of nano-particles of rutile-TiO_2 [1, 6, 31]. When discharged to 1 V, rutile-TiO_2(N,F) showed a capacity of 325 mAh g^{-1} which corresponds to an intake of ~1.0 mole of Li, whereas the first-charge capacity is 210 mAh g^{-1} (0.6 mole of Li) indicating an irreversible capacity loss of 0.4 mole of Li. The second discharge and charge capacities are 215 mAh g^{-1} and 208 mAh g^{-1} respectively, indicating good reversibility. However, slow capacity fading is seen and after 60 cycles, a capacity of 165 mAh g^{-1} is observed which corresponds to capacity retention of 78%.

For comparison, Li-cycling of rutile-TiO_2 obtained by the HEB of anatase-TiO_2 is also carried out. The voltage-capacity profiles and capacity vs. cycle

number plot are shown in Figure 3.7(c) and (d), respectively. As can be seen, the profiles in the voltage range, 1-2.8 V at a current of 30 mA g^{-1} are similar to those of rutile-TiO_2(N,F) and also resemble those reported in the literature on the nano-phase rutile-TiO_2, indicating a single-phase Li-intercalation/de-intercalation process. [1, 6, 27, 30, 31]

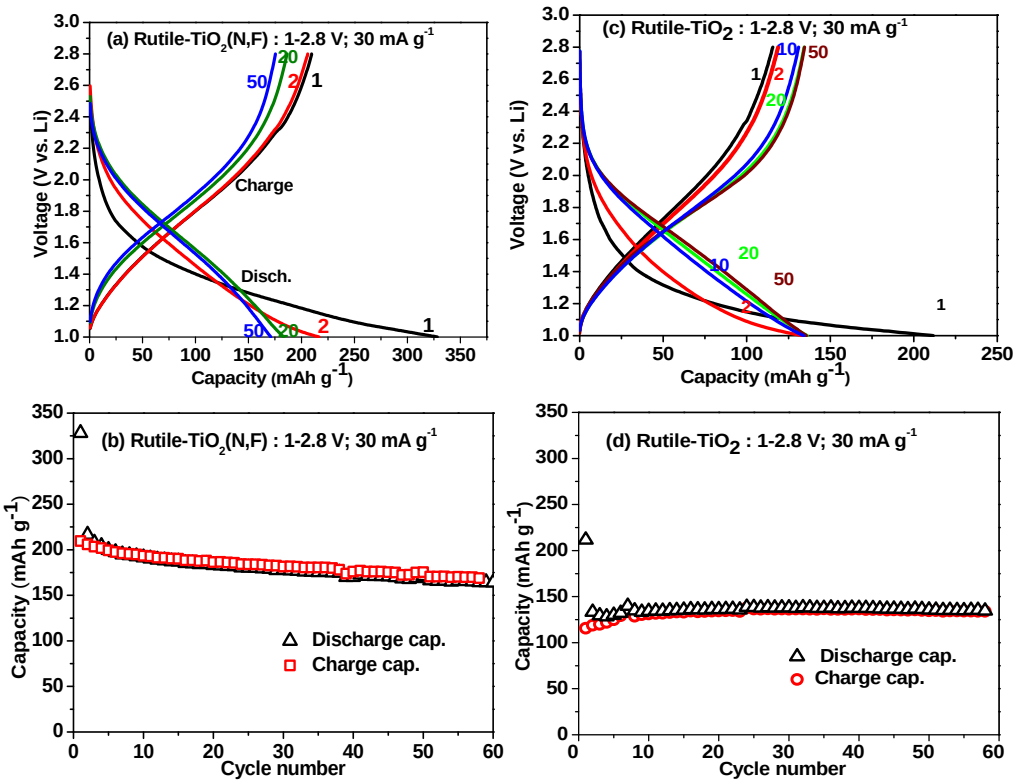

Figure 3.7 Nanophase rutile-TiO_2(N,F): (a) Voltage vs. capacity profiles. Numbers refer to cycle number. (b) Capacity vs. cycle number plot. Nanophase rutile-TiO_2: (c) Voltage vs. capacity profiles. Numbers refer to cycle number. (d) Capacity vs. cycle number plot. Voltage range: 1-2.8 V vs. Li; current: 30 mA g^{-1} (0.23C).

The observed first discharge capacity is 215 mAh g^{-1} whereas the first-charge capacity is 115 mAh g^{-1}. These values are smaller than those measured on rutile-TiO_2(N,F). The reversible capacity stabilizes by 10 cycles and remains constant at 130 (±5) mAh g^{-1} in the range of 10-58 cycles. This corresponds to ~0.4 mole of cyclable Li, which is smaller than that observed in rutile TiO_2(N,F) after

60 cycles. Assuming 1C = 130 mA g^{-1}, the employed current rate corresponds to 0.23 C. The present results compare well with the literature values reported on nano-rutile TiO_2 in the voltage range 1-3 V vs. Li : 175 (±5) mAh g^{-1} (current rate, 0.1C, 5-50 cycles) (Hu *et al.* [6]); 155(±5) mAh g^{-1} (current, 30 mA g^{-1}, 5-60 cycles) (Baudrin *et al.*[31]); 190 (±5) mAh g^{-1} (current rate, 0.2C, 2-30 cycles) (Kubiak *et al.*[27]); 183 mAh g^{-1} (current rate, 0.1C, after 30 cycles) (Qiao *et al.* [32]). It is clear from the above discussion that the Li-storage and cycleability of the nano-rutile-TiO_2(N,F) is on par, if not better than nano-rutile-TiO_2. This can be ascribed to the more open structure of the former compound and the beneficial effect of doping more electron-negative N^{3-} and F^- ions in comparison to O^{2-} ion. The contaminants such as Fe, Cr etc. in the powder sample which is instigating from stainless steel vial during HEB, may enhance the electronic conductivity of rutile TiO_2.

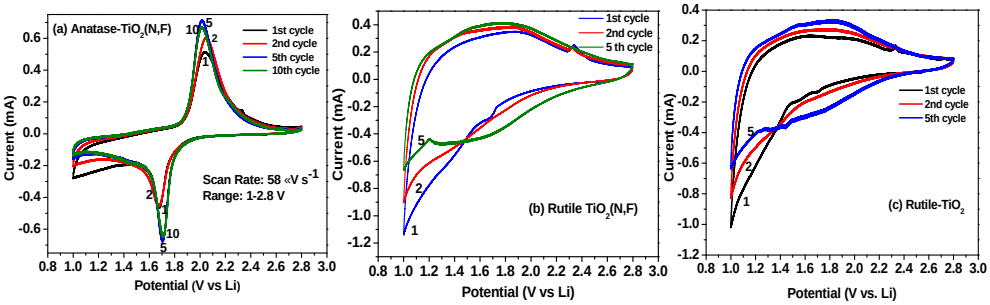

Figure 3.8 Cyclic voltammogramms: (a) Anatase-TiO_2(N,F). (b) Nanophase rutile-TiO_2(N,F). (c) Nanophase rutile-TiO_2. Potential window, 1-2.8 V; scan rate, 58 μVs^{-1}. Li metal was the counter and reference electrode. Numbers refer to cycle number.

3.3.2.2 Cyclic voltammetry

Cyclic voltammetry is a complementary technique to galvanostatic cycling and helps in understanding the nature and potentials at which the discharge–charge reactions take place in the electrode material. Figure 3.8(a) shows the cyclic voltammograms (CVs) of the anatase-TiO_2(N,F) in the potential window 1-2.8 V vs. Li recorded at the slow scan rate of 58 $\mu V\ s^{-1}$ up to 10 cycles. Selected cycles

are shown for clarity. The cathodic (Li-insertion) and anodic (Li-extraction) peaks occur at ~1.7 V and ~2V, respectively, during the first two cycles. During 5-10 cycles, these values are only slightly shifted and stabilize with an accompanying increase in the areas under the peaks (Figure 3.8 (a)). The voltage hysteresis (ΔV) is 0.3V. For comparison, the voltage plateaus in the galvanostatic voltage-capacity profiles occur at ~1.73 V for Li-insertion and at ~1.95 V for Li-extraction. For the commercial anatase-TiO_2, Subramanian *et al.*[29] reported the CV peaks at 1.55 V and 2.2 V, respectively for Li-insertion and extraction, with ΔV=0.65 V. Thus, the performance of TiO_2(N,F) is better than that of micron-size anatase-TiO_2.

The CVs of the first and second cycles of the nano-rutile-TiO_2(N,F) show a continuous decrease in the cathodic profiles and a broad anodic peak extending from 1.2 V to 2.4 V indicating that Li cycling occurs in a quasi-single-phase reaction (Figure 3.8(b)). The 5^{th} cycle CV shows a broad cathodic peak in the potential range, 1.3 V to 2.2 V. The corresponding anodic peak resembles those of the first two cycles. The CVs of the nano-phase rutile-TiO_2 shown in Figure 3.8(c) are exactly similar, indicating that the Li-cycling mechanism is similar in both nano-rutile-TiO_2(N,F) and nano-rutile-TiO_2. These results corroborate the galvanostatic discharge-charge profiles which did not show well-defined two-phase regions during cycling in both the compounds. For comparison, the CV studies on nano- rutile- TiO_2 by Kubiak *et al.* [27] indicate that the first cathodic scan shows two potential plateaus at 1.4 V and 1.1 V vs. Li, whereas the corresponding anodic scan is a smoothly shaped curve ascribed to a solid-solution domain Li-extraction reaction. The cathodic potential plateaus disappeared in the subsequent cycles, and very broad cathodic and anodic peaks appeared, both of which are centered at ~1.8 V. Kubiak *et al.*[27] concluded that the first Li-insertion

process results in an irreversible phase transformation to '$LiTiO_2$', which may have a hexagonal or cubic rock salt structure and the subsequent Li-cycling occurs as a single-phase reaction. Similar results and conclusions were drawn by Baudrin *et al.* [31] in their study of nano- rutile- TiO_2.

3.4 Conclusions

The Li-storage and cyclability of nitrogen and fluorine co-doped Ti-oxide of the composition, $TiO_{1.9}N_{0.05}F_{0.15}$ (TiO_2(N,F)) is reported for the first time. The anatase- TiO_2(N,F) is prepared by the ammonolysis of TiF_3. Up on high energy ball-milling (HEB), the sub-micron sized anatase TiO_2(N,F) gets converted to the nano-phase (10-20 nm) rutile-TiO_2(N,F). This anatase-to-nano-rutile transformation by HEB is also confirmed in undoped-TiO_2 (commercial). Both the polymorphs of TiO_2(N,F) and TiO_2 are characterized by XRD, SEM, HR-TEM and Raman spectra. Galvanostatic cycling of anatase- TiO_2(N,F) at 30 mA g^{-1} (0.3C) in the voltage range, 1-2.8 V vs Li, showed an initial discharge capacity of 135 mAh g^{-1} and a reversible capacity of 95 mAh g^{-1} is measured in the range 2-25 cycles. In the range, 25-60 cycles, the capacity fades at a rate of ~0.6 mAh g^{-1} per cycle. Under similar cycling conditions, nano-phase rutile-TiO_2(N,F) exhibited an initial discharge capacity of 325 mAh g^{-1} (~1.0 mole of Li per mole of TiO_2(N,F)) and a reversible capacity of 210 mAh g^{-1} (0.65 mole of Li) is observed after the first cycle. However, slow capacity-fading is seen, with a capacity-retention of 78% after 60 cycles. Under similar cycling conditions, nano-phase rutile- TiO_2 (obtained by HEB) exhibited a reversible capacity of 130 mAh g^{-1} (~ 0.4 mole of Li) which is stable in the range, 10-60 cycles in good agreement with the values reported in the literature. Cyclic voltammetry of anatase TiO_2(N,F) showed single high-intensity cathodic and anodic peak occurring at ~1.7 V and ~2.0 V,

respectively. These potentials are similar to those shown by anatase-TiO_2. On the other hand, nano- rutile-TiO_2(N,F) and nano-rutile TiO_2 showed broad cathodic and anodic peaks centered at ~1.8 V, a behaviour similar to the nano-phase rutile-TiO_2 reported in the literature. Thus, the Li-cycling properties of TiO_2(N,F) are much better than that of TiO_2 in its anatase and rutile polymorphs and this can be ascribed to a more open structure and the fact that N^{3-} and F^- ions are more electronegative than the O^{2-} ions. It can be concluded that the Li-cycling properties of TiO_2(N,F) can be optimised by increasing the extent of N^{3-} and F^- doping, morphology-modification and surface-coatings.

3.5 References

1. Yang, Z., et al., *Nanostructures and lithium electrochemical reactivity of lithium titanites and titanium oxides: A review.* Journal of Power Sources, 2009. **192**(2): p. 588-598.
2. Zhu, G.N., Y.G. Wang, and Y.Y. Xia, *Ti-based compounds as anode materials for Li-ion batteries.* Energy & Environmental Science, 2012. **5**(5): p. 6652-6667.
3. Li, Q., et al., *Synthesis of high-density nanocavities inside TiO_2-B nanoribbons and their enhanced electrochemical lithium storage properties.* Inorg Chem, 2008. **47**(21): p. 9870-3.
4. Armstrong, G., et al., *TiO_2(B) Nanowires as an Improved Anode Material for Lithium-Ion Batteries Containing $LiFePO_4$ or $LiNi_{0.5}Mn_{1.5}O_4$ Cathodes and a Polymer Electrolyte.* Advanced Materials, 2006. **18**(19): p. 2597-2600.
5. Xu, J., et al., *Electrochemical properties of anatase TiO_2 nanotubes as an anode material for lithium-ion batteries.* Electrochimica Acta, 2007. **52**(28): p. 8044-8047.
6. Hu, Y.S., et al., *High Lithium Electroactivity of Nanometer-Sized Rutile TiO_2.* Advanced Materials, 2006. **18**(11): p. 1421-1426.
7. Reddy, M.A., et al., *Lithium Intercalation into Nanocrystalline Brookite TiO_2.* Electrochemical and Solid-State Letters, 2007. **10**(2): p. A29-A31.
8. Kuhn, A., C. Baehtz, and F. García-Alvarado, *Structural evolution of ramsdellite-type $Li_xTi_2O_4$ upon electrochemical lithium insertion–deinsertion* Journal of Power Sources, 2007. **174**(2): p. 421-427.

9. Noailles, L.D., et al., *Lithium insertion into hollandite-type TiO_2.* Journal of Power Sources, 1999. **81–82**(0): p. 259-263.

10. Armstrong, A.R., et al., *Lithium-Ion Intercalation into TiO_2-B Nanowires.* Advanced Materials, 2005. **17**(7): p. 862-865.

11. Wagemaker, M., A.P.M. Kentgens, and F.M. Mulder, *Equilibrium lithium transport between nanocrystalline phases in intercalated TiO_2 anatase.* Nature, 2002. **418**: p. 397-399.

12. Kuhn, A., R. Amandi, and F. García-Alvarado, *Electrochemical lithium insertion in TiO_2 with the ramsdellite structure.* Journal of Power Sources, 2001. **92**(1–2): p. 221-227.

13. Asahi, R., et al., *Visible-Light Photocatalysis in Nitrogen-Doped Titanium Oxides.* Science, 2001. **293**(5528): p. 269-271.

14. Irie, H., Y. Watanabe, and K. Hashimoto, *Nitrogen-Concentration Dependence on Photocatalytic Activity of $TiO_{2-x}N_x$ Powders.* Journal of physical chemistry B, 2003. **107**: p. 5483-5486.

15. Irie, H., et al., *Visible-light induced hydrophilicity on nitrogen-substituted titanium dioxide films.* Chemical Communications, 2003(11): p. 1298-1299.

16. Yu, J.C., et al., *Effects of F- Doping on the Photocatalytic Activity and Microstructures of Nanocrystalline TiO_2 Powders.* 2002. **14**: p. 3808-3816.

17. Nukumizu, K., et al., *$TiN_xO_yF_z$ as a stable photocatalyst for water oxidation in visible light (570 nm).* Chemistry Letters, 2003. **32**(2): p. 196-197.

18. Li, D., et al., *Visible-Light-Driven N−F−Codoped TiO_2 Photocatalysts. 1. Synthesis by Spray Pyrolysis and Surface Characterization.* Chemistry of Materials, 2005. **17**(10): p. 2588-2595.

19. Li, D., et al., *Visible-Light-Driven N−F−Codoped TiO_2 Photocatalysts: Optical Characterization, Photocatalysis, and Potential Application to Air Purification.* Chemistry of Materials, 2005. **17**(10): p. 2596-2602.

20. Xie, Y., et al., *CTAB-assisted synthesis of mesoporous F–N-codoped TiO_2 powders with high visible-light-driven catalytic activity and adsorption capacity.* Journal of Solid State Chemistry, 2008. **181**(8): p. 1936-1942.

21. Seibel, H.A., et al., *Synthesis and characterization of color variants of nitrogen- and fluorine-substituted TiO_2.* Journal of Materials Chemistry, 2009. **19**(4): p. 471-477.

22. Wu, Y., et al., *Preparation of nitrogen and fluorine co-doped mesoporous TiO_2 microsphere and photodegradation of acid orange 7 under visible light.* Chemical Engineering Journal, 2010. **162**(2): p. 710-717.

23. Jung, H.-G., et al., *Mesoporous-anatase TiO_2 with high surface area and controllable pore size by F-ion doping-Applications for high power li-ion battery anode.* Journal of Physical Chemistry C, 2009. **113**(50): p. 21258–21263.

24. T.Ohsaka, F.Izumi, and Y.Fujiki, *Raman Spectrum of Anatase, TiO_2.* Journal of Raman Specroscopy, 1978. **7**(6): p. 321-324.

25. Yang, J., et al., *Fabrication of rutile rod-like particle by hydrothermal method: an insight into HNO_3 peptization.* Journal of Colloid and Interface Science, 2005. **283**(1): p. 102-106.

26. Tompsett, G.A., et al., *The Raman Spectrum of Brookite, TiO_2 (Pbca, Z = 8).* Journal of Raman Specroscopy, 1995. **26**: p. 57-62.

27. Kubiak, P., et al., *Electrochemical evaluation of rutile TiO_2 nanoparticles as negative electrode for Li-ion batteries.* Journal of Power Sources, 2009. **194**(2): p. 1099-1104.

28. Das, B., et al., *Nano-composites $SnO(VO)_x$ as anodes for lithium ion batteries.* Journal of Solid State Electrochemistry, 2011. **15**(2): p. 259-268.

29. Subramanian, V., et al., *Nanocrystalline TiO_2 (anatase) for Li-ion batteries.* Journal of Power Sources, 2006. **159**(1): p. 186-192.

30. Sudant, G., et al., *Electrochemical lithium reactivity with nanotextured anatase-type TiO_2.* Journal of Materials Chemistry, 2005. **15**: p. 1263-1269.

31. Baudrin, E., et al., *Structural evolution during the reaction of Li with nano-sized rutile type TiO_2 at room temperature.* Electrochemistry Communications, 2007. **9**(2): p. 337-342.

32. Qiao, H., et al., *Electrochemical charge storage of flowerlike rutile TiO_2 nanorods.* Chemical Physics Letters, 2010. **490**(4-6): p. 180-183.

Chapter 4 Electrospun α-Fe_2O_3 nanorods as stable, high capacity anode material for Li-ion battery[G]

4.1 Introduction

A new family of high energy anode materials beyond those based on insertion/de-insertion [1] (such as graphite) or lithium alloying/de-alloying [1] (such as Sn or Si) mechanisms was reported by Tarascon and coworkers. [2] The lithium storage mechanism is the conversion reaction in which transition metal oxides, fluorides, sulfides, and nitrides react with lithium leading to reversible in-situ formation and decomposition of Li_yX (where X is O, S, F, or N) accompanying the reduction and oxidation of metal nanoparticles. The reaction gives rise to high reversible capacities ranging from 400 to 1400 mAh g^{-1} between 3.0 V and 0.001 V vs. Li/Li^+. [3] Among various transition metal oxides that are prospective anode for LIBs, binary iron oxides such as α-Fe_2O_3 (hematite), spinel Fe_3O_4 are interesting due to their high capacity from conversion reaction, environment friendliness, abundance and low cost. [3, 4] Fe_2O_3 and Fe_3O_4 have a theoretical capacity of 1007 mAh g^{-1} and 926 mAh g^{-1}, respectively assuming 6 and 8 Li uptake/ extraction per formula unit. But these are yet to be used in Li-ion batteries due to the poor capacity retention, lithiation/delithiation kinetics and rate capability which are inherent to transition metal oxides undergoing conversion reaction with lithium.

In recent years, in order to improve the Li-storage properties, many synthesis techniques such as sol-gel synthesis, template methods, chemical precipitation, micro-emulsion technique, forced hydrolysis, hot plate method etc. have been adopted to prepare various nanostructures of hematite. [5] Larcher *et. al*. [6] found

[*] Christie T. Cherian (Major contributor), J. Sundaramurthy, M. Kalaivani, P. Ragupathy, P. Suresh Kumar, V. Thavasi, M. V. Reddy, Chorng Haur Sow, S. G. Mhaisalkar, S. Ramakrishna and B. V. R. Chowdari, J. Mater. Chem., 2012, 22, 12198-12204

that nanosize α-Fe_2O_3 made up of fine monolithic particles behaves differently from micron particles, since up to one Li per formula unit can be intercalated in the corundum structure without phase transformation. They demonstrated the significance of the need for careful control of the texture and particle size of α-Fe_2O_3 in enhancing the electrochemical performance. Bruce and coworkers [7] compared the Li-cycling of nano-size, mesoporous and μm-size α-Fe_2O_3 particles and concluded that nanoparticles with sufficient amount of added carbon is essential to ensure high performance. The nano-sized and mesoporous α-Fe_2O_3 enhance the Li transport as well as easing the strain of conversion reaction but the meso- α-Fe_2O_3 does not enhance electron transport. So the electron transport to and within the particle is important for achieving high rates. Reddy *et al*. [8] has reported a stable capacity of 680 mAh g^{-1} for α-Fe_2O_3 nanoflakes prepared by thermal treatment, when cycled in the range of 0.005 - 3 V at 65 mA g^{-1} current rate. Hassan *et al*.[5] prepared α-Fe_2O_3-C composite by a simple molten salt method and showed a stable capacity of 1550 mAh g^{-1} up to 30 cycles eventually increased to 2112 mAh g^{-1} by 100 cycles when cycled at 0.5C (1C= 1005 mA g^{-1}) in the range, 0.01- 3 V vs Li. This superior performance with reversible capacity double that of theoretical value is attributed to the combined effect of nanostructuring, the carbon layering on the α-Fe_2O_3 particles and the porous ultrafine carbon matrix. Sun *et al*. [9] prepared mesoporous α-Fe_2O_3 nanostructure with worm-hole like morphology and it showed a specific discharge capacity of 1293 mAh g^{-1} after 50 cycles when cycled in the range at current of 200 mA g^{-1} in the voltage range 0.005- 3 V. Nuli *et al*. [10] prepared α-Fe_2O_3 nanosphere, nanowires, nanosheets, and nanocuboids by hydrothermal synthesis and obtained a reversible specific capacity of 586 mAh g^{-1} , 549 mAh g^{-1}, 442 mAh g^{-1} and 360

mAh g^{-1} respectively after 30 cycles, in the voltage range between 0.01 V and 3 V at a current density of 20 mA g^{-1}.

Compared with other synthesis methods, electrospinning has emerged as a versatile and low cost method for producing long continuous porous fibers with diameters ranging from several micrometers down to a few nanometers by applying a high voltage on a polymer solution or melt. The process attracted growing interest in recent years triggered by potential applications of metal oxide nanofibers in sensors, solar cells supercapacitors and LIBs. [11-14] Much work is focused on the electrochemical behavior and Li-storage capability of transition metal oxide nanostructures which are fabricated by the post heat treatment of electrospun-nanofibers. [15-18] Presently nanorods (150 nm) of α-Fe_2O_3 have been prepared by the electrospinning technique, characterized and its Li-cycling performance is evaluated. Results show that electrospun α-Fe_2O_3 nanorods show a reversible capacity of 1080 mAh g^{-1} after 50 cycles when cycled in the range of 0.005- 3.0 V at a current rate of 0.05 C. Nano-size agglomerated particles in fiber like morphology helps in achieving better cycling stability and rate capability.

4.2 Experimental

Materials:

Polyvinylpyrrolidone (PVP; MW = 1,300,000) was purchased from Sigma-Aldrich, Singapore. Ferric acetylacetonate ($Fe(acac)_3$) was obtained from Fluka, Singapore. The above chemical reagents used were analytical grade and used without further purification. Ethanol (HPLC grade) and glacial acetic acid were purchased from Tedia, Singapore.

In a typical procedure, 1 g polyvinylpyrrolidone (PVP) polymer was added to 10 ml ethanol (10 wt.%), and stirred at room temperature for 1 h. After

complete dissolution of PVP, 0.6 g of $Fe(acac)_3$ was added to the above PVP solution with stirring for 6 h. The obtained solution was then loaded into a plastic syringe with internal diameter of pinhead, 0.859 mm. The pinhead was connected to a high-voltage supply that was capable of generating dc voltages of up to 30 kV. In the experiment, a voltage of 15 kV was applied for electrospinning (Electrospunra, Mikrotools Pte. Ltd, Singapore). An aluminum foil served as the counter electrode, and the distance between the capillary and the electrode was 15 cm. The as-electrospun PVP/ ($Fe(acac)_3$) composite nanofibers were placed in a vacuum oven for 12 h at room temperature in order to remove the solvent residuals, then calcined at 500^0C for 5 h in air, to obtain α-Fe_2O_3 nanorods.

The compound was characterized by powder X-ray diffraction (XRD) (Philips X'PERT MPD, Cu Kα radn.). For morphology studies, scanning electron microscopy (SEM) (JEOL JSM– 6700F, Field Emission Electron Microscope) and high resolution transmission electron microscope (HR-TEM) (JEOL JEM 2100 operating at 200 kV) were employed. Raman spectra (Renishaw Raman system 2000) were recorded at room temperature. Specific surface area and porosity distributions were determined from results of N_2 physisorption at 77 K with a Micromeritics Tristar 3000 using the Brunauer-Emmett-Teller (BET) and Barrett-Joyner-Halenda (BJH) multipoints methods. Samples were preheated under nitrogen flow for 1 h at 150°C.

The electrodes for Li-cycling were prepared by the doctor-blade technique using a mixture of the active material (Fe_2O_3 nanorods), Super P carbon (MMM Ensaco) and binder (Kynar 2801) in the mass ratio 70:15:15, using an etched Cu-foil (thickness 10 μm) as the current collector. The geometrical electrode area and mass of active material were 2 cm^2 and 2–3 mg, respectively. Coin-type test cells

(size 2016) were assembled in an argon-filled glove box (MBraun, Germany) and the cell components were Li metal (Kyokuto Metal Co., Japan) foil as counter electrode, glass micro-fiber filter (GF/F, Whatman Int.Ltd., Maidstone, England) as the separator and 1M $LiPF_6$ in ethylene carbonate (EC) and dimethyl carbonate (DMC) (1:1 by volume, Merck Selectipur LP40) as the electrolyte. The cyclic voltammetry and galvanostatic discharge-charge cycling of the cells were carried out at room temperature (25°C) by computer controlled MacPile II (Biologic, France) unit and Bitrode multiple battery tester (model SCN, Bitrode, USA), respectively. Details on electrode fabrication steps and instrumentation are also discussed in our published literature. [19]

4.3 Results and discussion

4.3.1 Crystal structure and morphology

In order to investigate the crystal structure of the electrospun fibers, XRD measurement is performed. It has been observed that as prepared electrospun fibers are X-ray amorphous. Figure 4.1 shows the XRD pattern of the elctrospun PVP/$Fe(acac)_3$ composite fibers heated to 500 °C and all the peaks match well with the rhombohedral- hexagonal phase of α-Fe_2O_3. In addition to that, relatively low intensity peak were observed at 2θ= 31.7°, 45.4° and at 55.3° indicating the presence of maghemite, γ-Fe_2O_3 with spinel structure. The spinel phase can be more stable at smaller particle sizes due to a lower surface energy compared to the hcp polymorph (α-Fe_2O_3) and so maghemite-like defects and the net lattice disorder are closely related to the particle size and growth kinetics, as pointed out by Chernyshova *et al*. [20]

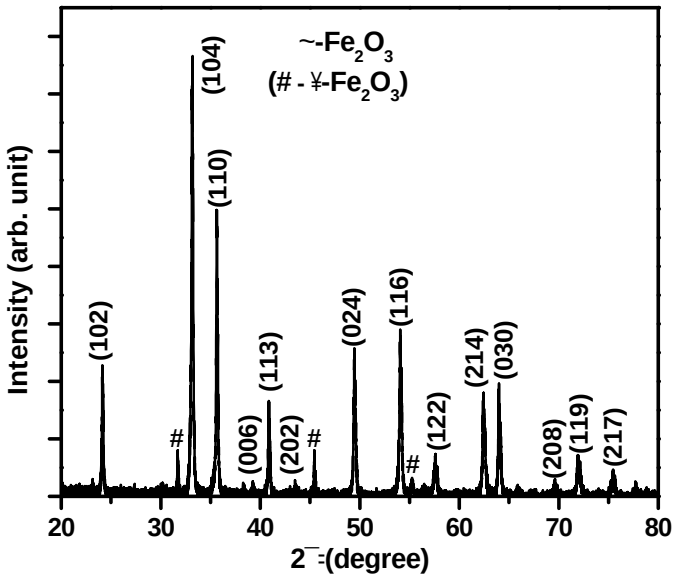

Figure 4.1 X-ray diffraction (XRD, Cu Kα radiation.) pattern of electrospun Fe_2O_3 nanorods. # symbol indicates impurity peaks due to γ-Fe_2O_3. Miller indices of α-Fe_2O_3 are shown.

Cheng *et al.* [21] also observed the presence of γ-Fe_2O_3 in α-Fe_2O_3 hollow-fibers prepared by direct annealing of the electrospun composite fibers. γ-Fe_2O_3 contains vacant sites in its spinel structure and the formula can be written as $(Fe^{3+})_t[Fe^{3+}_{5/3}, \ _{1/3}]_o$, where t and o refer to tetrahedral and octahedral sites respectively and represents vacancy. The lattice parameters of α-Fe_2O_3, evaluated from the Rietveld refined XRD data (space group *R-3c*) are: *a*= 5.03 Å and *c*= 13.75 Å which are in good agreement with that of the standard hematite structure, JCPDS Card No. 33-0664. The average crystallite size estimated from Scherrer's equation using TOPAS software is 133 nm.

Raman spectroscopy is an efficient tool to distinguish various iron oxides, hydroxides and oxy hydroxides. Hematite, α-Fe_2O_3 is isostructural with corundum (α-Al_2O_3) and belongs to the trigonal D_6^{3d} space group symmetry. According to space group symmetry and factor group analysis, the normal modes are: $2A_{1g}$ +

$2A_{1u} + 3A_{2g} + 2A_{2u} + 5E_g + 4E_u$. Among these, six are IR-active vibrations ($2A_{2u} + 4E_u$ modes) and seven are Raman-active vibrations ($2A_{1g} + 5E_g$ modes).

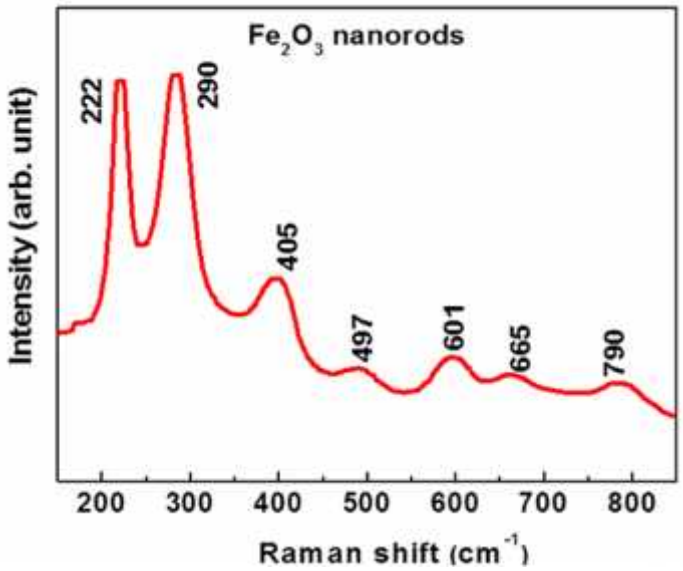

Figure 4.2 Raman spectra of electrospun Fe_2O_3 nanorods.Numbers refer to band positions in cm^{-1}.

In the literature, the two Raman active A_{1g} vibrational modes are observed at 225 and 498 cm^{-1} and the E_u modes are seen at 247, 293, 297, 412, 613 cm^{-1}. [22, 23] Figure 4.2 shows the Raman spectra of the Fe_2O_3 fibers. Well-established hematite bands are clearly visible at 222, 290, 405, 497 and 601 cm^{-1}.Two additional peaks are visible at 665 and 790 cm^{-1} confirming the presence of trace amount of maghemite (γ-Fe_2O_3).

Figure 4.3(a) shows the SEM image of electrsopun $Fe(acac)_3$/PVP fibers. As observed, the length of the fibers can reach mm range with an average diameter of 50 nm. The SEM image of the final products obtained after the 500°C heat-treated $Fe(acac)_3$/PVP fibers are shown in Figure 4.3(b) and nano-rod like morphology with an average diameter of 150 nm, can be clearly observed. Figure 4.3(c) and (d) shows the TEM image of heat-treated $Fe(acac)_3$/PVP fibers and nano- size,

agglomerated particles in fiber like morphology is evident from the images. Wang *et al.*[17] also noticed a similar morphology for Fe_3O_4 nanofibers via electrospinning synthesis . The HRTEM lattice image are shown in Figure 4.3(c) and the measured interplanar spacings match well with the d-value corresponding to the (102) plane of the XRD pattern of the α-Fe_2O_3 (Figure 4.1). SAED (selected area electron diffraction) pattern in Figure 4.3(d) consists of bright spots with (104) and (110) planes indicated.

It is well known that in the electrospinning method upon applying the potential, the electro-hydrodynamic and the dominancy effect of electrostatic and coulombic repulsive forces causes the fibers to stretch, elongate and change in size with a random distribution of the $Fe(acac)_3$ precursor along the PVP polymer matrix due to phase separation. The phase separation process involving polymer/precursor forms “islands" that account for the generation of different α-Fe_2O_3 nanostructures after calcination. Thus during calcination at 500^{o}C for 5 h, the polymer content in the composite fibers decomposes, causing the fiber to shrink. Further, the distributed precursors rearrange themselves by coalescing because of the shrinkage in the fiber and form nano-rod like morphology due to phase separation and precursor distribution. Thus at 15 kV potential and 6 wt% precursor concentration, nanoparticle embedded nano-rod like structures are formed as shown in Figure 4.3(c) and (d).

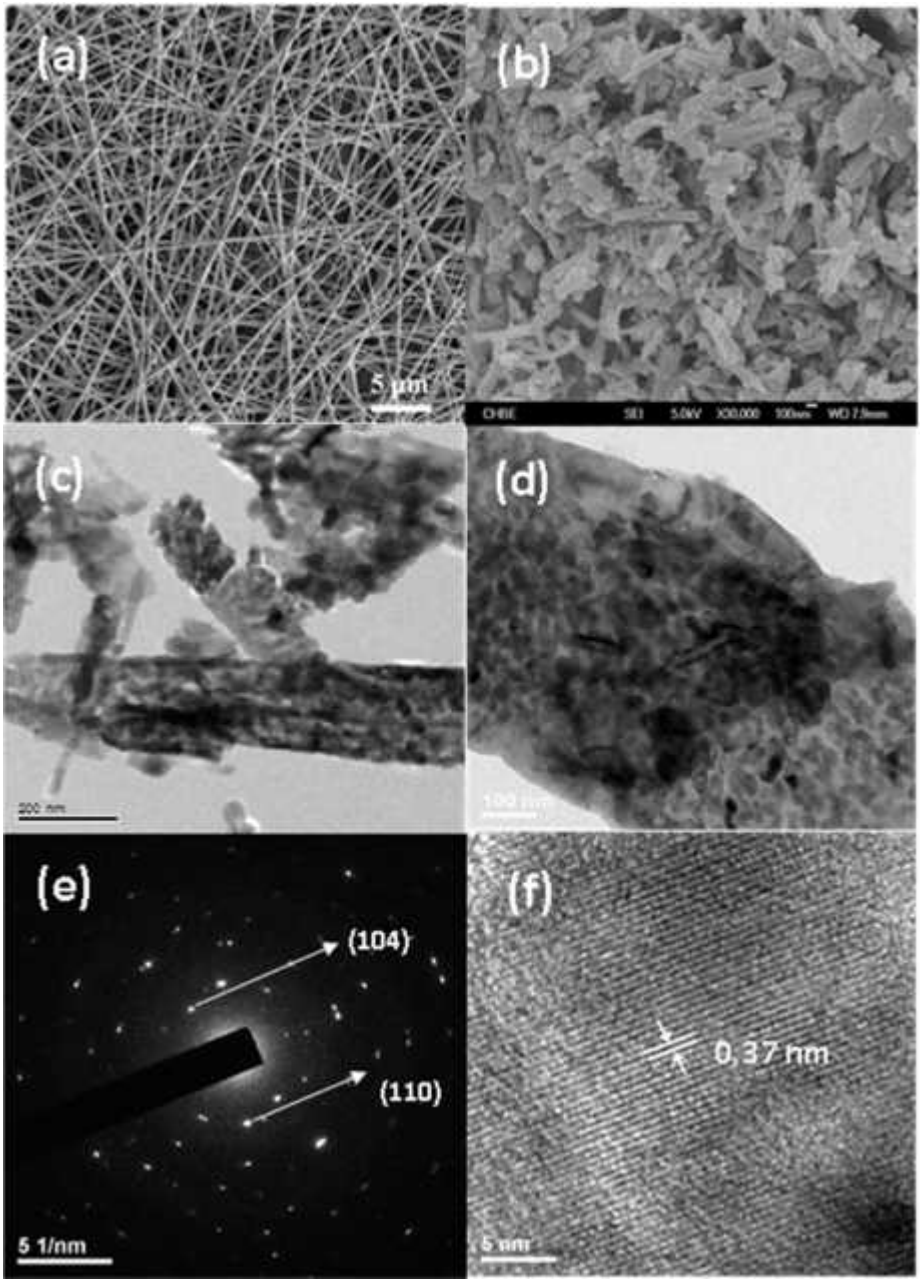

Figure 4.3(a) SEM photograph of electrsopun $Fe(acac)_3$/PVP fibers. Scale bar is 5000 nm. (b) SEM photograph of heat-treated $Fe(acac)_3$/PVP fibers. Scale bar is 100 nm. (c) TEM photograph of α-Fe_2O_3 nanorods. Scale bar is 200 nm. (d) TEM photograph of α-Fe_2O_3 nanorods. Scale bar is 100 nm. (e) SAED pattern of α-Fe_2O_3 nanorods. Miller indices (104) and (110) are shown. (f) HRTEM lattice image of α-Fe_2O_3 nanorods. Scale bar is 5 nm.

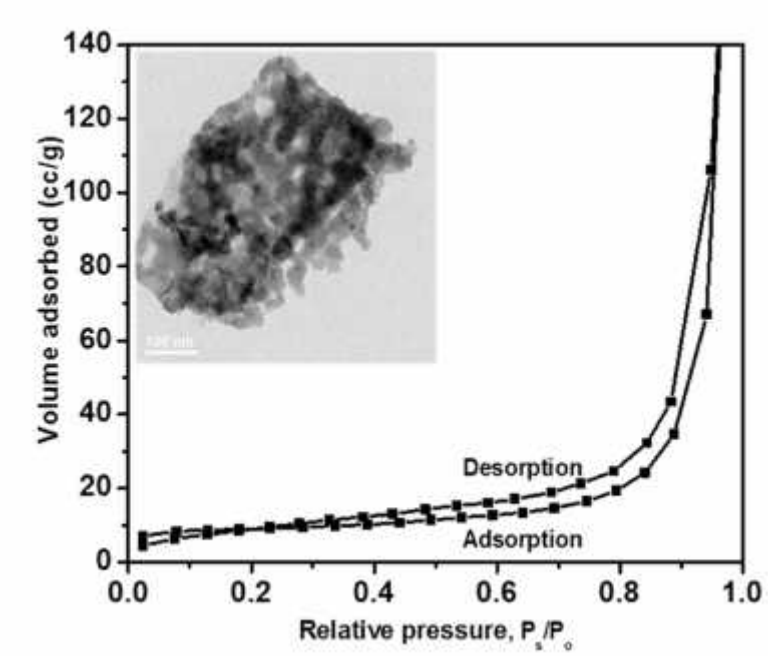

Figure 4.4 Nitrogen adsorption-desorption isotherm for α-Fe_2O_3 nanorods. Inset shows the TEM photograph of α-Fe_2O_3 nanorods.

To examine the specific surface area and the pore size, N_2 adsorption-desorption isotherm measurements are carried out. The curve shown in Figure 4.4 depicts a sloping adsorption and desorption branch covering a large range of P_s/P_o which is the characteristics of typical H3-type hysteresis loop. It is well known that H3 hysterisis loop is shown by materials with slit like macropores. [24] This is confirmed by the TEM image shown in the inset of Figure 4.4. The BET surface area and average pore radius are calculated to be 27.6 (±0.2) $m^2\ g^{-1}$ and 13.3 nm, respectively.

4.3.2 Electrochemical cycling

Discharge–charge cycling is carried out in the voltage window of 0.005–3.0 V (vs. Li) at a current of 50 mA g^{-1} up to 50 cycles at ambient temperature (RT), and the voltage versus capacity profiles are shown in Figure 4.5. The voltage profiles of only selected cycles are shown for sake of clarity.

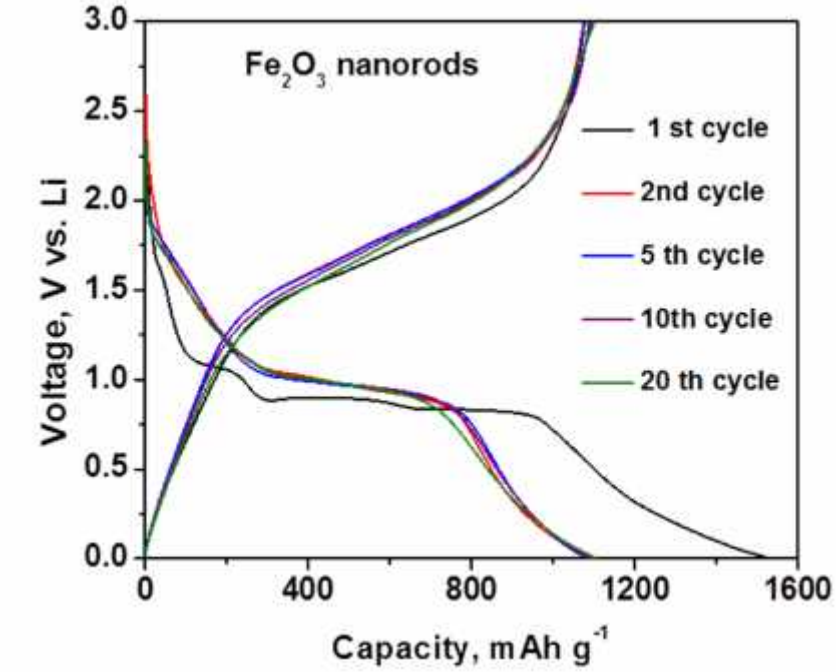

Figure 4.5 Voltage vs. capacity profiles of α-Fe_2O_3. Voltage range: 0.005- 3 V vs Li; current: 50 mA g^{-1} (0.05 C).

Firstly the cell is deep discharged from open circuit voltage (OCV= 2.6 V) to 0.005 V. The voltage steeply drops to 1.1 V giving a capacity of 100 mAh g^{-1} which corresponds to 0.6 mole of Li uptake per α-Fe_2O_3 (Figure 4.5).Then a small plateau like step at 1.1 V can be noticed, followed by a smooth voltage drop down to 0.9 V. This part comprises a capacity of 300 mAh g^{-1} which is equivalent to the uptake of 1.8 moles of Li, as shown in eqn. 4.2.

$Fe_2O_3 + Li^+ + e^- \longrightarrow Li_xFe_2O_3$

(x=0.6; voltage plateau, 1.1 V) eqn. 4.1

(x=1.8; voltage plateau, 0.9 V) eqn. 4.2

$Li_{1.8}Fe_2O_3 + 4.2Li^+ + 4.2e^- \longrightarrow 2Fe + 3Li_2O$ eqn. 4.3

$2Fe + 3Li_2O \longleftrightarrow Fe_2O_3 + 6Li^+ + 6e^-$ eqn. 4.4

Upon further discharge, an onset of long voltage plateau at 0.9 V can be seen, yielding a capacity of 980 mAh g^{-1}, corresponding to a total uptake of 5.8 Li per mole of α-Fe_2O_3 based on the complete reduction of Fe^{3+} to Fe^0 (eqn. 4.3). A similar Li-intercalation discharge profile was observed by Larcher *et. al*.[6] in nanometric hematite particles of 20 nm size and they concluded that up to 1 mole of lithium can be inserted in to α-Fe_2O_3 without disturbing its corundum structure and it is partially reversible, when it is charged (Li-extraction) from that voltage. However, micron sized α-Fe_2O_3 undergo an irreversible phase transformation from hexagonal to cubic close packing as soon as 0.05 mole of Li is inserted. [6] Continuation of the discharge reaction up to the lower cut-off (0.005 V) shows a sloping profile, results in the total first discharge capacity of 1515 mAh g^{-1}, corresponding to 9 moles of Li per mole of Fe_2O_3. Excess capacity can be regarded as originating from low voltage decomposition of the solvent in the electrolyte and subsequent formation of solid electrolyte interphase (SEI) and also a polymeric layer deposited on the surface of the Fe metal nano-particles that occurs in the 0.8-0.005 V region.

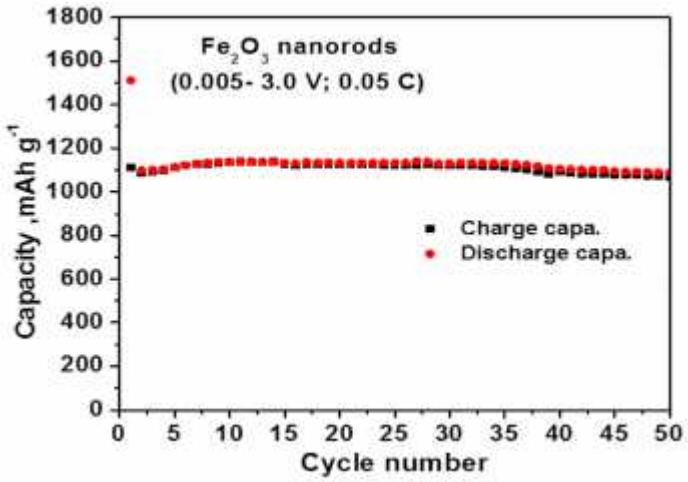

Figure 4.6 Capacity vs. cycle number plot of α-Fe_2O_3. Voltage range: 0.005- 3 V vs Li; current: 50 mA g^{-1} (0.05 C).

When the discharged electrode is charged to 3.0 V, a smooth voltage profile is observed till 1.5 V which is followed by sloping voltage plateau up to ~ 2.4 V and a steep rise up to 3.0 V. The first charge capacity is 1109 mAh g^{-1}(~ 6.6 moles of Li). From the second discharge onwards, the plateau like step at 1.1 V disappeared (Li-intercalation no longer happens) and the voltage continuously decreased till 1V followed by the voltage plateau (Figure 4.5). From second discharge onwards, conversion reaction is more favoured than intercalation reaction and so voltage like step at 1.1 V disappears during further cycles. The second discharge capacity is found to be 1095 mAh g^{-1}. Thus a large amount of lithium can be reversibly cycled in α-Fe_2O_3 by the conversion reaction of eqn. 4.3.The capacity vs. cycle number plot, shown in Figure 4.6 indicates that a reversible capacity of 1095 mAh g^{-1} is more or less stable up to 50 cycles. This remarkable capacity retention can be attributed to the unique morphology of Fe_2O_3 fibers. The excess capacity of ~90 mAh g^{-1} more than theoretical capacity (1007 mAh g^{-1}), can be due to the extra Li storage *via* non-faradaic mechanism called pseudo-capacitance which is an interfacial reaction due to the charge separation at the metal/Li_2O phase boundary. [25, 26] The excess capacity (~ 0.5 mole of Li) can also be due to the formation/decomposition of the polymeric layer mentioned earlier.

Cyclic voltammetry is a complementary technique to galvanostatic cycling and helps in understanding the nature and potentials at which the discharge-charge reactions take place in the electrode material. Figure 4.7 shows the cyclic voltammograms (CVs) of the α-Fe_2O_3 fibers in the potential window 0.005- 3V at the scan rate 58 μV/ Sec. It is clear from the CV curves that there is substantial difference between first and the subsequent cycles.

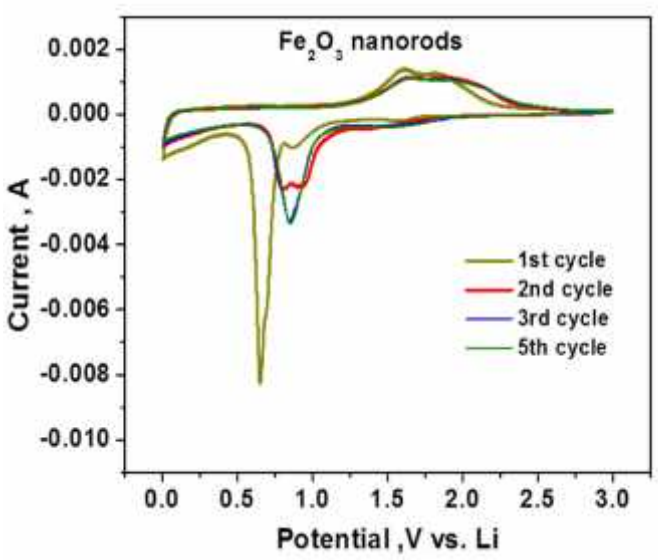

Figure 4.7 Cyclic voltammogramm of α-Fe_2O_3 nanorods. Potential window, 0.005-3 V; scan rate, 58 $\mu V\ s^{-1}$. Li metal was the counter and reference electrode.

The first cathodic scan results in a broad peak centered at ~1.6 V, small one at 0.86 V and a sharp high-intensity peak at 0.65V. The peaks at 1.6 V and 0.86 V corresponds to formation of $Li_{0.6}Fe_2O_3$ and $Li_{1.8}Fe_2O_3$ respectively without any crystal structure destruction. The large peak at 0.65 V is due to the decomposition of $Li_xFe_2O_3$ and the crystal structure destruction accompanied by the complete reduction of $Fe^{2+/3+}$ to Fe^0. The first anodic scan shows two peaks at 1.62 V and 1.84 V which corresponds to oxidation of Fe^0 to Fe^{2+} and Fe^{3+} ions to re-form Fe_2O_3. They got broadened and merged during further cycles. For the second cathodic scan, a broad split peak is observed at ~0.84 V which transforms to a well-defined sharp peak in further reduction cycles. Thus the CV curves complement the galvanostatic cycling data shown in Figure 4.5 and match well with the CV curves of α-Fe_2O_3 reported in the literature.[27] The curves corresponding to 3^{rd} and 5^{th} cathodic scans exactly overlap indicating the capacity stability.

The C-rate capability test was carried out on a duplicate cell with α-Fe_2O_3 fibers in the voltage range, 0.005-3V, at different current rates and the results are shown in Figure 4.8. The specific current was increased in steps from 0.1C to 2.5 C (1C = 1007 mA g^{-1}). The observed capacity of 1025 mAh g^{-1} after 30 cycles at 0.1C is unchanged at 0.2 C and stable up to 40 cycles. A decrease is observed in higher rates of 0.6 C, 1.2 C and 2.5 C and a capacity of 765 mAh g^{-1} is still obtainable at 2.5 C. After 70 cycles, the current rate is reduced from 2.5 C to 0.1 C and still a reversible capacity of 1090 mAh g^{-1} is obtained showing the excellent rate capability of the material. The structural and morphological characteristics of electrospun α-Fe_2O_3 nanorods enhance the transport of Li^+ ions and electrons within the composite electrode and surface incorporation of Li^+ into the electrochemically active particles achieving excellent rate capability.

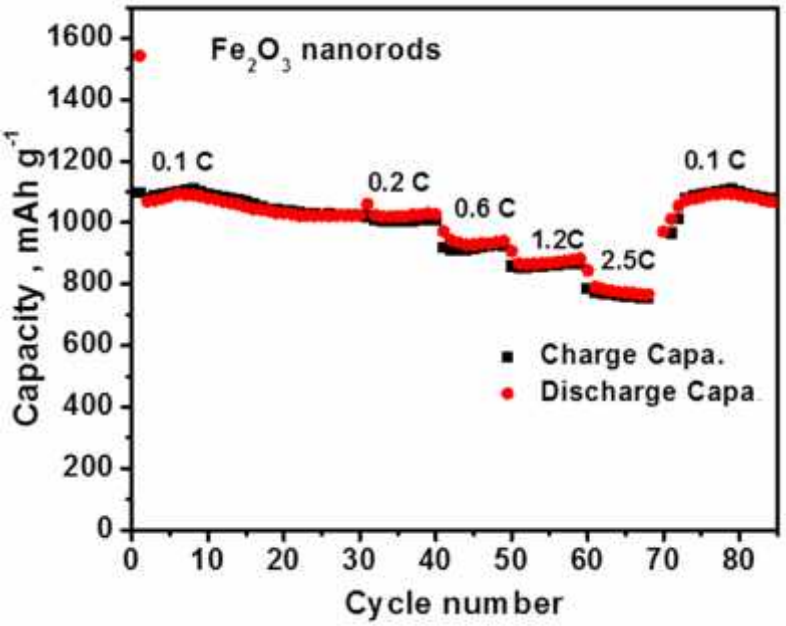

Figure 4.8 Capacity vs. cycle number plot of α-Fe_2O_3 nanorods at various C-rates. Voltage range: 0.005- 3 V vs Li.

Bruce's group [7] examined the factors influencing the conversion reaction of Fe_2O_3 using mesoporous, nanoparticulate and bulk α-Fe_2O_3 samples. Even if the

mesoporous structure can efficiently accommodate the strain during conversion reaction and enhance the area of contact between electrode and electrolyte, the capacity retention of mesoporous α-Fe_2O_3 was found to be bad. This was due to the μm- dimension of the mesoporous particles and hence poor e- transport within the particles. But the electrodes made of nanoparticles of α-Fe_2O_3 (60%) with high carbon content (30%) showed excellent cycling stability and a capacity above 1000 mAh/g after 50 cycles , which was better compared to electrodes with 70:20 ratio of active material (α-Fe_2O_3 nanoparticles) and carbon. [7] Liu *et al*. [28] studied the electrochemical performance of α-Fe_2O_3 nanorod and found that the performance of electrodes with less conductive carbon content is worse compared to that with high carbon content (40%). The nanorod electrode containing 40% conductive carbon showed a discharge capacity of 763 mAh g^{-1} after 30 cycles with capacity retention of 57%. [28] Nano-particle/rod can enhance the e^- transport within the particle but it may easily become disconnected as the particles expand and contract on charge/discharge cycles showing poor capacity. However, inter-particle connectivity can be improved either by increasing the carbon content or confining the nanoparticles in rod like structures. So it is clear that the morphology of α-Fe_2O_3 rods prepared by electrospinning is advantageous for the Li-storage. In the present case, nanocrystalline agglomerates of α-Fe_2O_3 are embedded in macroporous rod like structures which is evident from the isotherm curve and TEM photograph shown in Figure 4.3 and Figure 4.4. Also the presence of small amount of γ-Fe_2O_3 like surface defects can be helpful for electrochemical cycling of α-Fe_2O_3 particles, since γ-Fe_2O_3 has vacant sites in the lattice and thereby likely enhances the Li-ion mobility. [29]

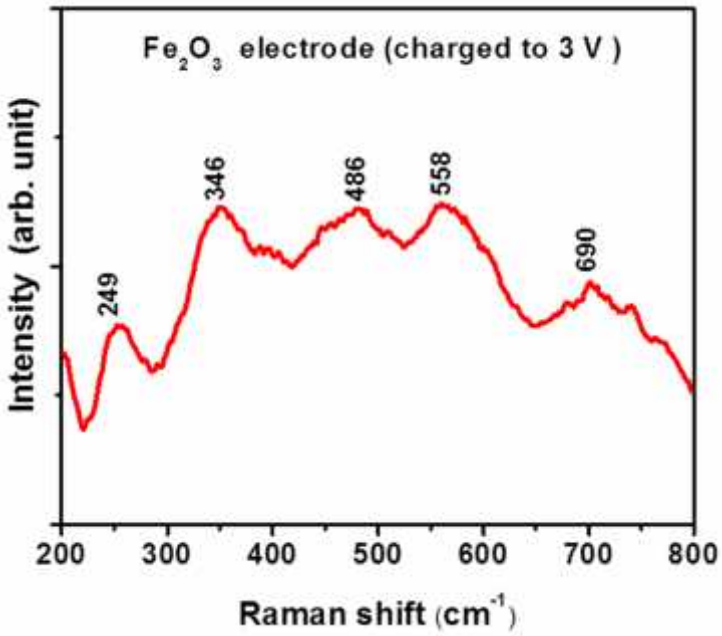

Figure 4.9 Raman spectra of cycled Fe_2O_3 electrode (electrode charged to 3 V, after the first discharge). Numbers refer to band positions in cm^{-1}.

α-Fe_2O_3 eventually transforms to γ-Fe_2O_3 on further cycling. The presence of large amount of γ-Fe_2O_3 is observed, from the Raman spectrum of cycled electrode of α-Fe_2O_3.The Raman spectrum of the electrode charged to 3 V, after the first discharge, is shown in Figure 4.9.It is qualitatively different from that of α-Fe_2O_3 (Figure 4.2). Maghemite is characterized by four Raman peaks at 381, 486, 670 and 718 cm^{-1}. [22, 23] From figure 4.9, Raman peaks at 346, 486 and 690 cm^{-1} can be attributed to the presence of maghemite. Due to the thermodynamic considerations at nanosize, the α-Fe_2O_3 forms nanosized γ-Fe_2O_3 phase upon cycling to 3 V as shown by Hariharan *et al*. [30]. Probably, some mechanistic studies based on X-ray analysis during the charge and discharge experiments may give information on phase transformation. Poizot *et al*. [3] pointed out that the SEI formation layer, if too large, will block the metal oxide particle reactivity towards lithium. The size of the precursor particle governs the SEI formation despite the nano-sized character of electrodes. Here the electrospun α-Fe_2O_3 nanorods

prepared by electrospinning have an average width of 150 nm and a length of 1μm which is not too small particle size to cause large SEI formation.

4.4 Conclusion

In summary, Fe_2O_3 nanorods with a novel morphology are prepared by the electrospinning of ferric acetyl acetonate/PVP precursor and subsequent heat treatment of fibers in air at 500°C for 6 h. SEM and TEM images show that the heat treated fibers transformed to macroporous rods with nanoparticles embedded in it. Electrochemical studies in the voltage range 0.005-3 V at 0.05 C (50 mA g^{-1}) revealed that electrospun α-Fe_2O_3 delivers high reversible capacity of 1095 mAh g^{-1} with capacity retention of 93% between 2-50 cycles. The novel morphology of electrospun α-Fe_2O_3 helps in the enhancing the inter-particle connectivity, giving a better cycling performance. With the aid of Raman spectroscopy, it is found that α-Fe_2O_3 gets converted to γ-Fe_2O_3 upon cycling which is more stable at nano-size.

4.5 References

1. Cabana, J., et al., *Beyond Intercalation-Based Li-Ion Batteries: The State of the Art and Challenges of Electrode Materials Reacting Through Conversion Reactions.* Advanced Materials, 2010. **22**(35): p. E170-E192.
2. Poizot, P., et al., *Nano-sized transition-metaloxides as negative-electrode materials for lithium-ion batteries.* Nature, 2000. **407**(6803): p. 496-499.
3. Poizot, P., et al., *Searching for new anode materials for the Li-ion technology: time to deviate from the usual path.* Journal of Power Sources, 2001. **97-98**: p. 235-239.
4. Taberna, L., et al., *High rate capabilities Fe_3O_4-based Cu nano-architectured electrodes for lithium-ion battery applications.* Nature Materials, 2006. **5**(7): p. 567-573.
5. Hassan, M.F., et al., *Solvent-assisted molten salt process: A new route to synthesise α-Fe_2O_3/C nanocomposite and its electrochemical performance in lithium-ion batteries.* Electrochimica Acta, 2010. **55**(17): p. 5006-5013.
6. Larcher, D., et al., *Effect of Particle Size on Lithium Intercalation into α-Fe_2O_3.* Journal of The Electrochemical Society, 2003. **150**(1): p. A133.
7. Jiao, F., J.L. Bao, and P.G. Bruce, *Factors influencing the rate of Fe_2O_3 conversion reaction.* Electrochemical and Solid-State Letters, 2007. **10**(12): p. A264-A266.
8. Reddy, M.V., et al., *~-Fe_2O_3 nanoflakes as an anode material for Li-ion batteries.* Advanced Functional Materials, 2007. **17**(15): p. 2792-2799.
9. Sun, B., et al., *Synthesis of Mesoporous α-Fe_2O_3 Nanostructures for Highly Sensitive Gas Sensors and High Capacity Anode Materials in Lithium Ion*

Batteries. Journal of Physical Chemistry C, 2010. **114**(44): p. 18753–18761.

10. Nuli, Y., et al., *Controlled synthesis of alpha-Fe_2O_3 nanostructures and their size-dependent electrochemical properties for lithium-ion batteries.* Journal of Power Sources, 2008. **184**(2): p. 456-461.
11. Cavaliere, S., et al., *Electrospinning: designed architectures for energy conversion and storage devices.* Energy & Environmental Science, 2011.
12. Krishnamoorthy, T., et al., *A first report on the fabrication of vertically aligned anatase TiO_2 nanowires by electrospinning: Preferred architecture for nanostructured solar cells.* Energy & Environmental Science, 2011. **4**(8): p. 2807-2812.
13. Ramaseshan, R., et al., *Nanostructured ceramics by electrospinning.* Journal of Applied Physics, 2007. **102**(11): p. 111101.
14. Viet, A.L., et al., *Nanostructured Nb_2O_5 Polymorphs by Electrospinning for Rechargeable Lithium Batteries.* Journal of Physical Chemistry C, 2009. **114**(1): p. 664-671.
15. Chen, L.-J., et al., *Synthesis and characterization of PVP/$LiCoO_2$ nanofibers by electrospinning route.* Journal of Applied Polymer Science, 2011. **121**(1): p. 154-160.
16. Zhu, C., et al., *Electrospinning of Highly Electroactive Carbon-Coated Single-Crystalline $LiFePO_4$ Nanowires.* Angewandte Chemie International Edition, 2011. **50**(28): p. 6278-6282.
17. Wang, L., et al., *Electrospinning synthesis of C/Fe_3O_4 composite nanofibers and their application for high performance lithium-ion batteries.* Journal of Power Sources, 2008. **183**(2): p. 717-723.

18. Mai, L., et al., *Electrospun Ultralong Hierarchical Vanadium Oxide Nanowires with High Performance for Lithium Ion Batteries.* Nano Letters, 2010. **10**(11): p. 4750-4755.

19. Cherian, C.T., et al., *(N,F)-Co-doped TiO_2: synthesis, anatase-rutile conversion and Li-cycling properties.* CrystEngComm, 2012.

20. Chernyshova, I.V., M.F. Hochella Jr, and A.S. Madden, *Size-dependent structural transformations of hematite nanoparticles. 1. Phase transition.* Physical Chemistry Chemical Physics, 2007. **9**(14): p. 1736.

21. Cheng, Y., et al., *Formation mechanism of Fe_2O_3 hollow fibers by direct annealing of the electrospun composite fibers and their magnetic, electrochemical properties.* CrystEngComm, 2011. **13**(8): p. 2863.

22. Hanesch, M., *Raman spectroscopy of iron oxides and (oxy)hydroxides at low laser power and possible applications in environmental magnetic studies.* Geophysical Journal International, 2009. **177**(3): p. 941-948.

23. Oh, S.J., D.C. Cook, and H.E. Townsend, *Characterization of iron oxides commonly formed as corrosion products on steel.* Hyperfine Interactions, 1998. **112**: p. 59-65.

24. Condon, J.B., *Surface Area and Porosity Determinations by Physisorption: Measurements and Theory*. First ed2006, Amsterdam, The Netherlands: Elsevier.

25. Jamnik, J. and J. Maier, *Nanocrystallinity effects in lithium battery materials.* Physical Chemistry Chemical Physics, 2003. **5**(23): p. 5215.

26. Shin, J.-Y., D. Samuelis, and J. Maier, *Sustained Lithium-Storage Performance of Hierarchical, Nanoporous Anatase TiO_2 at High Rates:*

Emphasis on Interfacial Storage Phenomena. Advanced Functional Materials, 2011. **21**(18): p. 3464-3472.

27. Chou, S.-L., et al., *High-surface-area α-Fe_2O_3/carbon nanocomposite: one-step synthesis and its highly reversible and enhanced high-rate lithium storage properties.* Journal of Materials Chemistry, 2010. **20**(11): p. 2092.
28. Liu, H., et al., *Electrochemical performance of α-Fe_2O_3 nanorods as anode material for lithium-ion cells.* Electrochimica Acta, 2009. **54**(6): p. 1733-1736.
29. Kanzaki, S., et al., *Nano-sized γ-Fe_2O_3 as lithium battery cathode.* Journal of Power Sources, 2005. **146**(1-2): p. 323-326.
30. Hariharan, S., K. Saravanan, and P. Balaya, *Lithium Storage Using Conversion Reaction in Maghemite and Hematite.* Electrochemical and Solid-State Letters, 2010. **13**(9): p. A132.

Chapter 5 Li-cycling properties of $NiFe_2O_4$ nanostructures

5.1 Introduction

Wide variety of binary and ternary oxides have been studied as prospective anode materials for Li-ion batteries which undergo Li-cycling via the 'conversion reaction' and those have been recently reviewed by Cabana *et al*.[1]. Iron based spinel oxides such as Fe_3O_4[2] , ferrites with general formula AFe_2O_4 (A= Zn, Ni, Co, Cu, Cd) [3-7] have been extensively studied for their Li-cyclability. The general composition for the spinel structure is represented as $A[B_2]O_4$ in which the number of B^{3+} ions is twice that of the A^{2+} ions. Normal spinel has a cubic close-packed (ccp) oxygen array in which A^{2+} ions occupy one-eighth of the tetrahedral 8a-sites and B^{3+} ions occupy one-half of the octahedral 16d-sites in the space group, *Fd*3*m*.[8] The spinel structure is flexible with regard to the distribution of A and B ions at tetrahedral and octahedral sites. When A ions occupy one-half of the octahedral 16(d) sites and B ions occupy the other half of the octahedral 16(d) sites as well as all of the tetrahedral 8(a) sites, namely, $(B)[A,B]O_4$, the structure is called an inverse spinel and the degree of inversion is unity. [8] Mixed spinels are those in which the degree of inversion lies between 0 and 1. In the literature, many years ago Chen *et al*. [9] studied the room temperature Li-insertion reactions of several cubic iron spinels, MFe_2O_4 with M^{2+} = Mn, Fe, Co, Ni, Cu, Zn and Cd by using butyl-Li. They found that the maximum amount of Li ions that may be incorporated in to the ferrites decrease in the order, inverse > "mixed" > normal spinel [9].However, the critical Li-ion concentration (x_c) above which the cubic spinel to rock salt transition occurs, is larger for normal spinels than for inverse spinels. That is x_c ~0.5 for $ZnFe_2O_4$ and ~0.1 for Fe_3O_4. [9]

$NiFe_2O_4$ has an inverse spinel structure where the Ni^{2+} and half of Fe^{3+} cations occupy octahedral site and remaining Fe^{3+} occupy the tetrahedral site, $Fe^{3+}[Ni^{2+},Fe^{3+}]O_4$. It undergoes Li-cycling via conversion reaction with a theoretical capacity of 915 mAh g^{-1}, corresponding to 8 moles of Li. Several efforts have been made to improve the long-term Li-cycling behavior of $NiFe_2O_4$ such as adopting different synthesis methods to control the particle size and morphology and partial substitution of host structure with metal cations. Tirado's group has done extensive work on the Li- cycling properties of $NiFe_2O_4$ and the origin of capacity fading in it, up on cycling. [5, 10, 11] They found that capacity fading occurs in $NiFe_2O_4$ up to 20 cycles irrespective of the preparation conditions and thereafter the capacity stabilizes or continues to fade depending on the temperature and/or method of synthesis. [10] Among $NiFe_2O_4$ phases that have been prepared by sol-gel method, those annealed at 1000°C showed good capacity retention, namely 550 mAh g^{-1} was observed after 50 cycles at 1 C-rate. The authors concluded that mutually interconnected sub-micron particles that define a macroporous system are essential to sustain high capacity values over a large number of cycles. [10]

Lavela *et al.* [12] partially substituted Fe^{3+} with Mn^{3+} in $NiFe_2O_4$ nanoparticles and studied its electrochemical performance. Capacities close to 800 mAh g^{-1} after 40 cycles and 750 mAh g^{-1} after 50 cycles were obtained for $NiMnFeO_4$ and $NiFe_2O_4$, respectively. Zhao *et al.* [13] prepared nano-sized $NiFe_2O_4$ (5-15 nm) with high surface area by hydrothermal method at 230 °C and found that the first discharge capacity reached a value of 1314 mAh g^{-1}. But the discharge capacity decreased to 790.8 mAh g^{-1} and 709.0 mAh g^{-1} at a current density of 0.2 mA cm^{-2} after 2 and 3 cycles, respectively. Zinc ferrite, $ZnFe_2O_4$ is a

normal spinel where only the Zn-ions occupy the tetrahedral site, $Zn^{2+}[Fe^{3+}_2]O_4$. Zn has been proven to be a good matrix element for conversion-based electrodes such as $ZnCo_2O_4$ and $ZnMn_2O_4$ since it can contribute additional capacity due to alloying-de-alloying reaction besides buffering the volume variation during conversion reaction [3, 4, 15, 16]. It is also known that the capacity stability of conversion-reaction based electrodes depends on the initial crystal structure which determines the local environment of the participating ions during Li-cycling. [15, 17] So it is of interest to study the effect of doping $NiFe_2O_4$ with varying amounts of Zn and the consequent cation redistribution, on the Li-cycling behaviour. Nano-size solid solutions, $(Ni_{1-x}Zn_x)Fe_2O_4$ are prepared and their Li-cycling behavior is studied.

Recently, Zhao *et al*. [14] prepared $NiFe_2O_4$/SWNT (single walled carbon nanotubes) composite with a loading ratio of 70 wt. % by hydrothermal method and studied the Li-cycling properties. They reported a stable reversible capacity of 776 mAh g^{-1} after 55 cycles when cycled in the range of 0.005-3.0 V at a current density of 150 mA g^{-1}. $NiFe_2O_4$ NPs (nanoparticles, 5 nm) were homogeneously anchored on the surface of the SWNTs and the excellent electrochemical performance of the composite was attributed to the synergistic effect between SWNT and $NiFe_2O_4$. Apart from the initial crystal structure and nano-size, inter-particle connectivity of the active material during Li-cycling is also an important factor affecting the capacity stability of $NiFe_2O_4$. [5, 18, 19] Inter-particle connectivity can be achieved by developing a conducting network throughout the electrode which can be realized by fabricating morphologically stout nanowires/nanofibers of $NiFe_2O_4$ or by addition of carbon nanofibers or carbon nanotubes along with the active material. Here, continuous nanofibers of inter-

connected nanoparticles of $NiFe_2O_4$ are synthesized by electrospinning, followed by heat treatment of the fibers. The electrochemical performance and morphological changes of the nanofibers during the Li-cycling are investigated in detail.

5.2 Experimental

5.2.1 Synthesis of $(Ni_{1-x}Zn_x)Fe_2O_4$ nanoparticles

The solid solutions, $(Ni_{1-x}Zn_x)\ Fe_2O_4$ (x= 0, 0.2, 0.4, 0.6, 0.8, 1) were prepared by citrate gel auto combustion method reported by Hankare *et al*. [20] Citric acid (Sigma Aldrich, 99.5 %), zinc nitrate hexahydrate (Sigma Aldrich, 98 %), nickel nitrate hexahydrate (Fluka, 98%) and ferric citrate hydrate (Merck, 98%) are used as starting materials. Zinc nitrate and nickel nitrate solutions, of required concentrations, are prepared and kept in separate beakers. Citric acid solution is prepared and added to the above solutions. A clear transparent solution of metal-citrate complex is obtained. The resultant solutions are added to iron citrate solution with constant stirring. The mixture was evaporated on hot plate slowly to obtain a porous mass. The compositions with varying x were heated at 700°C for 5 h in air.

5.2.2 Synthesis of $NiFe_2O_4$ nanofibres

Polyvinylpyrrolidone (PVP; Mw = 1,300,000) and Iron (III) acetylacetonate (Fe(acac)3), Nickel(II) acetate dihydrate are purchased from Sigma-Aldrich and Fluka, Singapore, respectively. Ethanol (HPLC grade) and glacial acetic acid are purchased from Tedia, Singapore and used as received. Firstly, 1 g of PVP is added in to 10 ml of ethanol solvent and stirred at room temperature for 1 h for complete dissolution. Then, 0.6 g of iron acetylacetonate

precursor is added to PVP solution and continuously stirred for few hours. Later, 1 ml of acetic acid is added followed by addition of 0.211 g of nickel acetate dihydrate to the solution and stirred again for few hours. Finally, 10 ml of completely mixed precursor solutions are loaded in a plastic syringe with a hypodermic needle (dia. 27G). Later, the hypodermic needle is connected to a high-voltage supply capable of generating direct current (DC) voltages of up to 30 kV. Electrospinning is carried out by applying a power supply of around 17.5 kV at the needle in a controlled electrospinning set-up (Electrospunra, Singapore). An aluminum foil is used as the counter electrode, and the distance between the needle and the collector are maintained at 15 cm. The as-spun composite nanofiber mats are placed in a vacuum oven at room temperature for 12 h to remove the solvent residuals. Then, the electrospun polymeric fibers are calcined at 500°C for 5 h in air at a heating rate of 5°C/min, and finally the calcined $NiFe_2O_4$ samples are obtained and stored carefully. Even slight changes in solution preparation and spinning conditions can affect the formation of nanofibres. Interconnected nanoparticles of $NiFe_2O_4$ are obtained when the electrospun precursors are heated to 600°C and 800°C for 5 h.

The compounds were characterized by powder X-ray diffraction (XRD) (Philips X'PERT MPD, Cu K_α and the data were refined using TOPAS software, R 2.1 version.) and high resolution transmission electron microscope (HR-TEM) (JEOL JEM 2100 operating at 200 kV). Brunauer-Emmett-Teller (BET) surface areas were determined from results of N_2 physisorption at 77 K using Tristar 3000 (Micromeritics, USA) and the powder samples were preheated under nitrogen flow for 1 h at 150 °C to remove adsorbed moisture. The Ni and Zn -content are determined by the inductively coupled plasma optical emission spectrometer (ICP-

OES; Perkin Elmer Dual-View Optima DV) system. Sample dissolution is carried out by Milestone microwave laboratory system, USA, using aqua-regia.

The electrodes for Li-cycling were prepared by the doctor-blade technique using a mixture of the active material ($Ni_{1-x}Zn_xFe_2O_4$ nanoparticles or $NiFe_2O_4$ nano-fibres), Super P carbon (MMM Ensaco) and binder (Kynar 2801) in the mass ratio 70:15:15, using an etched Cu-foil (thickness 10 μm) as the current collector. $Ni_{1-x}Zn_xFe_2O_4$ nanoparticle electrodes were heat treated in argon atmosphere at 240°C for 5 h and cooled to ambient temperature. This is to ensure melting and solidification of the binder and uniform distribution of the active mass on the electrode. Coin-type test cells (size 2016) were assembled using Li metal as counter electrode, glass micro-fiber filter as the separator and 1M $LiPF_6$ in ethylene carbonate (EC) and dimethyl carbonate (DMC) (1:1 by volume) as the electrolyte. Galvanostatic discharge-charge cycling and cyclic voltammetry of the cells were carried out at room temperature (25°C) by computer controlled battery tester (model SCN, Bitrode, USA) and Macpile II (Biologic, France) respectively. Details of electrode preparation, coin cell fabrication and sample handling for TEM are discussed in chapter 2 and also in our previous publication. [21]

5.3 Results and Discussion

5.3.1 Crystal structure and morphology

5.3.1.1 $(Ni_{1-x}Zn_x)Fe_2O_4$ nanoparticles

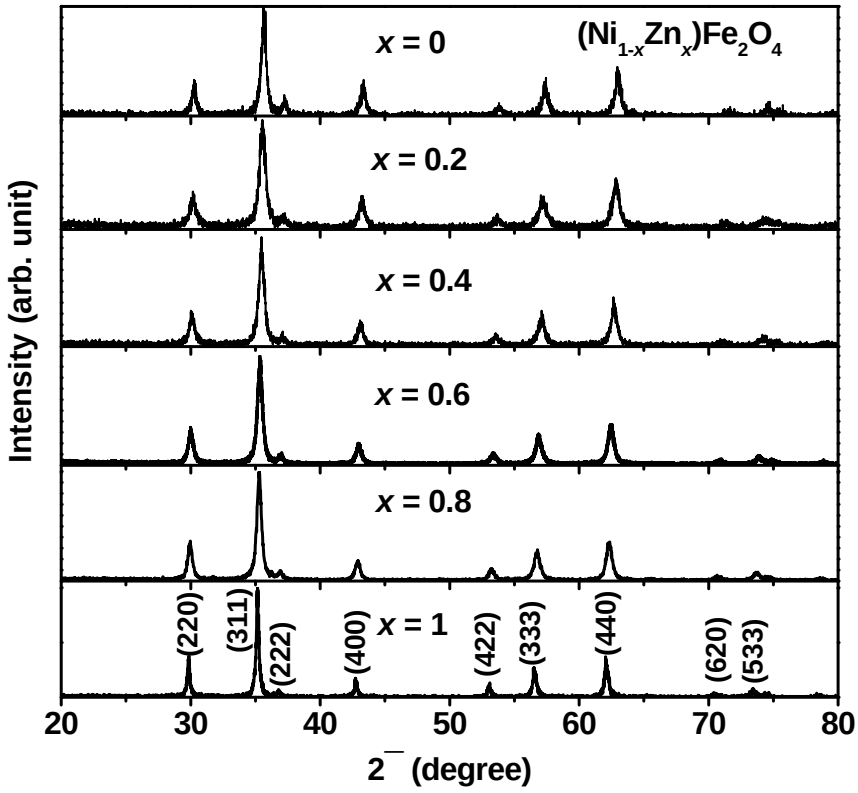

Figure 5.1 X-ray diffraction (XRD, Cu Kα radiation) pattern of $NiFe_2O_4$ nanoparticles. Miller indices of $NiFe_2O_4$ are shown.

The as-prepared compounds vary in color from dark brown to yellow with increasing Zn content. The powder XRD patterns of the compositions of $(Ni_{1-x}Zn_x)Fe_2O_4$, x=0, 0.2, 0.4, 0.6, 0.8, 1 are shown in Figure 5.1 and they revealed the formation of compound in phase pure form with the cubic spinel structure without any impurities.

The lattice parameter values (a) are obtained by the Rietveld refinement and are in good agreement with reported values of $NiFe_2O_4$ (JCPDS 86-2267) and $ZnFe_2O_4$ (JCPDS 82-1049).The variation of lattice parameter with the Zn concentration is given in Table 5-1 along with the Rietveld parameters. Since Zn^{2+} always prefers to occupy tetrahedral site, doping of Zn^{2+} in to $NiFe_2O_4$ displaces equal amount of

$(Ni_{1-x}Zn_x)Fe_2O_4$						
x	0	0.2	0.4	0.6	0.8	1
Lattice parameter (*a*) , Å	8.341(1)	8.355(4)	8.371(4)	8.399(7)	8.422(3)	8.441 (3)
R_{wp} (Weight-profile)	34	36	38	30	30	39
R_B (Rietveld-Bragg)	8.6	7.7	8.7	5.1	4.5	9.1
GOF (goodness of fit)	1.2	1.1	1.2	1.3	1.4	1.1
BET surface area (±0.2 m^2 g^{-1})	31.9	30.1	24.7	20.7	28.1	27.0
Zn wt. %						
Calc.	0	5.6	11.0	16.5	21.8	27.1
Exp.	0	5.6	10.1	16.3	21.0	27.3
Ni wt. %						
Calc.	25.0	19.9	14.8	9.9	4.9	0
Exp.	26.2	19.8	14.7	10.3	6.1	0
Crystallite size, nm (from Scherrer equation)	35	27	25	24	28	22

Table 5-1 Structure and other data of $(Ni_{1-x}Zn_x)Fe_2O_4$

Fe^{3+} from the tetrahedral site and the displaced Fe^{3+} occupy the octahedral sites of Ni^{2+} [20]. The cationic distribution at the tetrahedral site and octahedral site with varying x has been determined from the magnetization data by Hankare *et al*.[20]. Thus, we can expect a gradual linear increase in the lattice parameter with the increase in zinc content, since the ionic radius of Zn^{2+} (tetrahedral coordination: 0.60 Å) is greater than that of Fe^{3+} (tetrahedral coordination: 0.49 Å) [22]. On the

other hand, replacement of Ni^{2+} (r_i, octahedral coordination: 0.69 Å) by Fe^{3+} (r_i, octahedral coordination: 0.645 Å) produces only marginal decrease in the average ionic radius. The observed *a* values in the present study are in good agreement with those reported by Hankare *et al.* [20] and almost obeys the Vegard's law.

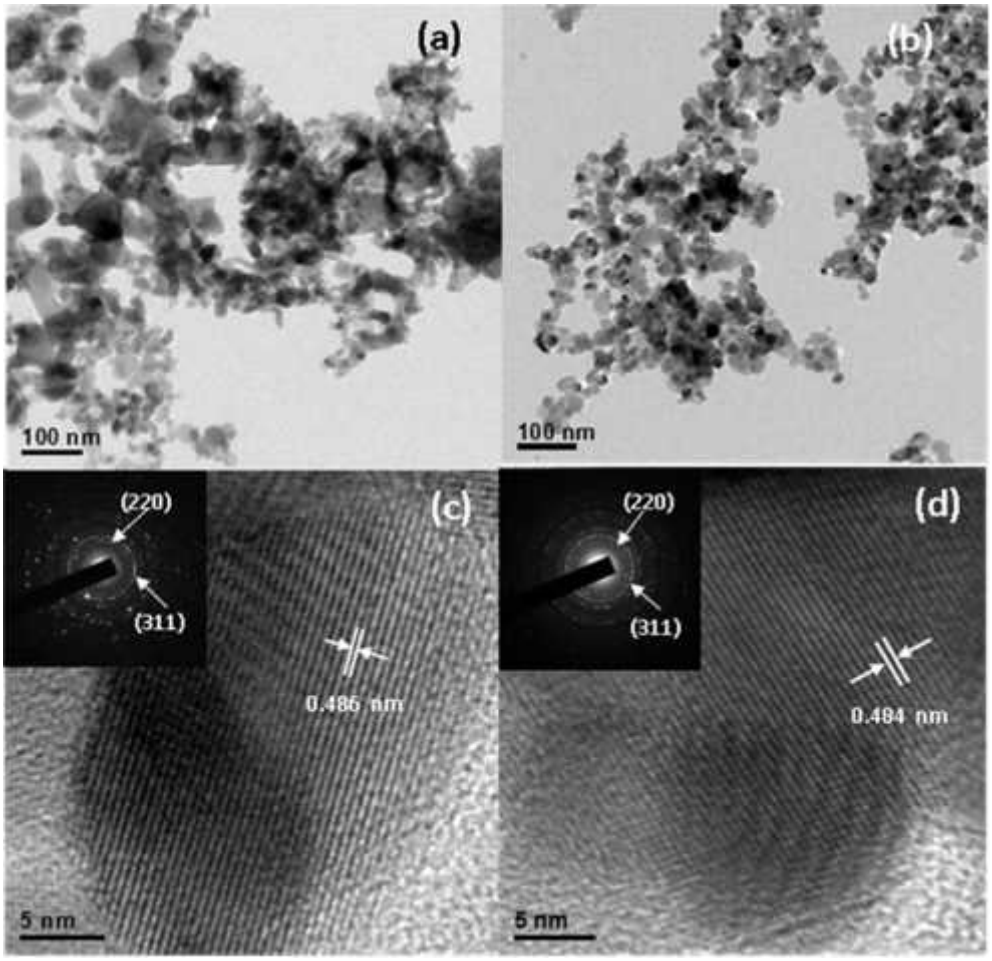

Figure 5.2 (a) and (b) TEM photographs of $NiFe_2O_4$ and $ZnFe_2O_4$ showing agglomerates of nanoparticles. Scale bar is 100 nm. (c) and (d) HRTEM lattice images of nano-phase $NiFe_2O_4$ and $ZnFe_2O_4$. Scale bar is 5 nm. Inset in (c) and (d) show the SAED patterns and selected Miller indices.

The particle morphology was examined by TEM. Figure 5.2(a) and (b) show that the $NiFe_2O_4$ and $ZnFe_2O_4$ powder consists of nanoparticles of size approximately 45 and 25 nm respectively. Figure 5.2(c) and (d) show the HRTEM lattice images of $NiFe_2O_4$ and $ZnFe_2O_4$. They show clearly the lattice fringes and the measured inter-planar spacings match well with the d-value corresponding to

the (111) plane of the XRD patterns of the compounds. Inset in Figure 5.2(d) shows the SAED (selected area electron diffraction) pattern consisting of diffuse rings and bright spots with (220) and (311) planes, indicating nano-phase nature. The particle size of $NiFe_2O_4$ is found to be slightly larger than that of the other compositions due to the high energy barriers for the formations of $NiFe_2O_4$ as compared to that of $ZnFe_2O_4$ [20]. The crystallite sizes of $(Ni_{1-x}Zn_x)Fe_2O_4$ are calculated by the Scherrer's equation from the Rietveld refined data and given in Table 5-1, compare very well with the particle size derived from the TEM data on x=0 and 1.

The values also compare well with the data reported by Hankare *et al*. [20] The BET surface area of the phases was found to be in the range of 32 to 21 $m^2 g^{-1}$ for various values of *x* (Table 5-1). These are typical of mixed oxides prepared at 700 °C. The elemental analysis of $(Ni_{1-x}Zn_x)Fe_2O_4$ phases was carried out and the obtained experimental wt. % of Zn and Ni for various compositions are given in Table 5-1. As can be seen, the values match fairly well with the calculated values.

$NiFe_2O_4$ nanofibres

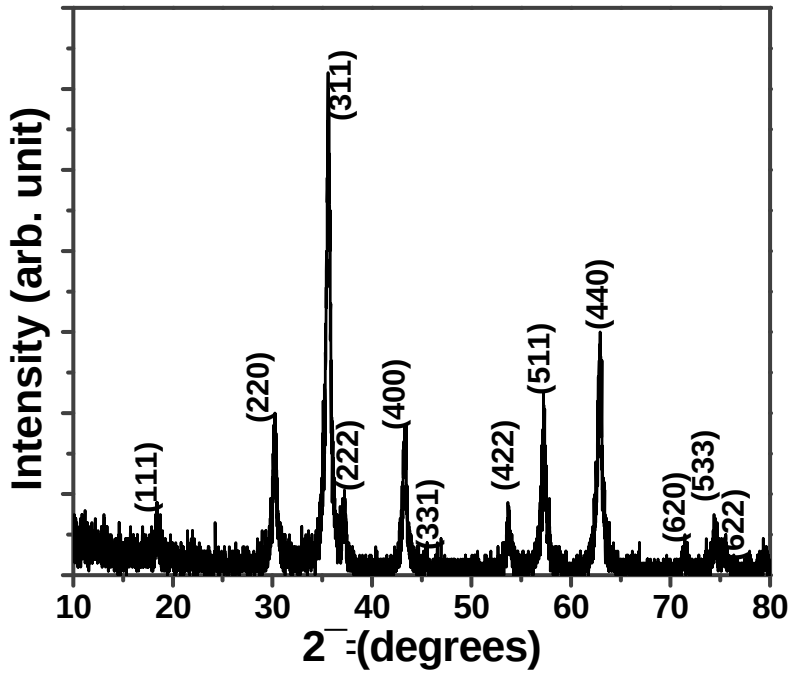

Figure 5.3 X-ray diffraction (XRD, Cu Kα radiation) pattern of $NiFe_2O_4$ nanofibers. Miller indices of $NiFe_2O_4$ are shown.

The powder XRD pattern of elctrospun polymer precursor fibres calcined at 500°C are shown in Figure 5.3 and it revealed the formation of cubic inverse spinel structure. The lattice parameter value, a (Å) = 8.342, is obtained by the Rietveld refinement and are in agreement with reported values of $NiFe_2O_4$ (JCPDS No. 74-2081). The crystallite size of the samples calcined at 500°C, 600°C and 800°C, calculated by the Scherrer's equation from the Rietveld refined data, are 12 nm, 21 nm and 29 nm, respectively.

The TEM images of the elctrospun polymer precursor fibres calcined at 500°C are displayed in Figure 5.4(c) and (d). After calcination at 500°C, the fibres remain intact and have an average diameter of 200 nm. A small portion of $NiFe_2O_4$ nanofibres is enlarged and shown in Figure 5.4(e). Scattered dark regions surrounded by bright areas can be noticed and hence the continuous nanofibers are

composed of interconnected nanoparticles of size 10-20 nm. The SAED (selected area electron diffraction) pattern displayed in Figure 5.4(f) consists of diffuse rings clearly indicating the nano-phase nature of the $NiFe_2O_4$ nanofibers. The d-values calculated from the concentric rings matches well with that of (220), (311), (400) and(440) $NiFe_2O_4$ planes

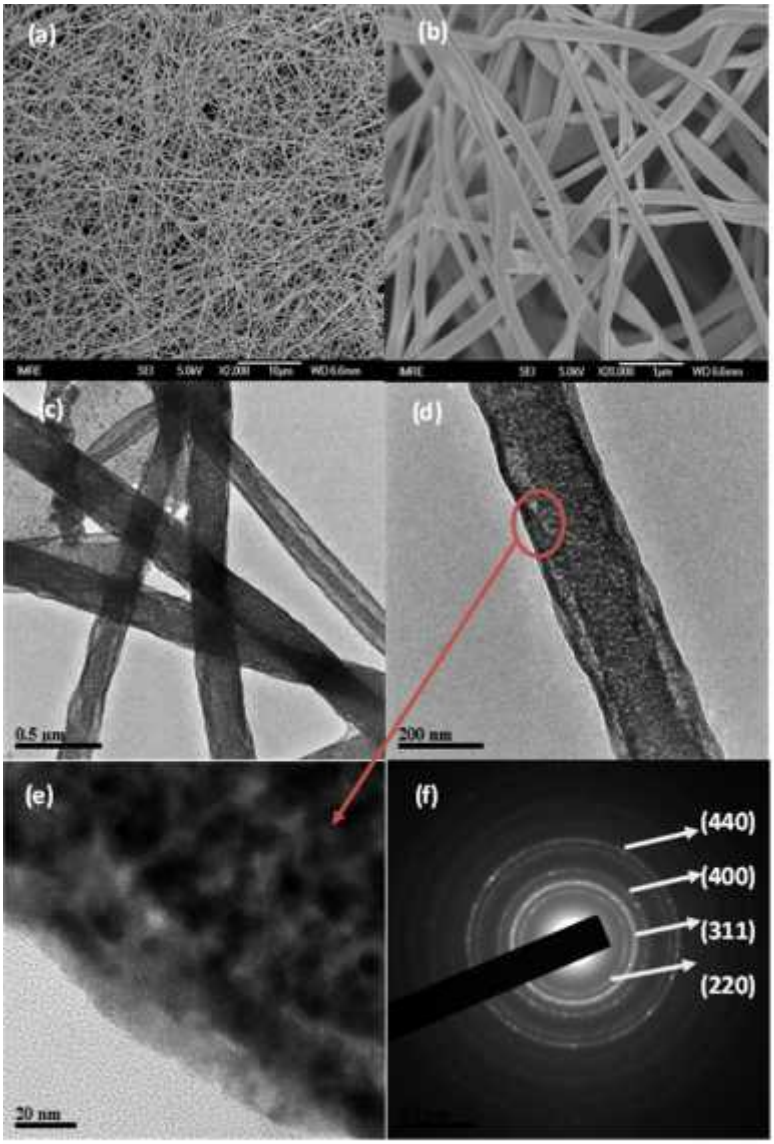

Figure 5.4 (a) SEM image of $NiFe_2O_4$ nanofibres. Scale bar is 10 μm. (b) SEM image of $NiFe_2O_4$ nanofibres. Scale bar is 1 μm. (c) TEM image of $NiFe_2O_4$ nanofibres. Scale bar is 500 nm. (d) TEM photograph of $NiFe_2O_4$ nanofibres. Scale bar is 200 nm. (e) Magnified image of an edge of the nanofibre. Scale bar is 20 nm. (f) SAED pattern of $NiFe_2O_4$ nanofibres. Miller indices are shown.

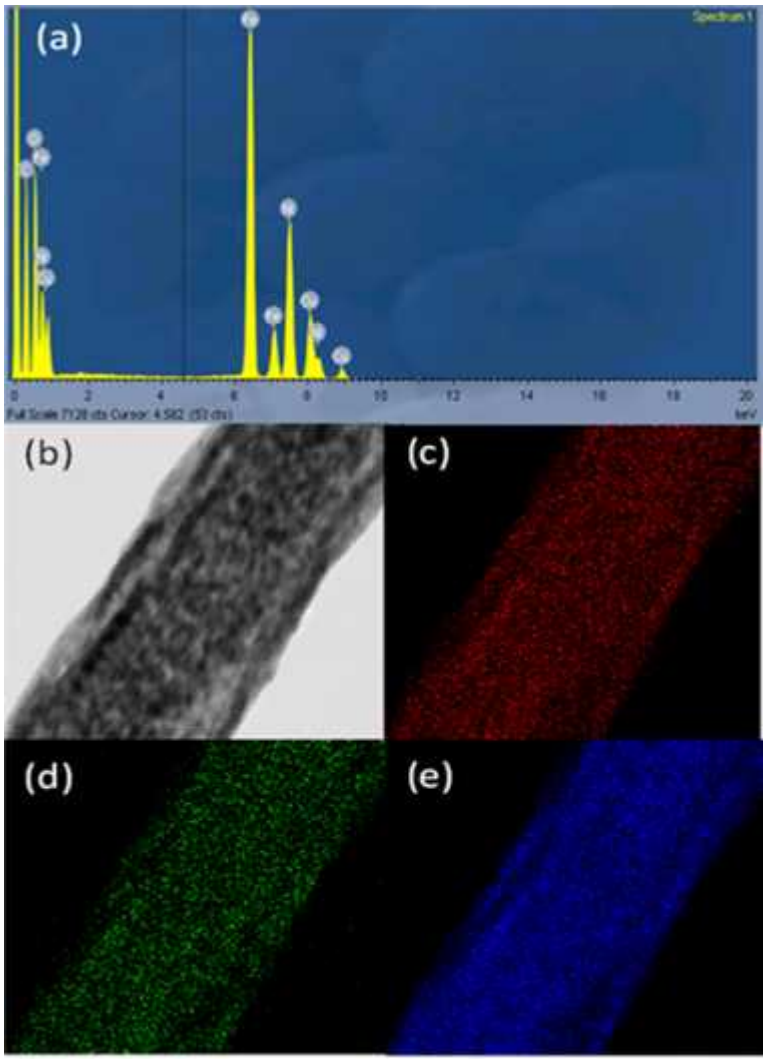

Figure 5.5 (a) Energy-dispersive X-ray (EDX) spectrum of $NiFe_2O_4$ nanofibre. (b) SEM image of the portion selected for EDX analysis. (c) to (e) EDX maps of Nickel (red), iron (green) and oxygen (blue), respectively.

Energy dispersive X-ray (EDX) spectrum in Figure 5.5(a) confirms the presence of Ni, Fe and O in stoichiometric quantities. EDX elemental mapping has also been used to evaluate the uniformity of distribution of nickel, iron and oxygen elements along the nanofibres. As shown in Figure 5.5(c), (d) and (e), these three elements are distributed homogeneously in the specific portion (Figure 5.5(b)) of the sample selected for the mapping studies.

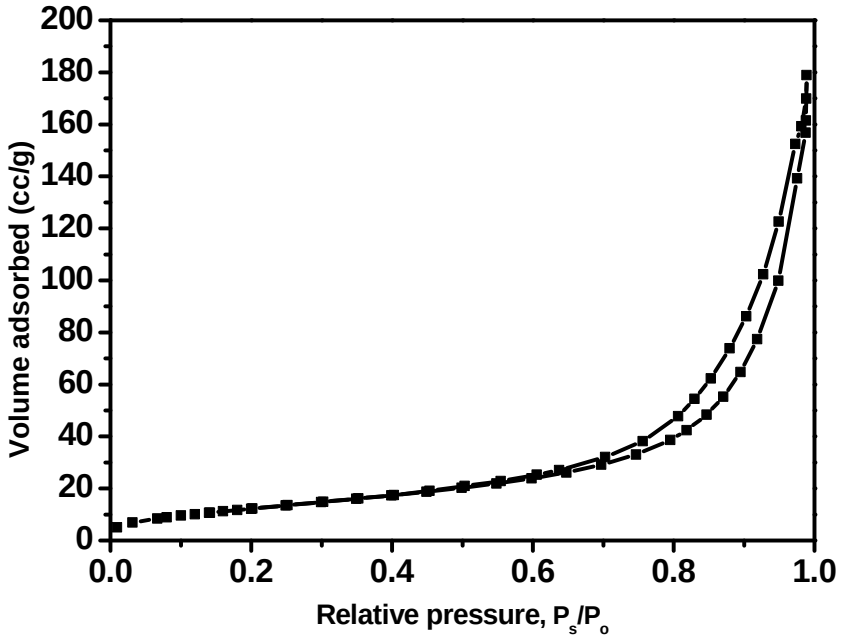

Figure 5.6 Nitrogen adsorption-desorption isotherm for $NiFe_2O_4$ nanofiber.

The nitrogen adsorption and desorption isotherms of the $NiFe_2O_4$ nanofibres are shown in Figure 5.6, using which the BET surface area value is calculated as 47 m^2 g^{-1}. $NiFe_2O_4$ nanofibers exhibit a type IV nitrogen isotherm which proceeds via multilayer adsorption followed by capillary condensation. [23] It is a typical adsorption/desorption isotherm of porous solids. Capillary condensation and evaporation do not take place at the same pressure, thus leading to the formation of a hysteresis loop in the range of 0.6–1.0 P/P_o. [23] Figure 5.7(a) and (b) show the low and high magnification SEM images of electrospun polymer precursor heated to 600°C whereas Figure 5.7(c) and (d) demonstrate the SEM images of electrospun polymer precursor calcined at 800°C. Thus Figure 5.7 reveals the formation of interconnected $NiFe_2O_4$ nanoparticles upon calcination at 600°C or 800°C.

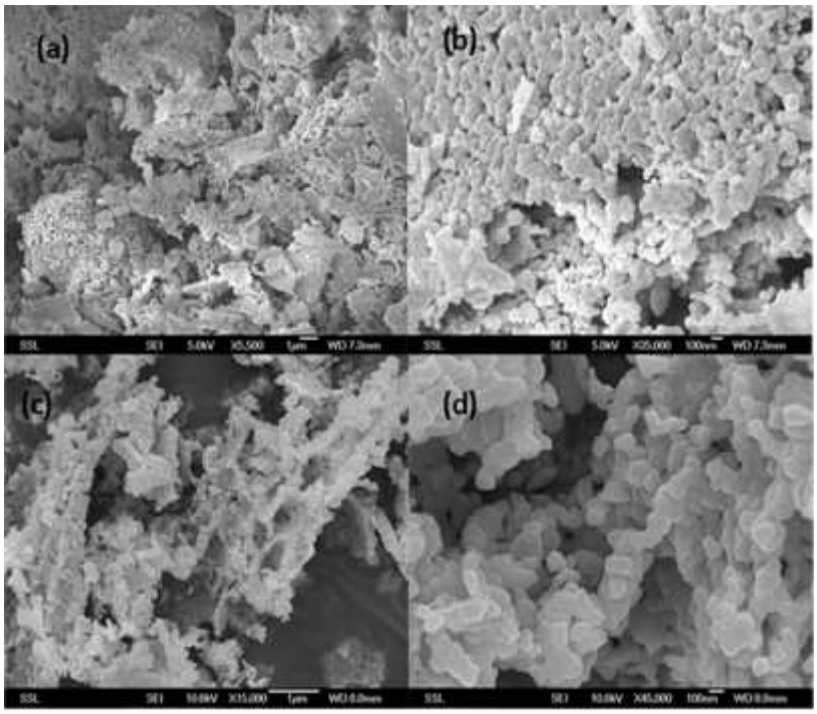

Figure 5.7(a) SEM image of $NiFe_2O_4$ nanoparticles after calcination at 600°C. Scale bar is 1 μm. (b) SEM image of $NiFe_2O_4$ nanoparticles after calcination at 600°C. Scale bar is 100 nm. (c) SEM image of $NiFe_2O_4$ nanoparticles after calcination at 800°C. Scale bar is 1 μm. (d) SEM image of $NiFe_2O_4$ nanoparticles after calcination at 800°C. Scale bar is 100 nm.

5.3.2 Galvanostatic Li-cycling properties

5.3.2.1 $(Ni_{1-x}Zn_x)Fe_2O_4$ nanoparticles

The electrochemical Li-storage and cycleability of all the compositions $(Ni_{1-x}Zn_x)Fe_2O_4$ were investigated by galvanostatic cycling in the voltage window, 0.005- 3.0 V *vs*. Li at a current of 50 mA g^{-1} up to 50 cycles. Voltage *vs*. capacity profiles of the selected cycles are shown in Figure 5.8. For the compositions, x= 0 and 0.2 (Figure 5.8(a), (b)), the first discharge curve starts from the open circuit voltage (OCV ~ 2.5-3 V) and shows a continuous decrease, to reach a voltage plateau region at 0.8 V. For x=0, up to the voltage plateau, a capacity of ~190 mAh g^{-1} (~1.7 moles of Li) is obtained due to the single phase Li-intercalation reaction to give $Li_{\sim 2}NiFe_2O_4$ (Figure 5.8(a)). Using butyl- Li, Chen *et al*. [9] have shown that $NiFe_2O_4$ spinel can incorporate up to 2 moles of Li without any change in

crystal structure. However, they reported that only 0.5 Li can be chemically intercalated in to $ZnFe_2O_4$. For the compositions with higher Zn content, x= 0.4, 0.6, 0.8, 1, two vivid voltage plateaus are present in addition to the one at 0.8 V, which shows that Li-intercalation takes place as a two-phase reaction ((c)-(f)). Two Li-insertion plateaus, one between 0.8 and 1 V and another between 1.3 and 1.5 V, can be clearly seen for $x \geq 0.6$. It is clear from the Figure 5.8(c) to (f) that before the onset of voltage plateau near 0.8 V, a capacity of 310-320 mAh g^{-1} is obtained which corresponds to insertion of ~ 3.5 moles of Li. Guo *et al.* [3] observed a similar behavior in hollow spheres of nano-$ZnFe_2O_4$ in which two vivid voltage plateaus were seen before 0.8 V when the electrode was first discharged to 0.005 V.

Based on XRD studies, the phase composition of the material is recognized to be modified from pristine spinel $ZnFe_2O_4$ to cubic $Li_{0.5}ZnFe_2O_4$ with a = 8.455 Å and space group, Fd3m (between OCV and 1.1 V) and then to simple cubic-$Li_2ZnFe_2O_4$ with a = 8.463 Å and space group, Fd3m(between 1.1 V and 0.8 V) [3, 24]. This behavior is exactly seen in pure $ZnFe_2O_4$ nanoparticles (x= 1) which is shown in Figure 5.8(f), and reperesented by eqns. 1 and 2 [3, 4, 24]. Guo *et al.*[3] and Ding *et al.*[24] have shown that eqns 5.1 and 5.2 are reversible when cycling is carried out in the range, 1-4.5 V or 0.8- 4.5 V vs. Li. However, in the present case, these reactions are not reversible since cycling is carried out in the range 0.005 – 3.0 V. Further reaction of Li with the intercalated phase, $Li_x(Ni_{1-x}Zn_x)Fe_2O_4$ leads to crystal structure destruction and reduction of metal ions followed by the formation of metal nanoparticles embedded in an amorphous matrix of Li_2O and is represented by the large voltage plateau at ~0.8 V (Figure 5.8 and eqn. 5.3).

$ZnFe_2O_4 + 0.5Li^+ + 0.5e^- \longrightarrow Li_{0.5}ZnFe_2O_4$ (e= electron) eqn. 5.1

$Li_{0.5}ZnFe_2O_4 + 1.5Li^+ + 1.5e^- \longrightarrow Li_2ZnFe_2O_4$ eqn. 5.2

$Li_2ZnFe_2O_4 + 6Li^+ + 6e^- \longrightarrow 4Li_2O + Zn + 2Fe$ eqn. 5.3

$Zn + Li^+ + e^- \leftrightarrow Li–Zn$ eqn. 5.4

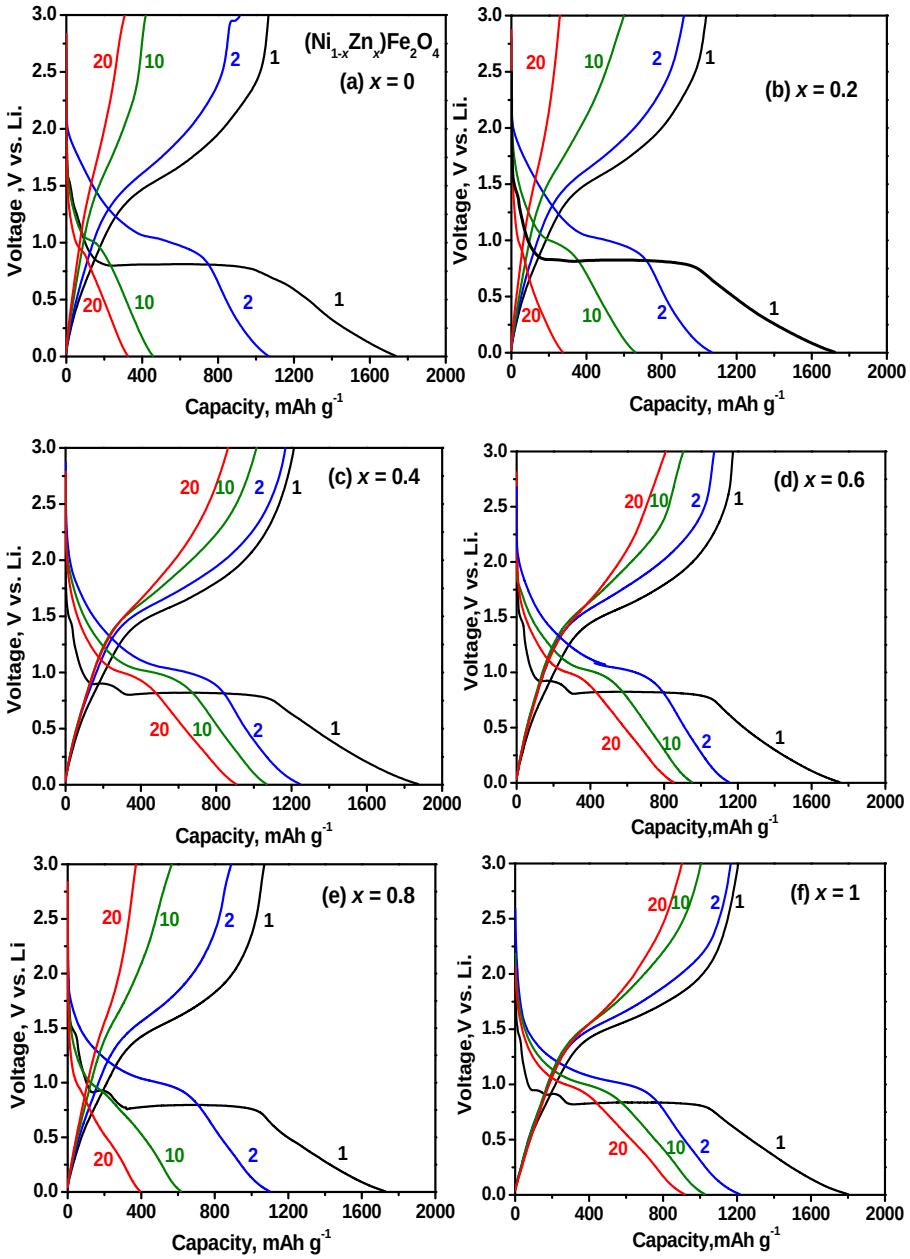

Figure 5.8 Voltage vs. capacity profiles of $(Ni_{1-x}Zn_x)Fe_2O_4$. (a) x= 0 (b) x= 0.2 (c) x= 0.4 (d) x= 0.6 (e) x= 0.8 (f) x= 1.0. Numbers refer to cycle number. Voltage range: 0.005- 3 V vs. Li; current: 50 mA g^{-1}.

For the compositions containing Zn, beyond the voltage plateau region, Zn nanoparticles react with Li to form Li-Zn alloy increasing the Li-storage capacity, as per the eqn. 4. Guo *et al*. [3] confirmed the existence on Li-Zn alloy and Fe in the 0.005 V- discharged $ZnFe_2O_4$ from the analysis of SAED pattern and TEM studies of discharged electrodes. Wang *et al*.[25] reported that Li begins to insert in to metallic zinc at ~0.26 V and the LiZn alloy was formed at 0.16 V *vs*. Li at room temperature. According to Wang *et al*. [26], during electrochemical reaction of Li with ZnO, Li-Zn alloy formation occurs at 0.35 V and multistep de-alloying process of Li-Zn alloy occurs in the range, 0.1 to 0.8 V. Since the weight % of Zn in $ZnFe_2O_4$ is only 27 %, the Li-Zn alloy formation is not clearly visible in the galvanostatic cycling profiles or in cyclic voltammetry of $ZnFe_2O_4$. However, the additional capacity due to alloying of Zn is clearly seen in the first discharge and second discharge capacities of $Ni_{1-x}Zn_xFe_2O_4$ for x=0 and x=1 given in Table 5-2.

Thus while $NiFe_2O_4$ shows a second discharge capacity of 1068 (±10) mAh g^{-1}, the value for $ZnFe_2O_4$ is 1215 (±10) mAh g^{-1}. In the charging process (Li- extraction), the initial spinel ferrite phase is not recovered but simpler oxides are formed after the de-alloying reaction of eqn.4, as per the conversion reactions shown in eqns. 5.5, 5.6 and 5.8 [3, 4, 24].

$Zn + Li_2O \leftrightarrow ZnO + 2Li^+ + 2e^-$ (Theor. Capa.= 658 mAh g^{-1}) eqn. 5.5

$2Fe + 3Li_2O \leftrightarrow Fe_2O_3 + 6Li^+ + 6e^-$ (Theor. Capa.= 1006 mAh g^{-1}) eqn. 5.6

Upon deep discharge to 0.005 V, the Li-intercalated phase, $Li_{\sim 2}NiFe_2O_4$ undergo crystal structure destruction and form metal nanoparticles as per eqn. 5.7. The electrochemically formed Ni and Fe nanoparticles are converted to respective oxides during charging and is a reversible process as shown in eqns. 5.6 and 5.8.

$Li_{\sim 2}NiFe_2O_4 + 6Li^+ + 6e^- \longrightarrow Ni + 2Fe + 4Li_2O$ eqn. 5.7

$Ni + Li_2O \leftrightarrow NiO + 2Li^+ + 2e^-$ (Theor. Capa.= 718 mAh g^{-1}) eqn. 5.8

Discharge capacity (±10) mAh g^{-1}						
x ($Ni_{1-x}Zn_xFe_2O_4$)	1st cycle	2nd cycle	10th cycle	30th cycle	50th cycle	Capacity-fading (10-50 cycles, %)
0	1735	1068	457	275	200	56
0.2	1722	1065	660	275	220	67
0.4	1875	1244	1069	715	432	60
0.6	1755	1155	947	775	570	40
0.8	1730	1110	615	340	294	52
1	1805	1215	1024	880	835	18

Table 5-2 Discharge capacities at selected cycles for different compositions of $(Ni_{1-x}Zn_x)Fe_2O_4$. Voltage range: 0.005- 3V; Current: 50 mA g^{-1}.

Figure 5.9 illustrates the capacity *vs.* cycle number plots extracted from galvanostatic cycling data. The first, second, tenth, thirtieth and fiftieth discharge capacity values of all compositions, $(Ni_{1-x}Zn_x)Fe_2O_4$ along with % capacity-fading are given in the Table 5-2. It is clear that capacity stability is enhanced with an increase in the Zn-content. The first discharge capacity values vary with *x* (Zn-content) and are in the range of 1720-1875 (±10) mAh g^{-1}. As mentioned earlier, the theoretical reversible capacity of $NiFe_2O_4$ and $ZnFe_2O_4$ and their solid solutions are in the range, 914 (*x*=0) – 1000 (*x*=1) mAh g^{-1}. In the present study, the observed excess capacity can be explained as due to formation of SEI (solid

electrolyte interphase) and an organic polymeric layer on the metal nanoparticles when the electrode potential decreases and approaches 0.005 V. For x= 0 and x= 0.2, the reversible capacity fades rapidly up to 30 cycles and thereafter reaches 200 and 220 mAh g^{-1}, respectively after 50 cycles. The behavior of $NiFe_2O_4$ is consistent with the many reports in the literature. [5, 10, 11] An enhancement in the capacity values with increasing Zn concentration is observed for x= 0.4 and 0.6. However, capacity-fading is observed for all compositions, the values ranging from 40 to 67 % for x =0.2 to 0.8 between 10-50 cycles (Table 5-2 and Figure 5.9).

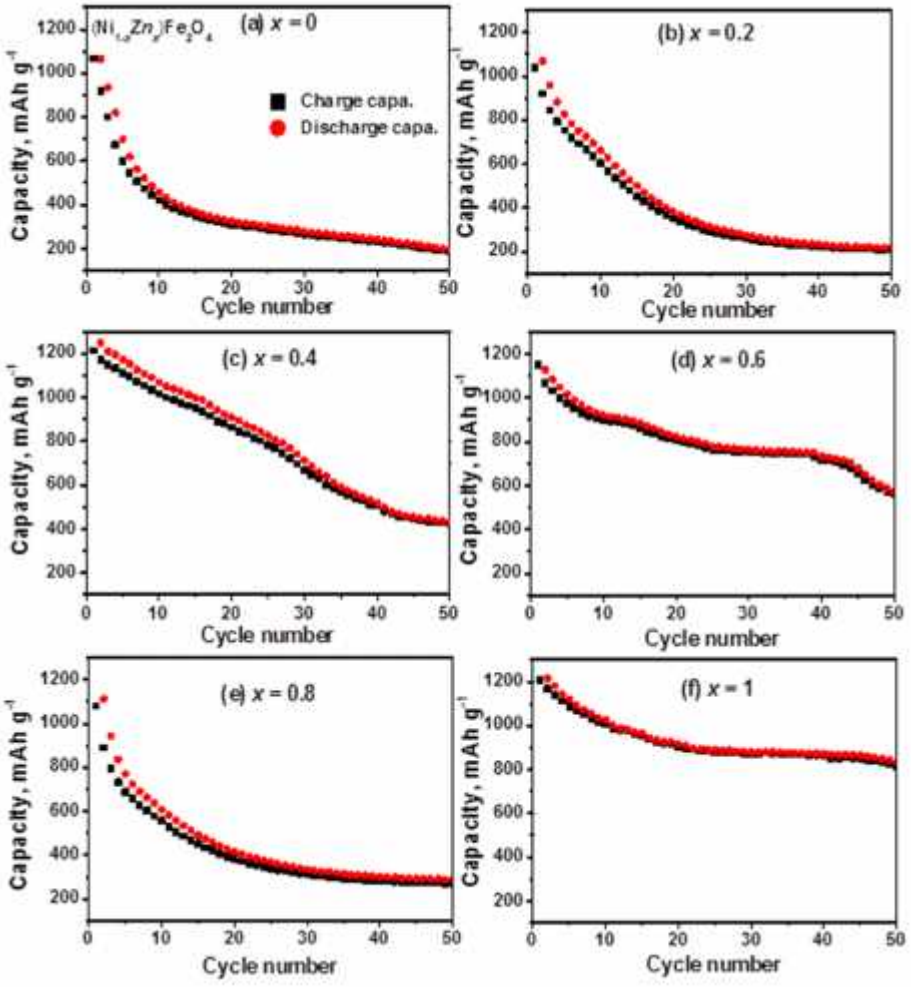

Figure 5.9 Capacity *vs*. cycle number plots for $(Ni_{1-x}Zn_x)\ Fe_2O_4$. (a) x=0 (b) x=0.2 (c) x=0.4 (d) x=0.6 (e) x=0.8 (f) x=1.0. Voltage range: 0.005- 3 V *vs*. Li; current: 50 mA g^{-1}. First discharge capacity values are not shown.

The phase with x =0.8 $(Ni_{0.2}Zn_{0.8})Fe_2O_4$ shows a trend in the capacity fading similar to that of x =0 and 0.2, even though it is expected to perform analogous to the phases with x= 0.6 and 1 (Figure 5.9).We repeated the synthesis and Li-cycling experiments on this phase (x= 0.8) and the results are reproducible within 5- 10 % with regard to the capacity values and their variations with the cycle number. The reason for this peculiar behavior is not known at present.

$ZnFe_2O_4$ (*x* =1) performs very well in comparison to the other compositions with varying *x* and the general trend of the discharge capacity with cycle number, up to 50 cycles (Figure 5.9 and Table 5-2), is in good agreement with the literature data[3, 4, 24]. The second discharge capacity of 1215 mAh g^{-1} gradually decreases to 900 mAh g^{-1} after 20 cycles and to 835 mAh g^{-1} after 50 cycles (83 % of theoretical capacity). The capacity fading between 10- 50 cycles is 18 %. For comparison, Guo *et al.*[3] observed a reversible capacity of 800-850 mAh g^{-1} between 2-50 cycles when the hollow spherical $ZnFe_2O_4$ is cycled in the range 0.005- 3 V at a current of 65 mA g^{-1}. Ding *et al.*[24] observed a second discharge capacity of 970 mAh g^{-1} which gradually degraded to 834 mAh g^{-1} after 50 cycles (14 % capacity fading) when the nano-structured $ZnFe_2O_4$ was cycled between 0.01 – 3 V at a current of 116 mA g^{-1}.

5.3.2.2 $NiFe_2O_4$ nanofibres

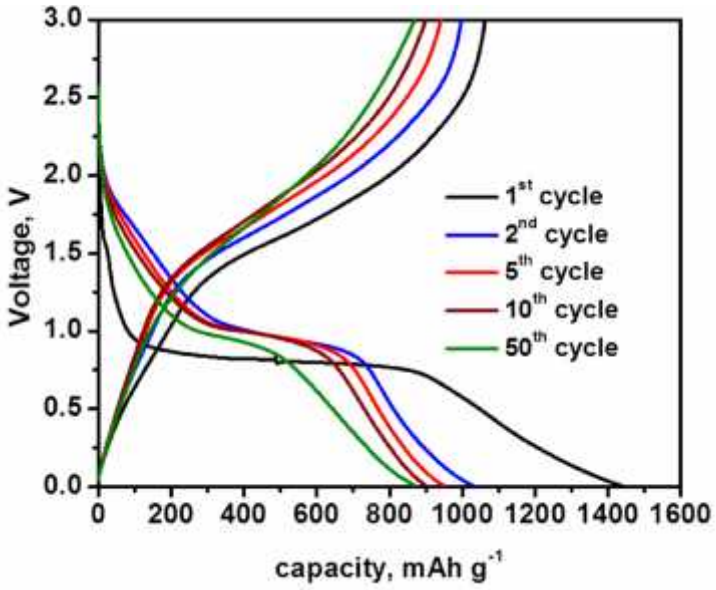

Figure 5.10 Galvanostatic charge-discharge profiles of $NiFe_2O_4$ nanofibres. Voltage range: 0.005- 3 V vs. Li, current: 100 mA g^{-1}.

Figure 5.10 shows the galvanostatic charge-discharge curves of selected cycles of $NiFe_2O_4$ nanofibre composite electrodes, cycled in the range of 0.005- 3.0 V at a current rate of 100 mA g^{-1}. 1 Li per formula weight corresponds to a capacity of 114 mAh g^{-1}. The first discharge capacity is around 1450 mAh g^{-1} due to an uptake of 12.7 moles of Li. From eqn. 5.1, during first discharge nickel ferrite can react only with 8 moles of Li, electrochemically forming Ni and Fe nanoparticles embedded in Li_2O matrix. The observed excess capacity can be explained as due to formation of SEI (solid electrolyte interphase) and an organic polymeric layer on the metal nanoparticles when the electrode potential decreases and approaches 0.005 V [19]. First charge capacity of 1000 mAh g^{-1} is obtained which is equivalent to 8.8 moles of Li. Theoretical reversible capacity of $NiFe_2O_4$, as indicated in eqn.(2) & (3), is 915 mAh g^{-1} which corresponds to reversible uptake and removal of 8 moles of Li. The average discharge-charge potentials are around 1 V and 1.5 V. This can lead to a low output voltage when combined with

conventional cathode materials. Figure 5.11 shows the capacity and coulombic efficiency vs. cycle number plot extracted from galvanostatic cycling data. Capacity fading is observed during initial 15 cycles and then stabilized at a capacity of 870 mAh g^{-1} for 40 cycles. Tirado's group also found such a capacity fading in $NiFe_2O_4$ for first 20 cycles irrespective of the preparation conditions and thereafter the capacity stabilizes or continues to fade depending on the temperature and/or method of synthesis. [27] This initial capacity loss can be considered as due to the 'formation' or 'conditioning' of the electrode during initial cycles. [4, 19] An electrochemical grinding effect produced during cycling may disaggregate the Li_2O/Ni-Fe agglomerations and provoke capacity fading observed during the first few cycles.

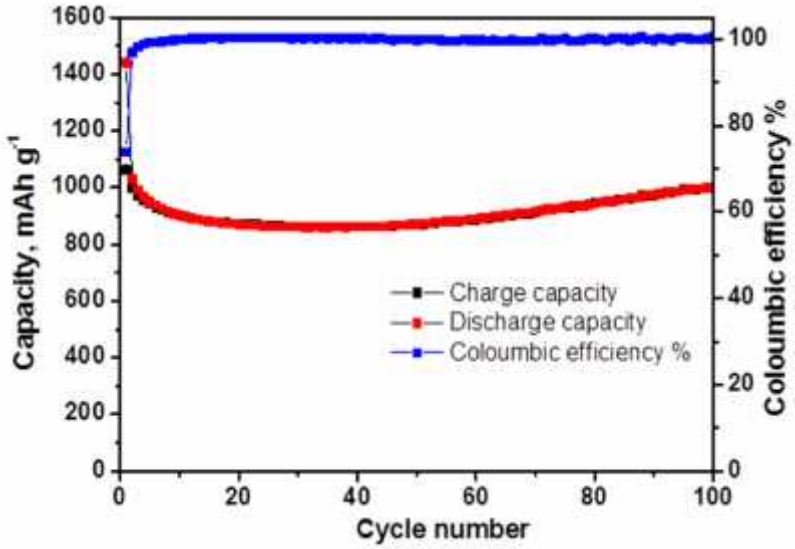

Figure 5.11 Capacity, Coloumbic efficiency vs. cycle number plot of $NiFe_2O_4$ nanofibres. Voltage range: 0.005- 3 V vs. Li.

For the electrospun $NiFe_2O_4$ nanofibres, 100 % capacity retention is observed between 20-40 cycles and then an increase in capacity with 15 % rise between 40-100 cycles. This sort of increasing tendency of capacity during the galvanostatic cycling is previously observed in several other transition metal oxide systems such

as Fe_3O_4, Zn_2MnO_4 and can be attributed to the reversible growth of a polymeric gel-like film resulting from kinetically activated electrolyte degradation. [28-30] The charge capacity after 100th cycle is 1000 mAh g^{-1} which is more or less equal to first charge capacity value.

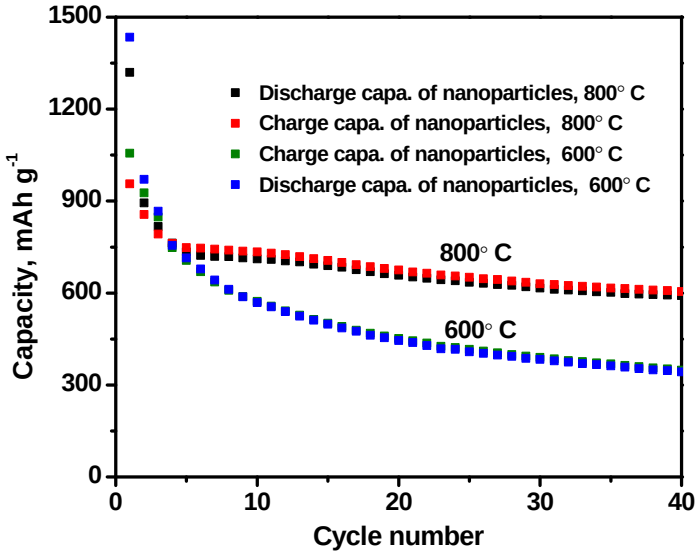

Figure 5.12 Capacity vs. cycle number plot of $NiFe_2O_4$ nanoparticles. Voltage range: 0.005- 3 V vs. Li.

The initial coulombic efficiency is around 80 % and increases to 100 % after 8 cycles. The 100 % coulombic efficiency is obtained until the 100th cycle and it is due to the stabilization of interface layer (SEI) between the electrode and electrolyte. As detailed in the experimental part, interconnected $NiFe_2O_4$ nanoparticles are obtained, upon the heat treatment of electrospun precursor at 600°C and 800°C for 5 h. For comparison, the Li-cycling performances of $NiFe_2O_4$ nanoparticles when cycled in the voltage range 0.005- 3.0 V at a current rate of 100 mA g^{-1}, are shown in Figure 5.12. The nanoparticles formed at 600°C delivers almost same first discharge capacity as that of the nanofibres. However, the capacity fades rapidly to 345 mAh g^{-1} at the end of 40th cycle. It was reported by Tirado *et al.*[10] that among $NiFe_2O_4$ phases that had been prepared by sol-gel

method, those annealed at high temperature (800-1000°C) showed better capacity retention, namely 550 mAh g^{-1} was observed after 50 cycles. In the present case also, the precursor heated to 800°C, showed an improved capacity of 600 mAh g^{-1} after 40 cycles in comparison with that heat treated at 600°C.

Undoubtedly, one of the reasons for the superior electrochemical performance of the $NiFe_2O_4$ nanofibres is its porous nature and eventual high surface area which are marked from the N_2 adsorption-desorption studies. High surface area allows large area of the active material to be accessible to electrolyte while porosity provides empty/vacant spaces to accommodate volume change during conversion reaction. [31, 32]

5.3.3 Electrochemical impedance studies on $NiFe_2O_4$ nanofibres

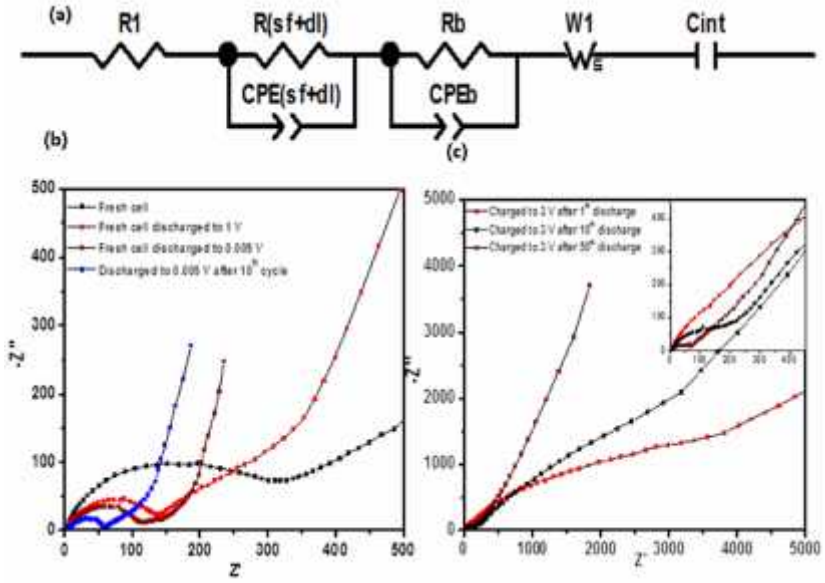

Figure 5.13 (a) The equivalent electrical circuit consisting of resistances (R_i), constant phase elements (CPEs), Warburg impedance (W_s) and intercalation capacitance (C_{int}).(b) Nyquist plots (Z' vs. −Z") of $NiFe_2O_4$ nanofibers at open circuit voltage and discharged-state (0.005V vs. Li) at various discharge–charge cycles. (c) Nyquist plots (Z' vs. −Z") of $NiFe_2O_4$ nanofibers in the charged-state (0.005 V vs. Li) at various discharge–charge cycles. Inset shows low high frequency region in expanded scale.

Electrochemical impedance studies were carried out on $NiFe_2O_4$ nanofibres at room temperature at selected voltages in the range of 0.005–3.0V vs. Li, at the current rate of 50 mA g^{-1} (0.05 C). The cells were discharged or charged to the selected voltage values, relaxed for 3 h at that voltage and the impedance spectra were measured. The EIS spectra in the frequency range 10^6~10^{-3} Hz are interpreted in terms of the following physical phenomena in an order of decreasing frequency: (i) a high frequency semicircle because of the presence of a surface layer; (ii) a medium frequency semicircle associated with charge transfer and (iii) the very low frequency (<1 Hz) incline line attributed to the solid state diffusion. The impedance data are analyzed by fitting to an equivalent electrical circuit shown in Figure 5.13(a), similar to the circuits reported in the literature. R_e (R1) denotes electrolyte resistance. R_{sf} and C_{sf} are resistance and capacitance of the solid-state interface layer formed on the surface of the electrodes, which correspond to the semicircle at high frequencies. R_{dl} and C_{dl} are faradic charge-transfer resistance and its relative double-layer capacitance, which correspond to the semicircle at medium frequencies. R_{sf} and R_{dl} can be together called charge transfer resistance (R_{ct}). Parameter values obtained after fitting is given in Table 5-3.

The contribution to R_b comes not only from the bulk resistance of the cell which reflects electric conductivity of the separator and electrodes, but also from the electrolyte trapped in the pores of the composite electrode and that due to the inhomogeneous coating of active material on the current collector. [33, 34] W is the Warburg impedance related to a combination of the diffusional effects of lithium ion on the interface between the active material particles and electrolyte, which is generally indicated by a straight sloping line at low frequency end. The

combination of R_{ct} and W is called faradic impedance, which reflects kinetics of the cell reactions. Low R_{ct} generally corresponds to a fast kinetics of the faradic reaction. Figure 5.13(b) shows the Nyquist plots (Z' vs. -Z") of the fresh cell at open circuit voltage (OCV), fresh cell discharge to 1 V, cell discharged to 0.005 V after 1st and 10th discharge step. Only one semicircle is seen in the high-to-medium-frequency range indicating that effects due to surface film and charge transfer are not separable. In this case, the curve fitting is carried out using $R_{(sf+dl)}$ combination since electronic and ionic charge transfer are involved in the discharge process. The fresh cell (OCV ~2.8 V) shows a broad depressed semicircle in the high/ intermediate frequency region (> 20 Hz), which reveals, after curve fitting, an impedance of 250 (± 3) Ω, attributed mainly to R_{sf}. The R_{sf} value is the measure of the hindrance for Li-ion conduction through the SEI layer. The associated capacitance (C_{dl}) is 20 (± 5) μF. According to Chamas *et al*. [35], in the pristine state, where the charge transfer is difficult, the impedance spectra evolve by a high frequency semicircle which is associated with a native SEI film at the electrode, followed by a low frequency line related to the mass transport and/or to the cell capacitance. The spectrum measured after discharge to 1 V and 0.005 V differs markedly from the initial one recorded at the OCV (Figure 5.13(b)). The spectrum at the end of first discharge to 1 V shows high frequency depressed semicircle with reduced diameter followed by a well-defined Warburg region(α=40-45°) and an intercalation capacitance region (α'=60-65°)at low frequencies. This indicates the contribution is only from R_{sf+ct} and bulk resistance R_b is negligible small.

At 0.005 V, apart from the high frequency semicircle the spectrum shows an undeveloped semicircle before the Warburg region which is almost a straight

line parallel to x-axis and it is an indication of contribution from the bulk resistance of the composite electrode (R_b) to the overall impedance. This can be due to the crystal structure destruction happening below 1 V. Accordingly, the R_b and CPE_b components in the circuit (Figure 5.13(a)) were used to fit the spectrum. Interestingly, at the end of deep discharge after 10 cycles, R_{sf+dl} value decreases considerably to 55 Ω. Thus from Figure 5.13(b), it can be concluded that during initial cycles, R_{sf+ct} values are high due to the initiation of the displacement redox reaction of Li with $NiFe_2O_4$ nanofibres. The gradual drop in R_{sf} values is indicative of the stabilization of SEI layers and this supports the stable capacity behavior of $NiFe_2O_4$ nanofibres after a few initial cycles. R_{ct} and R_b values increase during initial cycles which are in good agreement with capacity fading behavior noticed in initial ten cycles. During the initial cycles, the material undergoes large unit cell volume change due to electrochemical conversion reaction, producing cracking of the electrode and subsequent reduction in electronic conductive path. There will also be an increase in internal defects and isolated active regions, unreacted with electrolytes which can lead to an increase the charge transfer resistance. Thus by the end of tenth cycle, conditioning of the electrode will be completed and there will be better contact between active materials and electrolyte and therefore R_{sf+ct} will be stabilized thereafter.

Parameter Values	Fresh cell	First discharge to 0.005 V	Charge to 3 V after first discharge	Discharge to 0.005 V after 10^{th} charge	Charge to 3 V after 11^{th} discharge	Charge to 3 V after 50^{th} discharge
R_{sf+dl} (±5) Ω	250	96	3700	55	93	47
CPE_{sf+dl} (±5)μF	20	57	163	77	35	32

Table 5-3 Impedance parameters of $NiFe_2O_4$ at different voltages

Impedance spectra of the cell charged to 3 V after 1st, 10th and 50th discharge step are shown in Figure 5.13(c). For the cell charged to 3 V after 1st discharge, a large depressed semicircle which spans from 1MHz to 0.1 Hz can be clearly seen. It is followed by a Warburg region at frequencies less than 0.1 Hz. The curve fitting is carried out and the calculated resistance value is in the order of 3 KΩ. For the cell charged to 3 V after 10th discharge, two depressed semicircles, one with shorter diameter appears at high frequencies and the other with longer diameter occurs at intermediate frequency. Equivalent circuit fitting of the spectra indicates a decrease in R_{sf+ct} (93 Ω) and increase in R_b during 10th charge. For the 50th cycle, the resistance, R_{sf+ct} value significantly reduces to 47 Ω which is well evident from the small semicircle found in high frequency region > 40 Hz with a negligible charge transfer resistance (Inset of Figure 5.13(c)). The R_{sf+ct} value is almost same as that found in the fully discharged state after 10th cycle. This behavior corroborates very well with the stable capacity behavior shown by the $NiFe_2O_4$ nanofibre electrodes, between 10-50 cycles.

5.3.4 Ex-situ SEM and TEM Studies

The Li-cycling mechanism from the second cycle onwards (after structure destruction after the first-discharge) is through the conversion reaction and Li-alloying-de-alloying of Zn, as per the reversible reactions of eqn. 5.4, 5.5, 5.6 and 5.8. They are proposed based on the work of Guo etal [4], Sharma et al [5] and the group of Tirado. [6,11,12,13] Using HR-TEM and SAED patterns, Guo etal [4] have shown that in $ZnFe_2O_4$, nano-size Fe-metal and Li-Zn alloy particles are formed at the end of first-discharge up to 0.005 V *vs.* Li. Similarly, nano-size Fe_2O_3 and ZnO particles are formed at the end of first-charge up to 3 V. This is preceded by the de- alloying of (Li-Zn) to form Zn-metal (backward reaction of

eqn. 5.4).On the other hand, Sharma et al [5] found nano-size FeO and ZnO particles are formed at the end of first-charge. This discrepancy is possibly due to the sub-micron particle size of $ZnFe_2O_4$ employed by the authors.

5.3.4.1 $(Ni_{1-x}Zn_x)Fe_2O_4$ nanoparticles

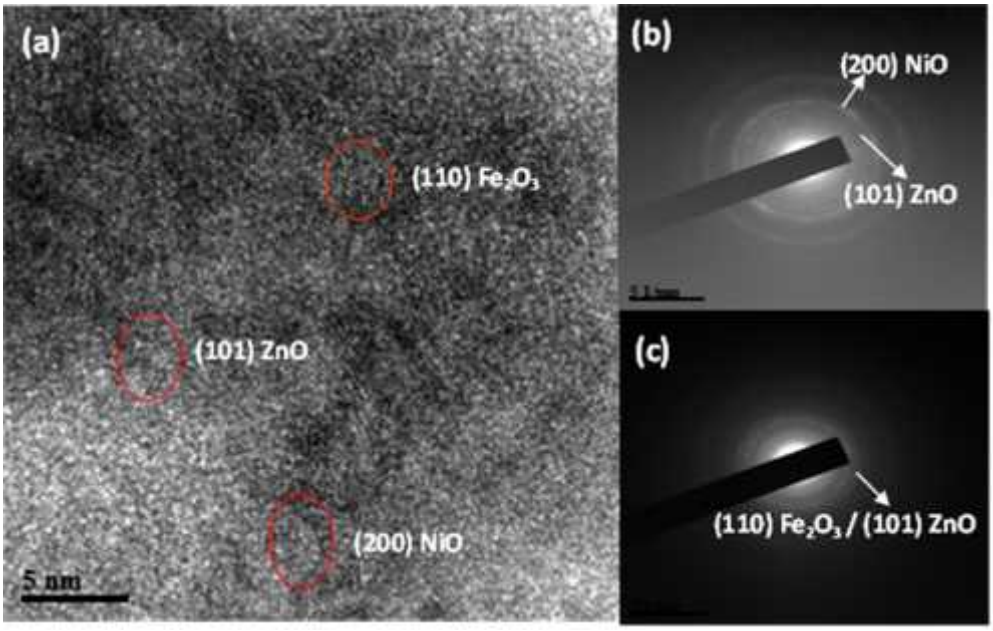

Figure 5.14 TEM photographs of particles of cycled electrodes of $(Ni_{0.4}Zn_{0.6})Fe_2O_4$ (2^{nd} cycle; charged to 3 V) (a) HRTEM lattice image. Circles indicate the metal oxides along with Miller indices. (b) and (c) SAED pattern in different regions. Metal oxides along with Miller indices are indicated.

Presently, ex-situ HR-TEM and SAED studies were carried out on the nano-phase, $(Ni_{0.4}Zn_{0.6})Fe_2O_4$ (x=0.6) of the charged electrode after 2 cycles to identify the oxide phases. The HRTEM lattice image (Figure 5.14(a)) clearly shows the nanocrystalline regions dispersed in Li_2O matrix. As expected, the presence of ZnO, NiO and Fe_2O_3 is clearly evident from the HRTEM image and SAED pattern (Figure 5.14(b) and (c)) as the evaluated d values match well with those in the JCPDS cards (ZnO:89-7102; NiO:89-7130; Fe_2O_3:89-8104).

5.3.4.2 $NiFe_2O_4$ nanofibers

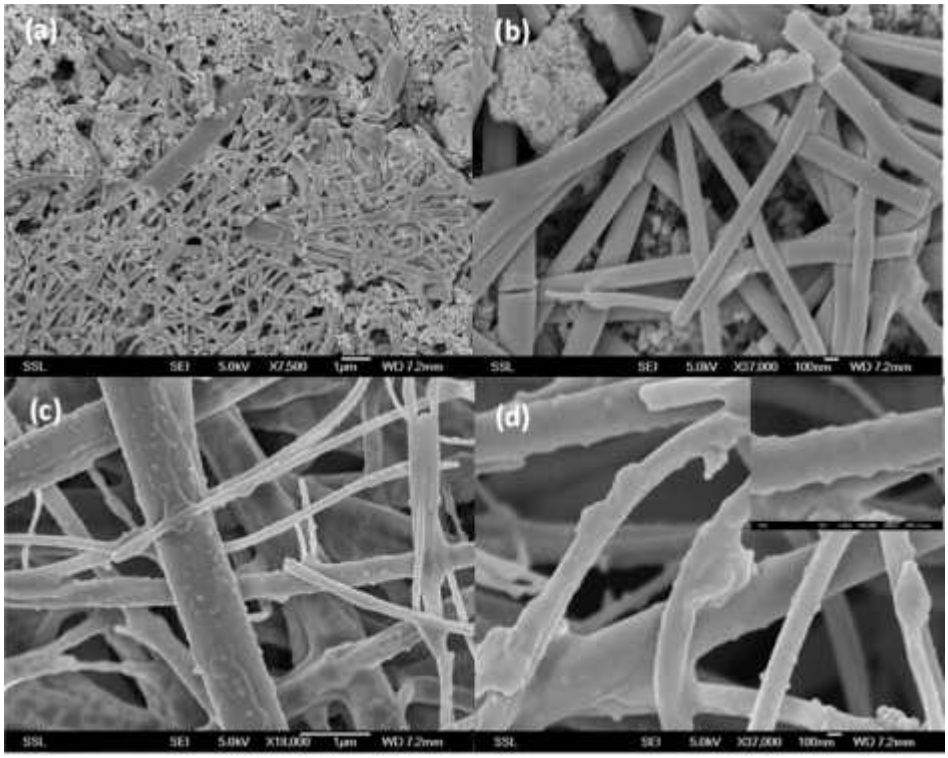

Figure 5.15 (a) SEM image of $NiFe_2O_4$ nanofiber electrode. Scale bar is 1μm. (b) SEM image of $NiFe_2O_4$ nanofiber electrode. Scale bar is 100 nm. (c) SEM image of cycled $NiFe_2O_4$ nanofiber electrode (after 50 charge-discharge cycles). Scale bar is 1μm. (d) SEM image of cycled $NiFe_2O_4$ nanofiber electrode (after 50 charge-discharge cycles). Scale bar is 100 nm. Inset shows cycled single nanofiber in expanded scale.

Figure 5.15 (a) and (b) show the SEM images of $NiFe_2O_4$ nanofibre-composite electrode before Li-cycling whereas Figure 5.15(c) and (d) display that of the cycled electrode after 50 charge-discharge cycles. As can be clearly seen, bare composite electrode consists of smooth interconnected fibres, surrounded by conducting carbon additive. The small lumps of particles observed in Figure 5.15(a) and (b) are Super P carbon added during electrode fabrication. It is obvious from the Figure 5.15(c) and (d) that the nanofibers remain unbroken upon Li-cycling but the surface smoothness of the fibres is lost due to the electrochemical reactions. Absence of capacity fading can be attributed to the unique morphology of the elctrospun fibres which remains intact throughout the cycling. It should be

noted that the particle lumps of conducting carbon can no longer be seen after Li-cycling. The inset of Figure 5.15(d) shows the closer image of cycled nanofibres and the observed 'bumby' surface morphology can be due to the presence of carbon additives which got embedded within the a surface layer formed during electrode-electrolyte interaction.

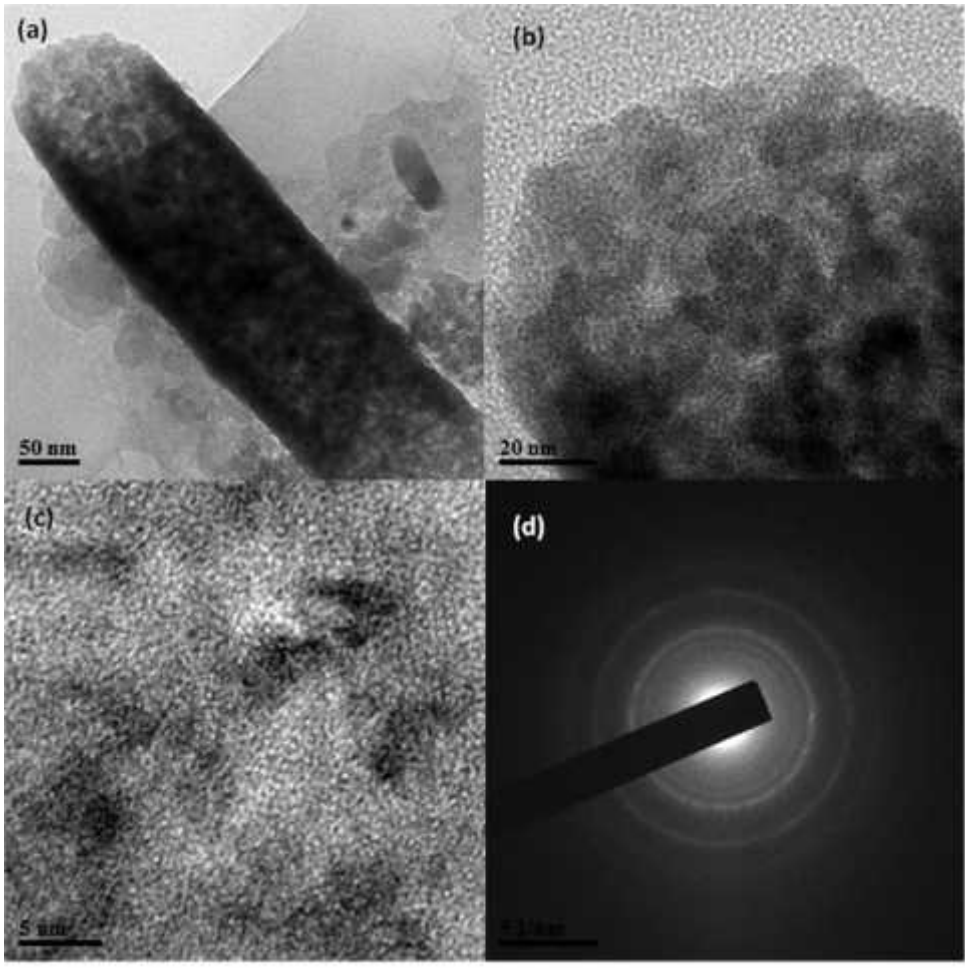

Figure 5.16 (a) TEM image of particles of cycled electrodes of $NiFe_2O_4$ nanofibers (100^{th} cycle; charged to 3 V). (b) Magnified TEM image of an edge of the selected nanofiber. Scale bar is 20 nm. (c) HRTEM image of $NiFe_2O_4$ nanofibers composite electrode after cycling. Scale bar is 5 nm. (d) SAED pattern of $NiFe_2O_4$ nanofibers composite electrode after cycling.

Interestingly, fibre like morphology is still preserved in the $NiFe_2O_4$ fibre composite electrodes even after 100 charge-discharge cycles which is well evident from TEM image shown in Figure 5.16(a). Figure 5.16(b) shows the magnified

image of the edge of the selected cycled nanofibre (after 100 cycles) with dark and light areas depending on the degree of crytallinity of the sample. It is obvious from the Figure 5.16(c) and (d) that the nanofibers remain unbroken upon Li-cycling but the surface smoothness of the fibers is lost due to the electrochemical reactions. The absence of capacity fading can be attributed to the unique morphology of the elctrospun fibers which remains intact throughout the cycling.

Ex-situ HR-TEM and SAED studies were carried out on the $NiFe_2O_4$ nanofibre charged electrode after 100 cycles to identify the crystallinity of the oxide phases formed during Li-cycling. The HRTEM lattice image (Figure 5.16(c)) clearly shows the nanocrystalline regions of size ~5 nm dispersed in amorphous matrix which can be considered as the presence of Fe_2O_3 and NiO in Li_2O. SAED pattern (Figure 5.16(d)) displays only diffuse rings which indicate the presence of predominant amorphous nature of the active material after 100 charge-discharge cycles.

5.3.5 Cyclic voltammetry

The cyclic voltammograms (CV) of the nanocrystalline $(Ni_{1-x}Zn_x)Fe_2O_4$, x= 0 to 1, up to 6 cycles at the slow scan rate of 58 μVs^{-1} between 0.005 and 3.00 V (*vs.* Li) were recorded. For clarity, CVs of the first two cycles are shown in Figure 5.17. It can be seen that the first cathodic scans of all compounds in the CV differ from the subsequent cycles. During first cathodic scan, all the phases showed a high intensity peak at 0.6 (±0.2) V *vs.* Li. This peak can be attributed to crystal structure destruction due to the reduction of Ni(II) , Zn(II) and Fe(III) to the corresponding metal nanoparticles and also the formation of SEI due to the reduction of solvents in the electrolyte (eqns. 5.3 and 5.7). For compositions x= 0.8 and 1, a small peak just before the onset of main peak centered at 0.6 V can be ascribed to the Li-

intercalation in to the spinel structure before the crystal structure destruction. For the composition x =0.6, the small peak is barely visible due to the smaller content of Zn (Figure 5.17(d)).Compared with the first cycle CV, the original cathodic peak at 0.6 V shifts to ~0.8 V in the second cycle for all *x* and other peaks disappear indicating a different mechanism.

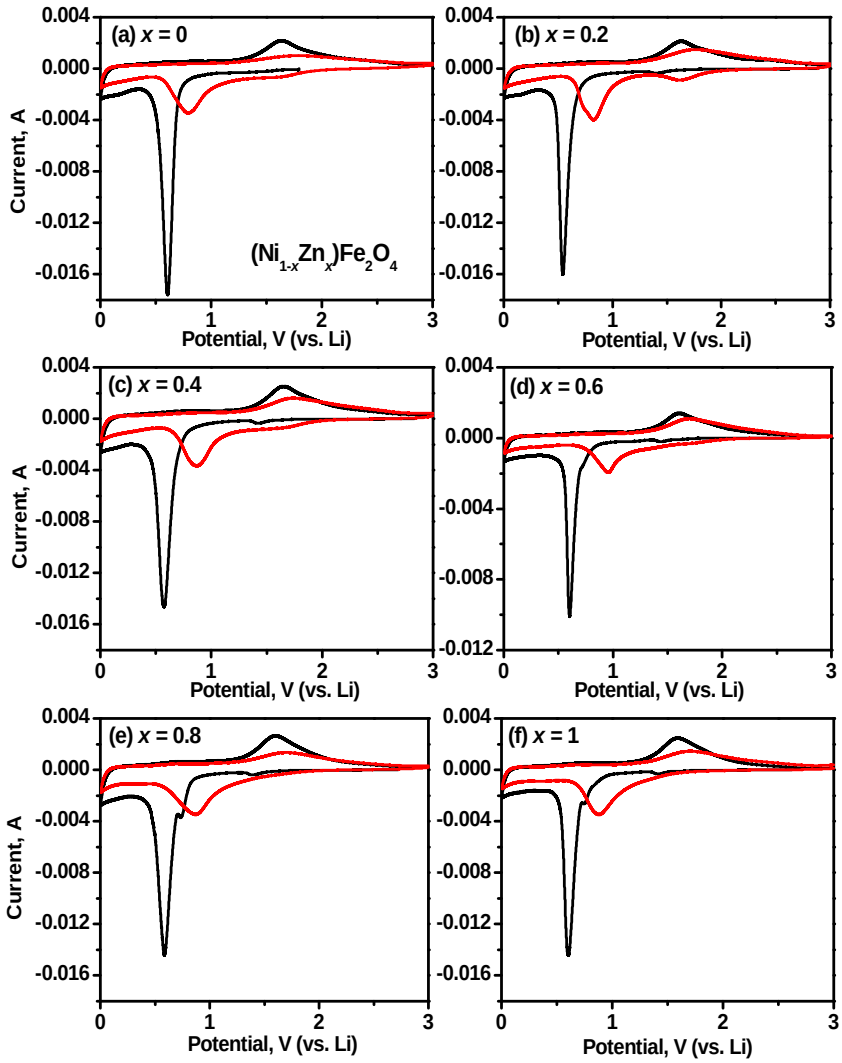

Figure 5.17 Cyclic voltammogramms of $(Ni_{1-x}Zn_x)$ Fe_2O_4. (a) x=0, (b) x=0.2, (c) x=0.4, (d) x=0.6, (e) x=0.8 and (f) x=1.0. Potential window, 0.005- 3 V; scan rate, 58 μVs^{-1}. Li metal was the counter and reference electrode. First cycle in black color and second cycle in red color.

The cathodic peak located at ~0.8 V is associated to the reversible reductive reaction of ZnO, NiO and Fe_2O_3 as per eqns. 5.5, 5.6 and 5.8. As mentioned earlier, due to smaller content of Zn (27 wt. %) in comparison to Fe in $ZnFe_2O_4$ and for the composition with x>0.6, the Li-Zn alloying reaction occurring below 0.35 V is not seen clearly in the CV curves (Figure 5.17). The anodic peak at ~1.6 V was observed in the first charge cycle for all the compositions which is slightly shifted and became broad in the subsequent cycles. The broad peak may include the peaks related to oxidation of Fe, Ni, Zn nanoparticles. According to literature reports, the oxidation of Fe^0, Ni^0 to Fe^{3+}, Ni^{2+}, respectively occurs at ~1.7 V [13] and that of Zn^0 to Zn^{2+} at ~1.5 V [36]. The area under the peak decreases in the subsequent cycles indicating capacity fading.

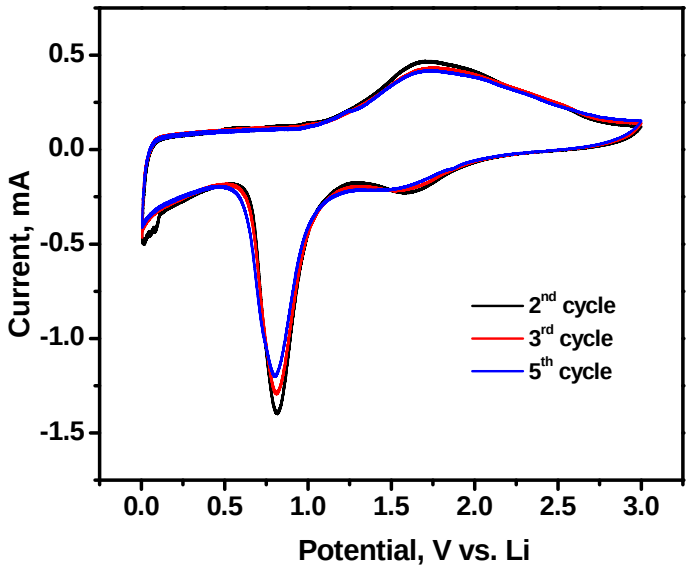

Figure 5.18 Cyclic voltammogram of $NiFe_2O_4$ nanofibers. Potential window, 0.005- 3 V; scan rate, 58 $\mu V\ s^{-1}$. Li metal was the counter and reference electrode.

The cyclic voltammograms (CV) of the $NiFe_2O_4$ nanofibers, at the slow scan rate of 58 μVs^{-1} between 0.005 and 3.00 V(vs. Li) were recorded and is shown in Figure 5.18. Two cathodic peaks located at 0.8 V and 1.45 V can be

attributed to the reductive reaction of Fe_2O_3 and NiO to Fe and Ni metal, respectively. A broad anodic peak at ~1.6 V was observed in the charge cycle which is slightly shifted and the broad peak may include the peaks related to oxidation of Fe, Ni nanoparticles as per eqn. 5.5 and 5.6. According to literature reports, the oxidation of Fe^0, Ni^0 to Fe^{3+}, Ni^{2+}, respectively occurs at ~1.7 V [13] and it agrees well with our data.

5.4 Conclusions

Sol-gel auto-combustion method using citric acid as the complexing agent was adopted to prepare nano-phase $(Ni_{1-x}Zn_x)Fe_2O_4$, x= 0 to 1. Rietveld- refined XRD data, HR-TEM and SAED show spinel structure with nanoparticles of size range 20 -50 nm are formed. Increase in x drives the system from inverse to normal spinel, i.e., a decrease in the degree of inversion and almost Vegard's law behavior for the cubic lattice parameter is observed after Rietveld fitting with positional parameters. Two phase Li-intercalation reaction (in the voltage 0.9 to 0.8 V) in to the spinel structure is found for the compositions with $x \geq 0.6$, during first-discharge with Li. Galvanostatic cycling studies in the voltage range, 0.005 -3 V vs. Li at a current of 50 mA g^{-1} show high reversible capacities, 1065 to 1215 mAh g^{-1} at the second discharge cycle but continuous decrease in capacity is noted up to 10-15 cycles for all x. The capacity fading between 10-50 cycles is $\geq$ 56 % for x = 0, 0.2 and 0.4 and where as it is 52 % for x = 0.8. For x= 0.6 and x=1, the respective values are 40 and 18 %, showing a capacity of 570 and 835 (±10) mAh g^{-1} at the end of 50 cycles.

$NiFe_2O_4$ nanofibers have been prepared by electrospinning of PVP-based precursors and subsequent annealing at 500 $^{\circ}$C. The nanofibers exhibited a high

discharge capacity of 870 mAh g^{-1} with superior cycling stability to $NiFe_2O_4$ nanoparticles. The fiber like morphology remains intact even after 100 charge/discharge cycles. The morphological robustness during conversion reaction is a unique feature and can be attributed to the porosity and interconnected nanoparticle framework of the nanofibers. The excellent electrochemical properties indicate that morphologically robust electrospun $NiFe_2O_4$ nanofibers can find promising applications in high capacity Li-ion batteries.

5.5 References

1. Cabana, J., et al., *Beyond Intercalation-Based Li-Ion Batteries: The State of the Art and Challenges of Electrode Materials Reacting Through Conversion Reactions.* Advanced Materials, 2010. **22**(35): p. E170-E192.
2. Taberna, L., et al., *High rate capabilities Fe_3O_4-based Cu nano-architectured electrodes for lithium-ion battery applications.* Nature Materials, 2006. **5**(7): p. 567-573.
3. Guo, X., et al., *Lithium storage in hollow spherical $ZnFe_2O_4$ as anode materials for lithium ion batteries.* Electrochemistry Communications, 2010. **12**(6): p. 847-850.
4. Sharma, Y., et al., *Li-storage and cyclability of urea combustion derived $ZnFe_2O_4$ as anode for Li-ion batteries.* Electrochimica Acta, 2008. **53**(5): p. 2380-2385.
5. Lavela, P. and J.L. Tirado, *$CoFe_2O_4$ and $NiFe_2O_4$ synthesized by sol–gel procedures for their use as anode materials for Li ion batteries.* Journal of Power Sources, 2007. **172**(1): p. 379-387.
6. Kalai Selvan, R., et al., *$CuFe_2O_4/SnO_2$ nanocomposites as anodes for Li-ion batteries.* Journal of Power Sources, 2006. **157**(1): p. 522-527.
7. Sharma, Y., et al., *Li-storage and cycling properties of spinel, CdFe2O4, as an anode for lithium ion batteries.* Bulletin of Materials Science, 2009. **32**(3): p. 295-304.
8. Ariyoshi, K., Y. Makimura, and T. Ohzuku, *Lithium Insertion Materials Having Spinel-Framework Structure for Advanced Batteries*, in *Lithium Ion Rechargeable Batteries*, K. Ozawa, Editor 2009, WILEY-VCH Verlag GmbH & Co. KGaA: Weinheim.

9. Chen, C.J., M. Greenblatt, and J.V. Waszczak, *Lithium insertion into spinel ferrites.* Solid State Ionics, 1986. **18 & 19**: p. 838-846.

10. Vidal-Abarca, C., P. Lavela, and J.L. Tirado, *Theorigin of capacity fading in $NiFe_2O_4$ conversion electrodes for lithium ion batteries unfolded by 57Fe mossbauer spectroscopy.* Journal of Physical Chemistry C 2010. **114**(29): p. 12828–12832.

11. Alcantara, R., et al., *Changes in oxidation state and magnetic order of iron atoms during the electrochemical reaction of lithium with $NiFe_2O_4$.* Electrochemistry Communications, 2003. **5**: p. 16-21.

12. Lavela, P., N.A. Kyerematen, and J.L. Tirado, *$NiMn_{2-x}Fe_xO_4$ prepared by a reverse micelles method as conversion anode materials for Li-ion batteries.* Materials Chemistry and Physics, 2010. **124**(1): p. 102-108.

13. Zhao, H., et al., *Fabrication and electrochemical performance of nickel ferrite nanoparticles as anode material in lithium ion batteries.* Electrochemistry Communications, 2007. **9**(10): p. 2606-2610.

14. Zhao, Y., et al., *Enhancing the lithium storage performance of iron oxide composites through partial substitution with Ni^{2+} or Co^{2+}*. Journal of Materials Chemistry, 2011. **21**: p. 19101-19105.

15. Sharma, Y., et al., *Nanophase $ZnCo_2O_4$ as a High Performance Anode Material for Li-Ion Batteries.* Advanced Functional Materials, 2007. **17**(15): p. 2855-2861.

16. Yang, Y., et al., *Nanocrystalline $ZnMn_2O_4$ as a novel lithium-storage material.* Electrochemistry Communications, 2008. **10**(8): p. 1117-1120.

17. Poizot, P., et al., *Searching for new anode materials for the Li-ion technology: time to deviate from the usual path.* Journal of Power Sources, 2001. **97-98**: p. 235-239.

18. Vidal-Abarca, C., P. Lavela, and J.L. Tirado, *The Origin of Capacity Fading in $NiFe_2O_4$ Conversion Electrodes for Lithium Ion Batteries Unfolded by 57Fe Mössbauer Spectroscopy.* Journal of Physical Chemistry C, 2010. **114**(29): p. 12828-12832.

19. Cherian, C.T., et al., *Li-cycling properties of nano-crystalline $(Ni_{1-x}Zn_x)Fe_2O_4$ $(0 \leqslant x \leqslant 1)$.* Journal of Solid State Electrochemistry, 2012. **16**(5): p. 1823-1832.

20. Hankare, P.P., et al., *Synthesis and characterization of nanocrystalline zinc substituted nickel ferrites.* Journal of Alloys and Compounds, 2010. **496**(1-2): p. 256-260.

21. Cherian, C.T., et al., *(N,F)-Co-doped TiO_2: synthesis, anatase-rutile conversion and Li-cycling properties.* CrystEngComm, 2012. DOI: 10.1039/C1CE05685A.

22. Shannon, R.D., *Revised effective ionic radii and systematic studies of interatomic distances in halides and chalcogenides.* Acta Crystallographica Section A: Foundations of Crystallography, 1976. **32**(5): p. 751-767.

23. Agarwala, S., et al., *Probing the morphology-device relation of Fe_2O_3 nanostructures towards photovoltaic and sensing applications.* Nanoscale, 2012. **4**(1): p. 194-205.

24. Ding, Y., Y. Yang, and H. Shao, *High capacity $ZnFe_2O_4$ anode material for lithium ion batteries.* Electrochimica Acta, 2011. **56**(25): p. 9433-9438.

25. Wang, J., P. King, and R.A. Huggins, *Investigations of binary lithium-zinc, lithium-cadmium and lithium-lead alloys as negative electrodes in organic solvent-based electrolyte.* Solid State Ionics, 1986. **20**(3): p. 185-189.

26. Wang, H., et al., *Evaluation of ZnO nanorod arrays with dandelion-like morphology as negative electrodes for lithium-ion batteries.* Electrochimica Acta, 2009. **54**(10): p. 2851-2855.

27. Zhao, Y., et al., *Enhancing the lithium storage performance of iron oxide composites through partial substitution with Ni^{2+} or Co^{2+}*. Journal of Materials Chemistry, 2011. **21**(47): p. 19101-19105.

28. Zhang, G., et al., *Formation of $ZnMn_2O_4$ Ball-in-Ball Hollow Microspheres as a High-Performance Anode for Lithium-Ion Batteries.* Advanced Materials, 2012. **24**(34): p. 4609-4613.

29. Zhou, G., et al., *Graphene-Wrapped Fe_3O_4 Anode Material with Improved Reversible Capacity and Cyclic Stability for Lithium Ion Batteries.* Chemistry of Materials, 2010. **22**(18): p. 5306-5313.

30. Grugeon, S., et al., *An update on the reactivity of nanoparticles Co-based compounds towards Li.* Solid State Sciences, 2003. **5**(6): p. 895-904.

31. Cho, J., *Porous Si anode materials for lithium rechargeable batteries.* Journal of Materials Chemistry, 2010. **20**(20): p. 4009-4014.

32. Ge, M., et al., *Porous Doped Silicon Nanowires for Lithium Ion Battery Anode with Long Cycle Life.* Nano Letters, 2012. **12**(5): p. 2318-2323.

33. Huang, J.S., et al., *Synthesis and characterization of $Li_3V_{2-x}Mg_x(PO_4)_3/C$ cathode material for lithium-ion batteries.* Journal of Power Sources, 2010. **195**(15): p. 5013-5018.

34. Levi, M.D. and D. Aurbach, *Impedance of a Single Intercalation Particle and of Non-Homogeneous, Multilayered Porous Composite Electrodes for Li-ion Batteries.* The Journal of Physical Chemistry B, 2004. **108**(31): p. 11693-11703.

35. Chamas, M., et al., *Electrochemical impedance characterization of $FeSn_2$ electrodes for Li-ion batteries.* Electrochimica Acta, 2011. **56**(19): p. 6732-6736.

36. Deng, Y., et al., *One-pot synthesis of $ZnFe_2O_4$/C hollow spheres as superior anode materials for lithium ion batteries.* Chemical Communications, 2011. **47**(24): p. 6828-6830.

Chapter 6 Li-storage and cycleability of molybdates, $AMoO_4$ (A= Co, Zn, Ni) as anodes for Li-ion batteries

6.1 Introduction

Large specific capacity can be achieved by utilizing all possible oxidation states of a compound through the 'conversion reaction' or displacement redox reaction in which the transition metal oxides/ fluorides/ nitrides can reversibly react with lithium to form corresponding metal nanoparticles embedded in Li_2O/ LiF/ Li_3N matrix. [1, 2] Wolframite-type metal molybdates are important inorganic materials that have a high application potential in various fields, such as in photoluminescence, microwave applications, catalysts and magnetic properties. Wolframite structure with the molybdenum in octahedral coordination are formed with relatively small bivalent cations ($MMoO_4$, ionic radius < 0.77 Å: M = Fe, Mn, Co, Ni, Zn). [3-7] Molybdates can also be considered as prospective anode materials due to the ability of the metal ions to exist in several oxidation states in these oxides, ranging from 3^+ to 6^+ for Mo and reversibly reacting with Li delivering high capacity, at potentials lower than 2 V. [8-11] MoO_3 is a well-known lithium insertion material and can accommodate a maximum of 1.5 lithium per molybdenum atom with theoretical capacity of ~280 mAh g^{-1}, in the voltage range 1.5-3.5 V.[12, 13] In the potential window of 0.0–3.0 V vs. Li, MoO_3 has been found to participate in conversion reaction, reversibly cycling 4-6 moles of Li, delivering high capacity in the range 745-1115 mAh g^{-1}. [8, 14] Hence MoO_3 can be considered as potential cathode as well as anode material for LIBs.

Among various metal molybdates, $CoMoO_4$ received much research interest due to their photocatalytic, magnetic and electrochemical properties.[15, 16] Three compounds with same stoichiometry, $CoMoO_4$ but of different structure are known

to form under atmospheric pressure: the low temperature α-phase (α-$CoMoO_4$), the high temperature β-isomorph (β-$CoMoO_4$), and the hydrate ($CoMoO_4$ nH_2O). [17, 18] Co^{2+} is in octahedral sites in all these isomorphs whereas Mo^{6+} is in octahedral coordination in α-$CoMoO_4$ and in tetrahedral coordination in β phase and hydrate phase. Since the Mo atoms are in an octahedral environment in α-$CoMoO_4$ and MoO_3 oxides, they have similar electronic properties. [17] Due to the similarities in the electronic properties of MoO_3 and α-$CoMoO_4$, Ding *et al*. studied the cathodic performance of hydrothermally synthesized $CoMoO_4$ microcrystals in the voltage range 1.2 – 4.0 V and achieved reversible discharge capacity of 130 mAh g^{-1}. [15]

Li-cycling properties of various other metal molybdates have also been explored by several research groups. Leyzerovich *et al*. studied the Li intercalation of lithium in various ternary metal molybdates such as $CuMoO_4$, $ZnMoO_4$, $NiMoO_4$ and $FeMoO_4$ in the voltage range 0.5 – 3.0 V and all those compounds were found to be unsatisfactory as electrode materials for lithium ion rechargeable batteries in the selected voltage range, due to rapid capacity fading.[19] Kim *et al*. investigated the electrochemical performance of $MnMoO_4$ in the voltage range 0.0-2.0 V and observed a discharge capacity of 1800 mAh g^{-1} accompanied by large irreversible capacity and amorphisation during first cycle. [20] Nidhi *et al*. examined the anodic performance of $CaMoO_4$ and found that 5 % carbon coated $CaMoO_4$ deliver a stable capacity of 400 mAh g^{-1} up to 40 cycles, when cycled in the voltage range 0.005- 2.5 V at a current of 60 mA g^{-1}. [8]

Herein, we report the Li-cycling behaviour of nanocrystalline $AMoO_4$ (A = Co, Ni, Zn) prepared via a modified citrate complex route assisted by microwave

irradiation, when cycled in the voltage range, 0.005- 3.0 V. $CoMoO_4$ showed better Li-cycling performance compared to zinc and nickel molybdates. In order to enhance the electrochemical performance of $CoMoO_4$, a polymer precursor method is adopted to prepare a macroporous system with interconnected particles.

6.2 Experimental

$AMoO_4$ (A= Zn, Co, Ni) nanoplates are synthesized via citrate complex route assisted by microwave irradiation. [21] The citrate solution is prepared by dissolving appropriate molar ratios of citric acid in de-ionized water (30 g of citric acid in 100 ml of water). Stoichiometric amount of cobalt nitrate and ammonium hepta molybdate are dissolved in citrate solution. The solution is made viscous by keeping the solution at a temperature of 100°C for 1 h under constant stirring. The solution is placed in the microwave irradiation system and the reactions are performed under ambient air for 30 min (microwave irradiation (with 1200 W, 2.45 GHz) for 1 h with 1 min interval after every 1 min of operation). The obtained precursor is heated to 600°C-700°C for 3 h to obtain the final product.

$CoMoO_4$ sub-micron particles are prepared by 'polymer precursor method', modifying the procedure reported by Pramanik *et al*.[22] 2.9 g of cobalt nitrate and 2.4 g of sodium molybdate solution are separately dissolved in 100 ml of distilled water and 5 ml of ammonia solution is added dropwise. The precipitate is filtered out, washed thoroughly and dried. 1 g of the dried powder is dissolved in 100 ml distilled water through complexation with ethylene di-amine tetra-acetic acid (1.8 g), in the presence of diethanolamine (8 ml). A polymeric reagent, which is an aqueous solution mixture of polyvinyl alcohol (1 g in dissolved in 10 ml) and sucrose (10 g dissolved in 20 ml) are added to the above solution under hot

conditions. The complete dehydration of the precursor solution generates a mesoporous carbon rich mass. The precursor material is heat treated at 500°C-700°C, 5h in air to obtain the final product.

The compound was characterized by powder X-ray diffraction (XRD) (Philips X'PERT MPD, Cu Kα radn.). For morphology studies, scanning electron microscopy (SEM) (JEOL JSM– 6700F, Field Emission Electron Microscope) and high resolution transmission electron microscope (TEM) (JEOL JEM 2100 operating at 200 kV) were employed. Raman spectra (Renishaw Raman system 2000) were recorded at room temperature. The electrodes for Li-cycling were prepared by the doctor-blade technique using a mixture of the active material ($CoMoO_4$), Super P carbon (MMM Ensaco) and binder (Kynar 2801) in the mass ratio 70:15:15, using an etched Cu-foil (thickness 10 μm) as the current collector. The geometrical electrode area and mass of active material were 2 cm^2 and 2–3 mg, respectively. Coin-type test cells (size 2016) were assembled in an argon-filled glove box (MBraun, Germany) and the cell components were Li metal (Kyokuto Metal Co., Japan) foil as counter electrode, glass micro-fiber filter (GF/F, Whatman Int.Ltd., Maidstone, England) as the separator and 1M $LiPF_6$ in ethylene carbonate (EC) and dimethyl carbonate (DMC) (1:1 by volume, Merck Selectipur LP40) as the electrolyte. The cyclic voltammetry and galvanostatic discharge-charge cycling of the cells were carried out at room temperature (25°C) by computer controlled MacPile II (Biologic, France) unit and Bitrode multiple battery tester (model SCN, Bitrode, USA), respectively.

6.3 Results and discussions

6.3.1 Structure and morphology

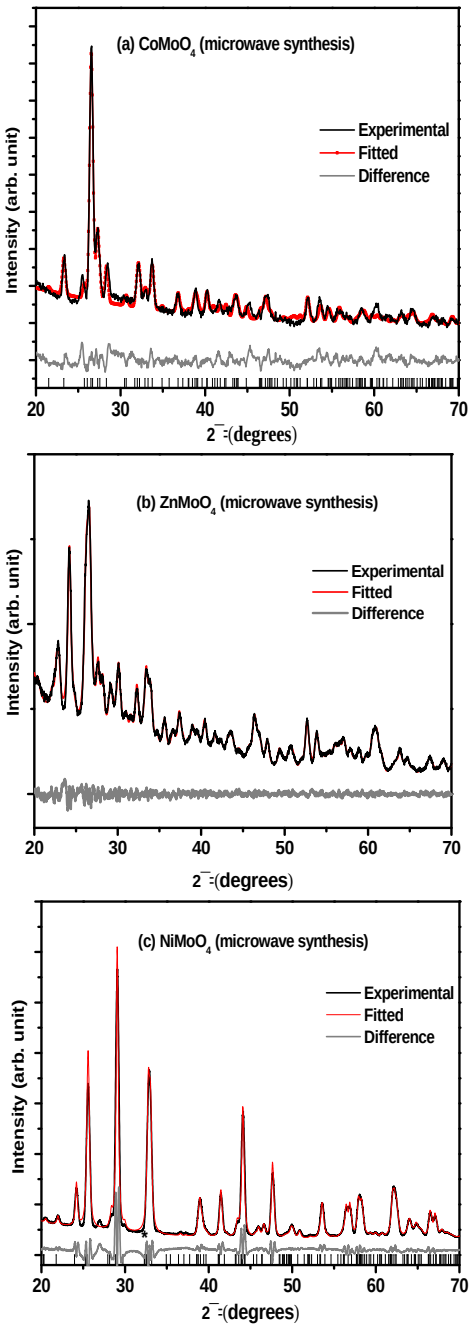

Figure 6.1 : X-ray diffraction (XRD) pattern (black line) compared with Rietveld refined profile (red line) (a) α-$CoMoO_4$ (b) $ZnMoO_4$ (c) $NiMoO_4$ nanoplates. The difference pattern and Miller indices are shown.

Error! Reference source not found.shows the XRD patterns of the microwave irradiated precursors of (a) $CoMoO_4$ (b)$ZnMoO_4$ and (c) $NiMoO_4$ samples, heat-treated to 600°C, 600°C and 700°C for 3 h respectively. The lattice parameters and the crystallite size obtained from Rietveld refinement of the XRD data are given in the Table 6-1. From TEM observations of the as-prepared $AMoO_4$ (A= Co, Zn, Ni) powders, nanoplate-like morphology is found. For instance, morphology of phase pure $CoMoO_4$ obtained by the heat treatment of microwave irradiated precursor material at 600°C for 3 h is shown in Figure 6.2(a). The corresponding SAED pattern is displayed in Figure 6.2(b). The SAED patterns shows diffuse rings which indicate better polycrystalline nano-phase nature of $CoMoO_4$ nanoplates.

Compound	Space group	*a* (Å)	*b* (Å)	*c* (Å)	α (deg)	β (deg)	γ (deg)	Crystallite size (nm)
$CoMoO_4$	Monoclinic C2/m	10.039	9.296	7.344	90	113	90	32
$ZnMoO_4$	Triclinic P-1	6.971	8.371	9.706	96	106	101	24
$NiMoO_4$	Monoclinic C2/m	9.584	8.756	7.663	90	114	90	36

Table 6-1 Lattice parameter values and crystallite size of molybdate nanoplates prepared by citrate assisted microwave synthesis.

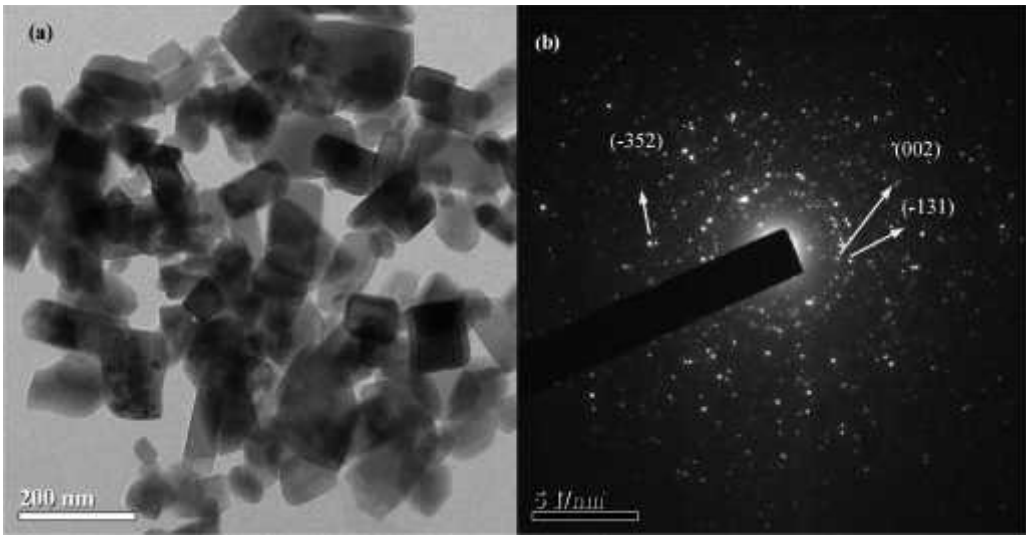

Figure 6.2 (a) TEM image of α-$CoMoO_4$ nanoplates. Scale bar is 200 nm. (b) SAED pattern of α-$CoMoO_4$ nanoplates. Miller indices are shown.

The powder XRD pattern of the $CoMoO_4$ synthesized via polymer precursor method is shown in Figure 6.3(a) and it reveals the formation of compound in phase pure form with the monoclinic structure. The lattice parameter values a (Å) = 10.72, b (Å) = 8.95, c (Å) = 6.99, $\beta = 115.63°$ are obtained by the Rietveld refinement and are in agreement with reported values of $CoMoO_4$ (JCPDS No. 21-0868). Figure 6.3(b) displays the Raman spectra of the $CoMoO_4$ particles with peaks at 335 cm^{-1}, 364 cm^{-1}, 690 cm^{-1}, 817 cm^{-1}, 880 $cm^{-1}$and 936 cm^{-1}.

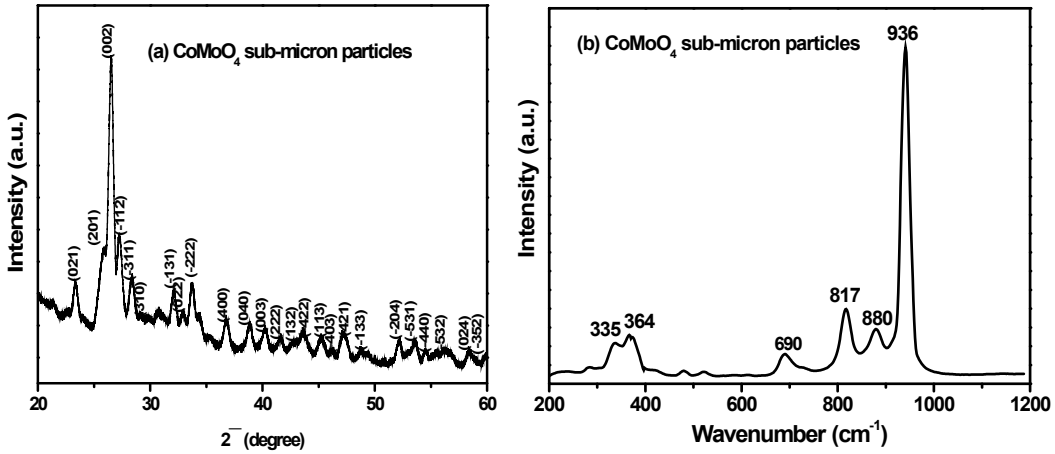

Figure 6.3 (a) X-ray diffraction (XRD, Cu Kα radiation) pattern of α-$CoMoO_4$ sub-micron particles. Miller indices of α-$CoMoO_4$ are shown. (b) Raman spectra of α-CoMoO4 sub-micron particles. Numbers refer to band positions in cm^{-1}.

According to Pasquan *et al*. [23], pure $CoMoO_4$ sample shows strong band at 940 cm^{-1} and weaker bands at 700, 813 and 880 cm^{-1}. The Raman bands at 880 cm^{-1}, 940 cm^{-1} and the broad band at 350 cm^{-1} can be assigned to Mo-O-Co stretching vibrations in cobalt molybdate. [24] The BET surface area and average pore diameter of $CoMoO_4$ samples obtained from nitrogen adsorption-desorption analysis are given in Table 6-2. The average pore diameter of the sample prepared by polymer precursor method is 160 nm which indicates the macroporous nature of the as-prepared compound.

$CoMoO_4$ preparation method	BET surface area (m^2 g^{-1})	Average Pore Diameter (nm)
Polymer method	0.85	160
Microwave synthesis	6.25	15

Table 6-2 BET surface area and average pore size of CoMoO4 samples obtained from N_2 physisorption analysis.

The particle morphology is examined by SEM and TEM. Figure 6.4(a), (b) and (c) show that the $CoMoO_4$ powder consists of interconnected sub-micron size particles forming a porous network. Figure 6.4(d) shows the SAED (selected area electron diffraction) pattern consisting of bright spots with (201), (002), (-131), (040), (-532) planes. Inset in Figure 6.4(d) shows the HRTEM lattice image of $CoMoO_4$. The measured inter-planar spacing matches well with the d-value corresponding to the (201) plane shown in the XRD pattern of the compound. Energy dispersive X-ray (EDX) elemental mapping has been used to evaluate the uniformity of distribution of cobalt, molybdenum and oxygen elements. As shown in Figure 6.5, these three elements are distributed homogeneously in the specific portion of the sample at sub-micron scale.

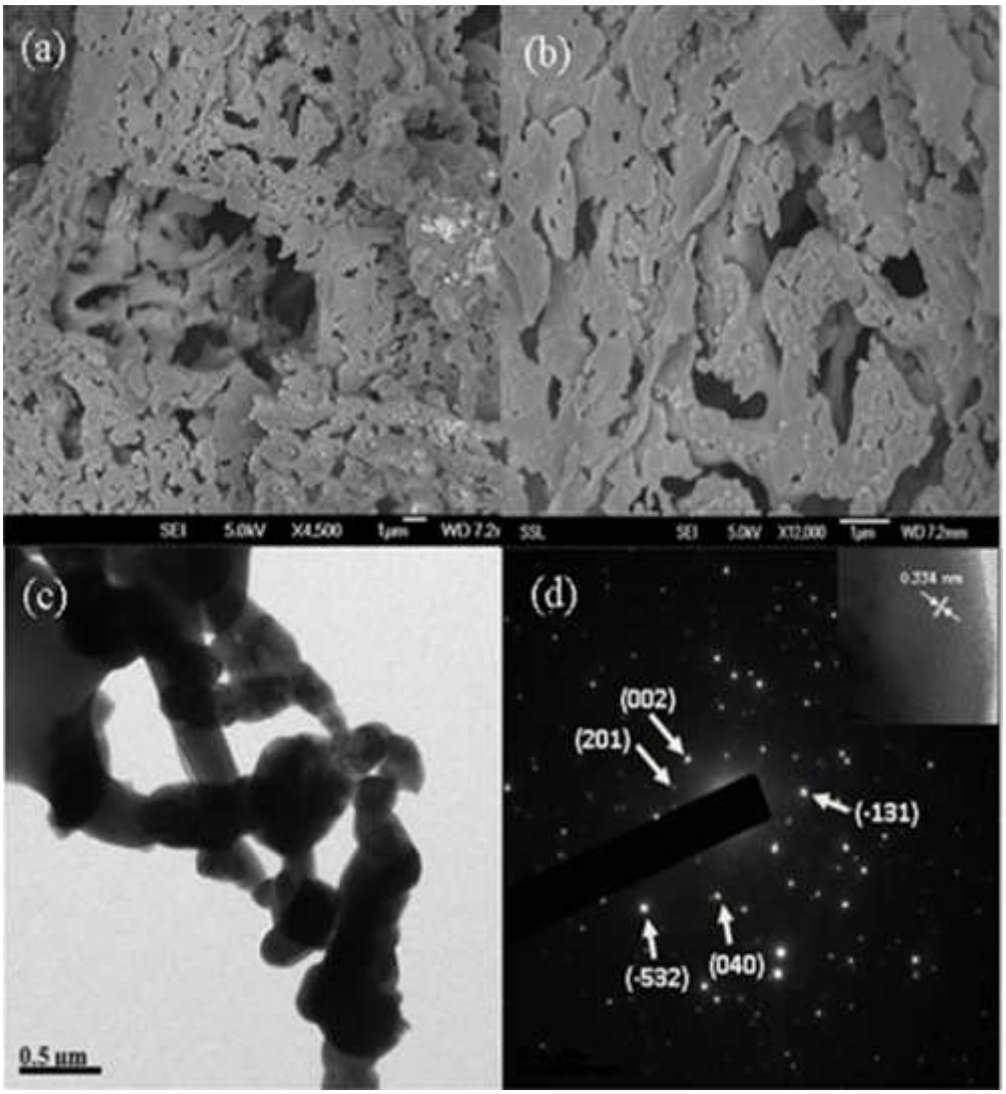

Figure 6.4 (a) SEM image of α-$CoMoO_4$ sub-micron particles. Scale bar is 1000 nm. (b) SEM image of α-$CoMoO_4$ sub-micron particles. Scale bar is 1000 nm. (c) TEM photograph of α-$CoMoO_4$ sub-micron particles. Scale bar is 500 nm. (d) SAED pattern of α-$CoMoO_4$ sub-micron particles. Miller indices are shown. Inset shows the HRTEM lattice image.

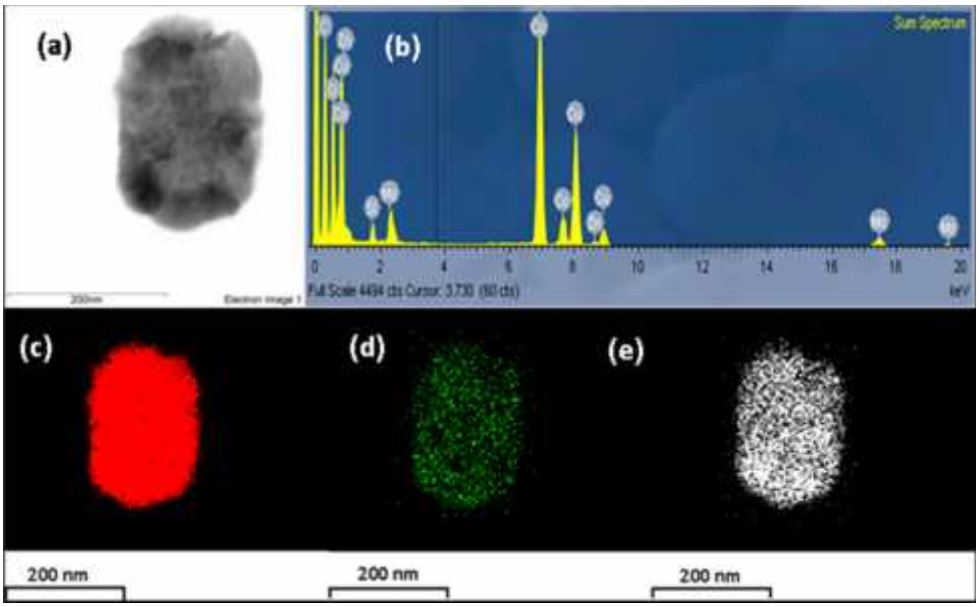

Figure 6.5(a) SEM image of micro- $CoMoO_4$, selected for energy-dispersive X-ray (EDX) analysis. (b) EDX spectrum of the product. (c), (d) and (e) EDX maps of cobalt, molybdenum and oxygen, respectively.

6.3.2 Li-cycling studies

6.3.2.1 $AMoO_4$ (A= Co, Zn, Ni) nanoplates

The electrochemical Li-storage and cycleability of $AMoO_4$ (A= Co, Zn, Ni) were investigated by galvanostatic cycling in the voltage window, 0.005- 3.0 V *vs*. Li at a current of 100 mA g^{-1} up to 60 cycles. Voltage *vs*. capacity profiles of the selected cycles are shown in Figure 6.6. From the Figure 6.6, it is clear that for all the three samples, the first discharge curve starts from the open circuit voltage (OCV ~ 2.0-2.5 V) and shows a continuous decrease, to reach a voltage plateau region at 0.8 V. Galvanostatic cycling profiles of $CoMoO_4$ and $NiMoO_4$ show a short vivid voltage plateau at 0.8 V before the onset of downward sloping voltage plateau at 0.6 V. This indicates a two phase Li-intercalation in to the lattice before the crystal structure destruction and reduction of metal ions followed by the

formation of metal nanoparticles embedded in an amorphous matrix of Li_2O as in eqn. 6.1.

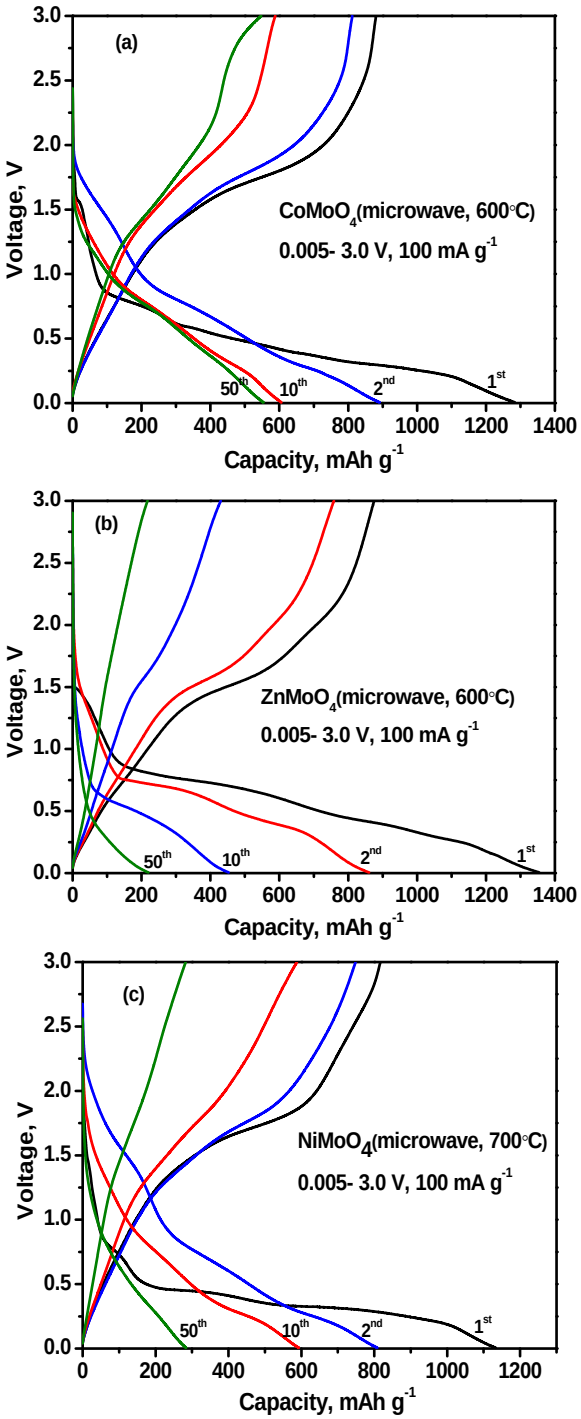

Figure 6.6 Galvanostatic charge-discharge profiles of (a)$CoMoO_4$ nanoplates (b) $ZnMoO_4$ nanoplates (c) $NiMoO_4$ nanoplates. Voltage range: 0.005- 3 V vs. Li, current: 100 mA g^{-1}.

On the other hand, for $ZnMoO_4$ such a two phase Li-intercalation region is not seen before the sloping voltage plateau due to structure destruction but beyond this voltage plateau region, Zn nanoparticles react with Li to form Li-Zn alloy increasing the Li-storage capacity, as per the eqn. 6.2.That can be the reason for the higher first discharge capacity of 1360 mAh g^{-1} shown by $ZnMoO_4$ nanoplates compared to other two molybdates. $CoMoO_4$ and $NiMoO_4$ deliver a first discharge capacity of 1290 mAh g^{-1} and 1140 mAh g^{-1}, respectively. Upon charging to 3 V, initial crystal structure is not reformed whereas Co, Ni and Mo nanoparticle react with their Li_2O matrix to form respective simpler oxides as shown in eqn. 6.3 and 6.4. For $ZnMoO_4$, Li-Zn alloy formed during deep discharge, de-alloys and the Zn nanoparticles oxidize to ZnO (eqn. 6.2 and 6.3). The reversible theoretical capacity calculated for CoMoO4, ZnMoO4 and NiMoO4 are 980 mAh g^{-1} (8 moles of Li), 1071 mAh g^{-1} (9 moles of Li) and 981 mAh g^{-1} (8 moles of Li), respectively.

$AMoO_4 + 8Li \rightarrow A + Mo + 4Li_2O$ (A= Co, Zn, Ni) eqn. 6.1

$Zn + Li \leftrightarrow LiZn$ eqn. 6.2

$Co/Zn/Ni + Li_2O \leftrightarrow CoO/ZnO/NiO + 2Li$ eqn. 6.3

$Mo + 3Li_2O \leftrightarrow MoO_3 + 6Li$ eqn. 6.4

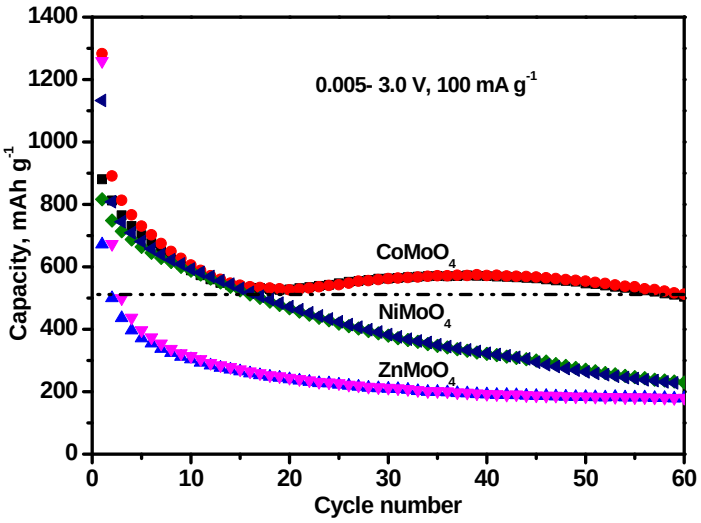

Figure 6.7 Capacity vs. cycle number plot of $CoMoO_4$, $NiMoO_4$ and $ZnMoO_4$.Voltage range: 0.005- 3 V vs. Li. Current: 100 mA g^{-1}

$CoMoO_4$ and $ZnMoO_4$ show a drastic capacity fading up to 15 cycles delivering a reversible capacity of 540 mAh g^{-1} and 270 mAh g^{-1} at the end of 15th cycle whereas $NiMoO_4$ demonstrate a constant capacity fading upto 60 cycles. The capacity fading % between 2nd -15th cycles for $CoMoO_4$, $ZnMoO_4$ and $NiMoO_4$ are 62%, 59 % and 36 %. $CoMoO_4$ nanoplates show an increasing tendency in the capacity values until 40 cycles thereafter fades to 510 mAh g^{-1} at the end of 60th cycle. The capacity retention % of $CoMoO_4$ nanoplates between 15-60 cycles is 94 %. On the other hand, $ZnMoO_4$ and $NiMoO_4$ deliver low capacity values, 182 mAh g^{-1} and 232 mAh g^{-1} respectively, after 60 cycles. Apart from delivering capacity from Co→CoO conversion reaction, Co can also act as better matrix element to buffer the volume variation during the conversion reaction of molybdenum. Even though it is obvious from the Figure 6.7 that $CoMoO_4$ nanoplates show superior Li-cycling performance compared to its Zn and Ni counterparts, the theoretical capacity is not attained due to the rapid capacity fading during initial cycles. Interconnected macroporous network was found to be beneficial for reducing the initial capacity fading in conversion reaction based oxide materials. [25] A

macroporous network of interconnected $CoMoO_4$ particles is prepared by polymer precursor method.

6.3.2.2 *$CoMoO_4$ sub-micron particles*

The Li-storage and cycling properties of $CoMoO_4$ submicron particles are investigated by galvanostatic cycling in the voltage window, 0.005- 3.0 V vs. Li at a current of 100 mA g^{-1}. Voltage vs. capacity profiles of the selected cycles are shown in Figure 6.8(a). The first discharge curve starts from the open circuit voltage (OCV ~ 2.5 V) and shows a sharp decrease to 1.3 V where a sloping voltage plateau sets in. This part comprises a capacity of 162 mAh g^{-1} which is equivalent to the uptake of 1.3 moles of Li (1 mole of Li corresponds to capacity of 122 mAh g^{-1}). The plateau is followed by a sloping region which starts at 0.9 V and extends up to 0.12 V yielding a capacity of 1184 mAh g^{-1}. A small voltage plateau can be seen at 0.12 V followed by continuous decrease in voltage up to the cut off voltage, 0.005 V. Upon charging to 3 V, a smooth voltage profile is observed till 1.0 V which is followed by upward sloping voltage plateau up to ~ 2.0 V and a gradual rise to 3.0 V.

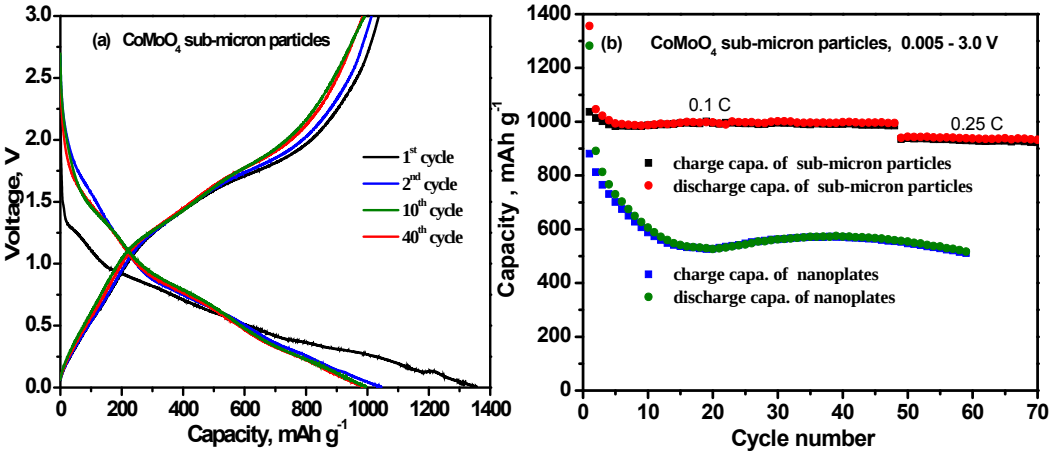

Figure 6.8 (a) Galvanostatic charge-discharge profiles of α-$CoMoO_4$ sub-micron particles. Voltage range: 0.005- 3 V vs. Li, current: 100 mA g^{-1}. (b) Capacity vs. cycle number plot of α-$CoMoO_4$ at various C-rates. Voltage range: 0.005- 3 V vs. Li.

The initial discharge and charge capacities are 1355 mAh g^{-1} and 1035 mAh g^{-1}, respectively. The irreversible capacity can be due to formation of solid electrolyte interphase (SEI) and an organic polymeric layer on the metal nanoparticles during first discharge. [26] The theoretically expected capacity value for the first discharge reaction involving crystal structure destruction of α-$CoMoO_4$ and reduction of the Mo^{6+} to Mo^0 and Co^{2+} to Co is 980 mAh g^{-1}. An excess capacity of 375 mAh g^{-1} during first discharge can be due to the extra Li-storage via an interfacial reaction due to the charge separation at the metal/Li_2O phase boundary. [27] First discharge to 0.005 V leads to crystal structure destruction followed by metal nanoparticles in an amorphous matrix of Li_2O as shown in eqn. 6.1. Eqn. 6.1 is not reversible due to the structure destruction and amorphisation occurring during first discharge. During subsequent charge –discharge cycles, the expected reversible capacity is 980 mAh g^{-1}, if 8 moles of Li can be reversibly extracted and inserted as per eqn. 6.3 and 6.4.

Figure 6.8 (b) illustrates the capacity vs. cycle number plots extracted from galvanostatic cycling data. Assuming 1C= 980 mAh g^{-1}, the applied current corresponds to a current rate of 0.1 C. A high reversible capacity of 990 (±10) mAh g^{-1} is obtained with 100 % capacity retention between 5- 50 cycles. When the current is increased to 0.25 C, a stable capacity of 940 mAh g^{-1} is delivered. For comparison, nano-plates of $CoMoO_4$ shows a drastic capacity fading for the first 15 cycles and a reversible capacity of 560 mAh g^{-1} is obtained after 50 cycles. The observed decrease in reversible capacity during initial 15 cycles (and subsequent increase and stabilization) can be attributed to the ‘formation’ or ‘conditioning’ of the electrode during which the formation of stable solid electrolyte interphase (SEI) on the metal nano-particles, the percolation of the electrolyte through the

active material i.e. Co, Mo/ Li_2O amorphous composite and the establishment of an intimate electronic contact of the composite with the current collector occur. [28] $CoMoO_4$ nanoplate composite electrodes need several cycles to complete the 'conditioning' phase whereas interconnected $CoMoO_4$ submicron particles efficiently overcome this phase without any capacity loss. This superior electrochemical performance can be attributed to the unique morphology obtained by the 'polymer based metal precursor' synthetic method set forth by Pramanik *et al*. [22]. The unique morphology of $CoMoO_4$, in which primary particles are mutually interconnected, has been considered beneficial for the electrochemical performance. It assures a suitable electrical conductivity and mechanical strength on a long extended electrode cycling. [25] The stable electrochemical performance of the interconnected sub-micron particles can also be due to the synergistic effect between CoO and MoO_3 during cycling.

6.3.3 Cyclic voltammetry studies

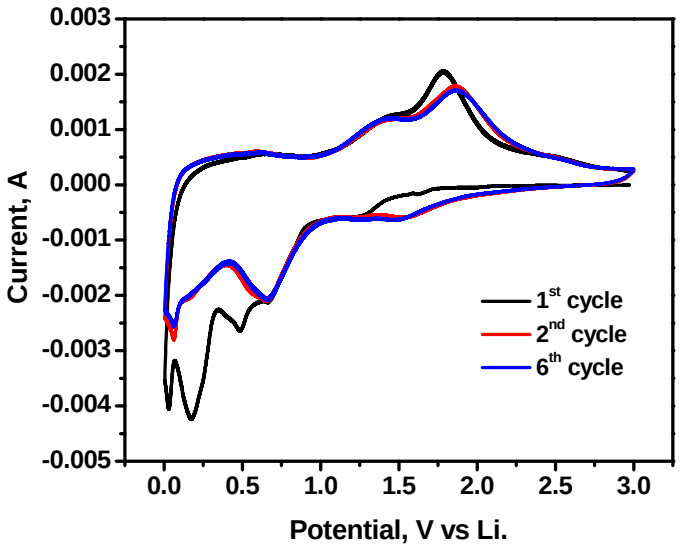

Figure 6.9 Cyclic voltammogram of α-$CoMoO_4$ sub-micron particles. Potential window, 0.005- 3 V; scan rate, 58 μV s^{-1}. Li metal was the counter and reference electrode.

Cyclic voltammetry is a complementary technique to galvanostatic cycling and helps in understanding the redox potentials at which the discharge-charge reactions occur. Figure 6.9 shows the CV curves of $CoMoO_4$ sub-micron particles in the potential window 0.005- 3V at the scan rate 58 μV Sec^{-1}. It is clear from the CV curves that there is substantial difference between first and the subsequent cycles. The first cathodic scan results in a shoulder peak at 0.67 V, broad peaks at ~0.5 V and 0.18 V and a sharp peak at a potential close to 0.005 V. The peaks at 0.5 V and 0.18 V is not seen in subsequent cycles. These two irreversible peaks during first cathodic scan are due to the crystal structure destruction accompanied by the complete reduction to Co^0 and Mo^0 metal nanoparticles and the formation of solid electrolyte interface (SEI) due to the reduction of solvents in the electrolyte. The first anodic scan shows two peaks at 1.4 V and 1.8 V which corresponds to oxidation of Co and Mo. The peak at 1.4 V can be attributed to the oxidation of Mo^0 to Mo^{4+} whereas the peak at 1.8 V can be due to the oxidation of Co to Co^{2+} and Mo^{4+} to Mo^{6+}. [14, 29, 30] They became broadened during further cycles. Second and further cathodic scans show peaks at 1.56 V, 0.66 V and 0.05 V while the anodic scans show peaks at 1.4 and 1.85 V. The curves corresponding to 2^{nd} and 6^{th} scans overlap indicating the reversibility of the eqns. 6.3 and 6.4 and hence the capacity stability.

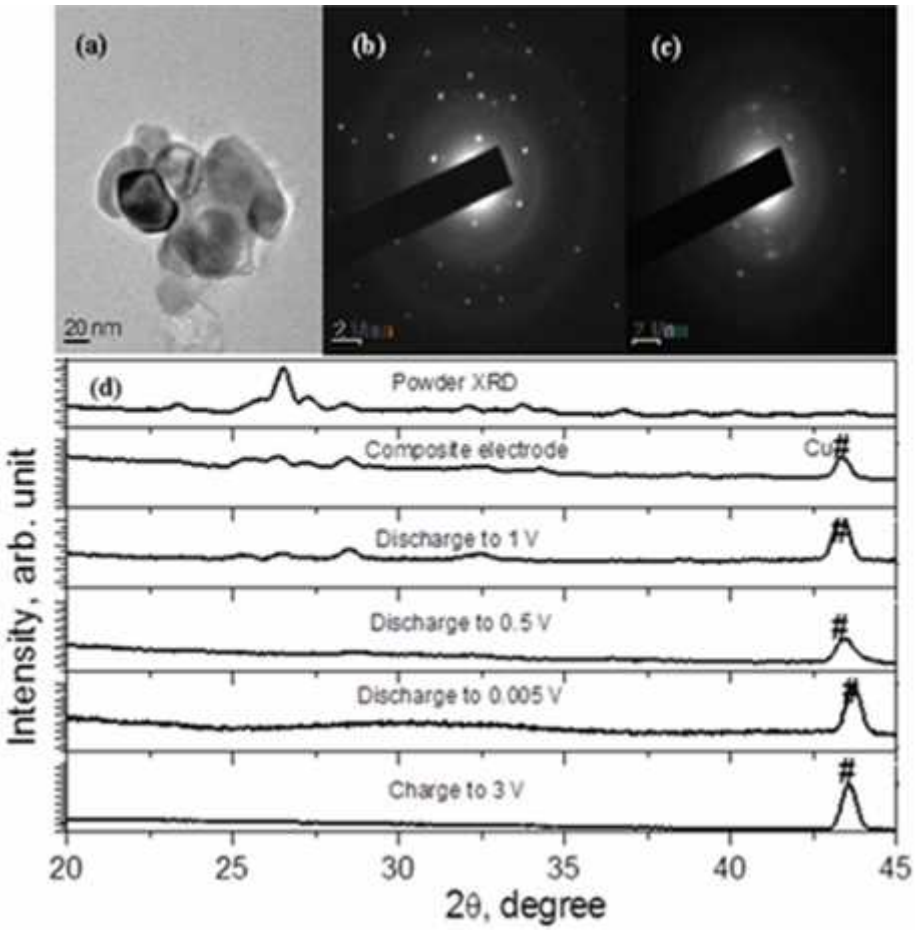

Figure 6.10(a) TEM image of particles of cycled electrodes of α-$CoMoO_4$ sub-micron particles (2^{nd} cycle; charged to 3 V). (b) and (c) SAED pattern of different regions. (d) XRD spectra of cycled α-$CoMoO_4$ electrode.

6.3.4 Ex-situ TEM and XRD studies

To investigate the nature of the products formed upon cycling, ex situ XRD and TEM studies were carried out on several duplicate cells. Ex-situ TEM image (Figure 6.10(a)) indicates that after two discharge-charge cycles, the micron-sized particles are broken down into particles of size 40 nm. The SAED patterns of the different portions of the sample collected from the electrode charged to 3 V after two galvanostatic charge-discharge cycles are shown in Figure 6.10(b) and (c). The SAED pattern in Figure 6.10(b) shows sharp distinct spots where as that in Figure 6.10(c) shows diffuse spots/rings and it is due to the coexistence of both crystalline and nano-amorphous phases after first 2 discharge-charge cycles. The d- values,

2.50 (±0.05) Å, 2.62 (±0.05) Å and 1.65 (±0.05) Å, derived by measuring the diameter of rings/spots about the center, can be assigned to the (101), (002) and (110) planes of hexagonal CoO (JCPDS 89-2803). The calculated d-values, 3.84 (±0.05) Å, 3.29 (±0.05) Å and 2.95 (±0.05) Å can be assigned to the (100), (011) and (101) planes of monoclinic MoO_3 (JCPDS 85-2405). Figure 6.10(d) shows the XRD patterns of $CoMoO_4$ powder, bare $CoMoO_4$ composite electrode, electrode after discharging to 1 V, 0.5 V, and 0.005 V and in the charged state (3 V). The diffraction lines due to the compound completely disappear in the XRD patterns of the electrodes discharged to 0.5 V and 0.005 V, indicating initial crystal structure destruction and amorphisation. The XRD pattern of the electrode charged to 3 V does not show any peak which indicate that the initial crystalline compound is not reformed during charging and the reversible reactions (eqns. 2, 3) involve amorphous nano-phase materials. Thus from ex-situ studies, it can be deduced that nano-phase, amorphous CoO and MoO_3 are undergoing conversion reaction/ displacement redox reaction as shown in eqn. 6.3 and 6.4. It should be kept in mind that there is no experimental proof for the 'conversion' reaction of MoO_3 (eqn. 6.4) where Mo^{6+} will be converted to Mo metal nanoparticles during deep discharge and MoO_3 will be reformed upon charging to 3 V. In the literature, it is assumed that high reversible capacity value delivered by MoO_3 during cycling in voltage range 0 V- 3 V can be due to the reformation of MoO_3 by the uptake of 6 moles of Li per formula unit [14, 31]. More sophisticated techniques are needed to prove the formation of Mo^{6+} from Mo metal nanoparticles.

6.4 Conclusion

Nano-plates of molybdates ($AMoO_4$, A=Zn, Mo, Co) are synthesized by urea assisted microwave synthesis and studied the role of counter cations (Co, Zn, Ni)

in the electrochemical performance of molybdates, in the voltage range 0.005- 3.0 V vs. Li at 100 mA g^{-1}. $CoMoO_4$ nanoplates exhibit a reversible capacity of 540 mAh g^{-1} after 15^{th} cycle and the capacity retention % between 15-60 cycles is 94 %. On the other hand, $ZnMoO_4$ and $NiMoO_4$ deliver low capacity values, 182 mAh g^{-1} and 232 mAh g^{-1} respectively, after 60 cycles. Thus cobalt is found to be a better matrix element for the Li-cycling of molybdates compared to zinc and nickel. Capacity stability of $CoMoO_4$ is further improved by preparing interconnected macroporous network of sub-micron particles, adopting 'polymer precursor method'. Li-reaction mechanism of α-$CoMoO_4$ sub-micron particles has been investigated by ex-situ XRD and HR-TEM. The material exhibits a high reversible capacity of 990 mAh g^{-1}, at 0.1 C, which is stable up to 50 cycles. The excellent cycling stability can be attributed to the unique morphology of inter-connected micron size particles and mutually beneficial effect of CoO and MoO_3 during cycling, thus making α-$CoMoO_4$, a promising anode material for Li-ion batteries.

6.5 References

1. Wang, F., et al., *Conversion Reaction Mechanisms in Lithium Ion Batteries: Study of the Binary Metal Fluoride Electrodes.* Journal of the American Chemical Society, 2011. **133**(46): p. 18828-18836.
2. Poizot, P., et al., *Nano-sized transition-metal oxides as negative-electrode materials for lithium-ion batteries.* Nature, 2000. **407**(6803): p. 496-499.
3. Young, A.P. and C.M. Schwartz, *High-Pressure Synthesis of Molybdates with the Wolframite Structure.* Science, 1963. **141**(3578): p. 348-349.
4. Li, Y., et al., *Room-temperature synthesis, growth mechanism and properties of uniform $CdMoO_4$ nano-octahedra.* CrystEngComm, 2011. **13**(7): p. 2649-2655.
5. Cui, J.-X., et al., *Formation of $FeMoO_4$ hollow microspheres via a chemical conversion-induced Ostwald ripening process.* CrystEngComm, 2012. **14**(20): p. 7025-7030.
6. Raju, G.S.R., et al., *A facile and efficient strategy for the preparation of stable $CaMoO_4$ spherulites using ammonium molybdate as a molybdenum source and their excitation induced tunable luminescent properties for optical applications.* Journal of Materials Chemistry, 2012. **22**(31): p. 15562-15569.
7. Peng, C., et al., *A general precipitation strategy for large-scale synthesis of molybdate nanostructures.* Chemical Communications, 2008(43): p. 5601-5603.
8. Sharma, N., et al., *Carbon-Coated Nanophase $CaMoO_4$ as Anode Material for Li Ion Batteries.* Chemistry of Materials, 2003. **16**(3): p. 504-512.

9. Tao, T., et al., *MoO_3 nanoparticles dispersed uniformly in carbon matrix: a high capacity composite anode for Li-ion batteries.* Journal of Materials Chemistry, 2011. **21**(25): p. 9350-9355.

10. Fang, X., et al., *Enhanced Li storage performance of ordered mesoporous MoO_2 via tungsten doping.* Nanoscale, 2012. **4**(5): p. 1541-1544.

11. Xia, F., et al., *Layer-by-layer assembled MoO_2-graphene thin film as a high-capacity and binder-free anode for lithium-ion batteries.* Nanoscale, 2012. **4**(15): p. 4707-4711.

12. Zhou, L., et al., *α-MoO_3 Nanobelts: A High Performance Cathode Material for Lithium Ion Batteries.* Journal of Physical Chemistry C, 2010. **114**(49): p. 21868-21872.

13. Sen, U.K. and S. Mitra, *Electrochemical activity of ~-MoO_3 nano-belts as lithium-ion battery cathode.* RSC Advances, 2012.

14. Meduri, P., et al., *$MoO_{(3-x)}$ nanowire arrays as stable and high-capacity anodes for lithium ion batteries.* Nano Lett, 2012. **12**(4): p. 1784-8.

15. Ding, Y., et al., *General Synthesis and Phase Control of Metal Molybdate Hydrates $MMoO_4 \cdot nH_2O$ (M = Co, Ni, Mn, n = 0, 3/4, 1) Nano/Microcrystals by a Hydrothermal Approach: Magnetic, Photocatalytic, and Electrochemical Properties.* Inorganic Chemistry, 2008. **47**(17): p. 7813-7823.

16. Xu, Z., et al., *Supercapacitive carbon nanotube-cobalt molybdate nanocomposites prepared via solvent-free microwave synthesis.* RSC Advances, 2012. **2**(7): p. 2753-2755.

17. Robertson, L., et al., *Cobalt–Zinc Molybdates as New Blue Pigments Involving Co^{2+} in Distorted Trigonal Bipyramids and Octahedra.* Chemistry of Materials, 2011. **23**(9): p. 2419-2427.

18. Livage, C., et al., *Solution process for the synthesis of the "high-pressure" phase $CoMoO_4$ and X-ray single crystal resolution.* Journal of Materials Chemistry, 2002. **12**(5): p. 1423-1425.

19. Leyzerovich, N.N., et al., *Electrochemical intercalation of lithium in ternary metal molybdates $MMoO_4$ (M: Cu, Zn, Ni and Fe).* Journal of Power Sources, 2004. **127**(1-2): p. 76-84.

20. Kim, S.-S., et al., *Reaction mechanisms of $MnMoO_4$ for high capacity anode material of Li secondary battery.* Solid State Ionics, 2002. **146**(3–4): p. 249-256.

21. Ryu, J.H., et al., *Synthesis of nanocrystalline $MMoO_4$ (M =Ni, Zn) phosphors via a citrate complex route assisted by microwave irradiation and their photoluminescence.* Materials Letters, 2006. **60**(13–14): p. 1702-1705.

22. Pramanik, P., *A novel chemical route for the preparation of nanosized oxides, phosphates, vanadates, molybdates and tungstates using polymer precursors.* Bulletin of Materials Science, 1999. **22**(3): p. 335-339.

23. Villa, P.L., F. Trifirò, and I. Pasquon, *Study of the interaction between $CoMoO_4$ and Al_2O_3 by Raman spectroscopy.* Reaction Kinetics and Catalysis Letters, 1974. **1**(3): p. 341-344.

24. Herrera, J.E. and D.E. Resasco, *Role of Co−W Interaction in the Selective Growth of Single-Walled Carbon Nanotubes from CO Disproportionation.* Journal of Physical Chemistry B, 2003. **107**(16): p. 3738-3746.

25. Vidal-Abarca, C., P. Lavela, and J.L. Tirado, *The Origin of Capacity Fading in $NiFe_2O_4$ Conversion Electrodes for Lithium Ion Batteries Unfolded by 57Fe Mössbauer Spectroscopy.* Journal of Physical Chemistry C, 2010. **114**(29): p. 12828-12832.

26. Cherian, C.T., et al., *Electrospun ~-Fe_2O_3 nanorods as a stable, high capacity anode material for Li-ion batteries.* Journal of Materials Chemistry, 2012. **22**(24): p. 12198-12204.

27. Zhukovskii, Y.F., et al., *Evidence for Interfacial-Storage Anomaly in Nanocomposites for Lithium Batteries from First-Principles Simulations.* Physical Review Letters, 2006. **96**(5): p. 058302.

28. Cherian, C.T., et al., *Li-cycling properties of nano-crystalline ($Ni_{1-x}Zn_x$)Fe_2O_4 ($0 \leq x \leq 1$).* Journal of Solid State Electrochemistry, 2012. **16**(5): p. 1823-1832.

29. Zhou, L., D. Zhao, and X.W. Lou, *Double-shelled $CoMn_2O_4$ hollow microcubes as high-capacity anodes for lithium-ion batteries.* Adv Mater, 2012. **24**(6): p. 745-8.

30. Wang, Y., et al., *Wintersweet-Flower-Like $CoFe_2O_4$ /MWCNTs Hybrid Material for High-Capacity Reversible Lithium Storage.* Chem Asian J, 2012.

31. Tao, T., et al., *MoO_3 nanoparticles dispersed uniformly in carbon matrix: a high capacity composite anode for Li-ion batteries.* Journal of Materials Chemistry, 2011. **21**(25): p. 9350.

Chapter 7 Effect of morphology, particle size and Li-cycling voltage range on the electrochemical performance of tin based oxides

7.1 Introduction

Li alloy forming elements (M= Sn, Si, Sb, Ge, Zn, Al, In, Bi, Cd etc.) are considered as prospective anode materials due to their ability of reversibly reacting with large amount of Li thereby delivering high capacity at relatively low voltage vs. Li. Sn and Si are the most relevant among Li alloying elements with a theoretical capacity of 990 mAh g^{-1} and 4200 mAh g^{-1}, respectively, forming $Li_{4.4}M$ alloy. Poizot *et al*.[1] achieved a break through by demonstrating the reversibility of displacement reaction of transition metal (TM) oxides with lithium, termed 'conversion reaction'. Upon lithiation or electrochemical reduction of TM oxides, nanometer scale metallic clusters are dispersed in amorphous Li_2O matrix and thus all possible oxidation states of compound can be utilized during charging, to achieve high reversible capacity. Upon lithiation or electrochemical reduction of TM oxides, nanometer scale metallic clusters will be dispersed in amorphous Li_2O matrix and thus all possible oxidation states of compound can be utilized during charging, to achieve high reversible capacity.

Several tin based binary and ternary oxides such as SnO [2, 3], SnO_2[4-7], $CaO.SnO_2$[8], $SnO(VO_x)$[9] and Co_2SnO_4[10], $CaSnO_3$ [11] , $M_{1/2}Sb_{1/2}SnO_4$ (M= V, Fe, In)[12, 13], Zn_2SnO_4[14] have been studied as anode materials since they can be reduced to Sn by Li and hence could be used as precursors for $Li_{4.4}Sn$ alloys. Lithia (Li_2O) that is formed on reduction acts as an 'inactive matrix' that surrounds the active alloying element Sn, helps to maintain the integrity of the microstructure of the composite electrode during (de-) alloying process. The major drawbacks of these oxides are cell polarization and first-cycle irreversibility. [15]

The oxide, SnO_2 (cassiterite) has been more extensively studied for their electrochemical performance. The electrochemical reaction of lithium with tin dioxide involves two main steps. First, tin dioxide is converted to lithia and metallic tin at less than 1 V as in eqn. 7.1.

$$SnO_2 + 4Li \rightleftarrows Sn + 2Li_2O \qquad \text{eqn. 7.1}$$

The so formed metallic tin reacts with lithium to form intermetallic phases at potentials less than 0.6 V:

$$Sn + 4.4Li \rightleftarrows Li_{4.4}Sn \qquad \text{eqn. 7.2}$$

Assuming a reversible alloying process of 4.4 Li per Sn, the maximum theoretical capacity for SnO_2 would be 781 mAh g^{-1} whereas for SnO, it would be 880 mAh g^{-1}. The lithia forms a matrix that basically remains electrochemically inactive below an upper cut-off voltage of 1.5 V. Dahn *et al.*[2, 16] consider the Li_2O matrix that is formed during first discharge as a 'glue', which helps to hold the Li-Sn regions together through the large volume changes in the alloying/ dealloying process. At room temperature there are eight distinct Li-Sn phases of which the crystal structures are known. These are Sn, Li_2Sn_5, LiSn, Li_7Sn_3, Li_5Sn_2, $Li_{13}Sn_5$, Li_7Sn_2, and $Li_{22}Sn_5$. [2, 16] The crystal structure of Li-Sn alloys with low concentration of lithium i.e. Li_2Sn_5 and LiSn has related layered structure and so structural transitions between these two phases are quite reversible. [2, 16] In-order to prevent the formation of higher concentration Li-Sn alloy phases, Dahn *et al.* [2] cycled SnO electrodes in a voltage range 0.4-1.3 V. It is found that over this voltage range, reaction of SnO with Li is more reversible compared to that in the voltage range 0-1.3 V. It should be noted that in this voltage range, only one mole lithium is reversible cycled exhibiting a capacity value of ~200 mAh g^{-1}, which is lower than that of carbon anode. Later Kim *et al.*[17] found that realization of $Li_{22}Sn_5$ phase at deep discharged state (0 V) is practically impossible and XRD

studies on the discharged electrodes after deep discharge to 0 V showed the presence of a mixture Li_5Sn_2, $Li_{13}Sn_5$ and Li_7Sn_2 with a maximum uptake of 3.5 moles of Li. Higher potential values in the upper cut off region may destroy the lithium oxide matrix. During the extraction of lithium at potentials of around 2 V, certain tin-oxygen interactions have been observed, and partial tin re-oxidation may occur. So the choice of Li-cycling voltage range is a crucial factor determining the capacity value and stability of Sn based oxides.

Other than choice of proper voltage range, the issue of capacity fading can be addressed by various approaches such as (i) using some counter (matrix) elements in conjunction with the alloy–forming anode, but at the cost of achievable reversible capacity. (ii) Decreasing the size to nanometer range so that relatively low number of atoms per grain leads to lesser volume change upon cycling and thus the mechanical strain generated within the particles are effectively reduced in comparison to micron-size particles. [15] (iii) Fabricating 1D nanostructures such as nanowires as electrode materials provides better accommodation of strain and efficient electron transport through an anisotropic 1D pathway, in addition to benefits of the nano-scale dimensions. [18] Our idea is to fabricate Zn and Sn based 1D nanostructures containing proper matrix element.

Zinc has been proven to be a good matrix element since it can contribute to capacity due to alloying-de-alloying reaction besides buffering the volume variation. [19, 20] Belliard *et al*. [14] investigated the electrochemical performance of ball-milled ZnO-SnO_2 composite and found that the cycling performance of the electrode was improved when a small amount of ZnO was added into the composites. Wang *et al*. [21] developed SnO_2/ZnO nanowire array on Cu substrates and cycled in the voltage range 0.005- 2.0 V at a current of 120 mA g^{-1}.

SnO_2/ZnO composite nanowire array showed a large reversible capacity of 556 mAh g^{-1} after 30 cycles and better cycling performance compared to that of SnO_2 nanotubes [22], SnO_2 hollow spheres [23], SnO_2 nanoparticles [21] and ZnO nanowires. [21] A composite oxide of Zn and Sn, Zn_2SnO_4, which has an inverse spinel structure, received much interest due to its application in gas sensors, dye sensitized solar cells and photo-electrochemical cells. [24-26] Previous studies on the Li-cycling behavior of Zn_2SnO_4 showed that when lithium ions are inserted, its inverse spinel structure will collapse and metallic Sn and Zn as well as Li–Sn and Li–Zn alloys will be formed. [27, 28] So the crystal structure destruction and huge unit cell volume variation accompanied by the conversion and alloying/de-alloying reaction can cause capacity loss during cycling. Rong *et al.* [28] prepared Zn_2SnO_4 nanoparticles by hydrothermal method and studied its electrochemical properties in the voltage range 0.005- 3 V. It delivered an initial discharge capacity of 1384 mA h g^{-1} which faded to 580 mAh g^{-1} after 50 cycles. Park *et al*. [29] fabricated 1D SnO_2 nanowires by thermal evaporation process and compared its electrochemical properties with that of SnO_2 powders in the range of 0.005-1.5 V. SnO_2 nanowires showed an initial discharge capacity of 1134 mAh g^{-1} and fading to 220 mAh g^{-1} after 50 cycles, which was better than SnO_2 powders.

In the present work, nano- and micron sized SnO samples are prepared by simple and versatile routes and the effect of proper voltage range and morphology on its Li-cycling performance are investigated. Influence of counter matrix element and nano-structuring on the electrochemical performance of Sn based oxides are studied by a representative system, Zn_2SnO_4. Its nanowires are synthesized directly on stainless substrates by thermal evaporation method and tested as anodes for lithium ion batteries. Its Li-cycling properties are compared with that of

hydrothermally prepared Zn_2SnO_4 nanoplates in two different voltage ranges; 0.005- 3 V and 0.005- 1.5 V. The structural and morphological evolutions of the Zn_2SnO_4 nanowires upon lithium insertion/de-insertion are studied and the effect of voltage range and morphology on the Li-cycling behavior of Zn_2SnO_4 is examined.

7.2 Experimental

SnO nanoparticles are prepared by high energy ballmilling, a slightly modified form of mechano-chemical reaction adopted by Yang *et al*. [30] The starting materials were anhydrous tin (II) chloride (1.9 g), anhydrous Na_2CO_3 (1.1 g) and NaCl (3.5 g). The compounds were weighed and taken in to glove box. NaCl was used as a diluent and added to the starting powder. All the precursors were put in a stainless steel vial along with zirconia balls. The vials were closed air tight and taken outside the glove box. The mixture was subjected to high energy ball-milling (HEB) (SPEX-8000D Mixer/Miller, USA), at 1400 rpm for 3 h. The ball to powder weight ratio was 4:1. Ballmilled powders were washed and dried thoroughly to obtain SnO nanoparticles. SnO microcrystals were prepared by an aqueous solution synthesis route put forward by Ken *et al*.[31] An aqueous solution containing 5M urea and 50 mM SnF_2 is prepared with 100 ml of distilled water in a Teflon beaker. It was kept at 80°C for 12 h. The resultant precipitate was collected, washed thoroughly and dried at 60°C to obtain the final product.

Zn_2SnO_4 NWs were synthesized by a vapour transport method involving co-carbothermal reduction of ZnO and SnO_2, using a horizontal tube furnace. A mixture of ZnO, SnO_2 and graphite powders was used as source powder, which was positioned at the closed end of a quartz tube. Stainless steel substrates were

placed nearer to the open end of the quartz tube. The small quartz tube was inserted into a large alumina tube, which was sealed and heated to 900°C at a rate of 20°C min^{-1} and held for 30 min in an argon / 1 % oxygen atmosphere with a flow rate of 80 sccm. The base pressure was 10^{-2} mbar, and process pressure was 2 mbar during NW growth. After growth, the furnace was allowed to cool down naturally in Ar atmosphere. The weight of the active material is calculated using high sensitive microbalance, Shimadzu Libror AEM-5200 model. Zn_2SnO_4 nanoplates are prepared via hydrothermal route using Na_2CO_3 as mineralizer, adopting a method reported by Annamalai *et al*. [32] The compounds were characterized by powder X-ray diffraction (XRD) (Philips X'PERT MPD, Cu Kα) and high resolution transmission electron microscope (HR-TEM) (JEOL JEM 2100 operating at 200 kV). For transmission electron microscopy (TEM) studies, the powder samples of the as-synthesized Zn_2SnO_4 are dispersed in acetone using ultrasonic device. Acetone containing Zn_2SnO_4 nanowires/nanoplates is dropped to a carbon supporting Copper grids. Stainless steel substrate coated with Zn_2SnO_4 nanowires are directly used as electrodes for Li-cycling. Coin-type test cells (size 2016) were assembled in an argon-filled glove box (MBraun, Germany) and the cell components were Li metal (Kyokuto Metal Co., Japan) foil as counter electrode, glass micro-fiber filter (GF/F, Whatman Int.Ltd., Maidstone, England) as the separator and 1M $LiPF_6$ in ethylene carbonate (EC) and dimethyl carbonate (DMC) (1:1 by volume, Merck Selectipur LP40) as the electrolyte. Electrode preparation procedure adopted for Zn_2SnO_4 nanoparticles is discussed elsewhere[33]. The cyclic voltammetry and galvanostatic discharge-charge cycling of the cells were carried out at room temperature (25°C) by computer controlled

MacPile II (Biologic, France) unit and Bitrode multiple battery tester (model SCN, Bitrode, USA), respectively.

7.3 Results and discussions

7.3.1 Structure and morphology

7.3.1.1 SnO nanoparticles and microcrystals

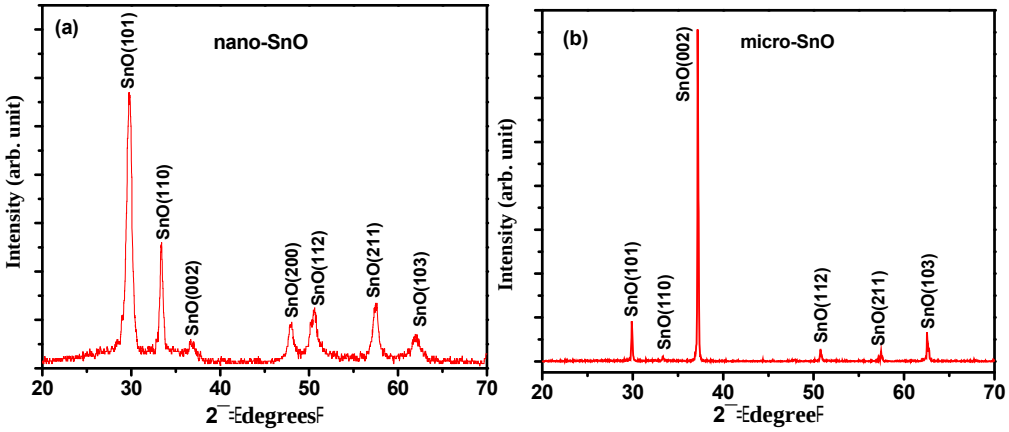

Figure 7.1 X-ray diffraction (XRD, Cu Kα radiation.) patterns (a) SnO nanoparticles. (b) SnO microcrystals. Miller indices of SnO are shown.

The powder XRD patterns of the SnO samples prepared by ballmilling and aqueous solution route are shown in Figure 7.1(a) and (b) respectively. It revealed the formation of compound in phase pure form in tetragonal structure without any impurities. For the preparation of SnO nanoparticles, a stoichiometric mixture of the starting materials was ballmilled to initiate the solid state displacement reaction shown in eqn. 7.3

$$SnCl_2+Na_2CO_3+ 6NaCl = SnO + CO_2 + 8NaCl \qquad \text{eqn. 7.3}$$

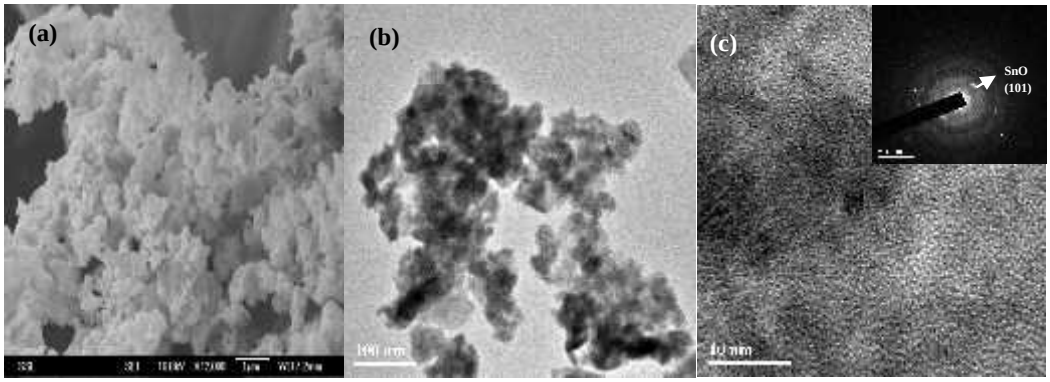

Figure 7.2(a) SEM photograph of nano-SnO. Scale bar is 1 μm. (b) TEM photograph of nano- SnO. Scale bar is 100 nm. (c) HRTEM lattice image of nano-SnO. Scale bar is 10 nm. (e) SAED pattern of nano- SnO. Miller index (101) is shown.

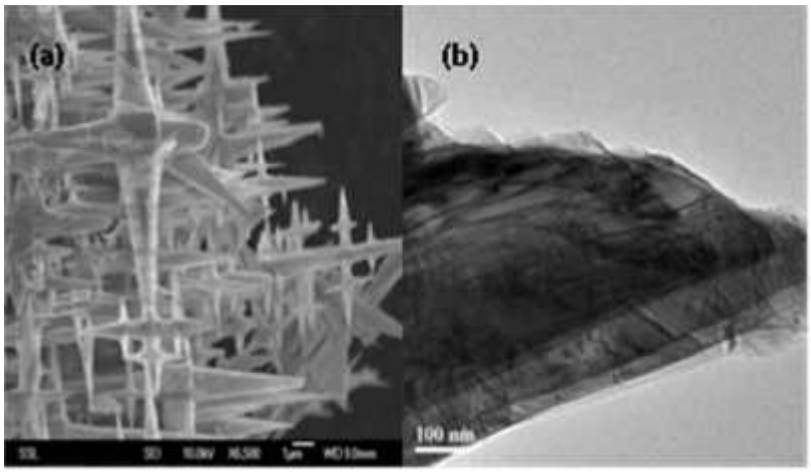

Figure 7.3 SEM photograph of micro-SnO. Scale bar is 1 μm. (b) TEM photograph of micro- SnO. Scale bar is 100 nm.

SnO samples prepared by ballmilling show broad peak indicating nanocrytalline nature of the material whereas sharp peaks of SnO prepared by aqueous solution synthesis confirm the formation of microcrystals. High intense hkl line (002) in the XRD pattern Figure 7.1(b) is due to the preferred orientation of SnO microcrystals. The lattice parameter values are obtained by the Rietveld refinement; with a=3.78 Å, c= 4.89 Å for SnO prepared by ballmilling and a=3.81 Å, c= 4.83 Å for SnO from aqueous solution synthesis. Figure 7.2 (a) to (c) displays the SEM and TEM images of SnO sample prepared by ballmilling. Nano-size, agglomerated particle like morphology is clearly evident from the Figure 7.2(a) and (b). The high

resolution lattice image in Figure 7.2 (c) shows randomly oriented nano-crystalline regions, and the measured interplanar spacing of 0.30(±0.02) nm matches well with the d-value (0.298 nm) of the Miller index, (101) of SnO nanoparticles. Inset of Figure 7.2(c) shows the SAED pattern of nano-SnO which consists of diffuse rings and spots confirming the co-existence of nano-crystalline and amorphous regions. Figure 7.3 (a) and (b) show SEM and TEM images of SnO microcrystals respectively. Stacked mesh like morphology can be clearly seen with a size of 100-500 nm for each structure.

7.3.1.2 Zn_2SnO_4 nanostructures

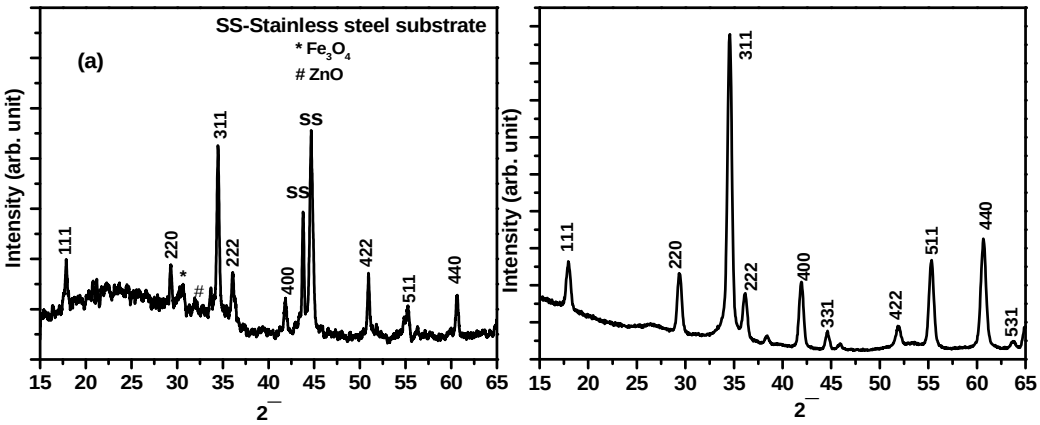

Figure 7.4 X-ray diffraction (XRD) patterns (Cu Kα radiation) of (a) Zn_2SnO_4 nanowires on stainless steel substrate. (b) Hydrothermally prepared Zn_2SnO_4 nanoplates. Miller indices are shown. 2θ in degrees.

XRD patterns of Zn_2SnO_4 nanowires (on stainless steel substrate) and nanoplates are shown in Figure 7.4 (a) and Figure 7.4 (b), respectively. Except the lines due to stainless steel (SS) substrate, the positions of the main peaks of Zn_2SnO_4 nanowires XRD pattern are consistent with JCPDS data (74-2184) of face centered spinel-structured Zn_2SnO_4 with a space group of Fd3m and lattice parameter of a = 8.650 Å. An impurity line corresponding to Fe_3O_4 (18 %) can be seen at 30.4° which is initiated from the SS substrate due to oxidation of Fe, during the synthesis.

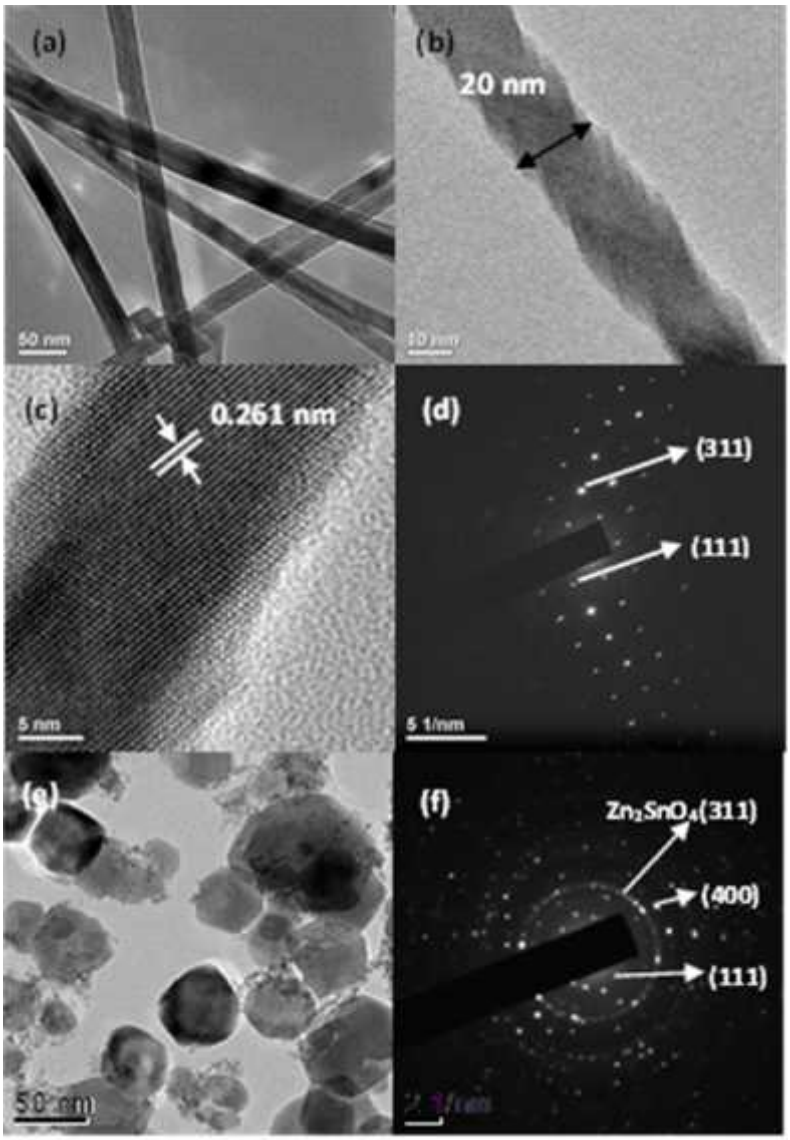

Figure 7.5 TEM photograph of (a) Zn_2SnO_4 nanowires. Scale is 50 nm. (b) Zn_2SnO_4 nanowires. Scale is 10 nm. (c) HRTEM lattice image of Zn_2SnO_4 nanowires. Scale is 5 nm. (d) SAED pattern of Zn_2SnO_4 nanowires. (e) TEM photograph of Zn_2SnO_4 nanoplates. Scale is 50 nm. (e) SAED pattern of Zn_2SnO_4 nanoplates.

Figure 7.5(a) shows a low-magnification TEM image of the Zn_2SnO_4 nanowires. The synthesized nanowires have uniform diameters of 20 -30 nm, and their lengths extend up to 10 μm (not fully captured in the image). As opposed to many conventional types of nanowires that present smooth surface morphologies, the most striking observation is that these nanowires exhibit periodic surface morphologies. A magnified TEM image focusing on a single Zn_2SnO_4 nanowire is

shown in Figure 7.5(b). Close examination reveals that the nanowire is formed through the self-assembly and fusing of a chain of inlaid rhombohedral crystals such that regular steps with a step size of about 10 nm develop on the nanowire surface.

Chen *et al*. [34] and Wang *et al*. [35] observed periodically twinned Zn_2SnO_4 nanowires during their TEM investigation on Zn_2SnO_4 nanowires synthesized by the thermal evaporation method. The HRTEM lattice image of NWs is shown in Figure 7.5(c) and the measured interplanar spacings match well with the d-value (0.260 nm) corresponding to the (311) plane. The selected area electron diffraction pattern (SAED) in Figure 7.5(d) consists of bright spots with (111) and (311) planes indicated. Nanoplate-like morphology of the hydrothermally prepared Zn_2SnO_4 sample is well evident from Figure 7.5(e) and the corresponding SAED pattern (Figure 7.5(f)) consists of bright spots superimposed on diffuse rings indicating nanocrystalline nature of the sample. The inter-planar distances (d-values) corresponding to these spots/rings are derived by measuring the diameter of two symmetric spots/rings about the center. The derived d-values are attributable to the (111), (311) and (400) planes of cubic-Zn_2SnO_4.

7.3.2 Li- cycling studies

7.3.2.1 SnO nanoparticles and microcrystals

The voltage range for Li-cycling studies on SnO is selected to be 0.005- 0.8 V. The choice of lower cut off voltage of 0.005 V is for the realization of high concentration Li phases so that high capacity can be obtained during cycling. An upper cut-off voltage of 0.8 V is chose, in order to prevent the re-formation of Sn. Electrochemically formed Sn nanoparticles may show a tendency to aggregate and

form large clusters in order to reduce surface free energy. The formation of large clusters can also lead to cracking of the electrodes and eventually an increase in the internal resistance.

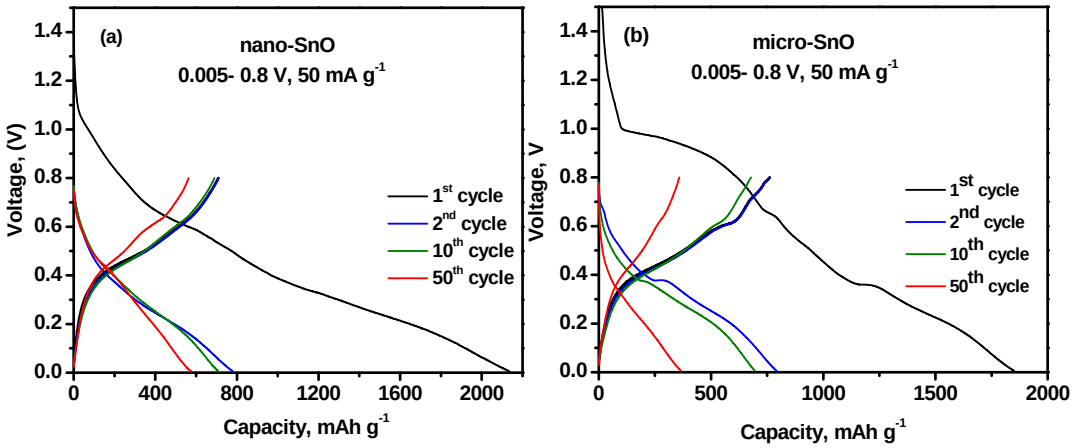

Figure 7.6 Voltage vs. capacity profiles (a) Nano- SnO (b) Micro- SnO. Voltage range: 0.005- 0.8 V vs. Li; current: 50 mA g^{-1} (0.07 C).

The galvanostatic cycling response in the form of voltage vs. capacity profiles of SnO nanoparticles and microcrystals, in the voltage range, 0.005- 0.8 V vs. Li at the current 50 mA g^{-1} are shown in

Figure 7.6(a) and (b) respectively. The profiles of selected cycles only are shown for the sake of clarity. Firstly, the cells are discharged from the open circuit voltage (OCV= 2.6 V) to 0.005 V vs. Li. For nano-SnO, the voltage steeply drops to ~1.1 V followed by a continuously sloping voltage profile, yielding a capacity of 2130 mAh g^{-1}. This corresponds to an uptake of 10.7 moles of Li per mole of SnO nanoparticles. In the case of micro-SnO, the voltage steeply drops to ~1.0 V followed by a plateau region up to a capacity of 730 mAh g^{-1} and afterwards, a downward sloping voltage profile is seen yielding a capacity of 1870 mAh g^{-1}. This corresponds to an uptake of 9.4 moles of Li per formula weight. The observed high initial discharge capacity can be due to uptake of more lithium during crystal structure destruction and solid electrolyte interphase (SEI) formation during the deep discharge. [36]

When the SnO nanoparticle electrode is charged to 0.8 V, voltage rises rapidly up to 0.35 V followed by a smooth upward sloping voltage plateau yielding a capacity of 578 mAh g^{-1}. Rapid increase in the slope is noticed afterwards, delivering a total first charge capacity of 706 mAh g^{-1}. Upon charging, the voltage profile of micro-SnO shows a sudden increase in voltage, then an upward sloping region at ~0.3 V followed by a small plateau region at 0.6 V. It is clear from the Figure 7.6(b) that before the onset of small voltage plateau near 0.6 V, a capacity of 530 mAh g^{-1} is obtained which corresponds to an uptake of ~ 2.6 moles of Li. The small potential plateau may possibly due to the coexistence of different alloy phases. An uptake of 2.6 moles of Li corresponds to the formation of $Li_{13}Sn_5$ phase. It is followed by an upward sloping region and delivering first charge capacity of 755 mAh g^{-1} which corresponds to 3.8 moles of Li. So the voltage plateau at 0.6 V can be considered as the co-existence of $Li_{13}Sn_5$ and Li_7Sn_2 phases. The second discharge capacity is 781 mAh g^{-1} whereas the corresponding charge capacity is 680 mAh g^{-1}.

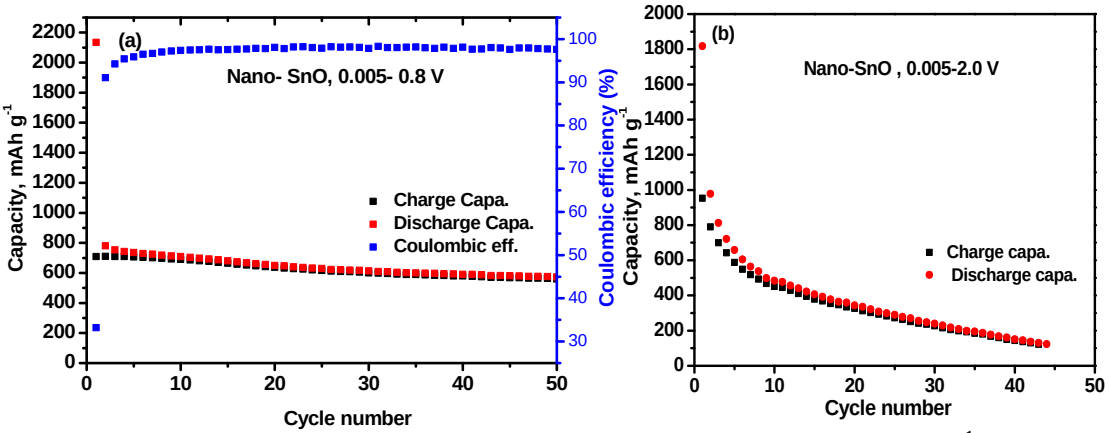

Figure 7.7 Capacity vs. cycle number plot of nano SnO. Current: 50 mA g^{-1} (0.07 C). (a)Voltage range: 0.005- 0.8 V vs. Li. (b) Voltage range: 0.005- 2.0 V vs. Li.

The voltage plateau in galvanostatic charge-discharge curves arise in micro-SnO can be due to the coexistence between Li-Sn alloy phases of different composition. These phases have different volumes per tin atom and hence the grains within the

particles will most likely crack and crumble during cycling, leading to capacity loss. [37] On the basis of electrochemical studies on SnO_2, SnO and Sn_2BPO_6, Dahn *et al*. [37] concluded that smooth voltage profiles and featureless differential capacity curves should generally cycle better than those with plateau-type voltage profiles. The present study upholds the findings of Dahn's group. The voltage profiles of nano- SnO show continuous sloping curves during both discharge and charge process which indicates that Li insertion/extraction reaction may be occurring through a solid solution domain[38]. The charge-discharge profiles of micro-SnO show sharp, distinct voltage plateau during initial cycles. The Li-cycleabiliy of both the samples can be well understood from the capacity-cycle number plot in Figure 7.7 and Figure 7.8. The capacity vs. cycle number plot, shown in Figure 7.7(a), indicates that a reversible discharge capacity of 738 (±3) mAh g^{-1} is maintained by SnO nanoparticles after 5 cycles with a capacity fading of 23 % between 5-50 cycles.

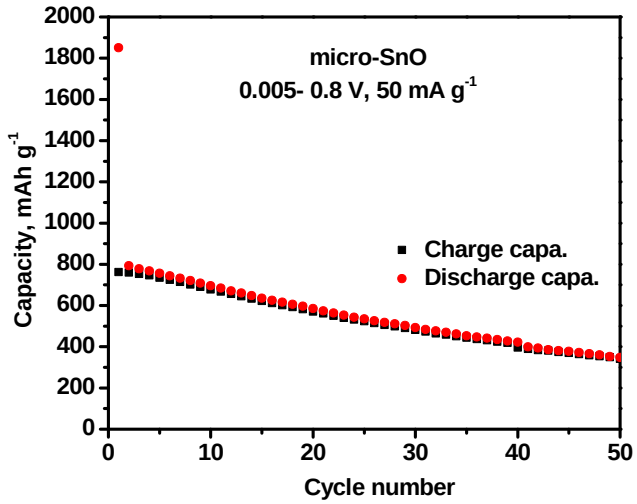

Figure 7.8 Capacity vs. cycle number plot of micro-SnO. Current: 50 mA g^{-1} (0.07 C). Voltage range: 0.005- 0.8 V vs. Li.

On contrary, when cycled in the range of 0.005- 2.0 V (Figure 7.7(b)), nano-SnO showed a capacity of 610 mAh g^{-1} after 5 cycles with its capacity rapidly fading to

120 mAh g^{-1} by 45 cycles. Figure 7.8 displays the capacity vs. cycle number plot for micro-SnO nanoparticles and it exhibits a reversible capacity of 791 mAh g^{-1} with capacity fading of 57 % between 1-50 cycles. So it is clear that nano-SnO shows a better electrochemical performance compared to micro-SnO when cycled in the voltage range of 0.005 V- 0.8 V. Rate capability of nano-SnO electrodes are investigated in various C rates assuming 1C= 700 mAh g^{-1} (Li_7Sn_2) which is the maximum capacity deliverable in 1 h. A current density of 100 mA g^{-1} correponds to 0.14C and the C-rate is changed in increasing order from 0.14 C to 1.12 C as shown in Figure 7.9(a). As can be seen, at each C-rate the capacity remained fairly stable with a capacity of 215 mAh g^{-1} observed at 0.84 C.

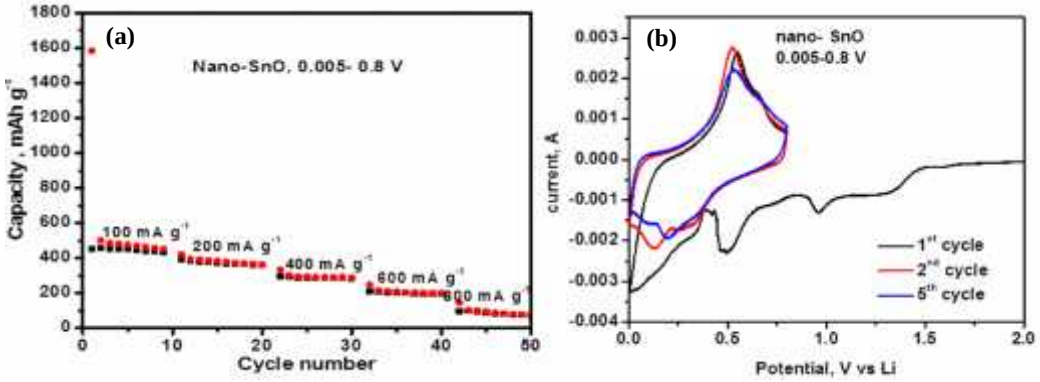

Figure 7.9 (a) Capacity vs. cycle number plot of nano-SnO at different C-rates. Voltage range: 0.005- 0.8 V vs. Li. (b) Cyclic voltammogram of nano- SnO. Potential window, 0.005- 0.8 V; scan rate, 58 μV s^{-1}. Li metal was the counter and reference electrode.

Cyclic voltammetry is a complementary technique to galvanostatic cycling and helps in understanding the nature and potentials at which the discharge–charge reactions take place in the electrode material. Figure 7.9(b) shows the cyclic voltammograms (CVs) of nano-SnO in the potential window 0.005- 0.8 V vs. Li recorded at the slow scan rate of 58 μV s^{-1} up to 10 cycles. No sharp peaks can be observed in CV curves which corroborates well with the galvanostatic charge-discharge voltage profiles with smooth curves. The first cathodic scan starts from

OCV=2.4 V and shows first broad peak at 1.3 V due to the reaction of SnO with two moles of lithium to form amorphous Li_2O and Sn. [37] The peaks at 0.95 V and 0.48 V corresponds to SEI formation and alloy reaction respectively. The first anodic curve shows a single broad peak at 0.55 V with an additional small shoulder peak at 0.66 V which indicates stepwise de-alloying of Li. The peak position shifts slightly to left during further cycling. The CV curve of third cycle shows well defined redox couple at 0.13 V/0.53 V which is related to alloying/de-alloying of various Li-Sn phases.

Ex-situ TEM studies

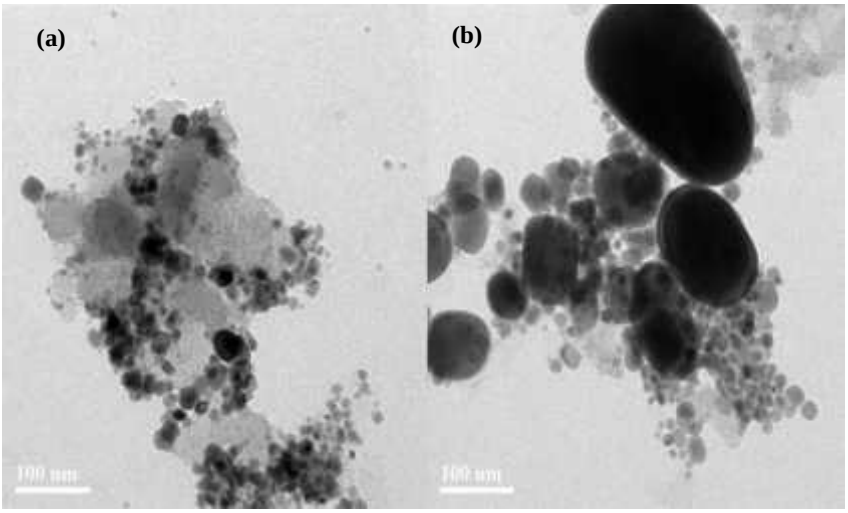

Figure 7.10 TEM images of particles of the cycled electrodes (after 2 discharge-charge cycles, voltage range: 0.005- 0.8 V) of (a) SnO nanoparticles (b) SnO microcrystals.

TEM studies are carried out on the powders scratched out from the charged electrodes of SnO nanoparticles and microcrystals, after 2 cycles to study morphology changes in the material. Figure 7.10 clearly shows that after 2 discharge-charge cycles, SnO nanoparticles prepared via ballmilling maintain its morphology with particle size of 20 nm. On the other hand, the stacked mesh like morphology of SnO microcrystals are destroyed upon cycling and transformed in to particles of size ~ 150 nm. Nanoparticles of conductive carbon added during

electrode fabrication can also be seen in Figure 7.10(a) and (b). From ex-situ TEM studies, it can be concluded that the unique morphology and nano-size of SnO samples prepared by ballmilling technique also have a beneficial effect on the Li-cycling behaviour of SnO, in the voltage range 0.005- 0.8 V.

7.3.2.2 Zn_2SnO_4 nanostructure

Cyclic voltammetry is carried out in the voltage range, 0.005 - 3 V, to identify the mechanism of the Li-cycling of Zn_2SnO_4 nanowire electrodes, with Li-metal acting as the counter and reference electrode. Figure 7.11 represents the cyclic voltammogram (CV) of the first 3 cycles of Zn_2SnO_4 nanowire electrodes cycled in the range of 0.005- 3 V, at the rate 58 μV sec^{-1}. First cathodic scan shows two major peaks at 0.4 and 0.6 V and a sharp peak at 0.05 V which corresponds to multistep electrochemical lithiation process (eqn. 7.4) and the formation of solid electrolyte interphase due to the reduction of solvents in the electrolyte followed by Li-alloying of Sn and Zn (eqn. 7.5 and 7.6).

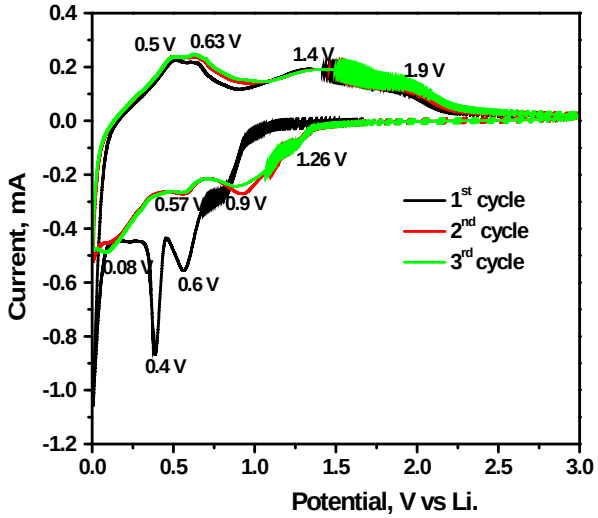

Figure 7.11 Cyclic voltammogramm of Zn_2SnO_4 nanowire electrode. Potential window, 0.005- 3.0 V; scan rate, 58 μV s^{-1}. Li metal was the counter and reference electrode.

$Zn_2SnO_4 + 8Li \rightarrow 2Zn + Sn + 4Li_2O$ eqn. 7.4

$Sn + 4.4Li \leftrightarrow Li_{4.4}Sn$ eqn. 7.5

$2Zn + 2Li \leftrightarrow 2LiZn$ eqn. 7.6

The peaks at 0.4 and 0.6 V disappears in subsequent cathodic cycles and three small peaks are emerged at 0.57 V, 1.26 V and 0.9 V. According to H. Wang et al.[39], Li-Zn alloy formation occurs at 0.35 V and multistep de-alloying process of Li-Zn alloy occurs in the range of 0.5-0.8 V vs. Li whereas de-alloying/alloying reaction of Li4.4Sn at voltages 0.3-0.5 V versus Li [40]. So during the anodic scan, the peaks at 0.5 V and 0.63 V correspond to de-alloying reaction of Zn and Sn. It is clear from the previous studies; Sn metal is converted to Sn^{2+} at 1.3 V (eqn. 7.7) whereas the oxidation of Sn^{2+} to Sn^{4+} and Zn^0 to Zn^{2+} (eqn. 7.8 and 7.9) happens above 1.5 V [29, 41-43]. So the peaks at 1.34 V and 1.9 V in the anodic curve can be assigned to conversion reaction of Sn to SnO and eventually to SnO_2 as in eqn. 7.7 and eqn. 7.8. The redox couple 0.9/1.34 V is attributed to the conversion reaction of SnO and 0.07 V/0.5 V and 0.57/0.63 V corresponds to Li-alloying-dealloying reaction of Sn and Zn, respectively (eqn. 7.5 , 7.6 and 7.7). It is noticeable from the cyclic voltammetry studies that the conversion of SnO to SnO_2 and Zn to ZnO can be excluded if we restrict the voltage window to 1.5 V.

$Sn + Li_2O \leftrightarrow SnO + 2Li$ eqn. 7.7

$SnO + Li_2O \leftrightarrow SnO_2 + 2Li$ eqn. 7.8

$Zn + Li_2O \leftrightarrow ZnO + 2Li$ eqn. 7.9

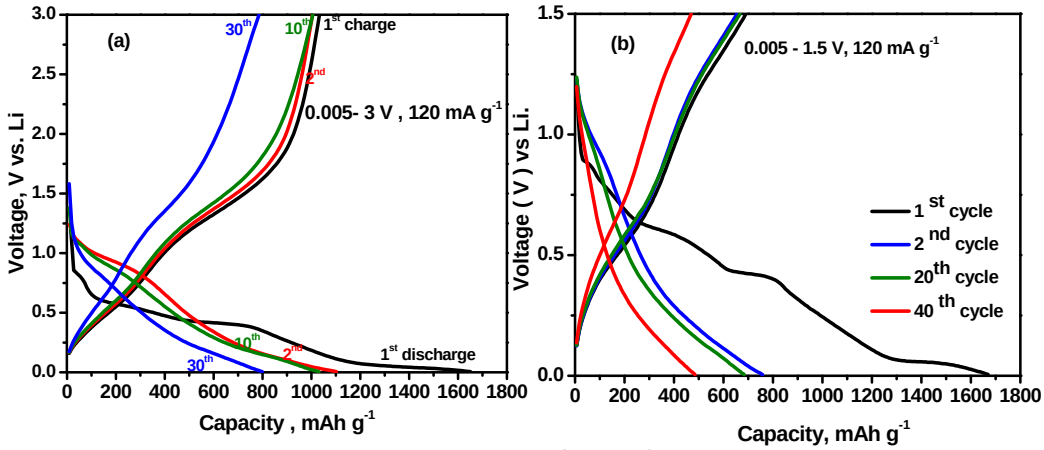

Figure 7.12(a) Voltage vs. capacity profiles of Zn_2SnO_4 NW electrodes. (b) Capacity vs. cycle number plot for Zn_2SnO_4 NW electrodes. Voltage range: 0.005- 3 V vs. Li; current: 120 mA g^{-1}.

Galvanostatic cycling studies of Zn_2SnO_4 nanowires and nanoparticles are carried out in two voltage ranges; 0.005- 3 V and 0.005- 1.5 V at the current rate of 120 mA g^{-1} to examine the effect of voltage range on Li-cycling performance. The charge-discharge profiles of the Zn_2SnO_4 NWs in the voltage range 0.005- 3 V and 0.005- 1.5 V are shown in Figure 7.12(a) and (b), respectively. First discharge capacity of ~1650 mAh g^{-1} is obtained in both the voltage ranges. During first discharge, the cell voltage steeply drops to 0.9 V. Then three plateau like steps at ~ 0.9 V, 0.6 V and 0.4 V can be noticed, yielding a capacity of ~1260 mAh g^{-1} corresponding to an uptake of 14.7 moles of Li per formula unit. This can be ascribed to the structural destruction up on Li insertion, subsequent formation of Zn and Sn nanoparticles in Li_2O matrix, accompanied with the uptake of 8 moles of Li per formula weight as shown in eqn. 7.4. So formed metallic Sn and Zn nano-domains undergo alloying reaction with Li to form Li–Sn, Li-Zn alloy phases which is clear from the extra capacity of 420 mAh g^{-1} obtained below 0.2 V. Theoretical capacity that can be yielded by the alloying-dealloying of Li with Zn and Sn is 547 mAh g^{-1} which corresponds to 6.4 moles of Li per formula wt. of Zn_2SnO_4. But first discharge capacity, 1650 mAh g^{-1}, obtained is higher than the

theoretical capacity of 1232 mAh g^{-1} which corresponds to 14.4 moles of Li according to eqn. 7.4, 7.5 and 7.6. Excess capacity can be regarded as originating from low voltage decomposition of the solvent in the electrolyte and subsequent formation of solid electrolyte interphase. It should be noted that the reformation of Zn_2SnO_4 structure is not plausible when the discharging is taken to completion i.e. up to 0.005 V. During the charging up to 3 V, a smooth voltage profile is observed till 0.7 V which is followed by sloping voltage plateau up to ~ 2 V and a steep rise up to 3.0 V. Upon charging, the electrochemical de-alloying process will be followed by the conversion reaction of Sn to Sn^{4+} and Zn to Zn^{2+}, yielding a higher reversible capacity of 1000 mAh g^{-1}. The achievable theoretical capacity limit upon charging to 3 V is 1061 mAh g^{-1} which corresponds to 12.4 moles of Li as per eqn. 7.4 to 7.9.

The capacity-cycle no. plot obtained from galvanostatic cycling data of Zn_2SnO_4 nanowires and nanoparticles in two voltage ranges; 0.005- 3 V and 0.005- 1.5 V at the current rate of 120 mA g^{-1}, are shown in Figure 7.13. In the voltage range of 0.005 to 3 V, a reversible capacity of 1000 mAh g^{-1} is maintained for 15 cycles and thereafter fades to 695 mAh g^{-1} after 40 cycles with a capacity fading of 15 % between 15-40 cycles. Thus the Li-reaction mechanism occurs via conversion reaction of ZnO and SnO_2 along with the alloying de-alloying of Sn and Zn. The unit cell volume of the lithiated products (after deep discharge) $Li_{22}Sn_5$, LiZn are 7739 $Å^3$ and 242 $Å^3$ whereas that of delithiated products (after charge to 3 V) Sn, Zn, SnO_2, ZnO are 108 $Å^3$, 72 $Å^3$, 30 $Å^3$, 48 $Å^3$ respectively. So the reactions shown in eqn. 7.5 to 7.9 are accompanied by a large unit cell volume variation which finally leads to a detachment of active material from the current collector.

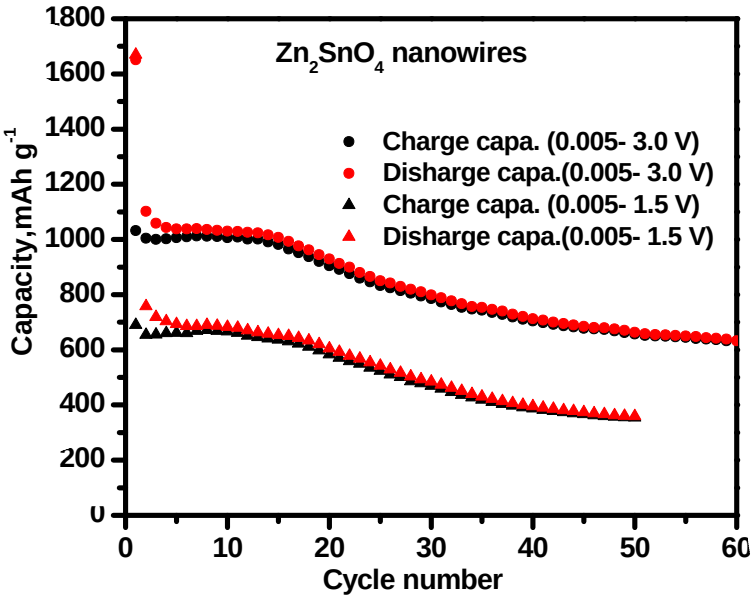

Figure 7.13 Capacity vs. cycle number plot for Zn_2SnO_4 electrodes. Voltage range: 0.005- 3.0 V vs. Li and 0.005- 1.5 V vs. Li; current: 120 mA g^{-1}.

If the potential limit is cut at 1.5 V, the oxidation of SnO to SnO_2 and Zn to ZnO can be circumvented thereby reducing the unit cell volume variation at the cost of achievable capacity, A total of 8.4 moles of Li is involved in the conversion reaction of SnO (eqn. 7.7) and alloying-de-alloying of Sn and Zn (eqn. 7.5 and 7.6) with a theoretical capacity of 719 mAh g^{-1}. The first discharge and charge capacities values are 1670 mAh g^{-1} and 690 mAh g^{-1}, respectively. Figure 7.13 shows the capacity vs. cycle no plot of the electrodes cycled in the range of 0.005 – 1.5 V. A reversible capacity of 670 mAh g^{-1} is obtained and remains constant for first 10 cycles thereafter it starts decreasing. After 40 cycles, a capacity value of 385 mAh g^{-1} is retained which is higher than the theoretical capacity of conventional graphite electrode.

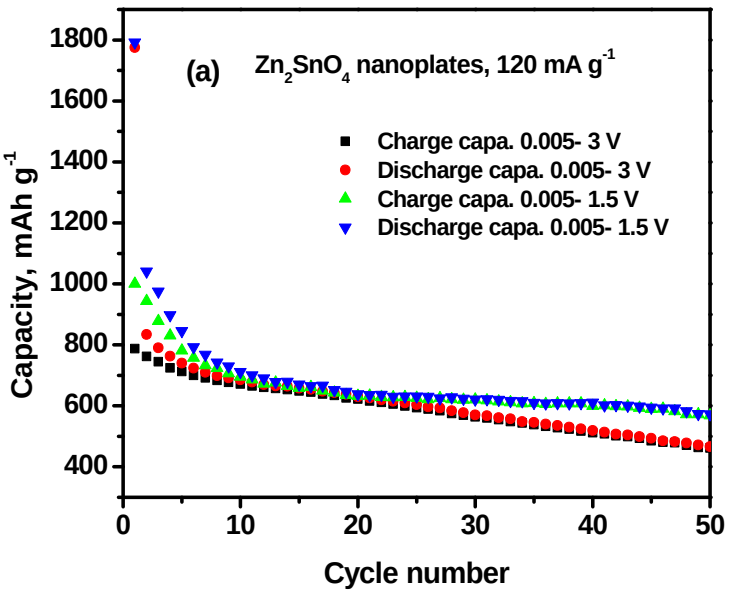

Figure 7.14 (a) Capacity vs. cycle number plot for Zn_2SnO_4 nanoplate electrodes. Current: 120 mA g^{-1}.

The capacity vs. cycle number plot derived from galvanostatic charge-discharge profiles of Zn_2SnO_4 nanoplates are shown in figure 7.14. In the voltage range 0.005- 1.5 V, it shows a first discharge capacity of 1800 mAh g^{-1} and rapidly fades 640 mAh g^{-1} by 20 cycles. Capacity retention of 90 % is obtained between 20-50 cycles. On the other hand, when cycled up to 3 V, a reversible capacity of 630 mAh g^{-1} is achieved after 20 cycles which gradually fades to 470 mAh g^{-1} after 50 cycles with capacity retention of 74 % between 20-50 cycles.

Ex-situ TEM studies

To investigate the morphology and microstructure of the products formed upon Li-cycling; the material is recovered from the nanowire electrodes charged to 1.5 V, after 2nd and 15th charge–discharge cycles. TEM images and SAED patterns are shown in Figure 7.15(a) to (d). After the second charge to 1.5 V, the width of the nanowires increased to ~55 nm (as-synthesized nanowires were 20 nm in width) and nanoparticles of size 40 nm started forming inside the wires.

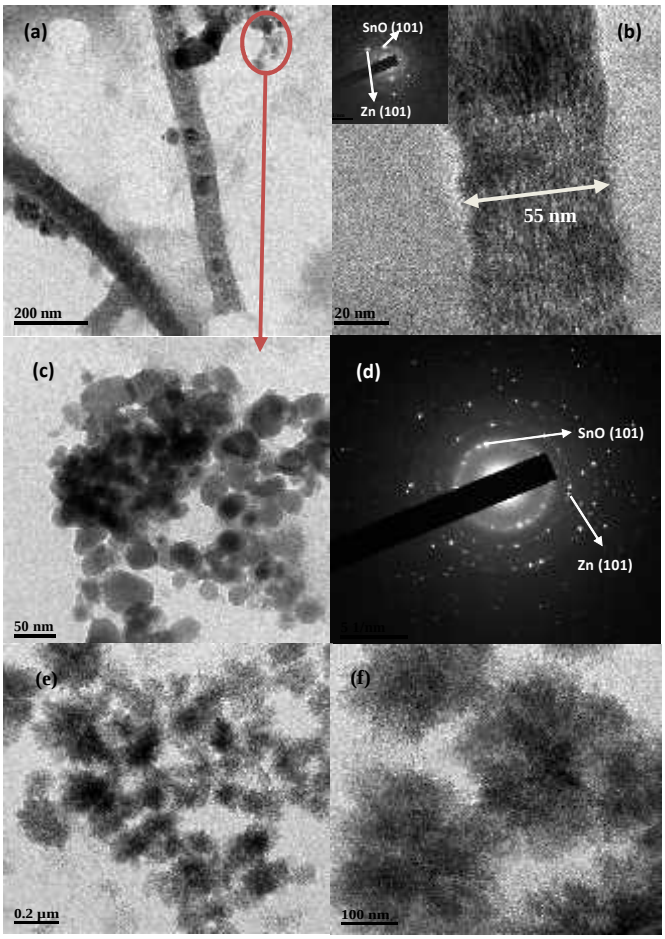

Figure 7.15 Zn_2SnO_4 nanowire electrode charged to 1.5 V after 2 cycles. (a) TEM image of the cycled nanowires. Scale bar is 100 nm. (b) TEM image of the cycled nanowires. Scale bar is 20 nm. Inset shows the SAED pattern and selected Miller indices. (c) TEM image of the nanoparticles formed from cycled nanowire electrode. Scale bar is 50 nm. (d) SAED pattern of circled region in (c). SnO and Zn along with Miller indices are indicated. (e) Zn_2SnO_4 nanoplate composite electrode charged to 1.5 V after 2 cycles. Scale bar is 0.2 µm. (f) Zn_2SnO_4 nanoplate composite electrode charged to 1.5 V after 2 cycles. Scale bar is 100 nm.

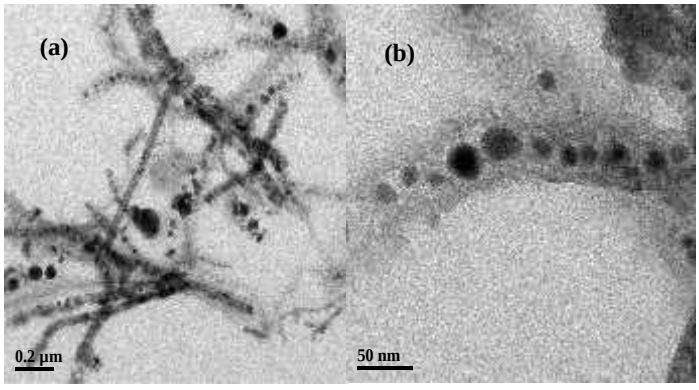

Figure 7.16 TEM image of Zn_2SnO_4 NW electrode charged to 1.5 V after 15 cycles. (a) Scale bar is 0.2 µm. (b) Scale bar is 50 nm.

The interplanar distance evaluated from the SAED pattern (Figure 7.15(b)) matches well with the d value of (101) plane of SnO and (101) plane of Zn. Figure 7.15(e) and (f) show the TEM image of Zn_2SnO_4 nanoplates after second charge to 1.5 V. Nanoplates like morphology got transformed in to interconnected nano-flowers and subsequently 'formation' or 'conditioning' of the electrode took place during initial cycles cycles, whereby the active material undergoes minor structural rearrangement and makes good electrical contact with the conducting carbon particles in the composite electrode, the current-collector and the liquid electrolyte. Figure 7.16 shows the ex-situ TEM images of Zn_2SnO_4 nanowire electrode material after 15 cycles, charged to 1.5 V. Nanowires have been completely broken down in to nanoparticles of size ~40 nm.

One dimensional nanowire like morphology of the electrode material can buffer the huge volume variation caused due to crystal structure destruction, alloying de-alloying reaction and conversion reaction only to some extent. After first 2 cycles, width of the nanowires is doubled and nano-sized particle formation starts along the nanowires (Figure 7.15(a)).By the end of 15 cycles, nanowires are completely broken down in to nanoparticles as can be seen in Figure 7.16. It can be confirmed that during charging to 1.5 V, the electrochemical de-alloying process will take place and the intermetallics formed during discharge process will be continuously separated in to Li, Sn and Zn nanodomains. The so formed Sn nanoparticles can get oxidized to SnO at a voltage of around 1.35 V but the Zn remains intact since oxidation of Zn to ZnO occurs just above 1.5 V. [20, 42] During first 15 cycles, Zn_2SnO_4 nanowire electrode showed capacity retention of 95 % whereas nanoplates showed drastic capacity fading, when cycled in both voltage ranges. In the voltage range 0.005- 3 V, nanowire electrode retains a capacity of 660 mAh g-

1 after 50 cycles and in the lower cut off voltage of 1.5 V, a capacity of 390 mAh g^{-1} is delivered after 50 cycles. The capacity fading % between 20-50 cycles, of nanowire electrodes in the voltage ranges 0.005- 3 V and 0.005- 1.5 V is calculated to be 72 and 60 % respectively.

7.4 Conclusions

In summary, Li-cycling behavior of micro and nano-sized SnO is investigated in the voltage range 0.005- 0.8 V. Nano-size aggregates of SnO are prepared by high-energy ballmilling followed by washing and subsequent drying at 60°C. Stacked mesh like microcrystals of SnO are synthesized in aqueous solution by simple precipitation at 80°C. Its cycling behaviour is studied in the voltage range 0.005-0.8 V. The voltage profiles of nano- SnO show continuous sloping curves due to solid solution behavior during both discharge and charge process whereas micro-SnO shows sharp, distinct voltage plateau due to the coexistence between Li-Sn alloy phases. In the selected voltage range, SnO nanoparticles showed better electrochemical performance with capacity retention of 77 % between 5-50 cycles compared to 43 % for SnO microcrystals. It can be concluded that high energy ballmilling technique can be adopted as a synthetic technique for the large scale production of SnO nanoparticles with novel electrochemical performance as anode material for LIBs. It is also clear that apart from the morphology, the particle size and voltage range also plays a crucial role in the cycling behavior of SnO.

Self-supported Zn_2SnO_4 nanowire on stainless steel electrodes are fabricated and its electrochemical performances are compared with hydrothermally synthesized Zn_2SnO_4 nanoparticles in two voltage windows 0.005- 3 V and 0.005 – 1.5 V. The capacity fading behavior observed in Zn_2SnO_4 nanowire electrodes, after 15

cycles, can be attributed to the complete destruction of nanowires to nanoparticles and eventual disconnection from the stainless steel substrate during further cycling.

7.5 References

[1] P. Poizot, S. Laruelle, S. Grugeon, L. Dupont, J.M. Tarascon, Nature, 407 (2000) 496-499.

[2] I.A. Courtney, J.R. Dahn, J. Electrochem. Soc., 144 (1997) 2045-2052.

[3] I.A. Courtney, W.R. McKinnon, J.R. Dahn, J. Electrochem. Soc., 146 (1999) 59-68.

[4] R. Liu, S. Yang, F. Wang, X. Lu, Z. Yang, B. Ding, ACS Applied Materials & Interfaces, 4 (2012) 1537-1542.

[5] C.A. Bonino, L. Ji, Z. Lin, O. Toprakci, X. Zhang, S.A. Khan, ACS Applied Materials & Interfaces, 3 (2011) 2534-2542.

[6] M.S. Park, G.X. Wang, Y.M. Kang, D. Wexler, S.X. Dou, H.K. Liu, Angew. Chem. Int. Ed., 46 (2007) 750-753.

[7] G. Derrien, J. Hassoun, S. Panero, B. Scrosati, Adv. Mater., 19 (2007) 2336-2340.

[8] Y. Sharma, N. Sharma, G.V. Subba Rao, B.V.R. Chowdari, Chem. Mater., 20 (2008) 6829-6839.

[9] B. Das, M.V. Reddy, G.V. Subba Rao, B.V.R. Chowdari, J. Solid State Electrochem., 15 (2010) 259-268.

[10] R. Alcántara, G.F. Ortiz, P. Lavela, J.L. Tirado, Electrochem. Commun., 8 (2006) 731-736.

[11] M. Mouyane, M. Womes, J.C. Jumas, J. Olivier-Fourcade, P.E. Lippens, J. Solid State Chem., 184 (2011) 2877-2886.

[12] M.V. Reddy, G.V. Subba Rao, B.V.R. Chowdari, J. Mater. Chem., 21 (2011) 10003-10011.

[13] M.V. Reddy, G.V. Subba Rao, B.V.R. Chowdari, J. Solid State Electrochem., (2012) 1-9.

[14] F. Belliard, P.A. Connor, J.T.S. Irvine, Solid State Ionics, 135 (2000) 163-167.

[15] X. Yuan, H. Liu, J. Zhang, in, CRC Press, 2011.

[16] I.A. Courtney, J.R. Dahn, J. Electrochem. Soc., 144 (1997) 2943-2948.

[17] Y.-J. Kim, M.-S. Park, H.-J. Sohn, H. Lee, J. Alloys Compd., 509 (2011) 4367-4371.

[18] C.K. Chan, H. Peng, G. Liu, K. McIlwrath, X.F. Zhang, R.A. Huggins, Y. Cui, Nat Nano, 3 (2008) 31-35.

[19] Y. Sharma, N. Sharma, G.V. Subba Rao, B.V.R. Chowdari, Adv. Funct. Mater., 17 (2007) 2855-2861.

[20] C. Cherian, M. Reddy, G. Rao, C. Sow, B. Chowdari, J. Solid State Electrochem., 16 (2012) 1823-1832.

[21] J. Wang, N. Du, H. Zhang, J. Yu, D. Yang, Mater. Res. Bull., 46 (2011) 2378-2384.

[22] J. Wang, N. Du, H. Zhang, J. Yu, D. Yang, The Journal of Physical Chemistry C, 115 (2011) 11302-11305.

[23] P. Wu, N. Du, H. Zhang, C. Zhai, D. Yang, ACS Applied Materials & Interfaces, 3 (2011) 1946-1952.

[24] B. Tan, E. Toman, Y. Li, Y. Wu, J. Am. Chem. Soc., 129 (2007) 4162-4163.

[25] M.A. Alpuche-Aviles, Y. Wu, J. Am. Chem. Soc., 131 (2009) 3216-3224.

[26] Z. Chen, M. Cao, C. Hu, The Journal of Physical Chemistry C, 115 (2011) 5522-5529.

[27] S.M. Becker, M. Scheuermann, V. Sepelak, A. Eichhofer, D. Chen, R. Monig, A.S. Ulrich, H. Hahn, S. Indris, PCCP, 13 (2011) 19624-19631.

[28] A. Rong, X.P. Gao, G.R. Li, T.Y. Yan, H.Y. Zhu, J.Q. Qu, D.Y. Song, J. Phys. Chem. B, 110 (2006) 14754-14760.

[29] M.S. Park, G.X. Wang, Y.M. Kang, D. Wexler, S.X. Dou, H.K. Liu, Angewandte Chemie - International Edition, 46 (2007) 750-753.

[30] H. Yang, Y. Hu, A. Tang, S. Jin, G. Qiu, J. Alloys Compd., 363 (2004) 276-279.

[31] K. Sakaushi, Y. Oaki, H. Uchiyama, E. Hosono, H. Zhou, H. Imai, Nanoscale, 2 (2010) 2424.

[32] A. Annamalai, D. Carvalho, K.C. Wilson, M.-J. Lee, Mater. Charact., 61 (2010) 873-881.

[33] C.T. Cherian, J. Sundaramurthy, M. Kalaivani, P. Ragupathy, P.S. Kumar, V. Thavasi, M.V. Reddy, C.H. Sow, S.G. Mhaisalkar, S. Ramakrishna, B.V.R. Chowdari, J. Mater. Chem., (2012).

[34] H. Chen, J. Wang, H. Yu, H. Yang, S. Xie, J. Li, The Journal of Physical Chemistry B, 109 (2005) 2573-2577.

[35] J. Wang, X.W. Sun, S. Xie, W. Zhou, Y. Yang, Crystal Growth & Design, 8 (2007) 707-710.

[36] C.T. Cherian, M. Reddy, G.V. Subba Rao, C.H. Sow, B.V.R. Chowdari, J. Solid State Electrochem., 16 (2012) 1823-1832.

[37] I.A. Courtney, J.R. Dahn, J. Electrochem. Soc., 144 (1997) 2943-2948.

[38] C.T. Cherian, M.V. Reddy, T. Magdaleno, C.-H. Sow, K.V. Ramanujachary, G.V.S. Rao, B.V.R. Chowdari, CrystEngComm, 14 (2012) 978-986.

[39] H. Wang, Q. Pan, Y. Cheng, J. Zhao, G. Yin, Electrochim. Acta, 54 (2009) 2851-2855.

[40] N. Sharma, J. Plévert, G.V. Subba Rao, B.V.R. Chowdari, T.J. White, Chem. Mater., 17 (2005) 4700-4710.

[41] J. Li, Y. Zhao, N. Wang, L. Guan, Chem. Commun., 47 (2011) 5238-5240.

[42] Y. Deng, Q. Zhang, S. Tang, L. Zhang, S. Deng, Z. Shi, G. Chen, Chem. Commun., 47 (2011) 6828-6830.

[43] D. Aurbach, A. Nimberger, B. Markovsky, E. Levi, E. Sominski, A. Gedanken, Chem. Mater., 14 (2002) 4155-4163.

Chapter 8 Conclusions

8.1 Summary

This thesis highlights the importance of the morphology, particle size and the Li-cycling voltage range on the Li-cycling performance of transition metal oxides (TMO). TMO anodes can be specified into insertion-type materials (such as $Li_4Ti_5O_{12}$, TiO_2 etc.), alloying-type materials (such as SnO_2, SnO etc.) and conversion-type materials (such as Fe_2O_3, $NiFe_2O_4$ etc.) The representative oxides from each group are prepared and the anodic performance of these materials is investigated.

The substitutional doping with nitrogen atom can enhance the charge transfer of TiO_2, because the conduction band of TiO_2 is broadened and shifted to give a narrow band gap. Our aim was to completely substitute oxygen anions with N^{3-} and F^- ions, so as to obtain TiNF instead of TiO_2. To end with, nitrogen and fluorine co-doped TiO_2 (TiO_2 (N,F)) has been synthesized by pyro-ammonolysis of TiF_3. The lattice parameters are evaluated from the Rietveld refined XRD data and the TiO_2 (N,F) has a more open structure than anatase-TiO_2 with larger *a* and smaller *c* value. The Li-storage and cycleability of nitrogen and fluorine co-doped TiO_2 of the composition, $TiO_{1.9}N_{0.05}F_{0.15}$ (TiO_2(N,F)) in the voltage range 1.0 - 2.8 V, is reported for the first time. Up on high energy ball-milling (HEB), the sub-micron sized anatase TiO_2(N,F) gets converted to the nano-phase (10-20 nm) rutile-TiO_2(N,F). Anatase-to-nano-rutile transformation by HEB is also confirmed in undoped-TiO_2 (commercial). Nano-phase rutile-TiO_2(N,F) exhibited a reversible capacity of 210 mAh g^{-1} (0.65 mole of Li) is observed after the first cycle, with a capacity-retention of 78% after 60 cycles. Nano-phase rutile- TiO_2 (obtained by HEB) exhibited a reversible capacity of 130 mAh g^{-1} (~ 0.4 mole of Li) which is

stable in the range, 10-60 cycles. Thus doping N^{3-} and F^{-} in to TiO_2 crystal structure is found to be beneficial for Li-cycling. Li-cycling properties of TiO_2(N,F) are much better than that of commercial micron size TiO_2 in its anatase and rutile polymorphs. This can be ascribed to a more open crystal structure and the fact that N^{3-} and F_- ions are more electronegative than the O^{2-} ions.

Among various transition metal oxides that are prospective anode for LIBs, binary iron oxide, α-Fe_2O_3 (hematite) and ternary iron oxide, $NiFe_2O_4$ are interesting due to their high capacity from conversion reaction, environment friendliness, abundance and low cost. Fe_2O_3 nanorods are prepared by the electrospinning and its Li-cycling performance is investigated in the voltage range 0.005- 3.0 V. Electrospun $Fe(acac)_3$/PVP fibers are sintered at 500°C for 5h to obtain α-Fe_2O_3 macroporous rods like structures with nanoparticles embedded in it. Electrospun α-Fe_2O_3 delivers high reversible capacity of 1095 mAh g^{-1} at 0.05C, with capacity retention of 93% between 2-50 cycles. A reversible capacity of 765 mAh g^{-1} is obtained at a current of 2.5 C. After 70 cycles, when the current rate is reduced from 2.5 C to 0.1 C, still a reversible capacity of 1090 mAh g^{-1} is obtained showing the excellent rate capability of the material. The novel morphology of electrospun α-Fe_2O_3 helps in the enhancing the inter-particle connectivity, giving a better cycling performance. The presence of large amount of γ-Fe_2O_3 is observed, from the Raman spectrum of cycled electrode of α-Fe_2O_3 and thus it is confirmed that α-Fe_2O_3 eventually transforms to γ-Fe_2O_3 during cycling.

$NiFe_2O_4$ can electrochemically react with 8 moles of Li delivering capacity of 915 mAh g^{-1} and moreover, both nickel and iron are abundant elements on earth and relatively non-toxic. Several efforts have been made to improve the long-term Li-

cycling behavior of $NiFe_2O_4$ such as adopting different synthesis methods to control the particle size and morphology and partial substitution of host structure with metal cations. Zn has been proven to be a good matrix element for conversion based reactions. Thus the effect of doping varying amounts of Zn and the consequent cation redistribution, on the Li-cycling behaviour of $(Ni_{1-x}Zn_x)Fe_2O_4$ is studied in the voltage range 0.005- 3.0 V. Two phase Li-intercalation reaction (in the voltage 0.9 to 0.8 V) in to the spinel structure is found for the compositions with high concentration of zinc ($x \geq 0.6$). $ZnFe_2O_4$ (x =1) performs very well in comparison to the other compositions with varying x values. It can be deduced that nano-sizing and the presence of Zn cation in the crystal structure do not help in improving the capacity stability of $NiFe_2O_4$ particles.

Inter-particle connectivity can be achieved by developing a conducting network throughout the electrode which can be realized by fabricating morphologically stout nanofibers of $NiFe_2O_4$ via electrospinning. Continuous $NiFe_2O_4$ nanofibers have been prepared by electrospinning of iron acetyl acetonate/nickel acetate/PVP-based precursors and subsequent annealing at 500 $^{\circ}$C. The nanofibers exhibited a high discharge capacity of 870 mAh g^{-1} with superior cycling stability to $NiFe_2O_4$ nanoparticles. Capacity fading is observed during initial 15 cycles and then stabilized at a capacity of 870 mAh g^{-1} by 20^{th} cycle. 100 % capacity retention is observed between 20-40 cycles and then an increase in capacity with 15 % rise between 40-100 cycles. In order to investigate the effect of morphology on cycling performance, micro-structural images of $NiFe_2O_4$ nanofibers are obtained before and after Li-cycling. Interestingly, the fiber like morphology remains intact even after 100 charge/discharge cycles. The morphological robustness of the electrospun $NiFe_2O_4$ nanofibers during conversion reaction is a unique feature that results in

high reversible capacity and good cycling stability. 100 % coulombic efficiency is achieved until 100^{th} cycle and it is due to the stabilization of interface layer (SEI) between the electrode and electrolyte.

Molybdates can also be considered as prospective 'conversion reaction' based anode materials due to the ability of the metal ions to exist in several oxidation states in these oxides, ranging from 3^+ to 6^+ for Mo and reversibly reacting with Li delivering high capacity, at potentials lower than 2 V. Here, nano-plates of molybdates ($AMoO_4$, A=Zn, Mo, Co) are synthesized by urea assisted microwave synthesis and studied the role of counter cations (Co, Zn, Ni) in the electrochemical performance of molybdates. $CoMoO_4$ nanoplates exhibit a reversible capacity of 540 mAh g^{-1} after 15^{th} cycle and the capacity retention % between 15-60 cycles is 94 %. On the other hand, $ZnMoO_4$ and $NiMoO_4$ deliver low capacity values, 182 mAh g^{-1} and 232 mAh g^{-1} respectively, after 60 cycles. Thus cobalt is found to be a better matrix element for the Li-cycling of molybdates compared to zinc and nickel. Capacity stability of $CoMoO_4$ is further improved by preparing interconnected macroporous network of sub-micron particles, adopting 'polymer precursor method'. The material exhibited a high reversible capacity of 990 (±10) mAh g^{-1} at a current density of 100 mA g^{-1}, with 100 % capacity retention between 5- 50 cycles. $CoMoO_4$ nano-plate composite electrodes need several cycles to complete the 'conditioning' phase whereas interconnected $CoMoO_4$ submicron particles efficiently overcome this phase without any capacity loss. The unique morphology of $CoMoO_4$, in which primary particles are mutually interconnected, has been considered beneficial for the electrochemical performance. It assures proper electronic conductivity and mechanical strength on a long extended electrode cycling.

Tin based binary and ternary oxides are prospective anode materials since they can be reduced to Sn by Li and hence could be used as precursors for $Li_{4.4}Sn$ alloys. The effects of voltage range and morphology on the Li-storage performance are evaluated for Sn based oxides systems such as SnO and Zn_2SnO_4 nanostructures. Nano-size aggregates of SnO are prepared by high-energy ballmilling followed by washing and subsequent drying at 60°C. Stacked mesh like microcrystals of SnO are synthesized in aqueous solution by simple precipitation at 80°C. Its Li-cycling behaviour is studied in the voltage range 0.005- 0.8 V. In the selected voltage range, SnO nanoparticles showed better electrochemical performance with capacity retention of 77 % between 5-50 cycles compared to 43 % for SnO microcrystals. SnO nanoparticles prepared via ballmilling maintain its morphology during Li-cycling with particle size of 20 nm. On the other hand, the stacked mesh like morphology of SnO microcrystals are destroyed upon cycling and transformed in to particles of size ~ 150 nm. It can be concluded that high energy ballmilling technique can be adopted as a synthetic technique for the large scale production of SnO nanoparticles with novel electrochemical performance as anode material for LIBs. It is also clear that apart from the morphology, the particle size and voltage range also plays a crucial role in the cycling behavior of SnO.

Self-supported Zn_2SnO_4 nanowires are fabricated on stainless steel electrodes by vapour transport method. Its electrochemical performances are compared with hydrothermally synthesized Zn_2SnO_4 nanoparticles in two voltage windows: 0.005-3 V & 0.005 – 1.5 V. For the first 10 cycles, Zn_2SnO_4 NW electrodes showed stable capacity whereas Zn_2SnO_4 nanoplate composite electrode showed drastic capacity fading. Zn_2SnO_4 NW electrodes show capacity fading after 10 cycles. It has been established from ex-situ TEM studies that complete destruction of

nanowires into nanoparticles after initial cycles contribute to the capacity fading of nanowire electrodes. The importance of morphological robustness during Li-cycling is established. An upper cut off voltage of 1.5 V is better than 3 V to obtain improved capacity stability in Zn_2SnO_4 composite electrode.

In conclusion, rutile nano-TiO_2(N,F) delivered higher capacity value compared to its undoped counterpart. However the capcity value is not good enough for high density application. Conversion reaction based oxide anodes can deliver high capacity compared to that of intercalation based oxides. Among various conversion based oxides, $CoMoO_4$ sub-micron particles and electrospun fibres of Fe_2O_3 and $NiFe_2O_4$ show high capacity with good capacity retention. The unique functionality of these oxides can be attributed to interconnected network-like morphology, providing better electron transport and strain accommodation. Cobalt can be considered as a good counter cation for the stable cycling performance of molybdates. Presence of two Li-alloying elements is proved to be detrimental to the Li-cycling performance and even nanowires may not withstand the enormous strain developed due to unit cell volume variation during cycling. In the present case, mutually interconnected Zn_2SnO_4 nanowires are transformed in to disconnected particles with in 20 charge-discharge cycles, leading to capacity fading.

8.2 Future work

On the basis of conclusions drawn from the present work, following suggestions are made for further study:

1. The internal resistance (impedance) of cells and polarization effects at the electrodes lower the practical voltage and the rate at which the

electrochemical reactions can take place. Fe_2O_3 and $NiFe_2O_4$ nanofiber electrodes show electrode polarization with a voltage hysteresis of ~0.6 V. The voltage hysteresis can be reduced by improving electronic and ionic conductivity by doping or surface coating. Carbon coating on these fibers can be done in this aspect. It is worthwhile to synthesize nano-composites of these oxides with noble metals so as to utilize the catalytic property of noble metal nanoparticles in enhancing the electrochemically driven 'conversion' reaction happening in oxide materials during Li-cycling.

2. In view of the excellent anodic performance of interconnected $CoMoO_4$ sub-micron particles, it is significant to fabricate lithium ion full cells using an appropriate cathode material.
3. Detailed study to investigate the reason for the difference in the capacity retention of $CoMoO_4$, $ZnMoO_4$ and $NiMoO_4$ sub-micron particles.
4. Nanofibers of molybdates such as $CoMoO_4$, $ZnMoO_4$, $NiMoO_4$ can be prepared and its electrochemical performance both as cathode and anode for lithium ion battery, can be investigated.
5. Whatever be the morphology, Sn based oxides are getting transformed in to nanoparticles after cycling, so conductive surface coating/conductive network is inevitable to ensure inter-particle connectivity and thus a stable capacity behaviour. Surface coating with carbon or mixing the oxides with carbon nanotubes can be adopted to improve its Li-cycling behaviour. It is prudent to fabricate Zn_2SnO_4 nanofibers by electrospinning and to observe the morphological variations after Li-cycling.

6. Synthesis and electrochemical studies of composites of NiO/Fe_2O_3 and CoO/MoO_3 and compare the Li-cycling performance with that of $NiFe_2O_4$ and $CoMoO_4$.
7. Last but not the least, the issue of high irreversible capacity loss during first discharge and charge cycle observed in almost all the oxide systems, should be tackled. For this purpose, some key aspects need further investigation:
    - Side reactions between electrode and electrolyte components.
    - Adding novel solvent additives to the electrolyte.
    - Effect of additives on the stability window of electrolytes during electrochemical reaction and on mechanism for lithium uptake/extraction.
    - Nature of the solid electrolyte interface (SEI) formed.